Radio Surveys of Star Formation in the Milky Way with the Next Generation of Interferometers

Author:
Mubela MUTALE

Supervised by:
Prof. Mark THOMPSON
Dr. Jan FORBRICH
Dr. James. L COLLETT

Centre for Astrophysics Research

School of Physics, Engineering and Computer Science

University of Hertfordshire

Submitted to the University of Hertfordshire in partial fulfilment of the requirements of the degree of Doctor of Philosophy.

July 2022

Abstract

This thesis embodies work that contributes towards building our knowledge on the birth of massive stars. It presents three projects that study young HII regions which, being a direct product of the birth of massive stars, offer a unique window into this process.

I have mapped a $2.3° \times 2.3°$ region around W49A with the first Galactic Plane survey to explore the subarcsecond and sub-mJy regime at 14 GHz. I have detected a total of 1238 compact sources from which I have identified 82 as young HII regions. I have derived SEDs for a subsample of the sources using 4 KuGARS sub-bands and CORNISH at 5 GHz. The derived spectrum shows that the HII regions are optically thick at 5 GHz and optically thin at 14 GHz. Their sizes imply they are in transition between the ultracompact (UC) and hypercompact (HC) stages. This process is contiguous with no sharp transition and no visible boundaries between the evolutionary stages, putting into question the need for multiple classifications. The observed trends suggest that HC and UC HII regions are in fact the same object. I have estimated the time they spend in high emission measure (EM) as an analogue to the lifetime of an HII region spent in the HC phase of its evolution. Using $10^8 \ pc \ cm^{-6}$ as an arbitrary boundary between high and low EM, I estimate that HII regions spend $\sim$41% of their lifetime in high EM, something of the order 10^4 years.

I carried out targeted observations toward 78 molecular clumps with star forming properties in the Outer Galaxy using the C-band of the VLA. This was in order to search for embedded UC HII regions, which would indicate ongoing star formation. Only 9 clumps have an embedded radio source, none of which are detected for the first time, implying massive star formation in the Outer Galaxy is not as prevalent as in the Inner Galaxy.

I present a catalogue of compact sources extracted from the MeerKAT-GPS, an L-band survey of the southern Galactic Plane covering around half the GP from $252° < l < 358°$, $2° < l < 60°$ and $|b| < 1.5°$ down to a nominal depth of $\sim$ 10-30 μJy. The catalogue contains 409790 compact sources above 5σ. I have extracted a subsample of 350 UC HII regions identified as counterparts to the RMS UC HII region samples in a search for extended emission associated with UC HII regions - this would conclusively explain the lifetime problem. However, I have found extended emission around $\sim 1/3$ of the sources, a lower ratio than found in previous studies ($\sim 8/10$). The lower ratio seen in this complete sample means we cannot rely entirely on extended components to explain the large number of observed UC HII regions.

Declaration

I declare that no part of this work is being submitted concurrently for another award of the University or any other awarding body or institution. This thesis contains a substantial body of work that has not previously been submitted successfully for an award of the University or any other awarding body or institution.

Except where indicated otherwise in the submission, the submission is my own work and has not previously been submitted successfully for any award.

Mubela Mutale
July 2022

Acknowledgements

I am deeply grateful to my principal supervisor, Prof. Mark Thompson, for guiding me through the dark maze of radio astronomy first through a master's degree and now a PhD. He has been the Michelangelo to my sistine chapel in more ways than one. Mark has been an amazing mentor in the science as well as the technical stuff, and has been a willing source of advice for basically everything else. I would like to thank my co-supervisor Dr Jan Forbrich for stepping into the role at such a critical time and for his help in guiding things to a graceful end. I would also like to thank Dr James Collett for being the third member of my supervisory team and for all the great mid-day discussions in the STRI.

Thanks to the University of Hertfordshire for funding my studentship and enabling me to pursue a career in astronomy, and the Centre for Astrophysics Research (CAR) for offering me the studentship and providing an ideal environment in which to do this. I am grateful to the staff at the NRAO for their support during the development of my data reduction and imaging pipelines, I came across every CASA bug possible and they were instrumental in helping fix them. And thanks to the University of Leeds' Physics and Astronomy department (Mark and Melvin) for trusting that I would successfully complete my PhD and offering me my first postdoc before I had completed my work on this thesis.

Without the unending support of my family, Emmanuel and Peggy (my parents) and Cupa (my brother), I would not be standing on this side of this thesis. Their encouragement and faith in me has meant everything.

I am thankful for the friends and colleagues I have made along the way: in CAR, the home of my PhD, as well as the larger radio astronomy and star formation communities. Thanks to the faculty members that gave their time and knowledge to my development. Elias Brinks and Martin Hardcastle, in particular, have devoted a tremendous amount of time to discussing concepts in radio astronomy that we all enjoyed, as well as dealing with mundane administrative tasks. Thanks to the PhD students and postdocs in CAR who became my friends and made the journey memorable.

Thanks to my examiners, Elias Brinks and Toby Moore, for taking on the tasks of reading my thesis and listening to me talk about it for several hours.

I could not have put this thesis together without the world of support that's been given to me throughout this journey, for that I am truly grateful.

Contents

List of Figures

List of Tables

List of Abbreviations

ALMA	**A**tacama **L**arge **M**illimetre **A**rray
CASA	**C**ommon **A**stronomy **S**oftware **A**pplications
CORNISH	**CO**ordinated **R**adio a**N**d **I**nfrared **S**urvey for **H**igh-Mass Star Formation
FITS	**F**lexible **I**mage **T**ransport **S**ystem
GLIMPSE	**T**he **G**alactic **L**egacy **I**nfrared **M**id-**P**lane **S**urvey **E**xtraordinaire
GMC	**G**iant **M**olecular **C**loud
GUI	**G**raphical **U**ser **I**nterface
IRAC	**I**nfra**R**ed **A**rray **C**amera
ISM	**I**nter **S**tellar **M**edium
JVLA	**J**ansky **V**ery **L**arge **A**rray
KuGARS	**Ku**-band **G**alactic **R**econnaissance **S**urvey
MC	**M**olecular **C**loud
MFS	**M**ulti-**F**requency-**S**ynthesis
MS	**M**easurement **S**et
NRAO	**N**ational **R**adio **A**stronomy **O**bservatory
OTFM	**O**n-**T**he-**F**ly **M**ap/Mapping
OTF	**O**n-**T**he-**F**ly
PAH	**P**olycyclic **A**romatic **H**ydrocarbon
PDRs	**P**hoton-**D**ominated **R**egion**s** or **P**hoto-**D**issociation **R**egion**s**
RFI	**R**adio **F**requency **I**nterference
RRL	**R**adio **R**ecombination **L**ine
SED	**S**pectral **E**nergy **D**istribution
SPW	**SP**ectral **W**indow
YSO	**Y**oung **S**tellar **O**bject

Chapter 1

Introduction

Massive stars ($M \gtrsim 8\ M_\odot$) are a central pillar in cosmic evolution hence an important part of astrophysics. They play a major role in the distribution of energy in galaxies; their stellar winds, ionizing radiation and supernovae deposit considerable amounts of energy in the interstellar medium (ISM). Their dominant effects are evident across the Universe through their feedback, synthesis and dispersal of heavy elements (Tan et al., 2014). Throughout their short main-sequence lifetimes, they run through processes that inherently affect the composition of star formation within a galaxy, and create HII regions as well as photon dominated regions through the ultraviolet photon flux they emit (Kurtz, 2005b). However, despite their importance, the process of high-mass star formation remains poorly understood. They present a significant observational barrier due to reaching the zero-age main-sequence (ZAMS) long before the process of accretion is complete. Because they reach the ZAMS while still undergoing heavy accretion, their heavy radiation and thermal pressure should terminate the infall of material thus stunting the star's growth at $\sim 8\ M_\odot$ (Palla and Stahler, 1993; Sánchez-Monge et al., 2013). Evidently, massive stars grow to sizes much larger than this, showing how little we know about the physics of high-mass star formation. Therefore, unlike low-mass star formation, high-mass star formation does not yet have a firmly established evolutionary model.

Massive star formation (MSF) is one of astrophysics' least understood problems. It is particularly difficult to study the birth of massive stars in the near-infrared and, more so, optical wavelengths because this process typically occurs within dense condensations

of molecular clouds, with visual extinctions of order a thousand (Kurtz, 2005b). Even though no dominating theory has arisen yet, a number of scenarios have been proposed. Stahler et al. (1980a,b) proposed that stars formed through accretion. This went on to be developed for low and intermediate mass stars (Palla and Stahler, 1993). It was later investigated for massive star formation and even though it worked well for low mass stars, accretion was deemed impossible for massive stars due to their high luminosities, which are able to reverse collapse (Bonnell et al., 1998; Stahler et al., 2000). Massive stars exert a radiation pressure on their surroundings that is greater than their gravitational attraction. The basic implication here is the more massive the star, the higher the luminosity and the greater the effect of radiation pressure on the accreting material. Therefore, the question of how massive stars can sustain accretion remained open for decades. However, several recent models show that radiation pressure can be overcome by high accretion rates, or Rayleigh Taylor instabilities in the accretion flow. Kuiper et al. (2012) pose a solution to the radiation pressure problem. In this solution, an anisotropy of the thermal radiation field can overcome the problem. In addition, they argue that Radiative Rayleigh-Taylor instabilities in the cavity regions are neither required nor do they occur in massive star formation. In another scenario, coalescence (Bonnell et al., 1998; Stahler et al., 2000), stars of greater than 10 solar masses are assumed to form when stars of intermediate masses merge. The less massive stars would prior to this have formed through accretion.

Other scenarios describe massive star formation through HII regions. Among these is the (Keto, 2003) gravitationally trapped model of HII regions. This model assumes the formation of a massive star by accretion onto young stellar objects (YSOs) through gravitationally trapped HII regions surrounding the star. In the early 2000s the conventional model assumed that UC HII regions represented the earliest manifestation of massive stars after forming via rapid accretion of ambient gas onto a protostellar hydrostatic core. In this model massive protostars evolve from prestellar cores, to hot cores, to UC HII regions to compact HII regions, to classical HII regions (Sewilo et al., 2004). The compact HII region is larger and has lower density than the UC HII region. However, Gaume et al. (1995) discovered a smaller and denser region than the UC HII region. The Hypercompact (HC) HII region, which they discovered near the NGC 7538 UC HII region, is 10 times smaller and 100 times denser than the UC HII region (Kurtz and Franco, 2002 ; Kurtz, 2002). Clearly, the physical parameters of HII regions span

orders of magnitude in scale, but the classes most closely linked to star formation are the smallest, densest and presumably the youngest stages (i.e. compact, UC and HC HII regions (Kurtz, 2005b)). The bright radio emission from these nebulae serves as a signpost of recent massive star formation.

1.1 The massive star formation environment

1.1.1 Molecular Clouds

Massive stars form in giant molecular clouds (GMCs). These are made up of filaments and clumps, therefore, their mass is not evenly distributed. Most of their mass lies in the low-density structures while only a small portion lies in the very dense parts. GMCs have typical sizes of tens of parsecs.

The most abundant element in the Universe is hydrogen. In the ISM, hydrogen is found to exist in three particular forms: free atomic hydrogen (HI), Molecular hydrogen (H_2), and interstellar atomic hydrogen that has been ionised (HII). In star-forming regions, the most prevalent of these is H_2, hence the dense molecular clouds in which stars are born. It is, however, easiest to observe hydrogen in its free atomic form, HI. This is because HI emits radio waves at a wavelength of 21 cm (1.4 GHz), associated with a hyperfine transition from a state in which the spins of the electron and proton are parallel to a state in which the spins are anti-parallel. Because the energy difference between these two states is really low corresponding to a very low temperature ($<<1$ K), HI can be excited in cold regions. Thus, it can be seen in the Milky Way and in many nearby galaxies. Hydrogen is much harder to observe when in molecular form, H_2. This is due to two major reasons: firstly, diatomic molecules have three excitation types: electronic, vibrational, and rotational, from highest to lowest in excitation scale. H_2 in the first rotational excited state, is 175 K above the ground state and the temperature at which molecules form in dense ISM is $\sim$10 K. Thus, molecules are unlikely to be in this excited state. Secondly, H_2 is a homonuclear molecule and therefore a transition to the first excited state is forbidden. This means that there are effectively no H_2 molecules in a molecular cloud in states capable of emitting (cf. Krumholz 2016).

1.1.2 Cores

Cores are smaller and denser and less massive than GMCs. They typically have densities of $\sim 10^7 cm^{-3}$. Cores are often only a few $M_\odot$, tend to be rounder than the lower density material around them, and are normally laid out across filaments of lower density gas. Cores are thought to be the forebears of single stars or star systems.

The prevailing thought is that star formation occurs within a core of gas and dust. The evolution is presumed to begin with gaseous sources with no traces of a star, followed by a core within which a protostar forms and evolves into a star which eventually ends up on the main-sequence. Therefore, it follows that this would begin with a cold cloud without a central point source. Within this cloud forms a protostar which gradually heats up the cloud while the gas in the cloud collapses onto the protostar, reducing the opacity. With time, after enough material has been accreted from the envelope onto the protostar, it progressively becomes transparent at shorter wavelengths, first in the near-infrared and then the optical, allowing direct observation of the star. Finally, after the accretion disk has fully been accreted, the star eventually contracts onto the main-sequence.

At its earliest stage the star-forming in the core will have a very low mass and hence a very low luminosity. Thus, it will only heat up the dust nearest to the centre of the core and by a very small amount. This will inherently make it difficult to directly trace the presence of the nascent star because the observed light output will be that of the thermal emission of the dust at its equilibrium temperature and thus the spectral energy distribution (SED) will appear much the same as before the star formed. However, the presence of an outflow or a sharp unresolved peak in the density flow can indicate the birth of a star. This type of object represents the earliest stage of star formation, and at this stage the object would fall into the so-called class 0. It will remain a class 0 object until it starts to heat up the dust around it beyond the dust's equilibrium temperature, consequently, emitting significantly in the infrared (IR); at this point, it evolves into a class I object. The cutting point for this is said to be when the source emits more than 0.5% of the bolometric output at wavelengths longer than 350 μm, that is, when the ratio of the sub-mm luminosity to the bolometric luminosity (L_{smm}/L_{bol}) is greater than 0.5% - where the sub-mm luminosity considers all wavelengths of 350 μm or longer. The evolution of the protostar from this point on is defined in terms of the IR SED. Therefore, the wavelength at which the SED peaks infers how evolved the

protostar is. During the earliest stages of the evolution, the envelope of dust around the protostar is optically thick at shorter wavelengths (visible and near IR). Ideally, this envelope absorbs all the radiation from the protostar. Nonetheless, the dust is in thermal equilibrium, and therefore re-radiates this energy. This emission will, however, be at longer wavelengths since the radius of the dust is much larger than the star and thus for the luminosity output of the dust to equal that of the star, this emission must be at a lower temperature, hence the longer wavelengths. We are able to observe the photosphere because the radiation shifts to longer wavelengths as it gets transmitted through the dust and at wavelengths longer than the characteristic sizes of the dust grains, the opacity roughly decreases as $\kappa_\lambda \propto \lambda^{-2}$, therefore the radiation eventually shifts to wavelengths at which the dust is optically thin, and consequently escapes. This essentially means we indirectly observe a stellar photosphere through a "dust photosphere". Therefore, the greater the column density of the envelope of dust, the further the radiation from the star will have to diffuse in wavelength in order to escape. Evidently, the wavelength at which the emission peaks or the slope of the spectrum at a fixed wavelength provides a good estimate to the amount of circumstellar dust. Objects whose SED peaks at longer wavelengths are early in their evolution while objects whose SED peaks closer to the optical are presumed to be more evolved having lost more of their envelopes (cf. Krumholz, 2016).

The infrared classification scheme used for classes I, II, and III was based on fluxes measured by the *Infrared Astronomical Satellite (IRAS)*. The infrared spectral index is therefore defined as,

$$\alpha_{IR} = \frac{d\,log(\lambda F_\lambda)}{dlog\lambda} \tag{1.1}$$

Where,

- α_{IR} is the infrared spectral index,

- λ is wavelength,

- F_λ is flux density as a function of wavelength.

This essentially means that positive values of α_{IR} indicate SEDs that peak in the longer wavelengths (further into the IR) while negative values of α_{IR} indicate SEDs that peak at

shorter wavelengths (closer to the optical). By this classification scheme, class I objects would therefore be sources with $\alpha_{IR} \geq 0.0$.

The more the envelope accretes, the more optically thin it becomes at the peak emitting wavelengths of the stellar photosphere, thus we see the stellar blackbody spectrum mixed in with the residual IR emission from the remnants of the warm, dusty gas surrounding the star. Stars in this class are known as class II objects (also known as T Tauri stars). Here, the SED appears as a stellar blackbody with additional emission in the near/mid-IR. Without the additional IR emission, these stars would have $\alpha \sim -1.6$, however, they have indices in the range $-1.6 < \alpha_{IR} < 0$. This is the last phase in which there is a disk of any significant mass and presumably the phase during which planet formation occurs.

The final group are the class III objects (weak line T Tauri stars). At this stage, the SEDs have $\alpha_{IR} < -1.6$. During this phase, there is no strong IR emission as the disk has begun to dissipate and is either optically thin in the IR, or has in fact completely dissipated. Therefore, any residual IR emission will be in the very far IR indicating cold circumstellar material distant from the star. Hence, the SEDs of these stars will appear as bare photospheres in the optical and mid-IR.

The evolution of high-mass stars is quite different from that of low mass stars. Our current knowledge on the evolution of massive stars comprises three main stages including infrared-dark clouds, hot molecular cores, and HII regions. The HII region phase, comprises multiple stages: the ultracompact, hypercompact, compact, classical, giant and supergiant stages (see Table 1.1).

1.1.3 Infrared-dark clouds

The infrared-dark cloud (IRDC) stage is the earliest phase of massive star formation to be observed. IRDCs are very dense, massive, inter-stellar clouds that are typically denser than the clouds from which low-mass stars form. IRDCs can have masses of the order 10^3 solar masses, and the temperature around IRDCs is typically around 10-20 K. Embedded in IRDCs are dark cores known as infrared-dark cores which have masses up to $\sim$100 $M_\odot$, radii that are typically ≤ 0.1 pc, and densities of up to $\sim 10^6$ cm^{-3}. Thus, these sites are known as the most likely to host massive star formation.

1.1.4   Hot cores

The dense interstellar clouds in which the process of star formation has just begun are known as hot molecular cores. This stage is believed to be the successor of the IRDC stage. The evolution from IRDCs to hot cores is thought to happen after newly forming stars have begun to heat the clouds within which they are forming. While hot cores have similar masses to IRDCs, they have much higher temperatures (100-200 K) and luminosities ($> 10^4$ L$_\odot$). When the stars are sufficiently hot and luminous, they begin to ionise their surroundings, and the HII region phase begins (see § 1.2).

1.1.5   Gravitational Collapse

1.1.5.1   Virial theorem and Jeans mass

A cloud's gravitational stability against gravitational contraction determines whether or not it collapses and goes through the process of star formation. The virial theorem states that; for a self-gravitating system in equilibrium,

$$
\begin{aligned}
2U + \Omega &= 0 \\
Or& \\
U &= -\tfrac{1}{2}\Omega
\end{aligned}
\tag{1.2}
$$

Where,

– U is the total thermal energy,

- Ω is the total potential gravitational energy.

In order for contraction to occur, the molecular cloud's mass must exceed a critical mass known as the Jeans mass. For this, we need the gravitational term in the virial theorem to overcome the pressure term. Therefore, for a molecular cloud to gravitationally collapse equation 1.2 becomes,

$$-\Omega > 2U \tag{1.3}$$

For a constant density cloud, this gives,

$$M_c > \left(\frac{5kT}{G\mu m_H} \right)^{\frac{3}{2}} \left(\frac{3}{4\pi\rho_c} \right)^{\frac{1}{2}} \qquad (1.4)$$

This is the critical mass, known as Jeans mass, required for contraction in a molecular cloud.

1.1.5.2 Fragmentation and accretion discs

Initially when the cloud collapses, its temperature remains constant so that the Jeans mass drops as the density increases. Consequently, denser fragments become unstable to collapse leading to star clusters. With time, the fragments will heat up and a hydrostatic core will form and if the cloud has a uniform rotation rate, conservation of momentum results in the cloud contracting parallel to the rotation axis. This leads to flattened rotating structures known as accretion discs.

1.1.5.3 Time scales

The time it takes for a cloud in free-fall to contract from its initial state to a state in which it has a radius much smaller than its original radius ($r_{final} \ll r_{initial}$) is called the free-fall time of the cloud,

$$\tau_{ff} = \left(\frac{3\pi}{32G\rho_0} \right)^{\frac{1}{2}} \qquad (1.5)$$

where, ρ_0 is the initial density of the cloud.

During the evolution of a newly formed star, its luminosity is supplied by the release of gravitational potential energy and is given by

$$L \simeq \frac{1}{2} \left[-\frac{d\Omega}{dt} \right] \qquad (1.6)$$

When a protostar has reached approximate hydrostatic equilibrium, it remains there and subsequently contracts quasi-statically. Quasi-static contraction of a star is sometimes referred to as Kelvin-Helmholtz contraction and the time-scale for evolution, as the star

contracts onto the main-sequence, is known as the Kelvin-Helmholtz contraction time-scale, τ_{K-H}. Thus, the time-scale for contraction from the protostellar hydrostatic core to the hydrogen burning main-sequence is given by,

$$\tau_{K-H} \sim \frac{GM^2}{R} \bigg/ L \tag{1.7}$$

and since for massive stars, $L \propto M^{3.3}$,

$$\tau_{K-H} \propto M^{-1.3}. \tag{1.8}$$

By this we see that for massive stars $\tau_{K-H} << \tau_{ff}$ and thus they arrive on the main-sequence while still deeply embedded in their molecular clouds. Therefore, because the massive star turns on its UV illumination while still accreting and embedded in a molecular cloud, it heats and eventually ionizes the circumstellar gas cloud thus creating an HII region. The HII region develops by expanding within the cloud.

1.2 HII regions

HII regions are made of interstellar atomic hydrogen that has been ionised by O- and B- type stars, which are young massive stars - the youngest HII regions are clouds of partially ionized gas in which massive star formation has recently taken place. Massive stars (> 8 $M_\odot$) evolve quickly and turn on their UV illumination before they finish accreting the material around them. HII regions are born when the UV radiation from the newly born star ionises the hydrogen in its ambient medium. Stars this massive are able to produce photons with energies above the ionization potential of hydrogen (13.6eV) in sufficient quantities to maintain the ionisation of the hydrogen in the region around the nascent star. An HII region is the region around the star within which the number of ionisations overwhelm the number of recombinations so that the gas remains ionised. As the HII region expands it could theoretically come into equilibrium: when the expansion of the HII region is large enough, it will reach a volume at which the number of ionisations exactly equals the number of recombinations. HII regions are important to the study of massive star formation because they are associated with

emission from transitions between energy levels of hydrogen and other atoms, and free-free (bremsstrahlung) emission in the radio. Bremsstrahlung is electromagnetic radiation produced by free electrons scattering off ions. It is produced when a charged particle is deflected by another charged particle causing it to decelerate and therefore lose energy and produce a photon. Evidently, HII regions are important because they allow us to see where recent massive star formation has taken place and since we can calculate their electron density, and Lyman photon flux, we can also determine the photon flux of the stars.

1.2.1 Evolution

The ionisation of hydrogen causes a drastic rise in temperature (~ 10 K to $\sim 10^4$ K) causing HII regions to be over pressured with respect to their surroundings, and expand over time. Therefore, the smallest of these regions are most likely to be the youngest and thus trace recent star formation. The three classes of HII regions that most closely trace recent massive star formation are the compact, ultracompact (UC), and hypercompact (HC) HII regions (Kurtz, 2005a). The sizes of HII regions span several orders of magnitude (see Table 1.1). The largest of them, all of which occur outside the Milky Way, are powered by clusters of massive stars, have diameters > 100 pc, and ionised masses $\gtrsim 10^5$ $M_\odot$. In the Milky Way, the size of HII regions is typically around 10 pc, but goes as low as 0.03 pc. In Fig. 1.1 are two common HII regions taken with the Hubble Space Telescope (HST): the Orion Nebula (left) and the Eagle Nebula (right). The colours in either image represent the different types of emission in them. In the Orion Nebula, the orange emission is hydrogen, the green is oxygen, and the red is sulphur and heated dust. In the Eagle Nebula, the blue emission is oxygen, the red is sulphur, and the green represents nitrogen and hydrogen. While larger HII regions like these are stellar nurseries, the smallest HII regions (0.03 - 0.5 pc), closely trace the formation of massive stars.

We have known about HII regions for a while now, the Orion Nebula was first observed in the 17th century and the Eagle Nebula in the 18th. However, compact HII regions were only discovered as recently as 1967, when radio observations (e.g. Ryle and Downes 1967; Mezger et al. 1967b,a) led to their discovery. The first detailed study and characterization of an HII region was carried out on W49, but was soon followed with similar

FIGURE 1.1: Three-colour images of the Orion Nebula (left) and the Eagle Nebula (right) taken with the HST.

studies e.g., DR 21: Ryle and Downes (1967), and G133.9+1.0: G. C. Aikman (c.f. Mezger et al. 1967a, and the references therein). In these radio studies, compact HII regions were generally defined as being very small ($d < 0.5$ pc), dense ($n_e > 10^4$ cm^{-3}), and high in emission measure (EM $> 5 \times 10^7$ pc cm^{-6}). Furthermore, the rate of recombination and the observed turbulent velocities led to the conclusions: these compact HII regions are ionised by one or more early O type stars, are likely to be a representation of an early stage in the evolution of an OB star, and must be expanding rapidly (Mezger et al., 1967a). Another defining quality of compact HII regions determined at around the same time, was their association to IR emission. Davidson and Harwit (1967) predicted that young massive stars would proceed towards the main-sequence while still embedded in a cocoon of dust, which would absorb the radiation of the star and re-radiate it as IR emission. This has since been verified (Neugebauer and Garmire, 1970; Low and Aumann, 1970) and later, widely used (Thompson et al., 2006; Urquhart et al., 2009a, 2013; Hindson et al., 2012; Purcell et al., 2013) as a defining attribute of young HII regions. HII regions were originally modelled as spherical ionised bubbles, which are formed by a star which ionises the gas closely surrounding it, and expand as a uniform medium (Spitzer, 1978). However, this model later collapses with studies using observations taken at high angular resolution. Wood and Churchwell (1989b) find that not all HII regions are spherically symmetric and present five morphologies that deviate from the standard Strömgren theory (Strömgren, 1939). They surveyed 75 UC HII regions in which they found 20% were cometary, 16% were core-halo, 17% were multiply

peaked, 4% were shell shaped, and 43% spherical or unresolved. Kurtz et al. (1994) find a similar distribution in their survey of 59 Infrared Astronomy Satellite (IRAS) sources: around half being unresolved and the remaining portion of the sample following the morphologies presented in Wood and Churchwell (1989b).

TABLE 1.1: Physical Parameters of HII Regions (Kurtz, 2005a)

Class of Region	Size (pc)	Density (cm^{-3})	Emis. Meas. (pc cm^{-6})	Ionized Mass $(\text{M}_\odot)$
Hypercompact	$\lesssim 0.03$	$\gtrsim 10^6$	$\gtrsim 10^{10}$	$\sim 10^{-3}$
Ultracompact	$\lesssim 0.1$	$\gtrsim 10^4$	$\gtrsim 10^7$	$\sim 10^{-2}$
Compact	$\lesssim 0.5$	$\gtrsim 5 \times 10^3$	$\gtrsim 10^7$	~ 1
Classical	~ 10	~ 100	$\sim 10^2$	$\sim 10^5$
Giant	~ 100	~ 30	$\sim 5 \times 10^5$	$10^3 - 10^6$
Supergiant	> 100	~ 10	$\sim 10^5$	$10^6 - 10^8$

1.2.2 Star formation tracers

Even though there is no universal agreement on the process of massive star formation, throughout the 1970s and 80s, the chief tracers of massive star formation were the compact and UC HII regions (e.g., Wood and Churchwell 1989b; Kurtz et al. 1994) and more recently the HC HII region (e.g., Gaume et al. 1995; De Pree et al. 1997; Kurtz et al. 2000; Kurtz 2005a; Hoare et al. 2007). The observation by Gaume et al. (1995) near the NGC 7538 UC HII region is noted as the first discovery of a HC HII region. While the number of observed UC HII regions has exploded in the last 30 years, the observational record of HC HII regions is still rather low. This could largely be due to the selection bias low frequency surveys have against objects whose spectra rise with frequency (c.f. § 1.2.4). Because the turnover frequency between the optically thick and thin regimes for thermal bremsstrahlung varies directly with electron density, low frequency ($\nu \leq 5$ GHz) surveys have an observational bias that preferentially selects against dense plasma ($n_e \gtrsim 10^5$ cm^{-3}) and steep positive spectrum objects go unseen (Mezger and Henderson, 1967; Thompson et al., 2016).

Young HII regions are the closest tracers of MSF, it therefore follows that mapping out their distribution will also tell us about the distribution of the massive stars that form them. Studies focused on UC and HC HII regions in the last 10 years have made considerable advances in this regard.

1.2.3 Recent advances in the field

Hindson et al. (2012) carried out an un-targeted survey of the G305 massive star-forming region in a search for compact radio emission associated with UC HII regions. They detected a total of 71 compact radio sources, 6 of which were identified as candidate UC HII regions and 5 of the candidates were found to have derived physical properties consistent with those of known UC HII regions. All 5 UC H II regions are located around the inner rim of the central cavity, within the photon dominated region (PDR), and coincident with areas where the mid-infrared emission is bright and compact. However, there was found no evidence of UC HII regions within the central cavity, outside the bounds of the PDR. All 5 UC HII regions are resolved. One is irregular while the other four have simple morphology: a compact core with some diffuse emission. Using these results in tandem with other star formation tracers, they build a picture of the history of star formation in the region and estimate a lower limit of $\sim 3 \times 10^{-3}$ M$_\odot$ yr^{-1} to the star formation rate for the region.

Urquhart et al. (2013) present a complete sample of molecular clumps containing compact and UC HII regions over a 50° portion of the Galactic Plane. This search improved on previous surveys because most UC HII regions at this point were identified through targeted observations of objects selected by their mid- or far-infrared colours (e.g. Wood and Churchwell 1989b; Kurtz et al. 1994; Walsh et al. 1998; Urquhart et al. 2007, 2009b). This constraint is not an issue in wide area radio surveys targeted at identifying UC HII regions (e.g., Becker et al. 1990, 1994; Zoonematkermani et al. 1990; Giveon et al. 2005; Murphy et al. 2010; Hindson et al. 2012). However, the majority of these radio surveys were carried out in snapshot[1] mode thus limiting the uv-coverage of the observations. This made it hard to reliably identify UC HII regions, since detected compact sources might be bright compact components of more extended emission (Kurtz et al., 1999; Kim and Koo, 2001). Furthermore, identification of UC HII regions at their typical 5 GHz flux densities is made difficult by the high volume of background sources (Anglada et al., 1998). In order to reliably put together a sample of UC HII regions, the emission from the radio sources must be consistent with thermal free-free continuum, must be associated with strong infrared emission indicating heated dust and must be associated with submillimetre emission indicating they are embedded in molecular clumps. The

---

[1] https://science.nrao.edu/facilities/vla/docs/manuals/oss/performance/snapshots

aim in Urquhart et al. (2013) was to put together a sample unaffected by the infrared colour selection bias that meant the samples were possibly contaminated by other IR bright objects such as planetary nebulae (PNe) and intermediate mass YSOs. Thus the sample used here was complete to optically thin, compact and UC HII regions driven by a ZAMS star of spectral type B0 or earlier, embedded in a 1000 $M_\odot$ clump. They identified 213 compact and UC HII regions associated with 170 clumps. The sample was identified by combining ATLASGAL 850 μm sub-mm, CORNISH 5GHz radio, and archival IR data.

Peters et al. (2010a) present the first three dimensional simulation of the gravitational collapse of a massive rotating molecular cloud heated by both ionising and non-ionising radiation. Their simulations show HII regions formed around young massive stars fluctuating between the UC and HC states throughout the main accretion phase. The fluctuation happens when denser material is accreted onto the stars and shields the ionising radiation. They show them as being gravitationally trapped when the the mass of the first protostars becomes adequate for the ionization of the accretion flow, and later shows the HII regions fluctuating between trapped and extended states. As an additional consequence to the radiation shielding, the models show that these HII regions drive bipolar neutral outflows characteristic of high mass star formation. Peters et al. (2010a) see several HII region morphologies in their simulations including shell-like, core-halo, cometary, spherical, and irregular. They attribute this range of morphologies to the complex interaction between gravitationally unstable gas filaments in the accretion disk and ionising radiation from the young stars. These results present an evolutionary scenario for HII regions that is considerably different from the standard Strömgren sphere model, in which the HII region expands monotonically. This alternative scenario presents a solution to the lifetime problem of UC HII regions (Wood and Churchwell, 1989b; Kurtz et al., 1999; Kim and Koo, 2001): the number of observed UC HII regions is greater than expected based on the lifetime estimated in Wood and Churchwell (1989b). In this scenario, the size of the HII region is not linked to the age of the protostar, provided fast accretion is maintained.

De Pree et al. (2014) examined the flickering of 1.3 cm sources in Sgr B2 by comparing them to counterparts from observations in 1989. The 1.3 cm VLA observations carried out in 2012, together with the 1989 observations provided a 23-year baseline over which to compare the relative peak flux densities for the HII regions in Sgr B2. De Pree et al.

(2014) found that 4 of the 41 UC HII regions contained in Sgr B2 showed significant variations in their peak flux density: three showed an increase and one showed a drop in flux density. The fast rates of accretion flows onto massive stars make them gravitationally unstable, consequently forming dense clumps and filaments. This result is in agreement with high-resolution numerical simulations that indicate HII regions surrounding young massive stars fluctuate throughout the main accretion phase (Peters et al., 2010a,b,c). All four sources with variations in peak flux density have previously been associated with broad radio recombination line (RRL) profiles (De Pree et al., 1996, 2011). De Pree et al. (2015) further explored this with high angular resolution 7mm continuum and recombination line observations of Sgr B2. This data was compared to archival 7mm continuum data, observed in 2001 (Sgr B2 North), and 2003 (Sgr B2 Main). They found one source in Sgr B2 North decreased by 21% between 2001 and 2012 and they found one source in Sgr B2 Main increased by 30% between 2003 and 2012. This source, F3c-Main, was seen increasing in flux density in the 1.3 cm observations of De Pree et al. (2014) between 1989 and 2012. Significant flux density changes are found in 4 sources at 1.3 cm while only 2 are found at 7mm in observations of the same field. This is explained by two effects that act together to reduce the variability at 7mm: the optical depth of free-free emission decreases with increasing frequency and the contribution of dust emission is higher at 7mm. The results imply that flux density variations are likely to occur in a small sample of sources on timescales of a few years. Thus the results in De Pree et al. (2014) and De Pree et al. (2015) support the hypothesis that UC and HC H II regions are possibly located in dynamically and morphologically complex and time-variable environments during the first 10^5 years of their evolution, producing short-timescale variability.

Kalcheva et al. (2018) presented the first high-resolution catalogue of UC HII regions. This complete sample of 239 UC HII regions was identified from the CORNISH 5 GHz survey. A comparison between the flux densities of the CORNISH survey observed from 2006-2008 and the MAGPIS survey observed from 1989-1991, showed 5% of the sources as being time variable. This variation in flux densities aligns with the results in the simulations of Peters et al. (2010a) and the observations of De Pree et al. (2014). From their high resolution survey of a large area of the Galactic Plane, Kalcheva et al. (2018) estimate the total number of UC HII regions in the Galaxy to be 750. The number of UC HII regions found in this survey is roughly a third lower than in previous large area

radio surveys. This work validated high-resolution blind radio surveys as the best way to build a bonafide sample of UC HII regions and being the largest complete survey up until this point, it set a basis for tests of future models of massive star formation.

Djordjevic et al. (2019) used a multiwavelength analysis of survey data to compile the most complete catalogue of compact and UC HII regions to date. They used UC HII regions identified in Urquhart et al. (2013, 2014c) in tandem with ATLASGAL (§ 2.3.1) and SASSy (§ 5). This study doubled the sample size of the original ATLASGAL-CORNISH study, bringing the total number of UC HII regions in the catalogue to 536 with a total of 445 host clumps. Furthermore, the study covers a wider range of the Galactic Plane (80%) giving a more complete picture of massive star formation. With the SASSy survey data, they extended the study to the Outer Galaxy and found disparity between the star formation in the Inner and Outer Galaxy. They found that the overall star formation efficiency is lower in the Outer Galaxy than in the Inner Galaxy.

Yang et al. (2019) carried out the largest unbiased search for HC HII regions to date. They did this through multiwavelength techniques by combining data from four radio surveys (THOR, CORNISH, MAGPIS, White et al. 2005), with far-IR and sub-mm Galactic Plane surveys (Hi-GAL, ATLASGAL). They found 120 positive spectrum HII regions in a pool of 534 radio sources with positive spectral indices. None of the HC HII regions identified in this sample is consistent with a typical HC HII region as defined in Kurtz (2005a), implying the widely accepted definition of HC HII regions requires amendment to account for extended emission at 5 GHz. They suggest that much like UC HII regions, HC HII regions have a hierarchical structure. UC HII regions are widely assumed to have flat and optically thin spectra, however, the results in the Yang et al. (2019) study show roughly half the surveyed HII regions as having positive spectral indices. This points to a combination of optically thin and thick emission in the Galactic population of UC HII regions.

Yang et al. (2021) looked at a population of young HII regions with the aim to identify HC HII regions. The prevailing assumption typically used in determining the physical properties of young HII regions is that their emission is optically thin. This assumption breaks when these objects are very young (i.e., UC and HC) HII regions. Consequently, their physical properties are underestimated. Yang et al. (2021) overcome this by fitting SEDs over a wide range of radio frequencies. They identify 16 HC HII regions and

8 HII regions in transition between the HC and UC phases. Their results match the evolutionary trends seen in earlier studies (e.g., Dyson et al. 1995; Mezger and Henderson 1967) i.e., the expansion of an HII region resulting in electron density decreasing while emission measure and diameter increase. They examine a wide range of evolutionary stages by including the Kalcheva et al. (2018) sample of UC HII regions which were presumed to be at a later stage in evolution. This reveals a decrease in turnover frequency as the HII region evolves, while the lyman flux does not present any distinct trend that correlates with the evolution of the HII region. The data neither shows significant correlation between the lyman flux and emission measure, nor between the lyman flux and electron density. This is likely due to very luminous HII regions expanding rapidly in their earliest stages and slowing down later in the evolution, appearing more like less luminous HII regions. The constant lyman flux with evolution of an HII region seen in this sample is in agreement with the evolutionary trends presented in Keto (2002), Hosokawa and Omukai (2009), and Hosokawa et al. (2010). The trends in this sample imply that the ionising flux of a young massive star remains constant during the early evolutionary stages of an HII region and that accretion is either reduced or stopped very early in the HC phase of an HII region.

1.2.4 Emission mechanism

Diffuse nebulae are large irregular patches of interstellar dust and gas. They tend to have very low densities (10^2 cm^{-3}) but contain large amounts of material, predominantly made of hydrogen. Their line emission in the optical regime comprises the Balmer lines of hydrogen and lines originating from transitions between energy levels of ions. In the radio regime, their emission comprises both continuum and spectral lines. The continuum emission is made up of bremsstrahlung, and the spectral line emission originates from transitions between very high energy levels of hydrogen and helium. The sources of excitation in these clouds of gas are early spectral type (OB) stars and the resulting gas temperature is of the order 10^4 K. With high effective temperatures ($2 \times 10^4 - 6 \times 10^4$ K), these stars emit a significant fraction of their radiation at energies high enough to cause and maintain photoionisation of elements such as hydrogen and oxygen and heat the dust in the nebulae. This interaction between nebulae and the radiation of ionising stars, makes them ideal components in studying the birth of massive stars.

Emission from the nebulae occurs in many forms. The continuous optical spectrum is produced by the recombination of electrons into the various levels - the distribution of photons is continuous because the electron energy is continuous. The spectra of the nebulae in the radio regime comprises two categories of emission: free-free continuum and spectral lines. Bremsstrahlung (or free-free) radiation occurs as the result of the acceleration of electrons in the fields of positive ions, which though emitted at a wide range of frequencies is observed in the radio regime. Recombination can produce hydrogen atoms in any of the excited levels, and downward radiative transitions from the levels produce a line spectrum. For this thesis, we focus on the continuum emission which is associated with the HII regions under discussion. The following derivation is adopted from Dyson and Williams (1980).

The absorption of free-free radiation within nebulae is important and the observed continuous spectrum must be interpreted allowing for this effect. Thus one must consider the transfer of the radiation through the nebula.

For this purpose, we define the following quantities:

- the radiation intensity, I_v, is the radiant energy in unit frequency interval at frequency v which crosses unit area per second per unit solid angle

- the emission coefficient, j_v, is the radiant energy emitted by the gas in unit frequency interval at frequency v per unit volume per second per unit solid angle

- κ_v is the absorption coefficient in units of m^{-1}.

In plane parallel geometry, the change in I_v between planes at positions s and s + ds is given by

$$\frac{dI_v}{ds} = j_v - \kappa_v I_v. \tag{1.9}$$

For a system in thermodynamic equilibrium, j_v and κ_v are connected by the Kirchhoff relationship

$$j_v = \kappa_v B_v(T) \tag{1.10}$$

where $B_\nu(T)$ is the Planck function at the temperature of the system. The electron gas has a Maxwellian distribution at a temperature T_e. Thus the emission and absorption coefficients for the bremsstrahlung are related by equation 1.9 with T put equal to T_e. Defining the optical depth at frequency ν by

$$d\tau_\nu = \kappa ds \tag{1.11}$$

equation 1.9 can be written in the form

$$\frac{dI_\nu}{d\tau_\nu} = B_\nu(T_e) - I_\nu. \tag{1.12}$$

And the solution of this equation is

$$I_\nu = B_\nu(T_e)(1 - e^{-\tau_\nu}). \tag{1.13}$$

In deriving this solution we have made the following assumptions. Firstly that T_e is constant throughout the nebula; secondly τ_ν is the total optical depth of the nebula, i.e., optical depth from one side to the other; thirdly $I_\nu = 0$ at $\tau_\nu = 0$, i.e., only radiation from the nebula is measured (there is no emission from any other sources).

Equation 1.13 has two obvious limiting forms. If $\tau_\nu \ll 1$, then

$$I_\nu \approx B_\nu(T_e)\tau_\nu. \tag{1.14}$$

If $\tau_\nu \gg 1$, then

$$I_\nu \approx B_\nu(T_e). \tag{1.15}$$

For bremsstrahlung, τ_ν has the form

$$\tau = A\nu^{-2.1}T_e^{-1.35}n_e^2 l \tag{1.16}$$

where A is a constant and l is the path length through the nebula. The quantity $n_e^2 l$ is the emission measure, ε, which is typically quoted in units of pc cm^{-6}. At radio frequencies, we can use the Rayleigh approximation to the Planck function,

$$B_\nu(T_e) \approx 2kT_e\nu^2/c^2 \tag{1.17}$$

where c is the velocity of light. We then find that if $\tau \ll 1$, (which, from equation 1.16 implies high frequencies),

$$I_\nu \propto \nu^{-0.1}. \tag{1.18}$$

At lower frequencies where $\tau \gg 1$,

$$I_\nu \propto \nu^2. \tag{1.19}$$

Where, in $I_\nu \propto \nu^\alpha$, α is the spectral index at frequency ν.

The radio-frequency continuous spectrum therefore has the characteristic shape shown as the solid line of Fig. 1.2. The actual numerical values of I_ν as a function of ν depend on the particular parameters (ε and T_e) of the given nebula. If we draw the straight lines corresponding to equations 1.14 and 1.15 and produce them to meet at the turnover frequency ($\nu_{turnover}$), the vertical dashed line in Fig. 1.2, then it is evident from these equations that at this frequency $\tau_{\nu_{turnover}} = 1$. Thus if T_e is known we can use the derived $\nu_{turnover}$ in equation 1.16 (with $\tau_{\nu_{turnover}} = 1$) and immediately find the emission measure ε. And if L can be estimated, then n_e, the electron density in the gas, can also be estimated.
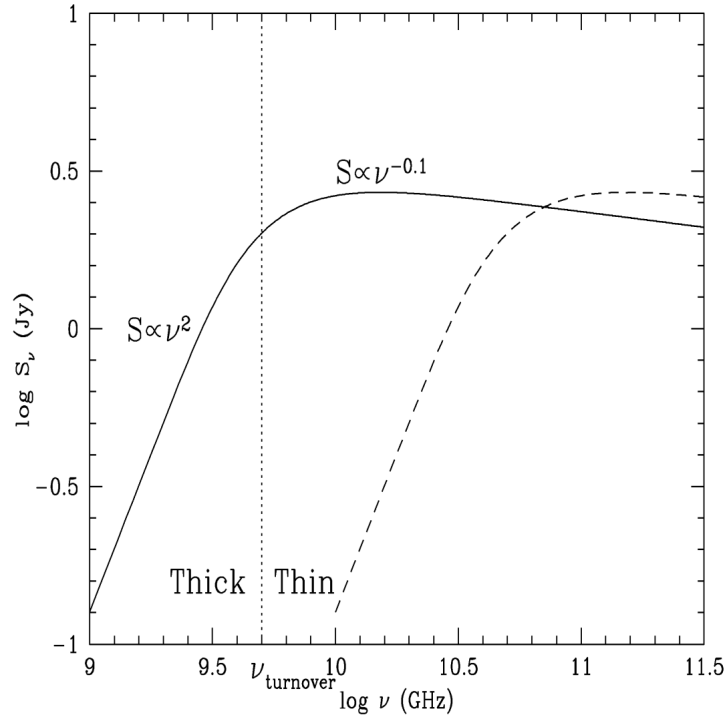
FIGURE 1.2: Bremsstrahlung emission from a spherical, homogeneous, isothermal HII region. The turnover frequency shown by the vertical dashed line, corresponds to 5 GHz or $\lambda = 6$ cm. The spectral index assumes intermediate values for frequencies near the turnover. At lower frequencies the ionised gas is optically thick, and the radio emission is proportional to ν^2; at higher frequencies the gas is optically thin, and the emission is proportional to $\nu^{-0.1}$. The dashed line shows the spectrum of an HII region with the same peak flux density, but with an emission measure 100 times higher; resulting in a turnover frequency that is 10 times higher. Such an HII region, if observed at 6 cm, would present a flux density 100 times lower its low emission measure counterpart.
Image courtesy of Kurtz (2005a)

The solid curve in Fig. 1.2 has a turnover frequency of 5 GHz ($\lambda = 6$ cm), $\varepsilon \sim 10^8$ pc cm^{-6}, and an UC HII region with a nominal size of 0.1 pc, this corresponds to $n_e \sim 3 \times 10^4$ cm^{-3}, and $T_e = 10^4$ K. The dashed curve represents an HII region that is 10 times smaller ($d \sim 10^{-2}$ pc), 30 times denser ($n_e \sim 10^6$ cm^{-3}), with $T_e = 10^4$ K, $\varepsilon \sim 10^{10}$ pc cm^{-6}, and a turnover frequency of about 50 GHz ($\lambda = 6$ mm).

1.3 Interferometry

Distant radio sources are observed using two or more telescopes in method known as radio interferometry. Fig. 1.3 shows the simplest setup of a radio interferometer. Radio telescopes sample different physical processes than optical ones. Whereas aspects
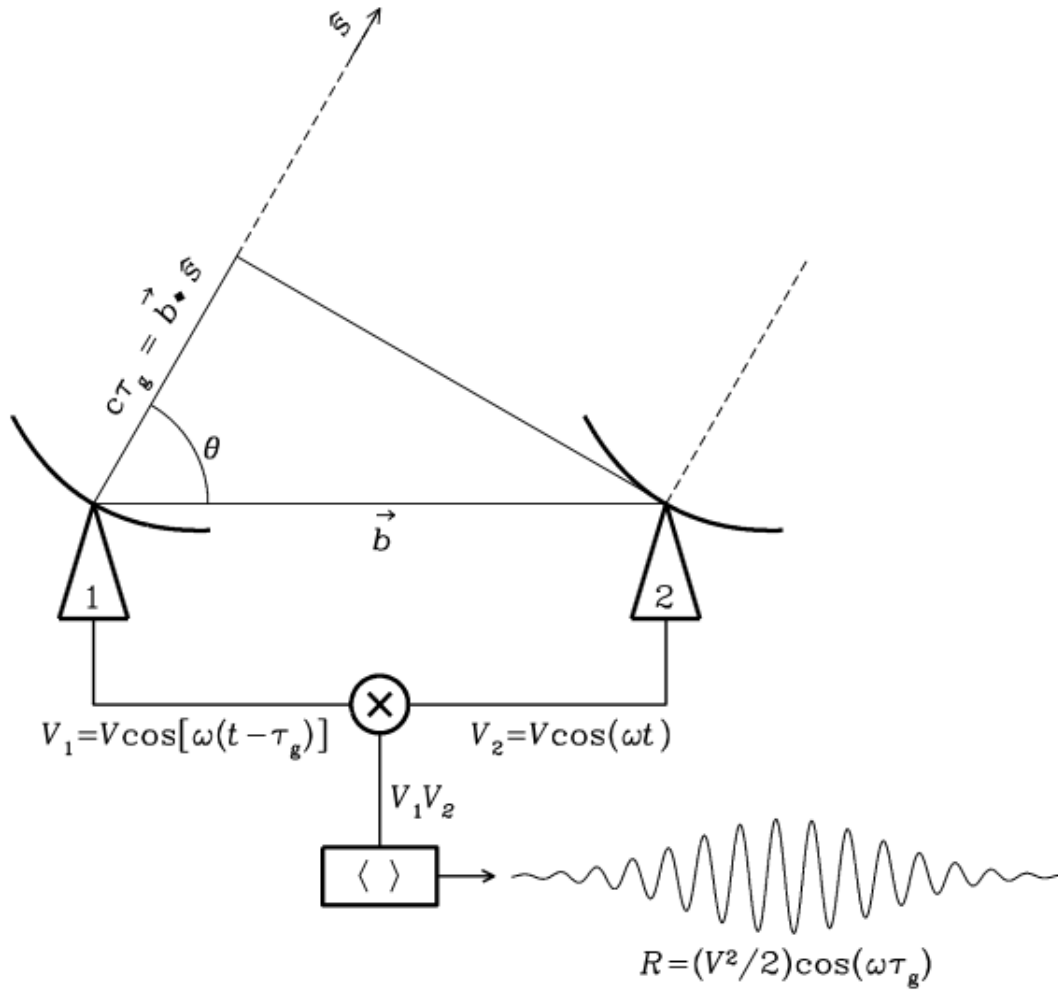
FIGURE 1.3: Block diagram of the simplest two-element interferometer observing in a very narrow frequency range. In this diagram, the centre frequency is $\nu = \omega/2\pi$, the voltage outputs of dish 1 and 2 are V_1 and V_2, respectively. The voltages are the same except for the delay $\tau_g = \vec{b} \cdot \hat{s}/c$ on V_2, where $\hat{s}$ is the unit vector in the direction of a distant point source and $\vec{b}$ is the vector baseline from antenna 1 to antenna 2. The correlator multiplies and time averages V_1 and V_2 to generate an output response with a delay and frequency dependent amplitude R that is proportional to the point-source flux density. *From* https://www.cv.nrao.edu/~sransom/web/Ch3.html

such as light pollution, turbulent air in the atmosphere, atmospheric absorption, bad weather, and interstellar dust clouds limit the effectiveness of optical telescopes, they do not present a problem in the radio regime as the Galaxy is largely transparent at radio wavelengths (Thompson et al., 2016). However, simply observing in the radio is not entirely sufficient as radio wavelengths are longer and produce a wider beam-width. As a consequence, the angular resolution of a single antenna is insufficient for most observations. Radio interferometers, which are ensembles of two-element interferometers, improve the angular resolution in observations of radio emission (Thompson et al., 2017)

The voltages V_1 and V_2 of antennas 1 and 2, respectively, are induced by radio emission incident on the antennas. These voltages, as a function of time at the receiving antenna, appear as very short parts of a random rythm that builds into a waveform with a Gaussian amplitude distribution (Thompson et al., 2017). The correlator multiplies and time averages the signal voltages, effectively filtering out high frequencies.

Essentially, the wavefront incident from a source in the direction of $\hat{s}$ arrives at the right antenna at a time τ_g before it reaches the left antenna. This is called the geometric delay and is given by:

$$\tau_g = \frac{\vec{b} \cdot \hat{s}}{c}, \tag{1.20}$$

where c is the speed of light, and $\vec{b}$ is the vector baseline from antenna 1 to antenna 2. Therefore, if the centre frequency is $\nu = \omega/2\pi$, the output of the multiplier will be:

$$
\begin{aligned}
F(t) &= 2\sin(2\pi\nu t)\sin 2\pi\nu(t - \tau_g) \\
&= 2\sin(\omega t)\sin \omega(t - \tau_g) \\
&= 2\sin^2(\omega t)\cos(\omega\tau_g) - 2\sin(\omega t)cos(\omega t)sin(\omega\tau_g).
\end{aligned}
\tag{1.21}
$$

Averaging this over time, and substituting the values $\omega(2\pi c/\lambda)$ and τ_g leaves us with,

$$F = \cos\omega\tau_g = \cos\left(\frac{2\pi\vec{b}\cdot\hat{s}}{\lambda}\right). \tag{1.22}$$

The correlator output voltage varies sinusoidally as the Earth's rotation changes the source direction relative to the baseline vector. These sinusoids are called fringes, and F is the fringe phase.

Alternatively, we consider the interferometer in Fig. 1.3[2], a quasi-monochromatic interferometer centred on the frequency $\nu = \omega/2\pi$, within a narrow band. V_1 and V_2 are the voltages of antennas 1 and 2, respectively, t is time, and τ_g (Eq. 1.20) is the geometric delay. $\hat{s}$ is the unit vector in the direction of a distant point source, and $\vec{b}$ is the vector baseline from antenna 1 to antenna 2. Then, multiplying the two voltages at the correlator we have,

---

[2]https://www.cv.nrao.edu/~sransom/web/Ch3.htmll

$$
\begin{aligned}
V_1 V_2 &= V \cos[\omega(t - \tau_g)] V \cos(\omega t) \\
&= V^2 \cos(\omega t) \cos[\omega(t - \tau_g)] \\
&= \left(\frac{V^2}{2}\right)[\cos(2\omega t - \omega \tau_g)].
\end{aligned}
\tag{1.23}
$$

To remove the high frequencies $(\cos(2\omega t - \omega \tau_g))$ from the final output R, we take a sufficiently long time average $(\Delta t \gg (2\omega)^{-1})$. We also take $\vec{b} \cdot \hat{s} = b \sin\theta$ to get,

$$
\begin{aligned}
R = \langle V_1 V_2 \rangle &= \left(\frac{V^2}{2}\right) \cos(\omega \tau_g) \\
&= \left(\frac{V^2}{2}\right) \cos\left(\frac{2\pi \vec{b} \cdot \hat{s}}{\lambda}\right) \\
&\approx \left(\frac{V^2}{2}\right) \cos\left(\frac{2\pi\theta}{\lambda}\right)
\end{aligned}
\tag{1.24}
$$

as the final output of the correlator. The output R multiplied by the beam's response per angle is the pattern produced on the image.

1.4 Main Goals

Young HII regions give us transitive access to the earliest stages in the development of massive stars (Peters et al., 2010a). Even though massive stars play an extremely important role in controlling the properties of the Universe on all scales, many details surrounding their early lives are not well understood. The interaction between a newly born star and its ambient medium is directly reflected in the HII regions formed from it, thus the most dense, most compact and presumably youngest HII regions provide an avenue through which to study single massive YSOs that have just begun to ionise their surroundings (Kurtz, 2005a).

In KuGARS, my primary goal is to detect and identify HC HII regions. I aim to determine their physical properties and estimate their statistical lifetime.

In SASSy, I aim to identify UC HII regions in Outer Galaxy clumps in order to better understand the rate and prevalence of massive star formation in the Outer Galaxy.

In the MeerKAT-GPS, my goal is to address the age problem of UC HII regions. I aim to construct a catalogue of all compact sources in the Galactic Plane detected in the survey. I aim to extract and use a sample of UC HII regions from the compact source

catalogue that will provide an unbiased perspective on the lifetime problem of UC HII regions.

1.5   Thesis Overview

In Chapter 2 a description of the surveys used in this thesis is presented. The observations, and science goals of the main surveys are outlined and a general description of the supplementary surveys is given. Chapter 3 focuses on the technical aspects of the Ku-GARS survey. The development process of the data reduction pipeline and the source detection procedures are described. In Chapter 4 I analyse the sources in the KuGARS compact source catalogue to identify HC HII regions and estimate their statistical lifetime. In Chapter 5 I present a search for radio counterparts to Outer Galaxy molecular clumps that in theory should host massive star formation. An automated process used to create the MeerKAT-GPS compact source catalogue is presented in Chapter 6. I then discuss the nature of the sources in the catalogue and analyse the known population of UC HII regions for extended emission by comparing them to 5 GHz emission. In this comparison, I attempt to address the 'age problem' of UC HII regions. And finally, Chapter 7 presents a summary and the main conclusions of this thesis, and the likely direction for future work.

Chapter 2

Surveys

2.1 The Pilot Ku-band Galactic Reconnaissance Survey (KuGARS)

2.1.1 Description

The Ku-band Galactic Reconnaissance Survey (KuGARS), is the first sub-arcsecond resolution (12-18 GHz) survey of the Galactic Plane. My primary aim is to discover and characterise the population of steep positive spectrum objects in the Galaxy. My goal is to perform a complete and unbiased survey for young HII regions, allowing their numbers, physical properties and statistical lifetimes to be determined.

KuGARS is the first Galactic Plane survey to explore the sub-arcsecond and sub-mJy regime at 14 GHz, and has significant scope for new and unexpected discoveries. In particular, KuGARS has high legacy value as the highest frequency radio component of a family of Galactic Plane surveys from the optical to 5 GHz, allowing ready cross-correlation with optical/IR/low frequency counterparts. The pilot to KuGARS is being carried out in order to validate the observing approach and fully test On-The-Fly (OTF) mapping (see § 2.1.3) at Ku-band. A 2.3°x2.3° region around W49A (Fig. 2.1) has been mapped in this self-contained project that will provide the first estimate of the statistical lifetime of HC HII regions.

Through matching volumes between the CORNISH & GLOSTAR UC HII region surveys, we can improve our understanding of the birth of HII regions by determining

their statistical lifetimes. Finding these objects requires a large area survey as massive YSOs/UC HII regions themselves are rare (only ~ 1000 in the Milky Way, Lumsden et al., 2013) it is likely that HC HII regions are even rarer. As Fig. 2.3 shows, there is no survey preceding KuGARS that can reach the same completeness limit for HC HII regions. A Ku-band survey is the only suitable way, in terms of sensitivity to steep spectrum sources and survey speed, to detect the youngest, most dense and earliest stage in the development of an HII region (Sjouwerman and Mills, 2013). The MeerGAL survey with MeerKAT will conduct a multi-epoch Ku-band survey of the southern GLIMPSE region at similar depths to KuGARS.

This pilot project allows us to place an initial constraint on the lifetime & properties of HC HII regions. However, I will need a much larger survey to place tight constraints on the frequency of these objects. The Galactic longitude range $l = 42°$ to $46°$ has the highest UC HII region surface density in the Milky Way, mostly due to the highly luminous W49A star-forming region (see Fig. 2.4 and also Urquhart et al., 2013) which itself contains almost 10% of the UC HII regions in the CORNISH survey. Also within this region are 20 6.7 GHz CH_3OH masers (Pandian et al., 2007). If the range of HC/UC HII and HC/CH_3OH maser ratios lies within the range of recent limited surveys (De Pree et al., 2014, Sánchez-Monge et al., 2013) I expect to detect between 10–26 HC HII regions. I regard this as a lower estimate as I have not counted potential HC HII regions associated with the numerous bright FIR sources from Hi-GAL (Molinari et al., 2010) that have similar characteristics to the HII region and maser-hosting clumps (see Figs. 2.1 and 2.2). This would more than double the known sample of HC HII regions recovered from unbiased surveys and finally allow an estimate of their statistical lifetime to be determined with better than 3σ precision.

The science I can carry out with these observations extends beyond HC HII regions and I expect to detect much more than just these objects. As Fig. 2.3 shows, I will also detect UC HII regions (although I will likely resolve out more extended compact HII regions).
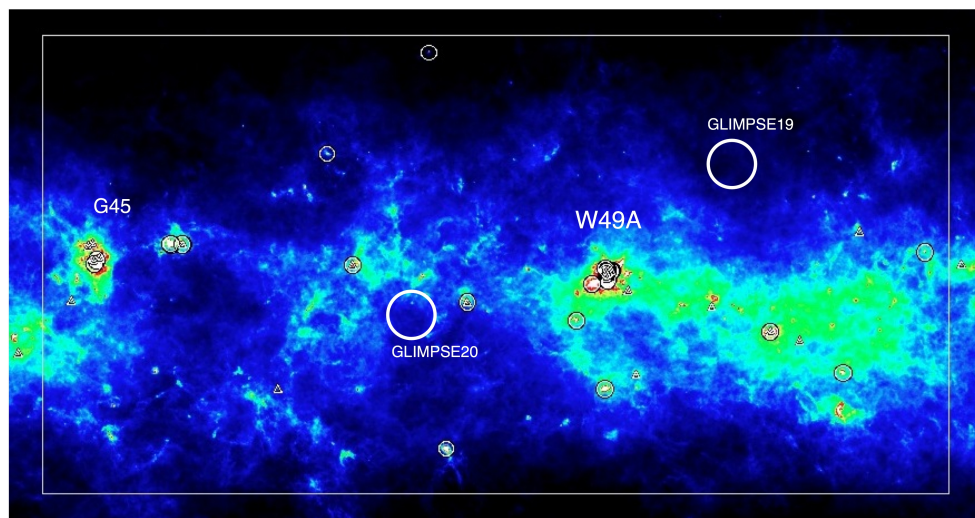
FIGURE 2.1: Herschel Hi-GAL 250 μm image of the $l = 42° - 46°$ region. CORNISH UC HII regions are indicated by circles and AMGPS CH$_3$OH masers by triangles over 250 μm Hi-GAL colourscale. The box shows the proposed 4°x2° region to be mapped. Regions of interest are indicated by text labels.
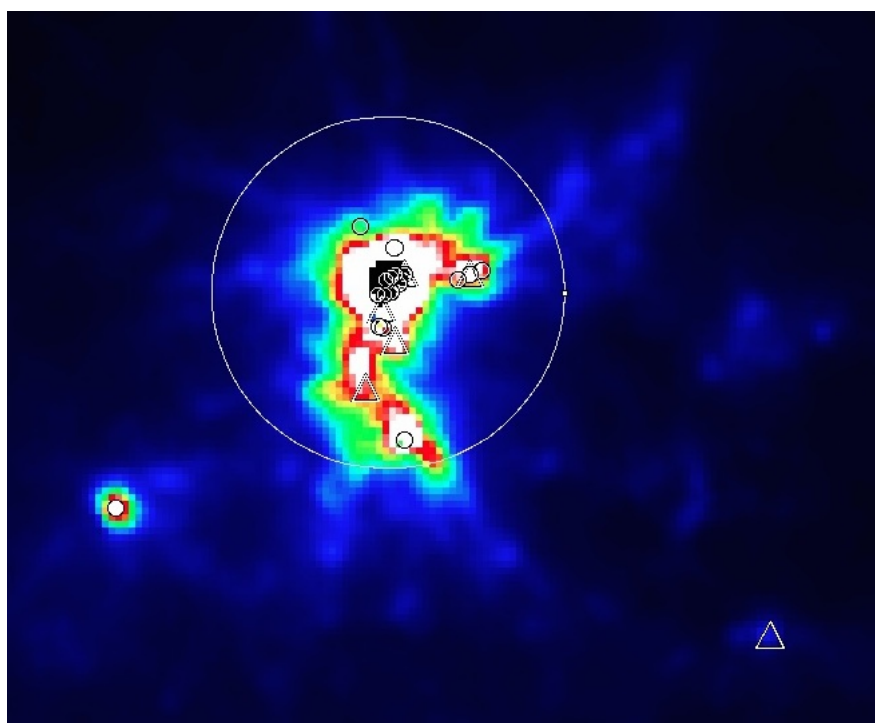
FIGURE 2.2: A close-up of the W49A complex. UC HII regions and CH 3 OH masers are indicated as before. The large circle represents the primary beam from De Pree et al's 1997 W49A study. Note that the colour-scale stretch is different between Figs. 2.1 and 2.2.
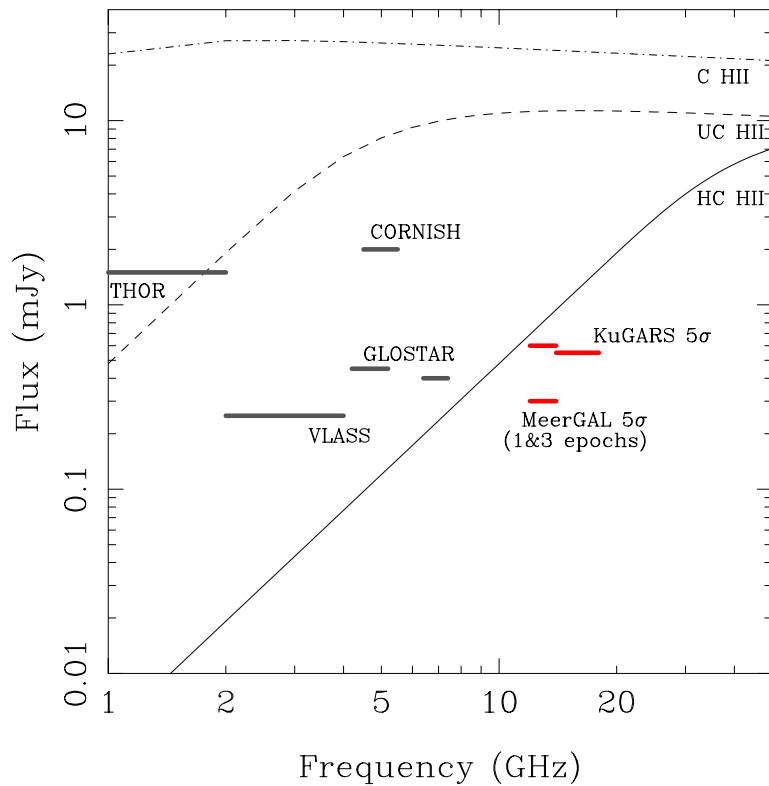
FIGURE 2.3: Theoretical spectra of homogeneous isothermal HII regions at a distance of 20 kpc. Solid, dashed and dot-dashed lines show spectra for hypercompact, ultra-compact and compact HII regions, respectively (with diameters 0.005, 0.05 & 0.5 pc and typical emission measures as given in Kurtz 2005). 5σ continuum sensitivities for MeerGAL (both for 1 and after 3 epochs), KuGARS, CORNISH, GLOSTAR (5 & 8 GHz bands) and VLASS-Galactic are indicated (figure from Thompson et al., 2016.
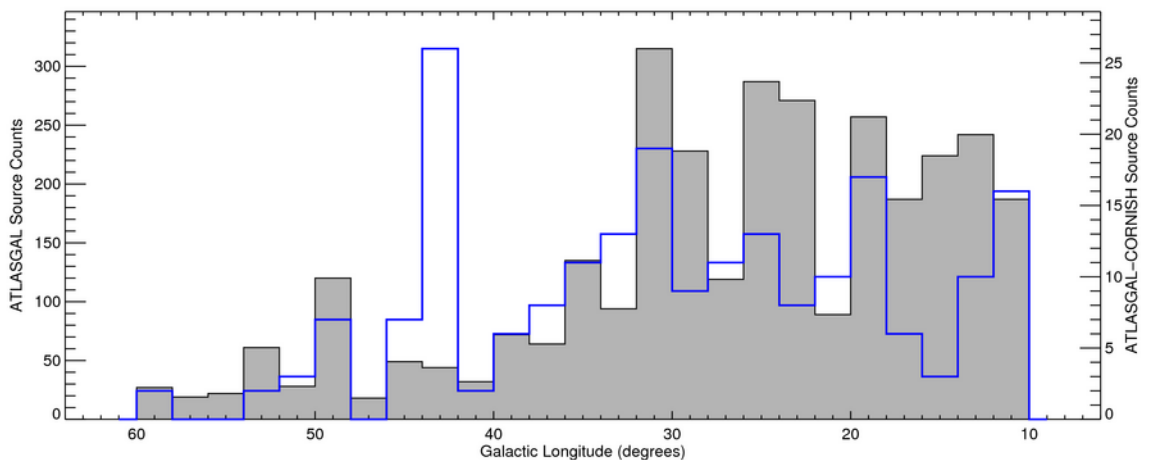
FIGURE 2.4: The Galactic longitude distribution of ATLASGAL clumps (shaded histogram) and CORNISH UC HII regions (blue histogram), showing the high surface density of UC HII regions between $l = 42° − 46°$.

2.1.2 Observations

In KuGARS the primary goal is to detect and identify HC HII regions out to the edge of the Milky Way. To maximise sensitivity to these steep spectrum objects the survey was observed in continuum 14-18 GHz, splitting this bandwidth into five 0.7 GHz wide channels (allowing for RFI losses) over the bandpass. The band was split into 5 in order to determine the spectral index of the emission - most HC HII regions will not have counterparts in the CORNISH survey. HC HII regions are faintest at 14 GHz and so this frequency drives the sensitivity requirements; a typical HC HII region at 20 kpc has a 14 GHz flux density of 0.9 mJy, which requires an rms of 0.18 mJy for a 5σ detection. In the KuGARS pilot, the sensitivity has been set slightly below this limit (0.11 mJy) in order to determine the optimum observing strategy for the larger KuGARS survey.
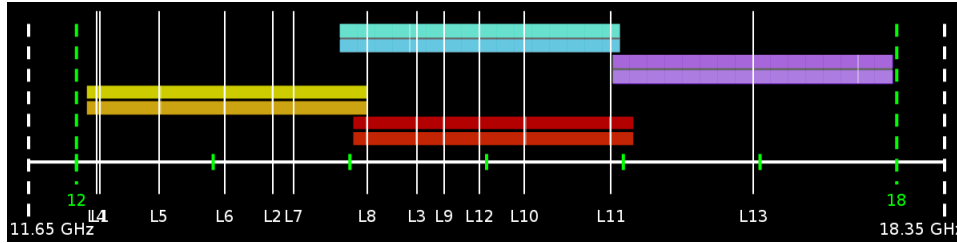
FIGURE 2.5: Correlator Setup during the KuGARS Observations. Total BI. BPs Used: 48 of 64. Total Data Rate: 59.97 MB/s or 215.89 GB/h. Total Spectral Points: 5184. Total Bandwidth: 4.232 GHz. Capability Mode: Shared risk.

To reach an rms noise of 0.11 mJy at 14 GHz requires an on-source time of 20s according to the VLA ECT (with 3 bit samplers, dual polarisation & natural weighting). A $2.3°x2.3°$ area has been mapped in OTF mode. Using a $\theta_{PB}(18GHz)/\sqrt{2}$ (where θ_{PB} is the angular resolution of the primary beam) spacing between $2°$ long scan rows resulted in 80 rows in total. Using a 1s dump time and a $0.25'/s$ scan rate to maintain 10 samples per $2.5'$ primary beam, each row took 10 minutes to complete (not counting overheads). The area was split into 8 blocks of 10 rows (Fig. 2.6). Each block contains 44 spectral windows: 32 continuum windows and 10 spectral line windows (Fig. 2.5). The observing time on each of these took ~2.5 hours, including 25% overheads. Each block was observed twice within a single 5 hour track to obtain 20s on source time and to improve the uv-coverage (a similar strategy was adopted by the CORNISH survey, Hoare et al., 2012; Purcell et al., 2013). The total time was therefore, 8 blocks x 2 repeats x 2.5 hours, or 40 hours.
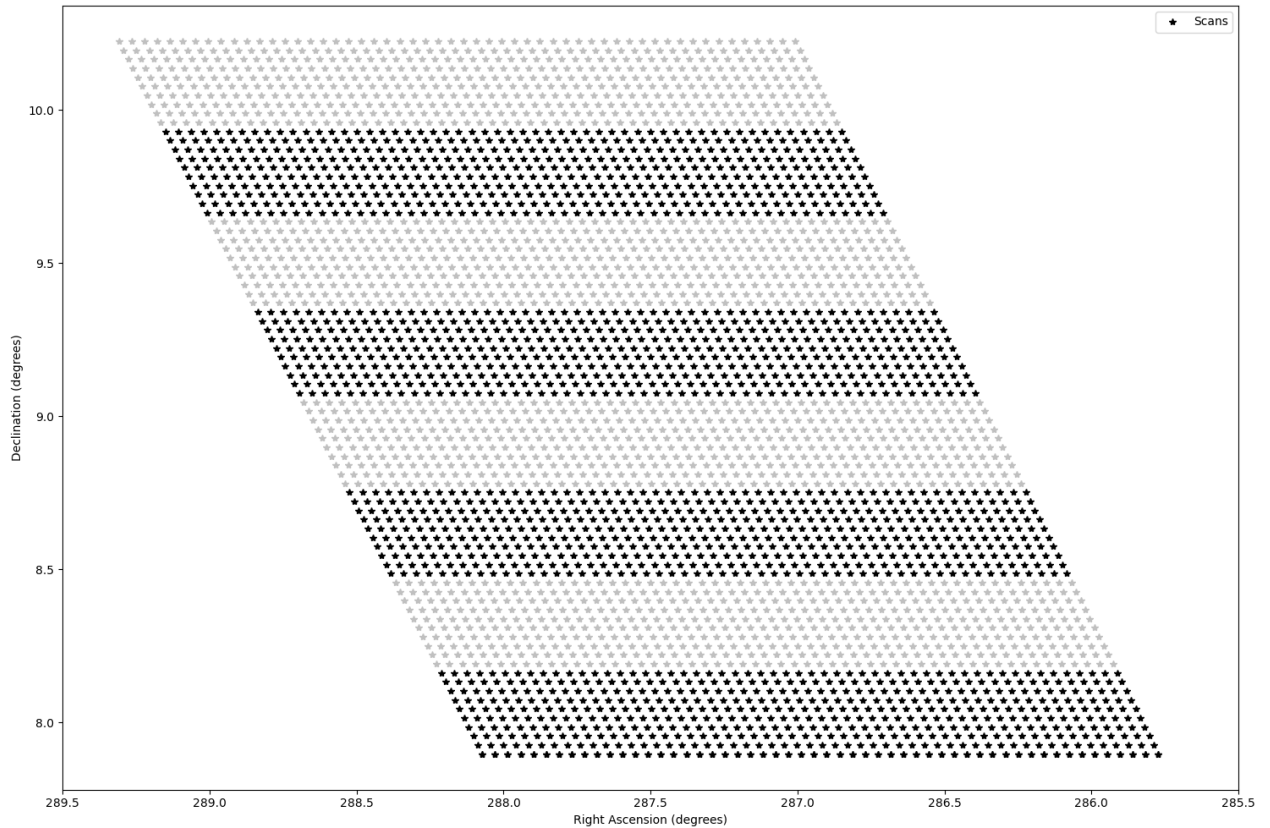
FIGURE 2.6: Survey observation layout: 8 blocks of 10 rows of 54 scans. Each star represents a unique scan, each row a stripe of scans, and each set of 10 stripes make up a block. The alternating colours are designed to draw a distinction between stripes belonging to successive blocks (black to grey and vice versa).

Unused baseline board pairs were allocated (keeping within the data rate limits of 60 MB/s) to maximise the scientific productivity of the survey with simultaneous spectral line observations of CH_3OH and OH masers, plus 8 Radio Recombination lines (RRLs) and H_2CO in absorption. The OH maser transition was observed with 0.1 km s^{-1} channels in order to measure the Zeeman splitting (possible for all masers > 1 Jy), whereas the CH_3OH maser and H_2CO lines were observed with 0.6 and 0.3 km s^{-1} wide channels, respectively. RRL line windows are centred on the hydrogen lines from H81α to H74α and have 5.7 km s^{-1} channels, which are sufficient to resolve these broad ($>$30 km s^{-1}) lines. I have obtained line sensitivities per channel of 41 mJy, 17 mJy, 22 mJy and 6 mJy for OH, CH_3OH, H_2CO and RRLs, respectively. This was suitable to detect the strong maser lines, plus observe H_2CO absorption against strong continuum and also RRL emission from all compact HII regions brighter than $\sim$50 mJy (binning to 10 km s^{-1} channels and stacking the 8 Hnα lines).

2.1.3 Observation Technique

The observations were carried out in On-The-Fly (OTF) mode. In the standard methods (step and integrate), the telescope remains fixed while data is collected. In OTF mode, the telescope scans across a field in Right Ascension (RA), smoothly and rapidly (with a constant slewing speed) while continuously recording observation information. For KuGARS, this technique provides a high observing efficiency. The telescope overhead is significantly reduced, properties of the atmosphere and the system such as antenna pointing and calibration change less, and "dead time" is minimized. On the other hand, sampling the sky properly in an interval shorter than the changes in the instrumental and atmospheric calibration requires a very high data rate (Mangum et al., 2000).

2.2 The MeerKAT Galactic Plane Survey (MeerKAT-GPS)

FIGURE 2.7: An overview of the MeerKAT radio telescope in the Karoo in the Northern Cape, South Africa. Image credit: SARAO.

The MeerKAT radio telescope (Fig. 2.7), located in the Karoo semi-desert region of South Africa, is a precursor to the Square Kilometre Array (SKA) telescope. MeerKAT will constitute a significant portion of the mid frequency portion of the SKA. MeerKAT currently comprises 64 offset Gregorian antennas with a nominal dish diameter of 13.5 metres (see Fig. 2.8). The array baselines range from a minimum of 29 metres to a maximum of 7700 metres. The array uses sub-octave band receiver systems which use two-stage Gifford-McMahon cryogenic coolers. The data links are run through optical fibre with the fibre cable strung on 33 kV power line poles and while the link is currently

limited to 10 Gb/s by the terminal equipment, the fibre has a higher link capacity. Currently, the MeerKAT antennas are equipped with dual (linearly) polarised receivers that cover the frequency range 570 MHz to 1670 MHz in two overlapping bands: a UHF-band receiver covering 580 MHz to 1051 MHz, and an L-band receiver covering 900 MHz to 1670 MHz. S-band receivers, provided by the Max Planck Institute for Radio Astronomy (MPIfR), are yet to be installed. These will cover the frequency range 1750 MHz to 3500 MHz. The dish design has several benefits. The configuration has a high aperture efficiency and therefore good sensitivity, low far sidelobes thus reducing, to some degree, terrestrial and airborne RFI as well the attenuation of strong radio sources outside the field of view. It yields a nearly circularly-symmetric main beam and inner sidelobe pattern and eliminates ground radiation, which reduces system temperature and therefore increases the sensitivity (Jonas, 2018).
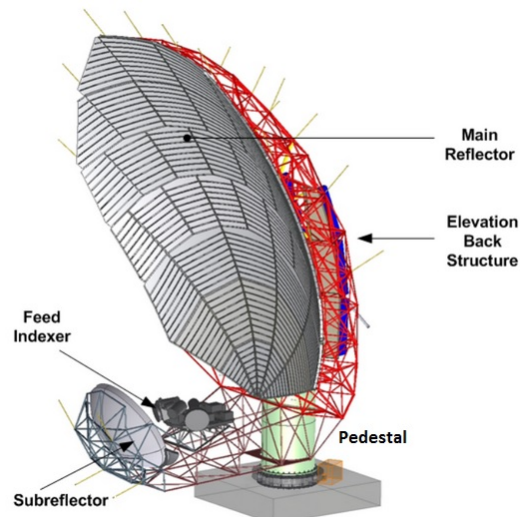
FIGURE 2.8: A schematic diagram of the MeerKAT dish structure showing the major elements of the design. The small rectangular box on the foundation cap is the isolation transformer. Image credit: Jonas (2018).

2.2.1 MeerKAT-GPS

The SARAO MeerKAT Galactic Plane Legacy Survey (Goedhart et al., in prep), is an L Band survey of the southern hemisphere of the Galactic Plane (GP). The MeerKAT GPS covers roughly half of the Galactic Plane from $252 < l < 358$, $2 < l < 60$ and $|b| < 1.5$ down to a nominal depth of $\sim$10-30 μJy. The observations were carried out in the L-band in 4k mode, producing 4096 channels with a channel width of 208.984 kHz, and consisted of $\sim$10 hour sessions, with about 1 hour of on source integration spread

over a wide range of parallactic angles. The scans maintained approximately uniform sensitivity over a series of hexagonally spaced pointings in a grid $\pm 1.5°$ about the mid-plane (Fig. 2.9). 60 antennas on the MeerKAT array were used and the dump interval was 8 seconds.
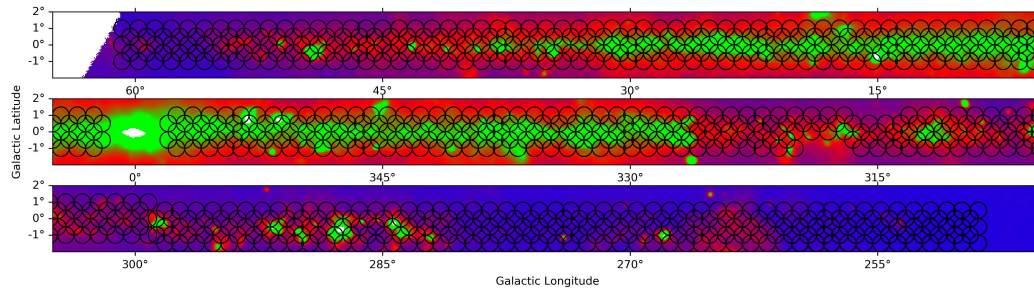
FIGURE 2.9: The area of the Galactic Plane covered by the MeerKAT Galactic Plane Survey. Individual pointing centres are shown by black circles, overlaid on a single-dish 1.4 GHz image from the CHIPASS (Calabretta et al., 2014) survey. Image credit: Goedhart et al. (in prep).

The pointings were imaged and combined into a linear mosaic with an $8''$ FWHM resolution and a $1''5$ pixel size - the mosaics are a set of overlapping $3° \times 3°$ primary beam corrected images. The data reduction and imaging, carried out by SARAO, used a pipeline based on OBIT, AIPS, and KATDAL for the calibration and editing and used the OBIT task MFIMAGE[1] to make wide-band, wide-field images. OBIT is a software package developed and maintained by Bill Cotton at the National Radio Astronomy Observatory (NRAO) for the handling of radio astronomy data, particularly interferometric and single dish OTF imaging. The NRAO Astronomical Image Processing System (AIPS) is a software package used for the calibration and editing of radio interferometric data, as well as the construction, display and analysis of radio astronomical images using Fourier synthesis methods. KAT Data Access (KATDAL),[2] is a package theat serves as a data access library to interact with the data produced by the MeerKAT telescope and its predecessors (KAT-7 and Fringe Finder). The entire dataset was phase self-calibrated, while both amplitude and phase self-calibration was applied to pointings with particularly bright emission. However, no direction dependent gains were applied and the overall cleaning was relatively shallow. The final format of the images was in the form of cubes which include total intensity, sub-band, and spectral index maps. The images used in the source finding have been created from the data cubes by calculating the zeroth moment which is done by taking the sum of the flux density and multiplying

---

[1]cv.nrao.edu/~bcotton/ObitDoc/MFImage
[2]https://github.com/ska-sa/katdal

this with the channel width for all channels and normalising the result by the total bandwidth to maintain the Jy/beam units. However, to take into account the effects of flagged data the zeroth moment images were constructed while taking into account varying bandwidth across images as well as to correct the bandwidth for flagged channels. The zeroth moment images are created by dividing each pixel by the bandwidth of the cube contributing to that pixel. Normalising by the total bandwidth underestimates the total flux density, this effectively gets worse for sources at the edge of the mosaics as a consequence of flagging and smaller primary beam size, at low and high frequencies, respectively. Dividing each pixel by the bandwidth of the contributing cube results in different effective frequencies and bandwidths of pixels at the edge of the image from those in the middle.

Observations carried out prior to 15 March 2019 were subjected to a timing error due to a 2 second error in the timetag/baseline coordinate calculation for archive data prior to this date, as well as a frequency error due to a half channel frequency offset in the calibration. Consequently, a rotation and scaling error has been introduced into the field. The position shift this produces at the edge of the primary beam is considerably reduced by the procedure of combining the pointings to form mosaics. I have examined the offset from the timing error by looking at a mosaic which was observed with and without the timing errors. In both versions of the G321.5 mosaic a set of bright and isolated sources (>1 mJy and $> 1'$ from any other source) was identified by the AEGEAN source finding algorithm (see § 6.1 for detailed discussion on the source detection).
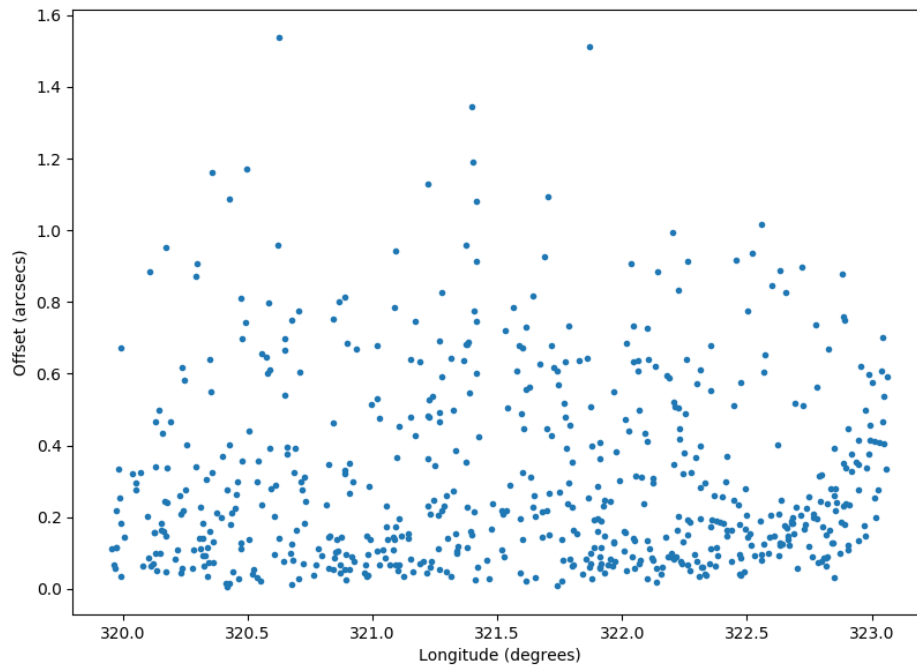
FIGURE 2.10: Effect of the timing offset in longitude. The plot shows the angular offset plotted against Galactic longitude.
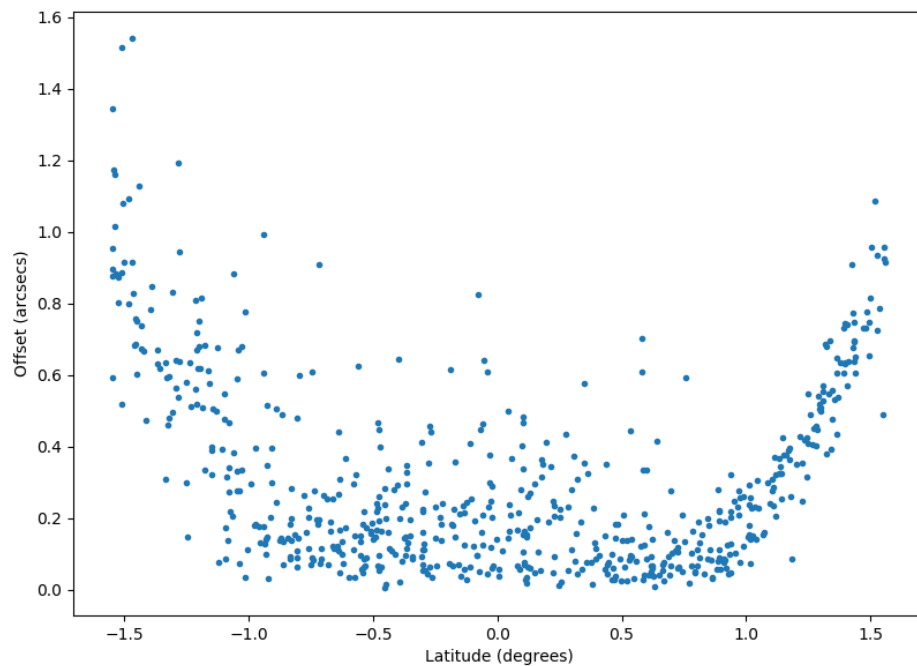
FIGURE 2.11: Effect of the timing offset in latitude. The plot shows the angular offset plotted against Galactic latitude.

Both the "corrected" and "uncorrected" catalogues were cross-matched and the angular offset between common sources was measured. Figs. 2.10 and 2.11 show the angular offset plotted against Galactic longitude and latitude. The plots show that the typical offset for most sources is less than $0\rlap{.}''5$. At the edges of the mosaic, particularly in latitude, this rises to $\sim 1\rlap{.}''5$.

2.3 Supplementary Surveys

2.3.1 ATLASGAL

The APEX Telescope Large Area Survey of the Galaxy (ATLASGAL: Schuller et al., 2009) is an 870 μm submillimetre survey of the inner Galactic Plane, covering the region $|l| < 60°$; $|b| < 1.5°$. The survey observations were imaged using the Atacama Pathfinder Experiment (APEX). ATLASGAL is an unbiased survey of the southern Galactic Plane with a typical noise level of 50-70 mJy beam^{-1}. The survey was carried out using the Large APEX Bolometer Camera (LABOCA) which is a 295-element bolometer array. At 870 μm, this has a beam size of $19\rlap{.}''2$. Thus. the telescope has excellent sensitivity and a large field of view ($11\rlap{.}'4$)

ATLASGAL presents all the massive, dense clumps in the Galaxy that are $\geq$1000 M$_\odot$ at a heliocentric distance of 20 kpc as well as a detailed census of the properties and spatial distribution of a sample of $\sim$8000 dense clumps located in the Galactic disc ($5° < |l| < 60°$).

2.3.2 CORNISH

The Coordinated Radio and Infrared Survey for High-Mass Star Formation (CORNISH: Hoare et al., 2012; Purcell et al., 2013), is an arcsecond resolution radio continuum survey of the Inner Galactic plane observed on the Very Large Array (VLA) in B and BnA configuration at 5 GHz. CORNISH covers the same region as, and has a similar resolution ($1\rlap{.}''5$) to the northern *Spitzer* GLIMPSE I region; $10° < l < 65°$ and $|b| < 1°$. Driven by the goal to study the formation of massive stars, this is a blind survey aimed at thermal sources such as UCH II regions. The survey has detected 3062 sources above a 7σ detection limit, with greater than 90% completeness at a flux density of 3.9 mJy.

2.3.3 Hi-GAL

The Herschel infrared Galactic Plane Survey (Hi-GAL: Molinari et al., 2010) is a large
area survey of the inner Galactic Plane observed on the *Herschel Space Observatory*.
The survey mapped the region $|b| \leq 1°$, $|l| \leq 60°$ and observed in five continuum bands
between 70 μm and 500 μm. The surveyed region contains the richest population of star
formation in the Galaxy, moreover, the region contains $\sim 80\%$ of the potential YSOs
within $|b| \leq 5°$ and therefore also hosts the majority of potential regions of star formation
in the Inner Galaxy (Molinari et al., 2010). The Hi-GAL first data release catalogues
contain 123,210, 308,509, 280,685, 160,972, and 85,460 compact sources in the five bands
70, 160, 250, 350, and 500 μm, respectively, in the longitude range $-70° \leq l \leq 68°$, and
covering latitude strip $|b| \leq 1°$ (Molinari et al., 2016). A band-merged catalogue of
100,922 compact sources extracted in the Inner Galaxy in the longitude range $-71° \leq
l \leq 67°$, and latitude $|b| \leq 1°$ is presented in Elia et al. (2017). The catalogue contains
specially matched sources and provides their properties as derived from fits to their
spectral energy distributions (SEDs) and heliocentric distances. Of these sources, 24,584
have a 70 μm counterpart and therefore considered protostellar, while the remaining
sources do not and are therefore considered starless. They use the catalogue to carry out
a precursory study of early stage star formation and explore the gravitational stability
of clumps in the context of their ability to form massive stars. A 360° catalogue of the
physical properties of 150,223 Hi-GAL compact sources is presented in Elia et al. (2021)
that completes and improves on the aforementioned catalogue particularly by providing
120,808 newly determined heliocentric distances. They use detection at 70 μm as the
basis for the classification of 23% of the total catalogue as protostellar sources, while
the rest are classified as gravitationally bound (pre-stellar) or unbound starless sources.
Furthermore, Elia et al. (2021) improved on the analysis of the Inner Galaxy clump
population presented in Elia et al. (2017) and presented the first unbiased catalogue of
Outer Galaxy clumps with the level of resolution and sensitivity provided by *Herschel*,
thus providing a homogeneous catalogue of the entire Galactic plane.

2.3.4 MSX

The Midcourse Space Experiment (MSX: Mill et al., 1994) is a measurement platform
in the fashion of an observatory, of the Ballistic Missile Defence Organisation, whose

primary objective is to collect phenomenology data relevant to the midcourse target detection phase in accordance with ballistic missile defence objectives. While this constituted the platform's primary focus, it also engaged in a range of civilian science objects in earth and atmospheric remote sensing and astronomy. There are eight astronomy experiments conducted on MSX, two of which are *A survey of the Galactic plane* (Price et al., 2001) and *A survey of the regions not covered by the Infrared Astronomical Satellite* (Egan and Price, 1996; Egan et al., 1999). MSX surveyed the entire Galactic plane within $|b| \leq 5°$ at a spatial resolution of $\sim 18''.3$. The survey was imaged in four mid-infrared bands between 6 and 25 μm and produced 1680 $1°.5 \times 1°.5$ images spread across the region with a $6''$ pixel spacing in each of the spectral bands. The MSX Infrared Astrometric Catalogue (Egan and Price, 1996), was purposed towards improving the pointing accuracy of infrared observations. The detectors on the MSX facility's infrared telescope, SPIRIT III, improve on the *IRAS* resolution by a factor of 30. The catalogue presents 177,860 astrometric stars. Of these, 61,242 have infrared counterparts in *IRAS* and the Catalogue of Infrared Observations. Price et al. (2002) presented a new class of objects identified in the images. The infrared dark clouds identified are obscured by background emission in the ISM and thus dark to $100\mu m$. However, submillimetre emission reveals cores in the form of the dark clouds and are thus indicative of class 0 protostars.

2.3.4.1 RMS

The Red MSX Source survey (RMS: Hoare et al., 2005; Urquhart et al., 2007, 2008, 2009a; Lumsden et al., 2013) provides a large Galactic sample of young massive protostars and HII regions. The catalogue was built from sources in the MSX Galactic plane survey (Price et al., 2001), specifically using the sources in v2.3 of the MSX point source catalogue (Egan et al., 2003). Using mid and near-infrared colour selection, the catalogue was constructed by identifying sources with colours consistent with known MYSOs and HII regions (Lumsden et al., 2002). The longitudinal range covered in this catalogue was limited to $10° < l < 350°$, leaving out the Galactic centre which is highly populated and therefore results in greater source confusion, and greater difficulty constraining kinematic distances.

2.3.5   WISE

The Wide-field Infrared Survey Explorer (WISE: Wright et al., 2010) mapped the entire sky in the mid-infrared in four bands centred on wavelengths 3.4, 4.6, 12, and 22 μm, with angular resolutions of $6\rlap{.}''1$, $6\rlap{.}''4$, $6\rlap{.}''5$, and $12\rlap{.}''0$, respectively. The sensitivity in WISE improved on the previous-similar mission, IRAS, with a 100 times better sensitivity, thanks to the 40 cm telescope used in the observations. The survey achieved better than 0.08, 0.11, 1 and 6 mJy sensitivities at 5σ, in each of the respective bands. Evidently, the science applications from WISE span a wide range of topics which extend beyond the survey science goals in Wright et al. (2010) which include Brown Dwarf stars; Ultra-luminous Infrared Galaxies; Red/Dusty Active Galactic Nuclei and Quasi-Stellar Objects; Asteroids; Comet Trails and Zodiacal Bands; Young Stars and Debris Disks; Interstellar Dust; Galactic Structure; Nearby Galaxies and Galaxy Clusters.

Marton et al. (2016) have identified YSO candidates from the AllWISE catalogue of the WISE mission. Their analysis led to 133 980 class I/II YSO candidates being identified through the support vector machine (SVM) method, which was trained using SIMBAD. With an estimated contamination level $< 1\%$, they successfully identified $> 90\%$ of the Class I/II YSOs in existing YSO catalogues used as a comparison. Thus showing better detection rates than other methods.

Chapter 3

Data Reduction and Imaging of the KuGARS survey

3.1 Calibration and Imaging in CASA

In the reduction of radio interferometric data, the calibration process generally follows a standard route but often needs to be uniquely tailored to the specific observation. This is true for both the calibration and imaging, however, here I will focus more on discussing the imaging than I will on the calibration as this is the more uniquely tailored portion of the KuGARS data reduction.

The $2.3°$x$2.3°$ map of KuGARS was divided into eight overlapping scheduling blocks. Each block covered a $2°\!.3 \times 0°\!.265$ area observed twice, before- and after-transit, to increase uv-coverage. Due to the large volume of raw data, the preliminary development of the data reduction procedures and pipeline focused on a subset of the full observation, which was then applied to all the data. It was found that the initial data reduction was considerably underestimating the source flux densities. Therefore, I begin by describing how I modified the clean method to address this issue. I then describe the relevant steps taken to build and develop the data reduction procedures - I describe how I have extended the calibration and imaging from a single spectral window to all 32 continuum spectral windows and amended the imaging to include more than one measurement set (MS). The before- and after-transit data were calibrated separately. To increase the uv-coverage, the two sets of data were imaged together.

The subset of data used to develop the imaging needed to be centred on a well studied region (e.g. W49A Dickel and Goss (1990); De Pree et al. (1997); Welch et al. (1987); Dreher et al. (1984)) containing sources with a high likelihood for detection in the survey. This makes it possible to compare the resulting images to existing studies in the literature and avoids inadvertently imaging an empty field of noise. Thus I centred the imaging on the massive star forming region W49A which, being the brightest star forming region in the Galaxy with a high population of the category of sources KuGARS is designed to detect, is an ideal choice for a test region. The development of the imaging pipeline began by determining the ideal imaging parameters and mode. These were used as base inputs in the process used to determine the ideal imaging parameters for multi-spw, multi-MS maps in KuGARS. I carried out four test steps: separately imaging the before and after transit MS on a single spw; creating an image using the combined MS on a single spw; separately imaging either MS on multiple spws; and imaging the combined MS on multiple spws. These steps are outlined in further detail in § 3.4 along with the quality checks used to test the fidelity of the imaging method.

From § 3.6 onwards, I describe the implementation of the imaging pipeline on the full survey and its challenges.

3.2 RFI Flagging

Radio sources are extremely weak, making them incredibly susceptible to interference from signals generated by earth and space based electronics. This is known as radio frequency interference (RFI). RFI signals are significantly stronger than radio sources and will therefore appear as distinct spikes in the data. This makes it possible to find and remove the RFI. In order to efficiently find and expunge all RFI each spectral window was inspected separately for each of the calibrators and the target. Due to the nature of On-The-Fly (OTF) mapping (see § 2.1.3), the visibilities of very bright sources stand out as distinct peaks (sometimes in several stripes), consequently appearing as RFI would in standard observations. Bad data was manually found by plotting the amplitudes of the data against frequency and against time. Using these plots, patterns that deviated from the normal trend of the data were identified, recorded, and flagged through a flagging script. This was done with extreme caution as traces of RFI left unflagged adversely

affect the final flux densities of the target sources and the presence of artefacts in the image.

3.3 Calibration

The calibration consisted of four main steps: *A priori* corrections, calibrator calibration solutions, bootstrapping flux density from the primary calibrator and applying the calibration solutions.

3.4 Imaging

To efficiently develop and verify my imaging strategies I carried out my imaging runs on a subset of the data - I used a 4000 square pixel image centred between W49 North and W49 South. The runs outlined in this section were carried out in CASA 5.3.0. However, the imaging runs in § 3.7 and in the final implementation of the imaging of the KuGARS data were done in CASA 5.6.2. As this project spans several years, several versions of CASA were necessarily used in the development. Many of the earlier versions had bugs (or features) that posed a challenge in obtaining optimal results in imaging KuGARS' OTF map data. I do not discuss the specifics of the hurdles in each version as the scope of this is beyond this thesis and its goals. I chose to use a non-interactive clean method to eliminate human error. It is likely that the OTF mode causes a "smear-like" effect on the sources that causes a grid-like artefact pattern. This effect is hard to deal with interactively as some of the target elements would appear as sidelobes or noise, effectively making it hard to assign clean regions accurately. However, in non-interactive cleaning, the clean algorithm looks for pixels with the highest peaks in flux density and iteratively adds them to the model, thus alleviating the problem of ambiguous sources - I discuss this in further detail in § 3.4.2.

3.4.1 uv coverage

The uv-coverage was optimised in two ways: combining spectral windows and combining before- and after-transit blocks. The frequency range of the KuGARS continuum data

extends from 14 GHz to 18 GHz and is divided into 32 spectral windows. During the data processing I split the block into four sub-bands, each with 8 spectral windows - allowing for in-band spectral indices to be determined without overly compromising the noise level. My multi-spectral window tests are carried out with a smaller subset of 5 spectral windows. In the second adjustment I increase the uv-coverage by combining the before transit blocks to the after transit blocks during imaging. This increases the hour angle, thus improving the uv-coverage.

3.4.2   Base imaging parameters

The deconvolution and imaging were implemented in the CASA task TCLEAN. I set the GRIDDER parameter to 'mosaic' and used the DECONVOLVER 'hogbom' and ran the task non-interactively. The TCLEAN task is based on the CLEAN algorithm, which is a method used for reconstructing a model image based on data from an interferometer. GRIDDER is a parameter in TCLEAN that selects the gridding convolution function used to process the re-sampling of the measured visibilities onto a regular uv-grid prior to an inverse Fast Fourier Transform - the option selected for this, mosaic, is an image of a patch of sky that is made up of more than one observed field. DECONVOLVER, also a TCLEAN parameter, selects which algorithm is used in the minor cycle - the option I selected here, hogbom, is a variant of the CLEAN algorithm that operates with a delta function sky model - it is most appropriate for fields of isolated point sources. To avoid "over-cleaning", I ran a zero iteration clean on the respective images to obtain their rms values. I set the threshold of the final clean at 5 times the rms of the zero-iteration image. Running TCLEAN non-interactively appears to take into account the scan pattern of the telescope and what seems to be a source smear caused by it - the artefacts created by the smear would be assumed some form of noise in an interactive clean, inherently meaning a significant portion of the flux density will not be recovered. However, to ensure I have sufficiently cleaned and the threshold is reached, I set the number of iterations to a high value and check the logger to determine the stopping criterion. A clean terminated by reaching the iteration limit would not have cleaned sufficiently and is therefore run again with a higher number of iterations until the clean terminates because it has reached the noise threshold.

The rms value is significantly influenced by the presence of strong emission - it will be very high in fields dominated by very bright sources and low in fields devoid of them. Thus, the rms value only comes close to the expected thermal noise level in fields devoid of, or far removed from strong emission. The sidelobes in maps with strong emission are removed by the process of cleaning and subsequent rounds of clean will further improve the final maps, when needed. However, more than one round of TCLEAN will not be possible on the full dataset for the purposes of this thesis, due to limited time and the magnitude of processing required.

Having successfully implemented the base parameters on a single spectral window in a single measurement set, I moved on to testing these parameters on more complex configurations of the data - combining spectral windows and measurement sets. I describe these tests in the following sections.

3.4.2.1 Spectral window 2 - before transit (am)

A zero iteration map of the second spectral window of the before transit block was created using the imaging parameters intended for the main map. The CASA task IMSTAT was then used to determine the rms noise in the image. This rms value (5 *mJy beam*$^{-1}$) was then used as the clean algorithm's noise threshold when creating the final map. TCLEAN was run with the GRIDDER set to 'mosaic', DECONVOLVER set to 'hogbom', SPECMODE set to 'mfs', WEIGHTING set to 'briggs' with a ROBUST value of 0.0, an IMSIZE of 4000 square pixels, a CELL size of 0.084 arcsecs, a THRESHOLD value of 5 *mJy beam*$^{-1}$ and the PHASECENTER set to 'J2000 19:10:18.101 09.05.43.998', which centres the imaging partway between W49 north and W49 south. TCLEAN terminated at 5058 iterations (iteration limit set at 12000) - therefore, the stopping criterion was the threshold limit. The source flux densities are shown in table 3.1. In this table, and hereafter, I have followed the naming convention used in Dreher et al. (1984) to identify the sources. New sources (yet to be identified) are labelled with a Ku prefix.

3.4.2.2 Spectral window 2 - after transit (pm)

Using the same procedure and parameters as in § 3.4.2.1 an after transit map was imaged (with an rms value of 5 *mJy beam*$^{-1}$). TCLEAN terminated at 5651 iterations (iteration

limit set at 12000) - the stopping criterion was the threshold limit, therefore, TCLEAN had cleaned sufficiently. The source flux densities on this block are shown in table 3.2.

TABLE 3.1: Before-transit source flux densities on spectral window 2 (rms 5 *mJy beam*$^{-1}$).

Source Name	Coordinates		Flux Density	
	RA	Dec	Peak	Integrated
	J2000	J2000	(mJy/beam)	(mJy)
	Left Group			
W49 South	19:10:21.761	+09:05:01.69	46.9	473.4
	Middle Group			
O	19:10:16.370	+09:06:06.97	55.0	129.9
	Right Group			
D (8)	19:10:13.159	+09:06:18.62	34.8	65.0
B (9)	19:10:13.141	+09:06:12.64	22.6	27.0
C (10)	19:10:13.211	+09:06:18.22	27.3	72.7
A (11)	19:10:12.885	+09:06:11.74	64.7	92.2
F (7)	19:10:13.354	+09.06.21.15	22.4	51.5

TABLE 3.2: After-transit source flux densities on spectral window 2 (rms 5 *mJy beam*$^{-1}$).

Source Name	Coordinates		Flux Density	
	RA	Dec	Peak	Integrated
	J2000	J2000	(mJy/beam)	(mJy)
	Left Group			
W49 South	19:10:21.761	+09:05:01.69	43.3	608.4
	Middle Group			
O	19:10:16.370	+09:06:06.97	71.0	165.9
Ku 3	19:10:15.523	+09.06.14.08	12.0	14.8
Ku 2	19:10:15.368	+09.06.15.01	16.3	16.2
	Right Group			
D (8)	19:10:13.159	+09:06:18.62	45.1	68.8
B (9)	19:10:13.141	+09:06:12.64	45.2	50.4
C (10)	19:10:13.211	+09:06:18.22	48.9	125.9
A (11)	19:10:12.885	+09:06:11.74	71.8	107.3
F (7)	19:10:13.354	+09.06.21.15	25.3	50.1
Ku 1	19:10:11.045	+09.05.20.12	38.1	27.9

The peak flux densities in either table show a deviation of ∼ 5 *mJy beam*$^{-1}$ (around the noise level in both images) from their respective counterparts, with a few outliers. Thus, directly inspecting tables 3.1 and 3.2 does not conclusively show how coherent the flux densities on the two maps are. However, Fig. 3.1 shows most of the points spread around the best fit line, again with a few outliers. There are larger deviations in the integrated flux densities, but this is most likely due to the varying apertures set in CASA VIEWER. I do not critically analyse the flux densities at this point, as the values improve when
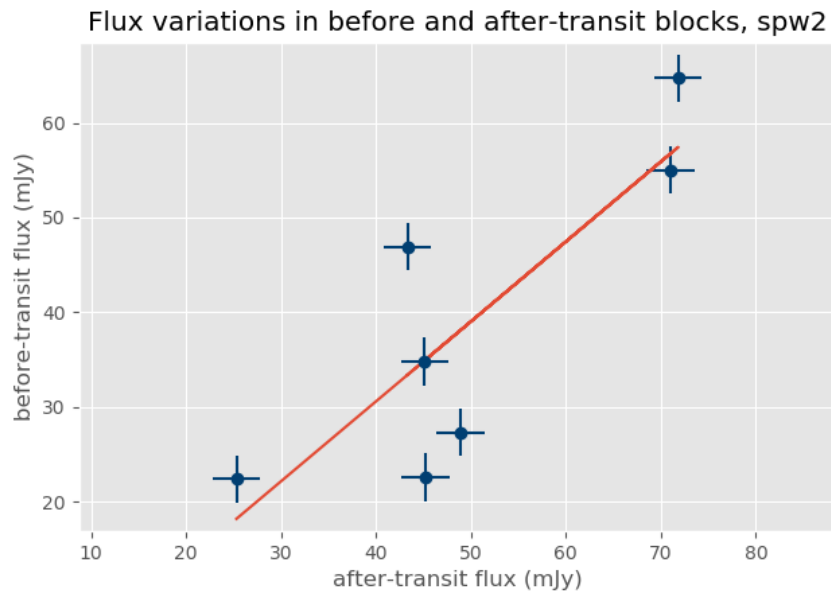
FIGURE 3.1: Plot showing the flux density trends/variations between before transit and after transit blocks. The blue dots are the respective sources, and the line of regression is shown in red. The error bars are set at either block's respective rms noise levels.

a more robust method is applied to these base parameters to implement the full survey imaging § 3.6.

3.4.2.3 Spectral window 2 - combined

Having validated the imaging parameters on either block, I moved to testing the parameters on imaging a map of the combined visibilities. Thus, using the same procedures and parameters as in § 3.4.2.1, the map was imaged with a noise threshold of 3.6 *mJy beam*$^{-1}$. In this case, however, the visibilities were assigned to the VIS parameter as a list of MS and the iteration limit was set to a higher value (20k iterations). The clean terminated at 16202 iterations and ended with a total model flux density of 3.91 Jy and peak residual of 3.58 *mJy beam*$^{-1}$. The source flux densities from the map of the combined visibilities are shown in table 3.3.

3.4.2.4 Spectral windows 2-6 - Before transit (am) and After transit (pm)

The previous sections show the fidelity of my clean methods on a single spectral window. In this and the following sections, I show the show the fidelity of my clean methods on multiple spectral windows. Therefore, keeping the base parameters in the TCLEAN task

TABLE 3.3: Combined MS source flux densities on spectral window 2 (rms 3.6 *mJy beam*$^{-1}$).

Source Name	Coordinates		Flux Density	
	RA	Dec	Peak	Integrated
	J2000	J2000	(mJy/beam)	(mJy)
	Left Group			
W49 South	19:10:21.761	+09:05:01.69	44.9	640.4
	Middle Group			
O	19:10:16.370	+09:06:06.97	63.5	173.5
Ku 3	19:10:15.523	+09.06.14.08		
Ku 2	19:10:15.368	+09.06.15.01	15.5	15.3
	Right Group			
D (8)	19:10:13.159	+09:06:18.62	43.7	86.1
B (9)	19:10:13.141	+09:06:12.64	41.8	53.3
C (10)	19:10:13.211	+09:06:18.22	46.7	142.9
A (11)	19:10:12.885	+09:06:11.74	73.8	127.7
F (7)	19:10:13.354	+09.06.21.15	24.2	59.1
Ku 1	19:10:11.045	+09.05.20.12	27.8	26.1

the same, I ran the task on a before transit MS calibrated across 5 spectral windows (spw 2-6). The rms noise on the MS was determined to be 2.5 *mJy beam*$^{-1}$ and used as the noise threshold when TCLEAN was run. The number of iterations was set to a significantly high value (30K) - the source flux densities are shown in table 3.4.

TABLE 3.4: Before-transit source flux densities on spectral windows 2 to 6 imaged with a cleaning threshold of 2.57 *mJy beam*$^{-1}$.

Source Name	Coordinates		Flux Density	
	RA	Dec	Peak	Integrated
	J2000	J2000	(mJy/beam)	(mJy)
	Left Group			
W49 South	19:10:21.761	+09:05:01.69	45.4	533.6
	Middle Group			
O	19:10:16.370	+09:06:06.97	59.4	158.0
Ku 3	19:10:15.523	+09.06.14.08		
Ku 2	19:10:15.368	+09.06.15.01	12.9	15.2
	Right Group			
D (8)	19:10:13.159	+09:06:18.62	40.7	109.5
B (9)	19:10:13.141	+09:06:12.64	35.5	53.0
C (10)	19:10:13.211	+09:06:18.22	23.5	234.9
A (11)	19:10:12.885	+09:06:11.74	69.2	124.6
F (7)	19:10:13.354	+09.06.21.15	24.5	49.9
Ku 1	19:10:11.045	+09.05.20.12	19.3	26.0

Again, using the same parameters, the after transit MS for spw 2 to 6 was imaged with an rms noise threshold of 2.54 *mJy beam*$^{-1}$. The source flux densities obtained from this MS are shown in table 3.5.

TABLE 3.5: After-transit source flux densities on spectral windows 2 to 6 imaged with a cleaning threshold of 2.54 *mJy beam*$^{-1}$.

Source Name	Coordinates		Flux Density	
	RA	Dec	Peak	Integrated
	J2000	J2000	(mJy/beam)	(mJy)
		Left Group		
W49 South	19:10:21.761	+09:05:01.69	40.2	690.9
		Middle Group		
O	19:10:16.370	+09:06:06.97	65.0	171.9
Ku 3	19:10:15.523	+09.06.14.08		
Ku 2	19:10:15.368	+09.06.15.01	16.5	16.8
		Right Group		
D (8)	19:10:13.159	+09:06:18.62	39.3	67.3
B (9)	19:10:13.141	+09:06:12.64	46.4	57.4
C (10)	19:10:13.211	+09:06:18.22	48.2	161.1
A (11)	19:10:12.885	+09:06:11.74	71.4	112.5
F (7)	19:10:13.354	+09.06.21.15	19.5	36.4
Ku 1	19:10:11.045	+09.05.20.12	29.8	44.1

The peak flux densities of most of the sources in either MS vary from their counterpart by roughly twice the noise. However, there are larger variations in the integrated flux densities. The expectation was that these would vary less with the increase in spectral windows - this variation in flux densities may be due to hidden RFI, a calibration error, or atmospheric variations as the two MS were observed a month apart. Again, the most likely reason for the difference in integrated flux densities, is the varying apertures in CASA VIEWER. Here also, I will focus on the variations in peak flux density. Fig. 3.2 shows these variations graphically - there are more data points (i.e. more detections), and less deviation from the line of regression.

Having successfully imaged both MS individually, I moved on to imaging the two MS as a single map. To create a single map from the two MS, I set the input of the VIS parameter to take the two MS as a list of strings and the output parameter IMAGENAME was set to a single image. I determined the rms noise of the dirty beam of the combined MS to be 1.81 *mJy beam*$^{-1}$ and therefore set the threshold at this value. The remaining TCLEAN parameters were kept the same.

Imaging the combined MS was not as straightforward as the preceding steps. In this instance, TCLEAN returned a segmentation fault (core dumped) error - forcing me to revisit my imaging strategy and take into account whether or not imaging this many
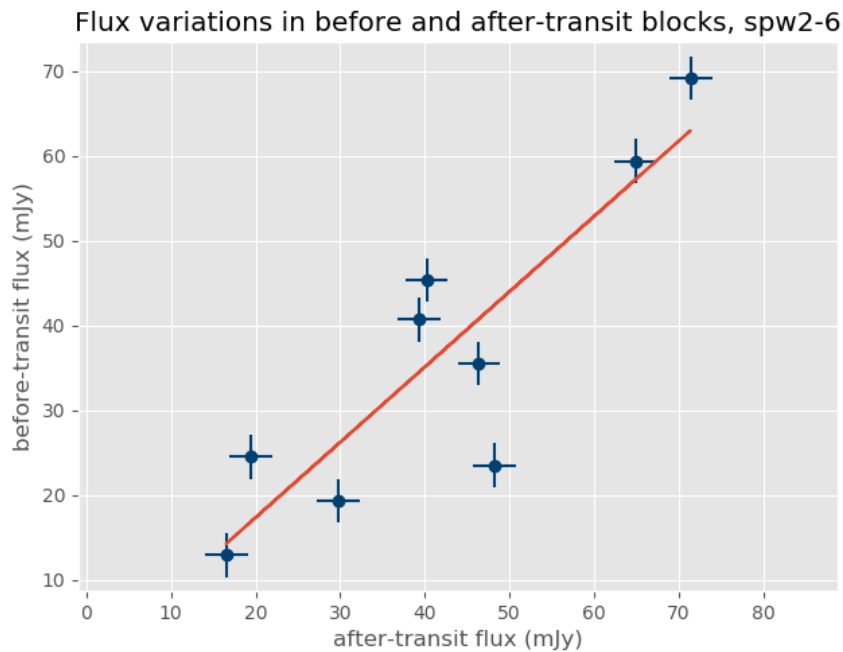
FIGURE 3.2: Plot showing the flux density trends/variations between before transit and after transit blocks. The blue dots are the respective sources, the red line of regression is shown in red. The error bars are set at either blocks respective rms noise levels.

spectral windows over such a broad survey was too computationally expensive. I, therefore, carried out memory checks and found that this was not the cause of the error. The problem was found to be related to a CASA bug caused by calibrating either MS in different versions of CASA. This produces core dumps as a result of CASA having issues with the weighting schemes. This problem is solved in one of two ways: concatenating the two MS or re-calibrating the MS using the same version of CASA. Therefore, I processed the rest of the data using the same version, CASA 5.3.0.

As in the previous sections, the stopping criterion for this map was the threshold limit. TCLEAN terminated with a total model flux density of 3.96 Jy and peak residual of 1.81 *mJy beam*$^{-1}$ after 21894 iterations. The individual source flux densities are shown in table 3.6. The peak flux densities in the combined images, single(spw2) and multiple (spw2-6), respectively, are generally within ± 2 *mJy beam*$^{-1}$ of each other and I recover more extended emission in spw2-6 than in spw2. Thus, my checks leave me confident in the fidelity of the clean method.

TABLE 3.6: Combined MS source flux densities on spectral windows 2 to 6 imaged with a cleaning threshold of 1.8 *mJy beam*$^{-1}$.

Source Name	Coordinates		Flux Density	
	RA	Dec	Peak	Integrated
	J2000	J2000	(mJy/beam)	(mJy)
		Left Group		
W49 South	19:10:21.761	+09:05:01.69	40.0	689.9
		Middle Group		
O	19:10:16.370	+09:06:06.97	61.0	178.8
Ku 3	19:10:15.523	+09.06.14.08		
Ku 2	19:10:15.368	+09.06.15.01	16.1	17.5
		Right Group		
D (8)	19:10:13.159	+09:06:18.62	41.7	123.6
B (9)	19:10:13.141	+09:06:12.64	44.0	62.3
C (10)	19:10:13.211	+09:06:18.22	48.2	219.1
A (11)	19:10:12.885	+09:06:11.74	74.2	142.9
F (7)	19:10:13.354	+09.06.21.15	22.8	58.1
Ku 1	19:10:11.045	+09.05.20.12	26.0	37.6

3.5 Discussion on test results

I have presented the 8 most distinct sources in W49A as three distinct groups: W49 North, O, and W49 South - their flux densities and positions were manually determined in CASA VIEWER. Figs. 3.3, 3.4, and 3.5, respectively, show the portions of the combined image of the before- and after-transit MS in which these detections lie. I have followed the naming convention of Dreher et al. (1984), and De Pree et al. (1997).

The first contours are set at the 3σ level (1.91 *mJy beam*$^{-1}$) and the subsequent contours are at 2, 4, 8, 16 and 32 times the 3σ level. At (1.91 *mJy beam*$^{-1}$), the first contour is higher than the final peak residual (1.81 *mJy'beam*$^{-1}$) and the rms noise in the image, (0.64 *mJy beam*$^{-1}$).

Most of the detections in W49A have been detected and named in previous studies (Dreher et al. 1984; Welch et al. 1987; Dickel and Goss 1990; De Pree et al. 1997) and have been observed in other galactic surveys (Benjamin et al. 2003; Molinari et al. 2010; Hoare et al. 2012) allowing for cross correlation and multi-frequency, multi-epoch spectral index analysis. Examining these sources over multiple studies will help determine the nature of their spectra. I expect to detect sources with strongly rising spectra in KuGARS - these sources will have gone undetected in low frequency studies. Source B

in Fig. 3.3, which is detected in KuGARS and De Pree et al. (1997) goes undetected in CORNISH. Source B is characteristic of the type of sources I aim to detect in KuGARS.
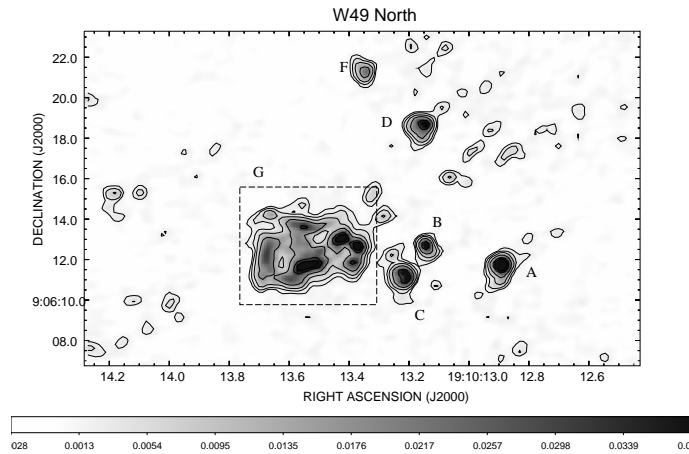
FIGURE 3.3: Gray scale image of W49 North, generated from combining the before and after-transit MS - spectral windows 2-6, ($\theta_{beam} = 0''.4$). First contours are at the 3σ level (1.91 *mJy beam*$^{-1}$). The subsequent contours are at 2, 4, 8, 16 and 32 times the 3σ level.

Fig. 3.3, shows several tentative detections around the central ring at the 3σ level. These will have to be closely examined to confirm they are sources and not sidelobes or artefacts - a comprehensive joint analysis of the source finder detections and visual detections will have to be carried out to weed out the fake detections.
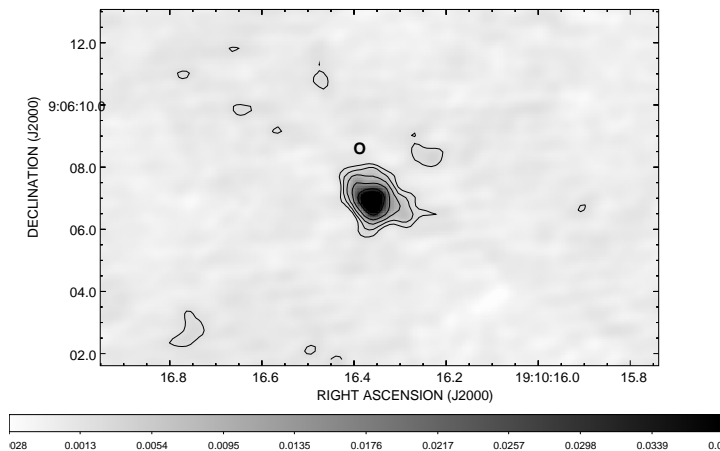
FIGURE 3.4: Gray scale image of the semi-isolated source O, of W49A, generated from combining the before and after-transit MS - spectral windows 2-6, ($\theta_{beam} = 0''.4$). First contours are at the 3σ level (1.91 *mJy beam*$^{-1}$). The subsequent contours are at 2, 4, 8, 16 and 32 times the 3σ level.

Sources with extended emission such as W49 South in Fig. 3.5, are expected to be missing a lot of their extended emission. KuGARS was observed in the B configuration
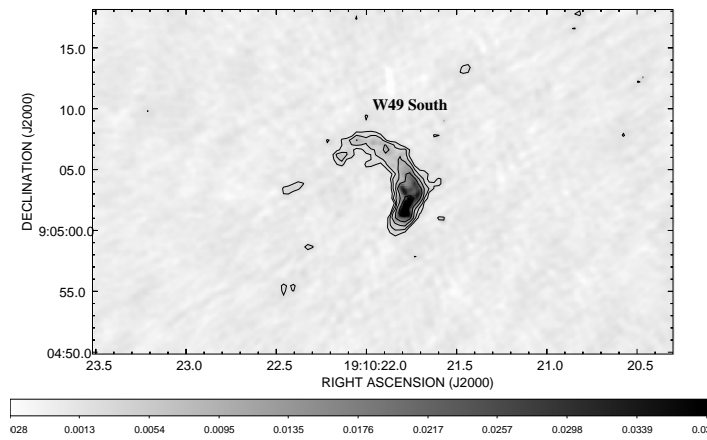
FIGURE 3.5: Gray scale image of W49 South, generated from combining the before and after-transit MS - spectral windows 2-6, ($\theta_{beam} = 0''.4$). First contours are at the 3σ level (1.91 *mJy beam*$^{-1}$). The subsequent contours are at 2, 4, 8, 16 and 32 times the 3σ level.

of the VLA and is therefore missing short spacings. Consequently, the flux densities are underestimated.

3.6 Improved imaging

The first stages in the development of an imaging strategy for the KuGARS data were limited to a subset of the full frequency range on a subsection of a single MS in order to optimise development time and test speeds. The imaging procedures discussed in § 3.4 show significant progress in the development of my imaging pipeline. I discussed the transition from "single MS, single spw" imaging to "multi-MS, multi-spw" imaging. Quality checks to validate the new clean method showed particular improvement in the flux density recovered for extended emission sources which had been a critical problem prior to the implementation of this new method. However, the imaging described in this section was still being carried out on a small portion of the data meant to test strategies to be used for full MS imaging. In this section, I describe the steps taken to extend the imaging to full MS and with that the entire survey.

3.7 Imaging parameters

My previous discussions have shown that my base imaging parameters (§ 3.4.2) are producing results with good image fidelity. I therefore move on to applying these imaging parameters to an entire measurement set. In OTF map observations, the MS will not have a fixed phase centre given the entire MS is a mosaic of multiple phase centres i.e., the scans (see Fig. 3.6). Thus, unlike standard observations, the clean algorithm requires the phase centre be specified for OTF map data.
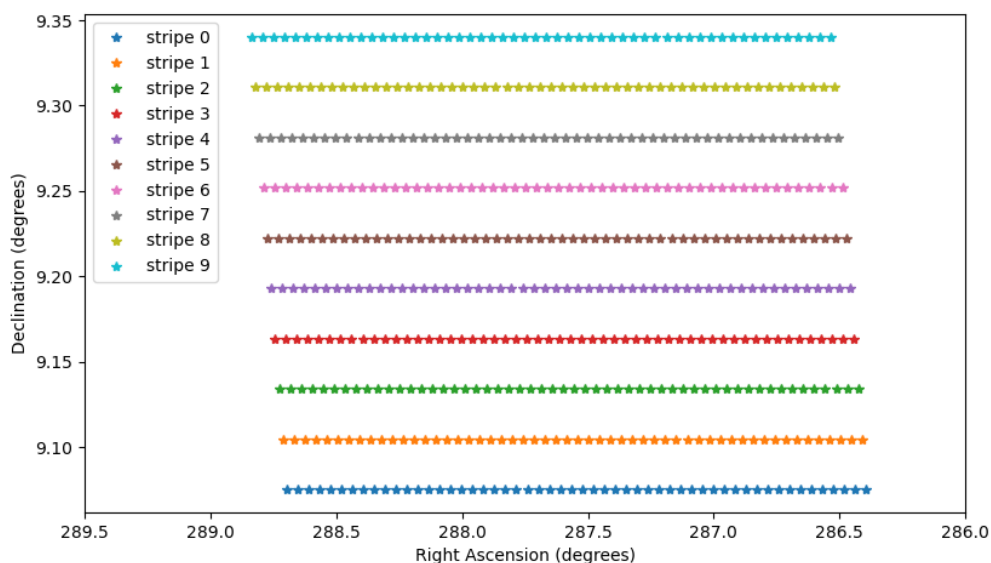
FIGURE 3.6: Full scan patterns on a KuGARS scheduling block. The map covers a 2.3° x 0.265° area divided into 10 observing stripes of 54 scans. Each stripe is uniquely colour coded.

In my previous discussion, the phase centre was set to the centre of the massive star forming region, W49A, which was a pre-determined choice given these coordinates are in the literature. Unfortunately, as the survey is a "blind" search, the coordinates of most of the objects I intend to detect are not available. In the most ideal setting, the entire block is deconvolved into a single image. At a spatial resolution of 0.42 arcsecs and a 5 pixel per beam sample, a map covering an area 2.3° x 0.265° requires an image size of $\sim(100000, 11400)$ pixels. Clearly, the computational power to achieve this is obscene and therefore unlikely. As an alternative, I geometrically divided the map into 21 cutouts, with the geometrical centre on each cutout as the phase centre (Fig. 3.7). Care was taken in the design to determine the phase centres in a way that gives overlap between adjacent cutouts. As this is a "blind" search, the source positions cannot be

pre-determined, thus there exists the possibility that the edge of one or more cutouts could slice a source. Therefore to alleviate edge effects, overlaps were written into the design.
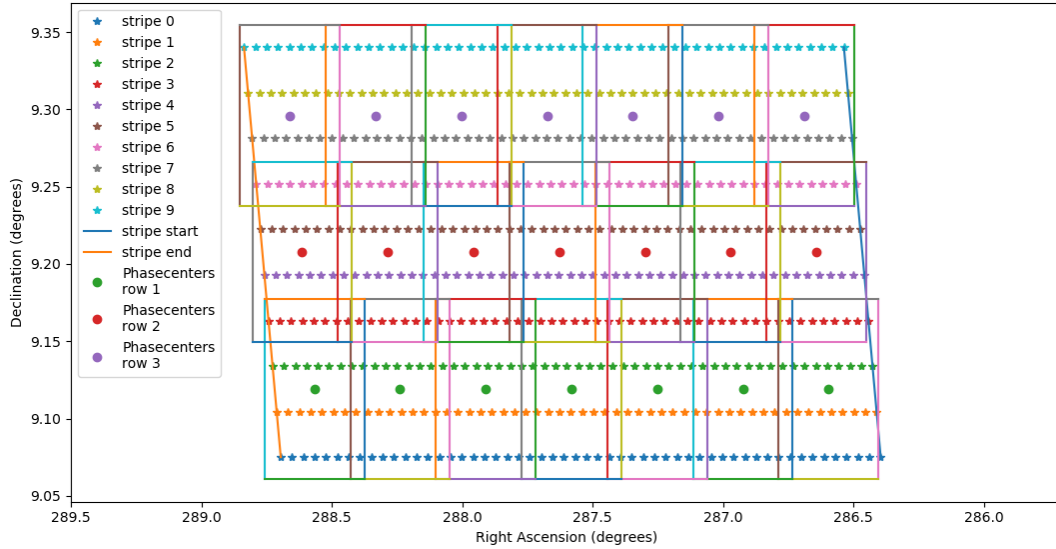
FIGURE 3.7: A 2.3° x 0.265° map divided into 10 stripes of 54 scans pattern overlaid with cutouts to be used when imaging. Each cutout has a geometrically determined phase centre. Each stripe is uniquely colour coded. The cutout tiles each have a size of 22.9 arcmin x 7 arcmin.

With this, I was able to produce the first set of images on a full block. The imaging was carried out using the base parameters used during the testing process and run non-interactively through a script. Each cutout was imaged iteratively by passing a list of phase centres produced by a python script written to determine, plot, and print out their coordinates. As before, the stopping criterion used was the threshold limit set to the rms noise of the dirty map. In ∼90% of the cutouts, this produced the expected result. However, a non-convergence was returned by the other ∼10% of the cutouts. On further inspection, these were found to have "missing data" in the form of blank (black) patches (Fig. 3.8). Inspecting the rest of the data revealed less prevalent cases of this "missing data" phenomenon in a few other cutouts. It therefore became obvious that the problem was not with the data but with something fundamental in the clean method being used. The problem arose because I was including more data than was required to image each cutout, by not explicitly specifying which fields to include in the imaging of each cutout. By including fields not meant to contribute emission to the

cutout, during the mosaic gridding step, all the extra fields get gridded onto the same uv-grid as the contributing fields. Consequently, their emission also gets included in the image. I discuss this in more detail in the following section.
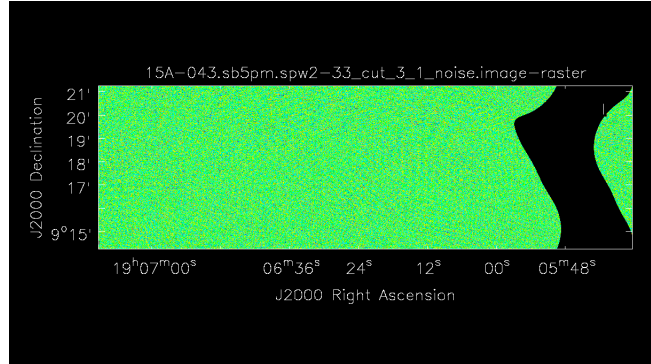
FIGURE 3.8: Dirty map of a cutout showing the "missing data" feature. The feature is presented as a black patch to the far right of the image.
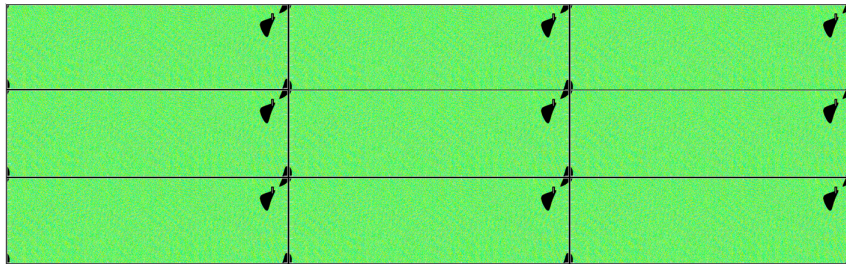
FIGURE 3.9: Tiled images of a cutout showing an alignment of the "missing data" in the corners of the image that is indicative of aliasing.

3.7.1 Identifying the correct fields for each cutout and choosing a proper image size

In interferometric OTF map imaging via cutouts, it is important to identify and include only the contributing fields for each tile. Not specifying the right subset of fields includes more emission than required (or less) and not specifying a subset at all includes every single OTF map field.

3.7.1.1 Image size and aliasing

Due to the nature of interferometry and Fourier transforms, when making an interferometric image from a MS, subset or otherwise, it is crucial to make the image large enough to include all of the sky area being imaged plus a buffer to avoid aliasing. Aliasing is

a phenomenon that occurs as a consequence of a Fourier sum being made over data that is regularly spaced. It becomes impossible to discriminate between phase changes, thus gridding data generates a regularity that allows emission from outside an image to become folded into it. The solution is to make an image big enough to encompass the emission within the "folding" range; big enough to include all the real emission that lies within the transform area. Therefore, if the image is too small to cover all the data included, then the data that should not be in the image is aliased (folded back) into the image. If a $1° × 1°$ image is made that includes a pointing on a source which in reality lies $0.1°$ outside of the region being imaged, this source can be aliased in and will actually appear to be $0.1°$ inside the region being imaged. By including all the target fields during my imaging, I caused aliasing to happen to some of my images (e.g. Fig. 3.8, Fig. 3.9).

It is possible to get aliasing when imaging data from a single pointing, if the image size is not made at least as big as the primary beam. It therefore follows that this can occur even if only the correct pointings are included in the image, but some of the them are located near the image edge. KuGARS was observed in the Ku-band in the B-configuration of the VLA. This corresponds to a primary beam with full width half maximum (FWHM) of about 2.8 arcmin. That means the primary beam still has significant sensitivity 1.4 arcmin from the pointing centre. If an image is made with one of the (contributing) pointings inside the image edge, there could be emission detected from a source at the edge of the FWHM of the primary beam, 0.2 arcmin outside the image. That source would be aliased in and appear 0.2 arcmin inside the image. Fig. 3.9 illustrates the effect of aliasing. The image shown, is a tile of one of the cutouts. In this case, however, the aliasing is evident due to the "missing data" rather than a source as this is largely a field of noise. Tiling allows a comparison of the corners together, showing that the blank regions line up with the other corners.

In order to avoid aliasing, the image size needs to be large enough that all the pointings contributing significant emission lie toward the centre of the image, rather than the edge. This leaves two imaging options: image the entire observing block or create multiple tiles. The first option requires imaging all the fields at once by making a single image that covers the entire observation; the image would need to be $> 2.3°$ wide and $>0.265°$ tall. This would require an image $> 100,000$ pixels by > 11400 pixels and as stated before, the memory footprint would be untenable. This leaves the second option of creating

multiple tiles. However, correctly implementing this requires identifying and using only the fields needed for each individual tile. With a primary beam FWHM of 2.8 arcmin, the image size must be set so that every pointing is ≥ 1.4 arcmins from the edge of the image. So, for the image size used in Fig. 3.7, 22.9 arcmin $\times$ 7 arcmin I want all the fields within an area 25.6 arcmin $\times$ 9.8 arcmin. Furthermore, I need to make the image large enough to avoid aliasing from all the fields at just inside or just outside the edge of the image. Therefore, to ensure I am completely avoiding aliasing, I will put all of the contributing fields within the central quarter of the image; for an image size of 22.9 arcmin $\times$ 7 arcmin, I will make an image that is 45.8 arcmin $\times$ 14 arcmin. This will make a larger image than the area of interest and will be masked around the edges. The central region (22.9 arcmin $\times$ 7 arcmin) can then be cut out to leave only the region of interest for each tile. There may be some aliasing from the larger area of the data used (outer pointings in the 25.7 arcmin $\times$ 9.8 arcmin region) but any such aliasing will appear outside of the important central region of 22.9 arcmin $\times$ 7 arcmin.

3.7.2 Setting CONJBEAMS to True

Setting CONJBEAMS to TRUE in TCLEAN instructs it to define beams with frequency (by convolving the beams from symmetrical frequencies above and below the central frequency) such that the extent of the calculated primary beam is roughly constant with frequency across the bandwidth. Because of the primary beam shape, not setting CONJBEAMS to TRUE results in source intensities away from the pointing centre being attenuated (their apparent intensity drops). In a single-pointing image, this does not affect a source at the phase-centre of the image, but has an increasingly more significant effect as you move out away from the phase-centre with the result of limiting the possible dynamic range of the image. For a mosaic (especially using OTF mapping) sources that are at the phase-centre in one "pointing" are far from the phase-centre in other "pointings" so this will always affect mosaic images.

3.7.3 Common restoring beam

As one of my goals is to measure SEDs, it is ideal for the images to have a common restoring beam across all the frequency channels and tiles in the survey. The beam shape is dependent on declination, and the beam size is dependent on frequency. This means

that each subband will have a different restoring beam and the measured flux densities will be distorted. Accurate SED measurements require proportionately measured flux densities thus making it necessary to impose a common restoring beam.

When applying an "imposed" beam, the aforementioned effects must be considered carefully. A problem arises when the imposed beam is smaller than the "real" synthesised beam, in that this results in super-resolution in the images because the imaging algorithm is being forced to fill in gaps for which there are no Fourier components. Conversely, choosing a larger beam falsely reduces the resolution of the image. This will generally occur to some extent, but becomes a problem when taken to the extreme.

In the CASA task TCLEAN the restoring beam can be placed in one of three categories. When left to its default, TCLEAN determines the restoring beam by fitting a Gaussian to the PSF main lobe. This results in an elliptical beam, in the form [major, minor, pa]. Alternatively, the user has the option to set the restoring beam parameter to common. This determines a beam to which all the beams in an image can be convolved, it looks at all the possible beams and chooses the beam with the largest area and uses that. Finally, the user can explicitly set a specific resolution element for the restoring beam, either as an elliptical beam in the aforementioned format or as a circular Gaussian beam. I chose the latter of the user defined options as this avoids issues with the position angle. However, in order to be certain I was not changing the shape of the beam enough to cause resolution problems, I imaged the phase calibrators and restored them to their native beams. I then used these values to determine the beam elongation on the phase calibrators and used this as a basis to determine whether or not a circular Gaussian beam was feasible for this data.

Fig. 3.10 shows beam elongation as a function of scan number. The phase calibrators are positioned at the start of each observing stripe and therefore are at different declination. Thus, this plot essentially shows the beam elongation as a function of declination. The scan numbers and respective declinations increase in proportion from lowest to highest. The plot is colour coded to represent each scheduling block. The general trend shows the beam being most elongated at the lowest scan (or declination), it gradually reduces with the elongation tending toward one as the scan number (declination) approaches its highest value. The mean beam elongation is ∼1.3. Fig. 3.11 shows how the beam elongation varies with spectral window (or frequency). Again, the plot is colour coded to
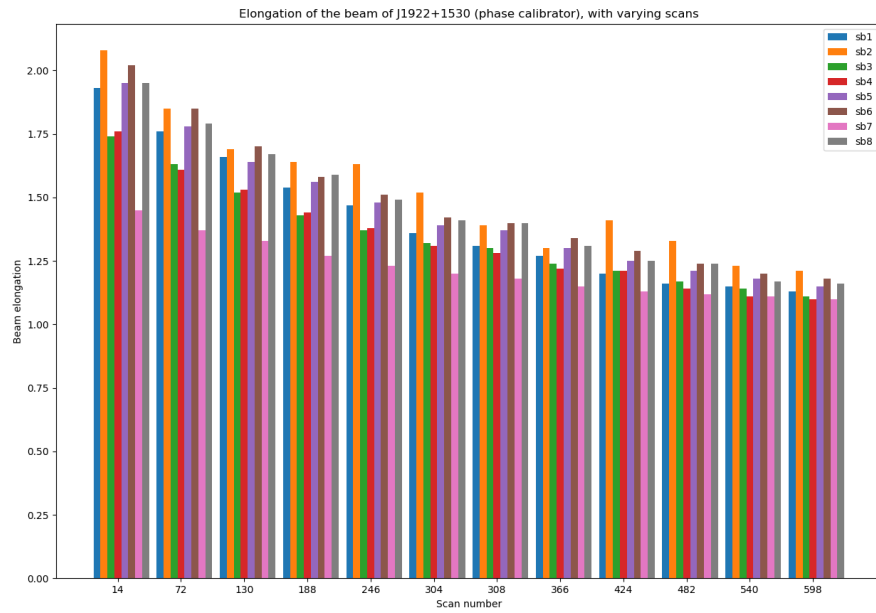
FIGURE 3.10: Histogram of the beam elongation of the phase calibrator. The plot shows the variation of the beam elongation with scan number. Each scan number represents the phase calibrator at the start of each stripe. Each colour represents a block.

the representative scheduling blocks. Here, the general trend does not show as distinct a variation in elongation within a block, that is the beam elongation does not significantly vary with frequency. There is a slightly higher variation between subsequent blocks. This deviation is, however, roughly ± 0.2 the value of the preceding block, and the average elongation is found to be 1.36. As the beam does not appear vastly elongated, I find it feasible to set the beam to restore to a circular Gaussian element. And, to avoid any super resolution effects, I have chosen to restore to the resolution at the lowest frequency (0.42 arc seconds).
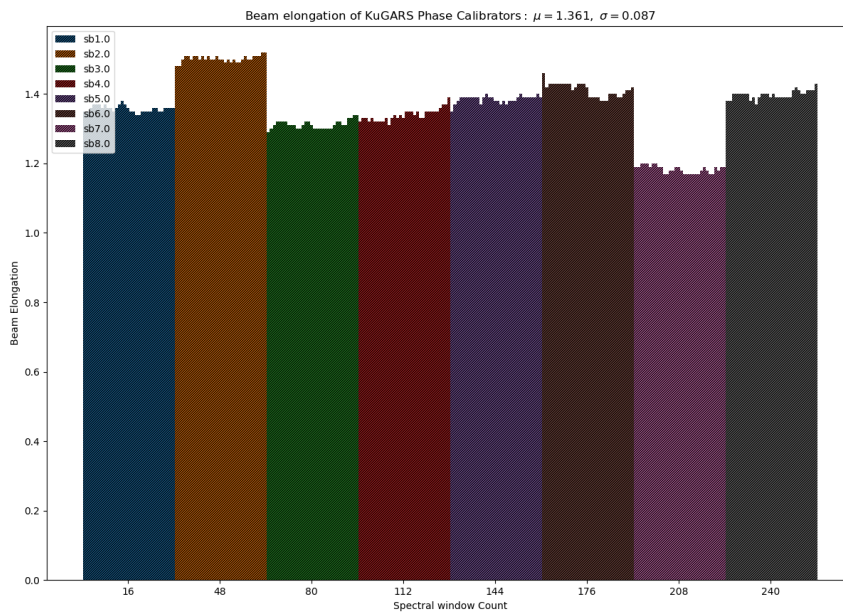
FIGURE 3.11: Histogram of the beam elongation of the phase calibrator. The plot shows the variation of the beam elongation with spectral window (x-axis). Each colour represents a block.

3.8 Full Survey Imaging

In the final implementation of the imaging, I have taken into account all the parameters discussed in § 3.6 in combination with the base parameters determined in § 3.7. To optimise the spacing between cutout centres, field overlap, as well as the image sizes with respect to the available computational power, I have sub-divided each scheduling block into 3 rows of 6 columns to give 18 cutouts per block. To account for aliasing I have made the image sizes larger than the field of interest, so that the field of interest occupies the central quarter of the image. However, because the stripe start and end positions were determined in Galactic coordinates and the data observed in ICRS, the scheduling blocks are skewed to the left. To account for this I have included a buffer that edges the two extreme corners into the central portion of the image. Thus, each cutout will have a size of 62.7 arc minutes wide and 17.9 arc minutes tall, as shown in Fig. 3.12.
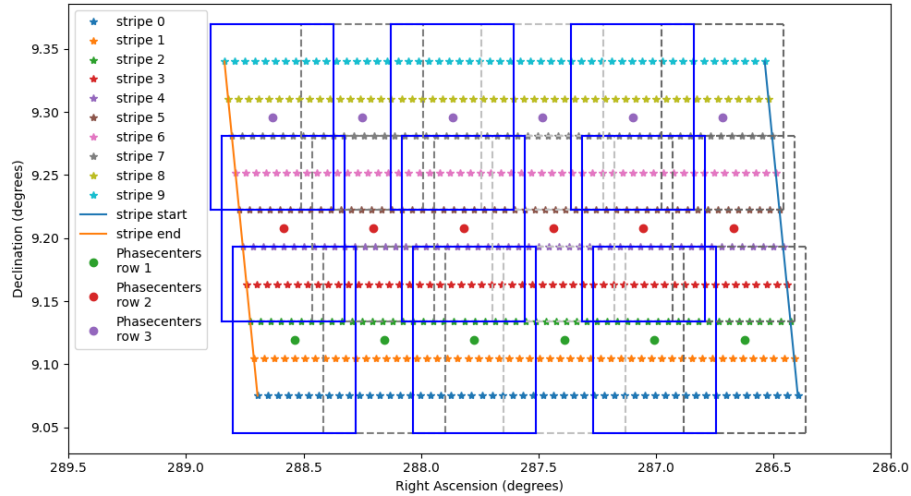
FIGURE 3.12: A 2.3° x 0.265° map divided into 10 stripes of 54 scans. Overlaid with the final cutout pattern used in the KuGARS' imaging. Each stripe is uniquely colour coded. Each cutout has a geometrically determined phase centre. The cutout tiles each have a size of 62.7 arcmin x 17.9 arcmin.

As expected, some tile edges were positioned across one or more sources. In most cases the source was faint and had no negative effect on the imaging, in others the source was bright and resulted in a non-convergence. Therefore, the fields within which these bright sources occurred were removed from the imaging and deconvolved separately.

3.9 Cataloguing

The survey covers a large portion of the sky ($4° \times 2°$), and therefore the image properties of the eight scheduling blocks also vary. The brightest regions, such as those centred on, or imaged close to the massive star forming region W49A, have higher RMS values than those located in more thinly populated regions. Moreover, scheduling blocks imaged with a bright source just outside the field of view, are riddled with sidelobes. The more densely populated regions also have more prominent artefacts, most taking on the shape of point spread function-like sidelobes. However, the artefacts are barely seen in regions with very bright isolated point sources, most likely due to dynamic range. As expected, the varying image properties mean varying noise properties as well. The survey noise distribution ranges from 45.6 *μJy beam*$^{-1}$ to 4.78 *mJy beam*$^{-1}$ (Fig. 3.13). The lower RMS values are representative of noise dominated regions while the higher RMS values are representative of regions containing bright sources.
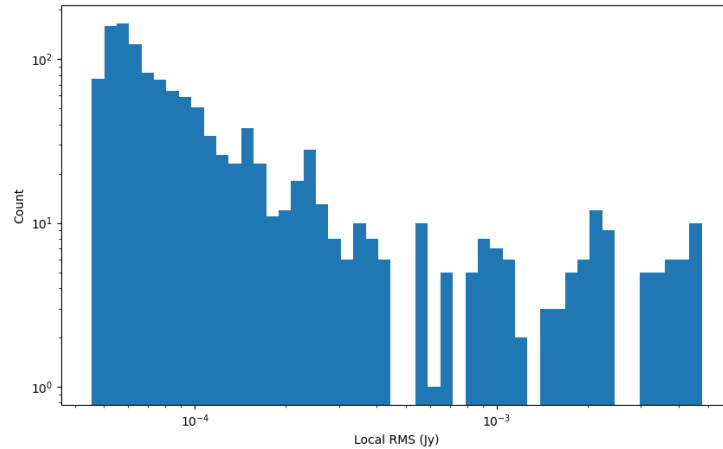
FIGURE 3.13: Histogram illustrating the noise distribution across the KuGARS survey. The plot shows the local RMS of the sources in the compact source catalogue. The recorded RMS values range between 45.6 $\mu Jy\ beam^{-1}$ and 4.78 $mJy\ beam^{-1}$.

The sources in the KuGARS compact source catalogue were extracted using the AEGEAN (Hancock et al., 2012, 2018) source finder. The images used to generate this catalogue were processed using the full 4 GHz bandwidth to maximise the sensitivity. I have extracted 1238 sources ranging from 214 μJy to 0.79 Jy (see Fig. 3.14). Source extraction was the first part of a series of tasks that led to putting together a complete and reliable catalogue. Every science application requires that the source positions and uncertainties are correctly measured and reported, and will thus be limited by the correctness of the catalogue extracted from the images. The steps taken to ensure the fidelity of the catalogue have been discussed in this section.
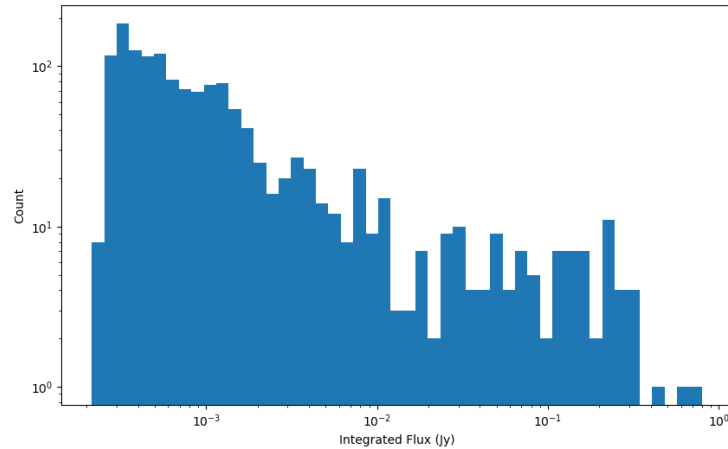
FIGURE 3.14: Histogram of the KuGARS compact source catalogue integrated flux densities. There are ∼1.2k compact sources between 214 μJy and 0.79 Jy.

3.9.1 Background Estimation

The background and noise estimation were carried out using BANE rather than AEGEAN's in-built algorithm. The background and noise estimation performed by AEGEAN and BANE use algorithms called zones and grid, respectively. I have chosen grid over zones because the zones algorithm is most efficient at the centre of each zone but tends to become inaccurate towards the edges, consequently the source finder's false detections increase beyond what is reasonably expected from simple Gaussian statistics. The grid algorithm is similar to the zones algorithm, however it takes a sliding box-car approach. By working on two spatial scales, an inner (grid) scale and an outer (box) scale, it calculates the background and noise properties of all the pixels within a box centred on a grid point (Hancock et al., 2018).

3.9.1.1 FLOODFILL

I have used AEGEAN to detect and extract the source positions and properties. This source finding algorithm is based on the FLOODFILL algorithm, used by Murphy et al. (2007), Hales et al. (2012), and the references therein. FLOODFILL uses two thresholds, called the seed and flood thresholds, that are used to identify (seed) the island and to limit the growth of the island, respectively. The seed threshold value is the same as, or higher than the flood threshold. The seed threshold is the lower limit for pixels that are

used to seed an island, while the flood threshold is the lower limit for pixels around the seed pixel that are included in the island. The algorithm begins by identifying the seed pixel ($\geq \sigma_{seed}$) and then moves on to identifying which adjacent pixels are above the flood threshold before adding them to the island. This is repeated for every succeeding set of adjacent pixels until the pixel values fall below the flood threshold. I have used the default values for AEGEAN's seed and flood thresholds: $\sigma_{seed} = 5$ and $\sigma_{flood} = 4$ (Hancock et al., 2012).

3.9.2   Source Detection

A full-band catalogue of the KuGARS data, containing 1238 compact sources, has been extracted using AEGEAN and BANE. The Source finder detected 1544 distinct components, of which 306 were identified as sidelobes through visual inspection. The AEGEAN-TOOLS are written to run on FITS files, thus the KuGARS CASA images have been exported to FITS format to make them readable to this software. First BANE is used to estimate the background and noise of the individual cutouts on each KuGARS block to produce a pair of noise and background FITS files corresponding to each cutout. Then AEGEAN, using the BANE outputs as inputs, is run on the FITS images to extract the catalogue.

The imaging strategy I employed meant that the KuGARS sources were extracted from multiple images which are cutouts made from the larger observing blocks (see § 3.8). The individual image source tables were then concatenated into a master catalogue. Furthermore, the data were imaged in two sets: first, the full band containing all the spectral windows; second, four sub-bands, each containing eight spectral windows. To ensure consistency in the SED measurements, I have applied the standard source extraction to the full-band images, because they are the most sensitive, and used CASA's IMIFT task for the source extraction on the sub-band images.

3.9.3   Table Format and Filters

3.9.3.1   Unique Identifiers

The output tables have been kept in the native output format of the source finder. However, I have taken into account that the KuGARS images comprise multiple cutouts on

multiple blocks, and therefore have written-in a column to identify which block-cutout combination the source was extracted from. This, in combination with the island and source columns, provides each row with a unique identifier. Each row in this column, labelled file_id, has a 3 digit number with the first, second and third digits indicating the block, row (stripe), and column, respectively. The file_id, island, and source columns are then combined to form unique source identifiers - eight digit numbers formed by joining the elements of these columns in appearing order. The island and source numbers are zero padded for values below 100 and 10, respectively. Therefore, the final implementation uses this number (Source ID) as the unique identifier in a master catalogue constructed by concatenating all the cutout catalogues.

3.9.3.2 Filtering

There are six flags AEGEAN can set during the source finding process (Hancock et al., 2012). The values in the flag column can either represent one flag or a combination of two or more flags. The base flag identifiers are all powers of 2, and an identifier used for a combination of two or more flags is formed by the sum of the flags it represents, thus the individual flags can easily be identified. The catalogue predominantly comprised sources with flags 0, 4 and 21 (flags: 1, 4, and 16). All sources with flags > 4, have been discarded as these are highly unreliable and unlikely to have physical measurements.

3.9.3.3 Auxiliary Flags

The realness of a measurement can be determined by checking it against its uncertainty. Ideally, for a measurement to be real it should have a value greater than its uncertainty, and be at least three times greater than its uncertainty to be reliable. Therefore, I have written-in an auxiliary flag column (aux_flags) with values determined by checking each peak flux density measurement against the error in peak flux density and assigning one of the following flags appropriately:

0 - if the peak flux density is 3 times the error in the peak flux density. **Real measurement**

1 - if the peak flux density is greater than the error in peak flux density by less than 3 times its value. **Upper limit**

2 - assign a flag of 2 if the peak flux density is less than the error in the peak flux density. **Non-physical measurement**

3.9.4 Sub-band source extraction (IMFIT)

The CASA image-plane component fitting (IMFIT) task fits one or more two dimensional Gaussians to sources in an image. The fit output is returned as a dictionary with a key reporting whether the fit converged or failed as a boolean, and another reporting the fit results. The results key is a subdictionary containing a list of one or more components reflecting the fit results.

The sub-band images were sub-divided to produce image cutouts matching the same pattern as the full-band images. Here, the source extraction has been performed using photometry by employing CASA's IMFIT task. As the purpose of generating sub-band images is to facilitate measuring in-band spectral indices, the source positions and sizes in the full-band catalogue have been used in the photometry measurements carried out on the sub-bands. Using the full-band provides the highest sensitivity, and applying the same sizes and positions to the respective sub-bands ensures consistency in the spectral index measurements.

Preliminary source detection carried out on the sub-bands with AEGEAN in the default setting have revealed a discrepancy in the number of detected sources in the respective sub-bands. The same has been observed in the photometry measurements. The highest drop in detections is observed in the highest frequency band which has 167 fewer detections than the full-band catalogue. Each successful measurement in the sub-band catalogues has been checked against its uncertainty to find and remove non-physical measurements. I have kept measurements with a value 3 times the uncertainty as real and flagged measurements whose uncertainty is greater as non-physical and flagged the rest as upper limits.

To create the master multi-band catalogue, I have used a pairwise crossmatching technique where I match one band with the next and join them. For the crossmatch, I have used the Starlink Tables Infrastructure Library Tool Set (STILTS), which is a set of command-line tools designed to deal with the processing of tabular data. I have used a 1or2 join which returns an output for each row whether it is represented in both tables

or in only one of them. When a value exists in only one table, a "masked" value is used as a place holder for the table for which it does not exist. This keeps the column dimensions equal, making it possible to horizontally concatenate the tables. Furthermore, to maintain dimensional consistency, I have used the band with the most sources in all the pairwise matches and horizontally stacked the respective sub-band tables in increasing order.

To achieve this, I have carried out the following steps:

1. Estimate background and noise on full-band images using BANE.

2. Run AEGEAN on full-band images with BANE outputs as inputs.

3. Run IMFIT on the sub-band images using the full-band catalogue source coordinates and sizes to determine the position and size of the IMFIT apertures.

4. Run a pairwise crossmatch (using a 1or2 join) on the sub-bands and horizontally concatenate them.

    i. Crossmatch bands 1 and 2 - this will be the base table. Columns are in form col and col_2.

    ii. Crossmatch bands 3 and 1 - add left columns to base table enable rename kwarg. Columns are now in the form col.., col_2.., col_3...

    iii. Crossmatch bands 4 and 1 - add left columns to base table again, with rename kwarg. Columns are now in the form col.., col_2.., col_3.., col_4...

    iv. Rename band 1 columns so that they are in the form col_1.

3.10 Completeness

An essential step in determining the fidelity of the source finding process is to test the completeness of the catalogue. The completeness of the catalogue is a measurement of the expected number of sources, found above a particular significance level (e.g. 90 or 95% complete), that are reliable. The test estimates what fraction of sources at a given flux density level we expect to detect given the noise and source density in a map or survey. The steps taken to do this will follow a generally similar pattern from survey to survey, but can and will be nuanced in the details of the sub-processes. To begin

with, a region on which to run the test needs to be selected. This can be a sub-region or full image on one or multiple tiles of the survey, depending on the variations across the survey region. Moreover, the selected region can either be free of sources and background or can be a region with other sources and background emission. The former tests the recovery of sources not affected by confusion with other sources or the background, the latter tests source recovery that is affected by background and source confusion. Next, an input catalogue of sources with random positions is created. The sources are generated using Gaussian functions with randomly chosen l and b (or ra and dec) values within the image. The input catalogue should have a fixed FWHM but different flux density values chosen to have a uniform distribution between a low and a high value. The low value should be $\sim 1\sigma$ (where σ is the standard deviation of the map) and the high value should be $\sim 10\sigma$. A map of a subsample of the input catalogue which has a zero background and a gaussian centred on each of the chosen positions should then be created and added to the chosen FITS image to produce a new image. To avoid overloading the image with fake sources, this process should be done iteratively, only adding $\sim 10\%$ of the total number of real sources in the image at each time. The source finder is run on the new FITS image using the exact configuration of parameters used to detect the real sources. The sources matching the input catalogue are then pulled out. If the image used contains real sources, the real sources are subtracted from the catalogue so as not to contaminate the statistics of the test. This process is repeated until all the input catalogue sources have been injected into the template image and extracted. The result is plotted in a histogram of the fraction of recovered sources (i.e. the number of sources detected/the number of sources in the input catalogue) against the flux density (or SNR). This shows what the recovery percentage of sources is for various flux densities. This will ideally show $\sim 95\%$ source recovery between 5σ and 7σ.

Every image, including those with no real sources, will have some background. Thus, a phenomenon called 'flux boosting', where low flux density sources are recovered with higher flux densities, is likely to be seen. In particular, this phenomenon, also known as Eddington bias (Eddington, 1913), occurs when positive fluctuations in noise coincide with the locations of low SNR sources thus resulting in higher flux densities for these sources. A plot of the flux density of a recovered source against the flux density of the injected source will show the extent to which this has occurred. This will generally show a 1:1 line with some scatter and the low flux densities will be boosted.

3.10.1 Detection ratio

The completeness of the KuGARS observations as a function of peak source flux density was estimated by repeatedly injecting compact artificial sources into 8 representative subregions, each from a unique scheduling block. The RMS in these subregions ranges between 52.9 and 127 $\mu Jy\ beam^{-1}$ which is adequately representative of the noise properties across the KuGARS survey. The peak flux densities and the coordinates of the artificial sources were randomly generated, and ranged from 0.2 to 6 $mJy\ beam^{-1}$. A constant FWHM of 0.42 arcsec was used for all the injected sources. The subregions used were 4096 square pixel cutouts taken from the survey images. The selected regions therefore contained pre-existing sources, thus the simulation was written to account for this and therefore tests the recovery as a function of source confusion. To avoid source contamination, the source finder was run on the native images as well as the artificial source infused images to identify and remove real sources from the test. The test results showed a lower recovery rate at the lower flux densities which shows that source detection is difficult for faint sources around the noise limit, whereas we see a $\sim 100\%$ recovery for the very bright sources.
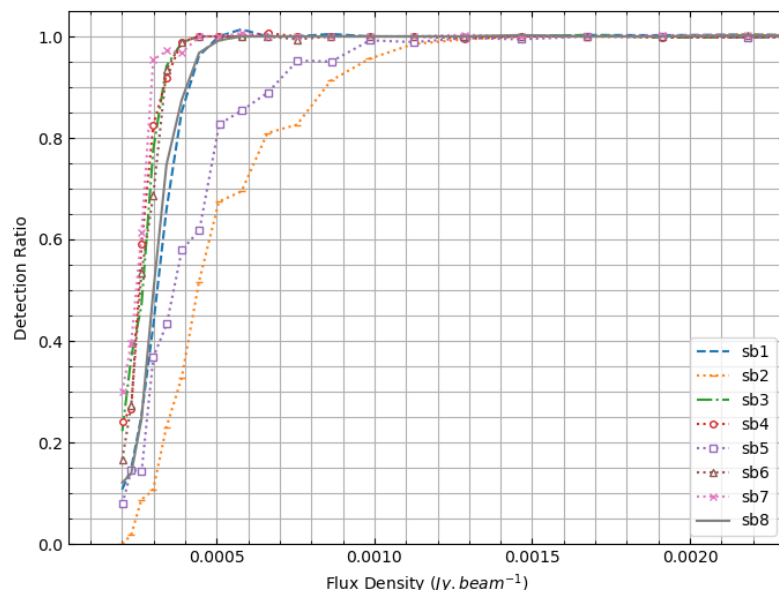
FIGURE 3.15: Completeness of the KuGARS point source catalogue. The completeness tests of eight representative subregions overlaid on the same plot to highlight similar traits and deviations.

The fraction is $\sim 99\%$ or above for sources with peak flux densities greater than 0.4 *mJy beam*$^{-1}$, in sb3, sb4, and sb6; greater than 0.5 *mJy beam*$^{-1}$, in sb1, sb7, and sb8; greater than 1.14 *mJy beam*$^{-1}$ in sb5, and greater than 1.29 *mJy beam*$^{-1}$ in sb2. This corresponds to a $\sim 99\%$ completeness at 7σ or above for all the regions except sb2, sb5 and sb7 which are $\sim 99\%$ complete at 10σ (sb2) and 9σ (sb5 and sb7). All the fields are 95% complete at 7σ or greater except sb2 which is 95% complete at 8σ or greater (Figs. 3.15 and 3.16). The images produced from radio observations are dynamic range limited, an effect caused by instrumental artefacts, imaging artefacts and incomplete calibration of the instrumental response (Braun, 2013). The dynamic range of an image is the ratio between the peak brightness on the image and the RMS noise in a region presumed to be free of emission. Calibration errors are likely to result in image errors that portray similar characteristics to the sidelobes in the beam given that they are constrained to the same (u, v) cells sampled by the data (Perley, 1999). These sidelobes are predominantly greatest near the peak, consequently, the image errors will be greater in regions containing structure.
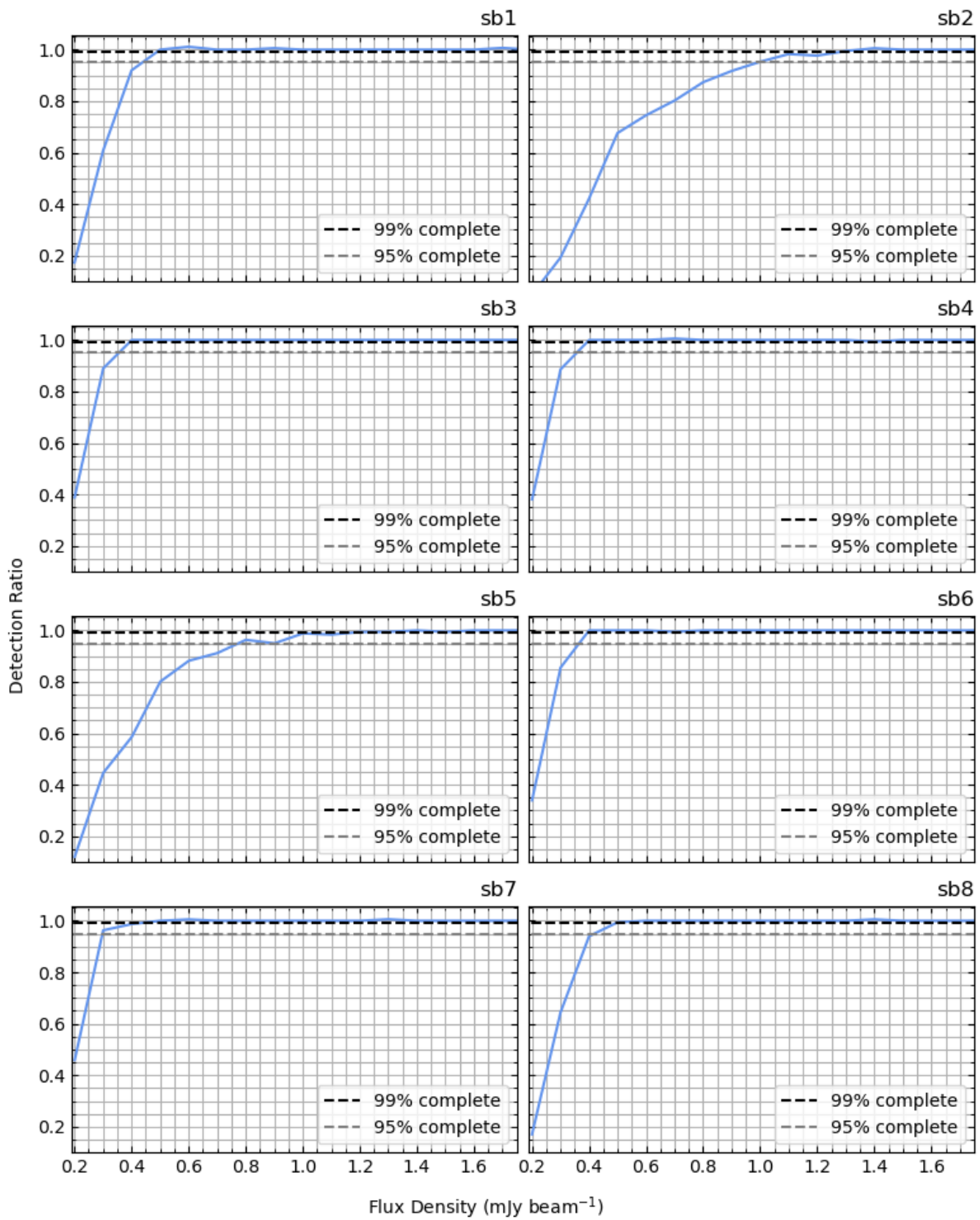
FIGURE 3.16: Completeness of the KuGARS point source catalogue shown as the fraction of sources detected as a function of peak source flux density. The completeness has been tested over eight representative regions in the KuGARS survey with varied background and noise properties. The individual plots show where the fraction is equal to 0.99 and 0.95.

3.10.2 Flux boosting

In Fig. 3.17 I have shown the effect of the background noise in the survey on low flux density sources. The injected and detected flux densities have been plotted against each other to show any "boosting" in the detected flux densities. A solid purple line has been used to show the line of equality. The black dashed line is a best fit of the data. In each of the regions these lines are in fairly good agreement, implying the output is generally equal to the input. However, there is still a fair bit of scatter centred around the y=x line in all the regions, the severity of which is directly related to the noise properties of the respective regions. The flux boosting effect is most evident at the lower flux densities where the data shows a shift depicting a boost in the detected flux densities. Both the scatter and the lower flux density shifts are most apparent in sb2 and sb5, which have the highest mean noise levels in the sub-sample, followed by sb1 and sb8 which have the next highest levels. The remaining regions have lower rms noise levels and the shift is less apparent.

Sources that fall below the noise threshold get shifted up and are thus detected with a higher flux density (Fig. 3.18). This is a consequence of background and instrumental noise present in the field. The central part of a field tends to be predominantly affected by confusion noise and coincides with the lowest instrumental noise in the map (Borys et al., 2003).
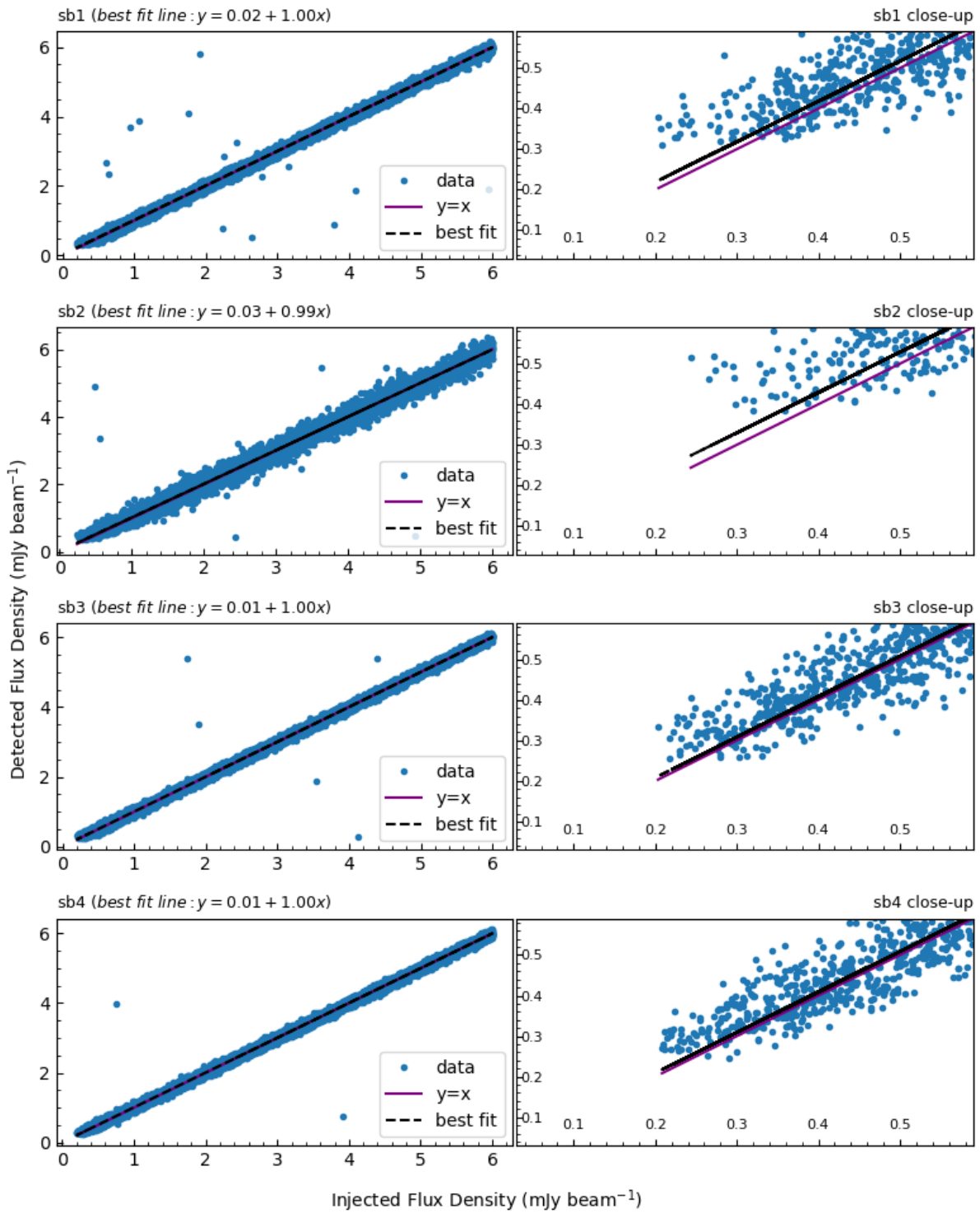
FIGURE 3.17: Extent of flux boosting in the detected sources shown by plotting the detected flux densities against the injected flux densities. The left column shows the full range of the data while the right column is a close-up of the lower flux densities, where the flux boosting is most evident. The purple lines represent the data when y=x, the black dashed lines are best fits of the data.
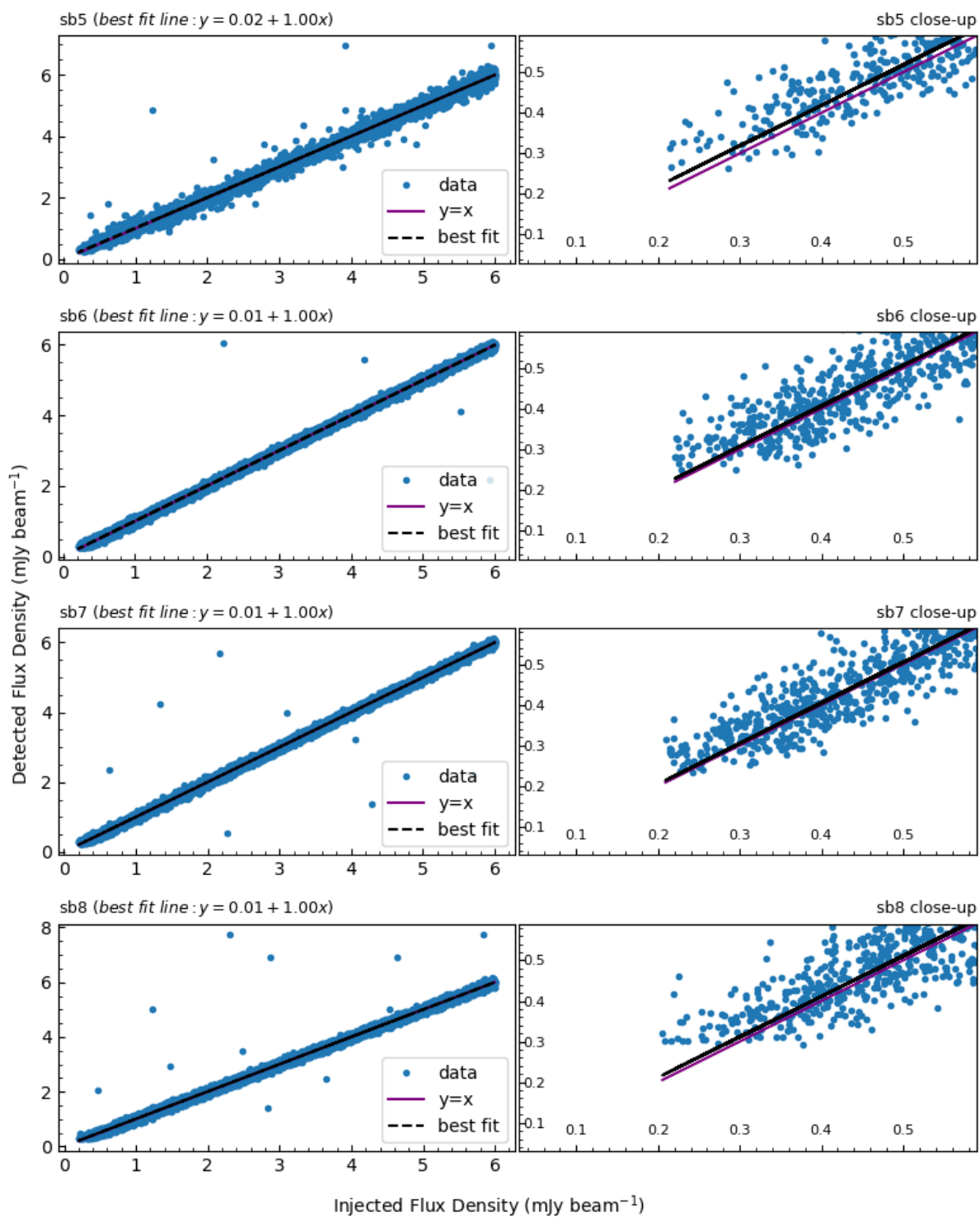
FIGURE 3.17: Continued.
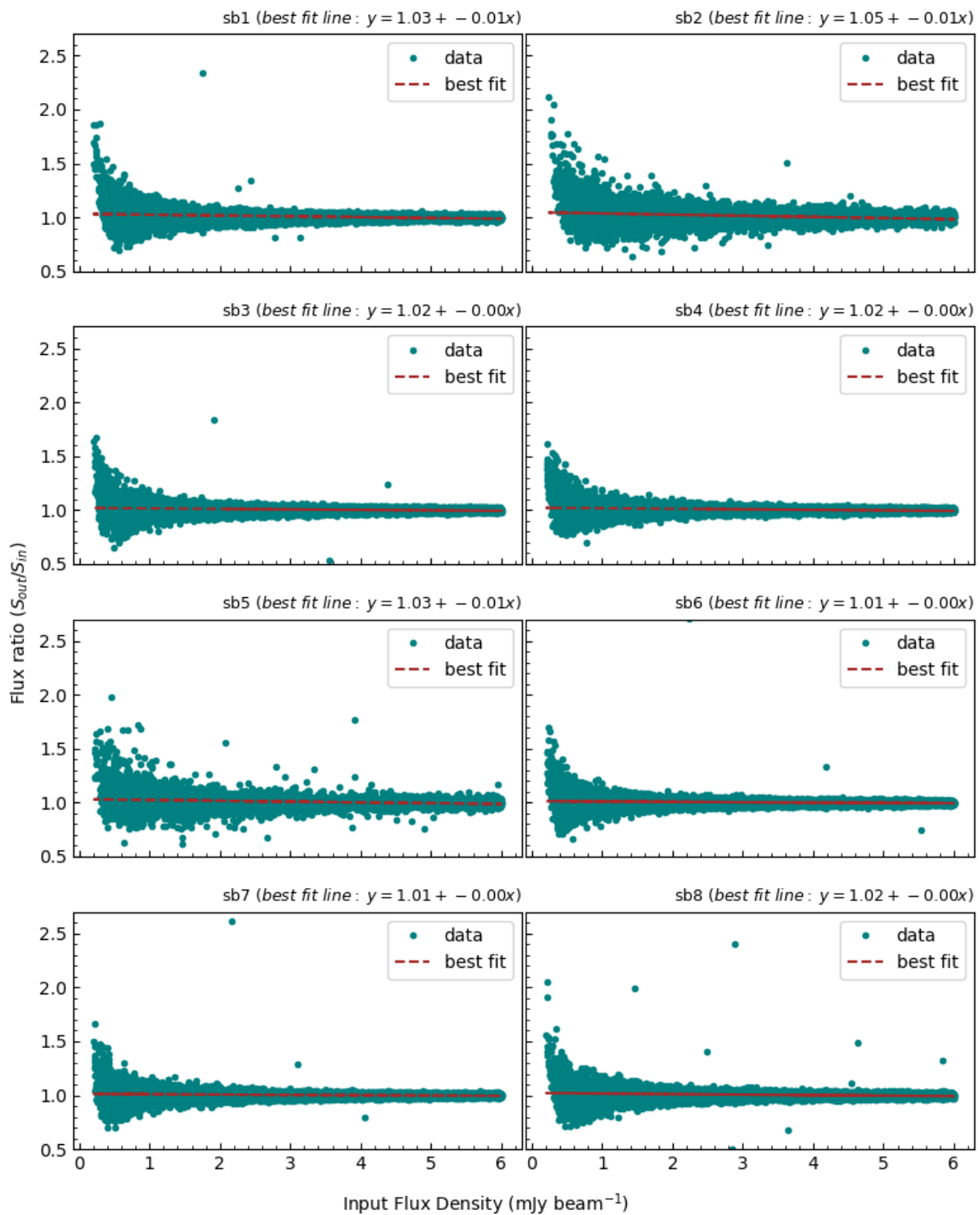
FIGURE 3.18: KuGARS source recovery flux density bias ratio. The ratio of the output to input flux densities is plotted against the input flux density and represented by the teal data points. The brown dashed line is the line of equality. The plots show the fainter source flux densities are shifted up when they fall below the noise threshold.

TABLE 3.7: An excerpt of the KuGARS full-band point source catalogue (the full catalogue can be found in Appendix B). The first two columns are source identifiers, the next two give the source coordinates in the J2000 epoch. Columns 5 to 8 are the observed flux densities and their respective errors. Columns 9 and 10 are the major and minor axes of the FWHM and column 11 is the position angle. The errors in peak and integrated flux density are given as individual columns in the table. The major and minor axes both have a typical error of 0.02 arcsecs and the position angle has a typical error of 0.37°.

Source Galactic name	Source Index	RA J2000	Dec J2000	Peak (mJy/beam)	error	Integrated (mJy)	error	Major arcsec	Minor arcsec	PA (°)
G41.4660+0.8363	1115500	19:04:05.76	+07:58:24.30	0.37	0.07	0.37	0.07	0.42	0.42	0.0
G41.5017+0.7481	1126200	19:04:28.73	+07:57:53.05	1.53	0.28	1.55	0.28	0.42	0.42	-0.04
G41.6777+0.4478	1127100	19:05:52.96	+07:58:59.71	0.36	0.06	0.37	0.06	0.42	0.42	0.01
G41.6126+0.3431	1130300	19:06:08.25	+07:52:38.16	1.63	0.15	3.28	0.36	0.89	0.4	-18.95
G41.7563+0.9086	2210800	19:04:22.45	+08:15:52.07	0.67	0.12	0.68	0.12	0.42	0.42	-0.02
G41.8440+0.9063	2214300	19:04:32.69	+08:20:29.10	0.45	0.08	0.46	0.08	0.42	0.42	-0.01
G41.9724+0.8972	2314700	19:04:48.95	+08:27:04.56	0.55	0.09	0.54	0.11	0.43	0.41	-84.29
G42.0280+0.9268	3113100	19:04:48.75	+08:30:51.55	1.52	0.06	1.94	0.09	0.51	0.44	-1.18
G42.0315+0.9569	3114200	19:04:42.64	+08:31:52.30	0.32	0.06	0.32	0.06	0.42	0.42	-0.02
G42.0574+0.9300	3114900	19:04:51.35	+08:32:30.79	0.33	0.06	0.34	0.06	0.42	0.42	-0.01
G42.0891+0.9747	3212400	19:04:45.21	+08:35:25.82	0.27	0.05	0.28	0.05	0.42	0.42	-0.03
G42.1634+0.9683	3215600	19:04:54.88	+08:39:13.08	0.3	0.05	0.31	0.05	0.42	0.42	-0.02
G42.1776+0.9731	3216200	19:04:55.41	+08:40:06.28	0.34	0.06	0.35	0.06	0.42	0.42	-0.02
G42.2196+0.8967	3216400	19:05:16.58	+08:40:14.57	0.41	0.06	0.42	0.08	0.44	0.41	15.28
G42.1634+0.9683	3312100	19:04:54.88	+08:39:13.11	0.32	0.06	0.33	0.06	0.42	0.42	-0.03
G42.2445+0.9350	3315400	19:05:11.10	+08:42:37.48	0.38	0.05	0.37	0.06	0.42	0.4	-17.06
G42.2349+0.9781	3316000	19:05:00.73	+08:43:17.81	0.3	0.05	0.3	0.05	0.42	0.42	-0.02
G42.2966+0.9692	4111600	19:05:09.52	+08:46:20.58	0.33	0.06	0.34	0.06	0.42	0.42	-0.03
G42.3323+0.9799	4113800	19:05:11.18	+08:48:32.26	0.3	0.04	0.3	0.04	0.42	0.42	-0.03
G42.3573+0.9354	4114000	19:05:23.58	+08:48:38.80	0.37	0.05	0.34	0.05	0.45	0.37	4.94
G42.3847+0.9402	4116900	19:05:25.59	+08:50:14.22	0.26	0.05	0.26	0.05	0.42	0.42	-0.02
G42.3828+0.9845	4119100	19:05:15.82	+08:51:21.48	0.41	0.05	0.43	0.07	0.51	0.36	89.23
G42.5349+0.9272	4312100	19:05:45.14	+08:57:53.18	0.35	0.06	0.35	0.06	0.42	0.42	-0.02
G42.6526+0.9453	5111300	19:05:54.36	+09:04:39.41	0.86	0.06	3.08	0.24	0.86	0.73	-83.0
G42.6535+0.9455	5111400	19:05:54.42	+09:04:42.89	2.75	0.08	2.71	0.09	0.42	0.41	5.92
G42.6534+0.9454	5111401	19:05:54.42	+09:04:42.25	0.71	0.08	0.55	0.06	0.38	0.36	80.61
G42.6549+0.9459	5111500	19:05:54.50	+09:04:47.78	0.46	0.06	0.83	0.16	0.71	0.45	29.29
G42.7656+0.9255	5116700	19:06:11.27	+09:10:08.11	0.41	0.07	0.42	0.07	0.42	0.42	-0.01
G42.7306+0.9215	5210200	19:06:08.20	+09:08:09.62	0.89	0.16	0.9	0.16	0.42	0.42	-0.02
G42.9634+0.9145	6110200	19:06:35.73	+09:20:22.21	1.18	0.21	1.19	0.21	0.42	0.42	-0.02
G43.1426+0.8924	6212500	19:07:00.55	+09:29:18.59	0.33	0.05	0.47	0.09	0.54	0.47	12.33
G43.1523+0.9375	6214000	19:06:51.88	+09:31:04.05	0.25	0.05	0.26	0.05	0.42	0.42	-0.02
G43.1722+0.9775	6216000	19:06:45.46	+09:33:14.11	0.3	0.05	0.3	0.05	0.42	0.42	-0.02
G43.2759+0.9545	6316600	19:07:02.03	+09:38:07.31	0.35	0.06	0.35	0.06	0.42	0.42	-0.02
G43.3991+0.8951	7113700	19:07:28.67	+09:43:02.82	0.92	0.05	0.98	0.06	0.45	0.42	0.58
G43.3930+0.9788	7210800	19:07:09.89	+09:45:01.84	0.27	0.05	0.27	0.05	0.42	0.42	-0.03
G43.4948+0.9016	7213200	19:07:37.98	+09:48:19.48	0.35	0.05	0.28	0.05	0.41	0.34	-87.31
G43.5175+0.9156	7310700	19:07:37.50	+09:49:55.20	0.45	0.07	0.45	0.09	0.43	0.41	-86.72
G43.5230+0.9593	7311500	19:07:28.65	+09:51:25.28	0.31	0.05	0.31	0.05	0.42	0.42	-0.03
G43.6275+0.9052	7314400	19:07:52.08	+09:55:29.54	0.3	0.05	0.3	0.05	0.42	0.42	-0.01
G43.8538+0.9586	8215400	19:08:05.89	+10:09:01.06	0.71	0.11	0.72	0.11	0.42	0.42	-0.02
G43.8223+0.9505	8310500	19:08:04.13	+10:07:07.02	0.56	0.1	0.57	0.1	0.42	0.42	-0.03
G43.8066+0.9838	8310600	19:07:55.15	+10:07:11.92	0.59	0.1	0.59	0.11	0.42	0.42	-0.04
G43.8117+0.9769	8310800	19:07:57.22	+10:07:17.03	0.55	0.09	0.56	0.09	0.42	0.42	-0.04
G43.8800+0.9814	8313200	19:08:03.91	+10:11:02.68	0.37	0.07	0.38	0.07	0.42	0.42	-0.03

3.11   The Catalogue

The KuGARS catalogue contains 1238 sources extracted using the procedures described in § 3.9. An excerpt of the catalogue is shown in Table 3.7, and the full catalogue in Appendix B. The data presented in these tables were extracted from the full band images of the KuGARS survey data. The sources extracted from these images portray a broad range of properties. The distribution of the total flux density of the extracted sources as a function of Galactic longitude and latitude is shown in Fig. 3.19. The brightest detections in the survey are located between $l = 43°$ & $l = 43.5°$ where W49A, one of the brightest star forming regions in the Milky Way, is located. In Galactic latitude, the flux density distribution peaks around b= 0°, which follows as we expect looking down the mid-plane, we are likely to see a high density of sources (Wood and Churchwell, 1989a).

The catalogue peak flux densities range from 246 *μJy beam*$^{-1}$ to 0.279 *Jy beam*$^{-1}$, the integrated flux densities range from 0.214 mJy to 0.796 Jy (Fig. 3.14). The mean noise varies widely across the observed field, being highest in the regions with the most complex structures and lowest in the regions free of source emission, the local mean noise ranges from ~ 46 *μ*Jy to 4.78 mJy (Fig. 3.13). The point source catalogue contains a short range of compact source sizes, the majority of which are smaller or equal to 2 beams (0.84 arcseconds). The distribution shown in Fig. 3.20 shows the angular sizes peaking at the beam. The source finder was sensitive to and detected 57 sources that are greater than 2 beams, with the largest being equal to $\sim$6 beams.
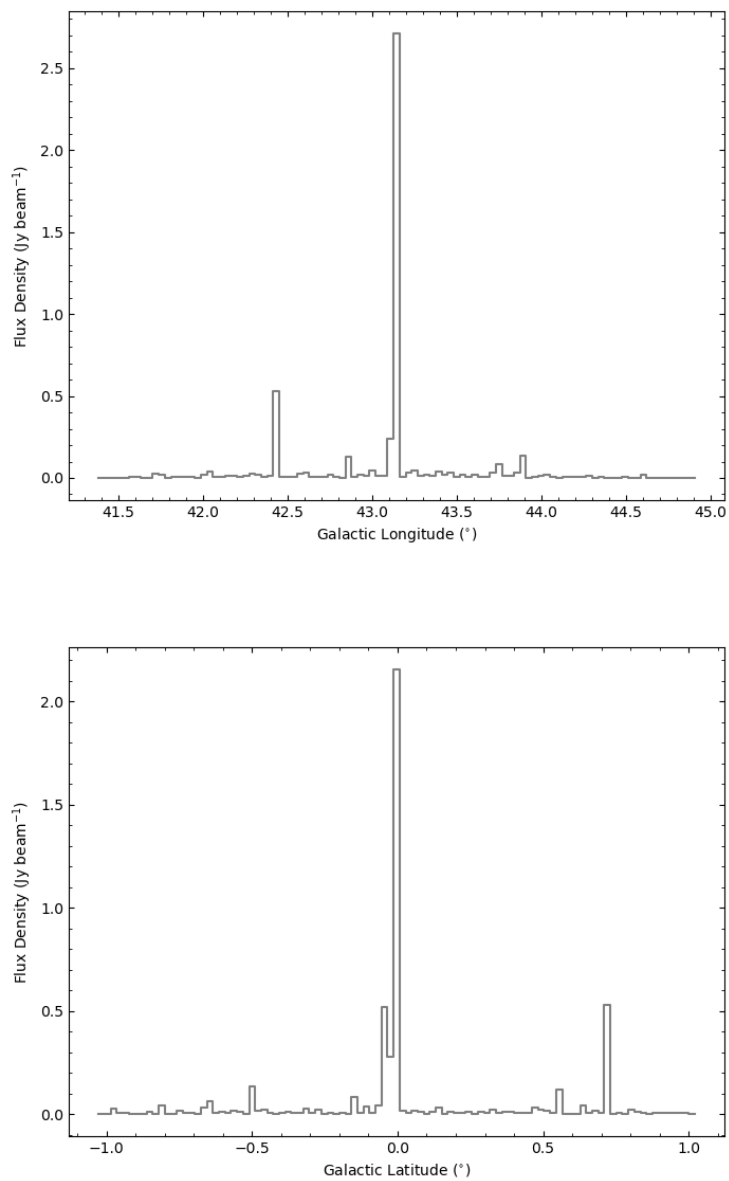
FIGURE 3.19: Total flux density distribution of the catalogue sources as a function of Galactic Longitude and Latitude. The distributions contain sources extracted along Galactic plane in the $41° < l < 45°$, $|b| \leq 1°$ region.
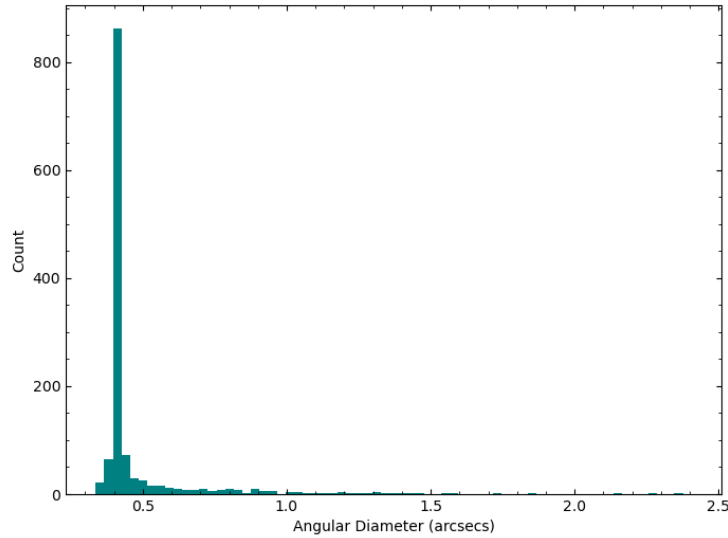
FIGURE 3.20: Distribution of the angular diameters of the KuGARS compact sources. The distribution shows that the majority of the sources are $\sim$ beam sized.

3.12 Summary

I have detailed the data reduction process, showing the methods I have developed to circumvent the hurdles presented by the large volume of data. The imaging process outlined shows the steps taken on subsets of the data to build a robust imaging method which was later applied to the full dataset. The size of the data meant imaging a complete scheduling block as a single map was untenable, thus each block was subdivided into 18 overlapping cutouts. The imaging strategy was also designed to take into account the science goals, which include measuring SEDS. Therefore, a common restoring beam was imposed on the output images. For this, a circular Gaussian beam was used. This was not done without caution. The feasibility of imposing such a beam was verified through analysing the beams of the calibrators to determine the degree of elongation present in the observations. This was found to be $\sim$1.3. Furthermore, to avoid the effects of super resolution, the beam was restored to the resolution of the lowest frequency. Using a compact radio source finder, AEGEAN, I have detected 1238 sources in the $4° \times 2°$ region covered in the survey. The source flux densities range from 246 $\mu Jy\ beam^{-1}$ to 0.279 $Jy\ beam^{-1}$ and 214 μJy to 0.796 Jy for peak and integrated flux densities, respectively. Their mean noise ranges from 45.6 $\mu Jy\ beam^{-1}$ to 4.78 $mJy\ beam^{-1}$. The fidelity of

this catalogue was tested through completeness simulations run on a subset of the data. This revealed that the catalogue is 95% complete at 7σ or higher in all but the second scheduling block which is 95% complete at 8σ or higher.

In this chapter I have discussed the technical aspects involved in the KuGARS survey. In the next, I will delve into the analysis and interpretation of the continuum data. I will discuss the nature of the sources, particularly HII region candidates, and the methods used to identify them.

Chapter 4

The Pilot Ku-band Galactic Reconnaissance Survey

4.1 Introduction

The pilot Ku-band Galactic Reconnaissance Survey is the precursor to a potential Ku band large area survey of the northern hemisphere of the Milky Way with the aim to discover and characterise the population of steep positive spectrum objects in the Galaxy. By conducting a pilot survey I can assess the likely true population of such objects in the Milky Way and quantify the benefit of carrying out a wider survey. Previously, I described the survey and observation details in § 2.1, I then discussed the data reduction and extraction of sources from the continuum data cubes in Chapter 3. Here, I discuss the analysis and interpretation of the continuum data.

4.2 Identifying Young HII Regions

Young HII regions cannot definitively be identified via radio or IR emission alone. Classifying them with confidence depends on multiwavelength analyses - the source must be associated with radio, IR, and submillimetre emission. The radio shows the free-free emission from the HII region; being an HII region means it is associated with hot dust thus should emit in the IR; and the fact that it is young means it should still be embedded in a molecular clump which means it should show submillimetre emission.

This identification technique has been successfully used in previous studies, including Thompson et al. (2006); Urquhart et al. (2009a, 2013); Hindson et al. (2012); Purcell et al. (2013), to distinguish UC HII regions from otherwise similar objects.

4.2.1 Association of KuGARS sources with submillimetre emission

I have identified potential young HII regions by determining which compact radio continuum sources are embedded in molecular clumps as traced by 850 μm emission. This was done by crossmatching the ATLASGAL clump catalogue with the full-band KuGARS compact source catalogue. The match was run with a max separation error of 40 arc seconds, roughly twice the beam of the APEX telescope. The join parameter, which determines which rows are included in the output table, was set to "1and2" to create an output row for each row represented in both tables. The find parameter, which determines what happens when a row in one table can be matched by more than one row in the other table (e.g. include all matches, or only the best), was set to "best1" thus for each row in table 1, only the best match from table 2 was selected - rows from table 1 will only have one occurrence, but rows from table 2 may appear multiple times. To account for clumps having multiple compact sources embedded in them, KuGARS was set as table 1 (i.e. the best match) which meant each KuGARS source would only match one ATLASGAL clump, while the clumps could match multiple KuGARS sources. Collectively, 82 compact sources were found to be embedded in a total of 12 clumps. The matched sources have been graphically represented by overlaying the radio image with ATLASGAL contours and radio source markers to show the 14 GHz emission embedded in 850 μm emission (Fig. 4.1).

4.2.2 Association of KuGARS sources with IR emission

There are 82 compact sources found to be embedded in an ATLASGAL clump and, therefore, 82 candidate HII regions. These sources have further been investigated for IR brightness by matching them against emission from the WISE 22 μm band. Being bright in the MIR is an additional indication of ongoing star formation, and therefore points to the likelihood the radio sources are young HII regions. The sources in this sample are coincident with strong mid-IR emission (Fig. 4.2). Moreover, some of the sources are highly saturated at 22 μm (see G43.166+0.011, G43.148+0.013, G43.165-0.028). The

radio sources devoid of IR emission are likely to be extragalactic, or compact sources that are similar to HII regions in the radio regime such as planetary nebulae. In § 4.4 I will examine the physical properties of these sources to determine whether or not they are consistent with young HII regions.
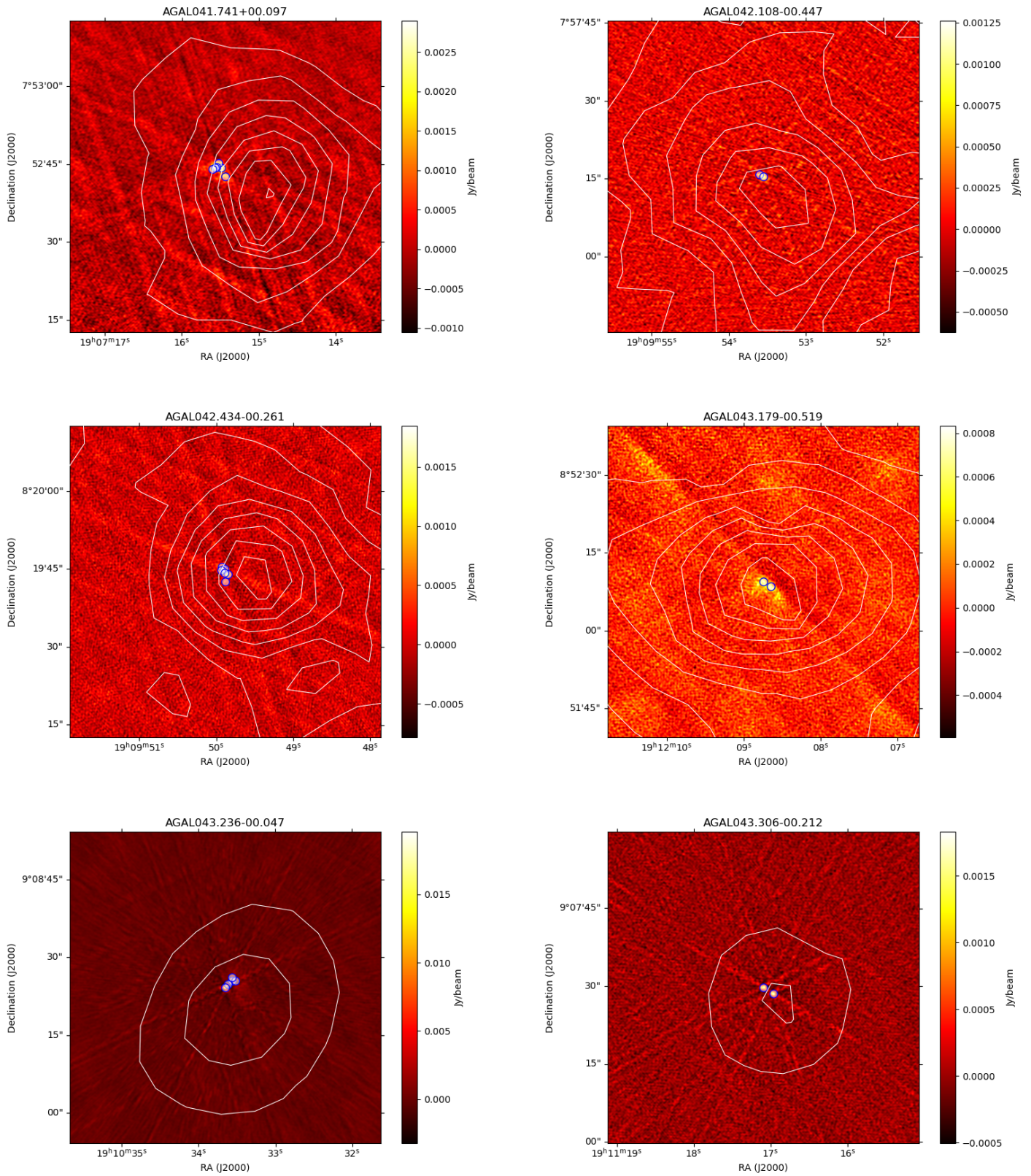
FIGURE 4.1: ATLASGAL contours, and radio source markers overlaid on the Ku-GARS colourscale. The ATLASGAL clumps are represented by grey contours and the KuGARS sources embedded in the clumps are shown as blue circles.
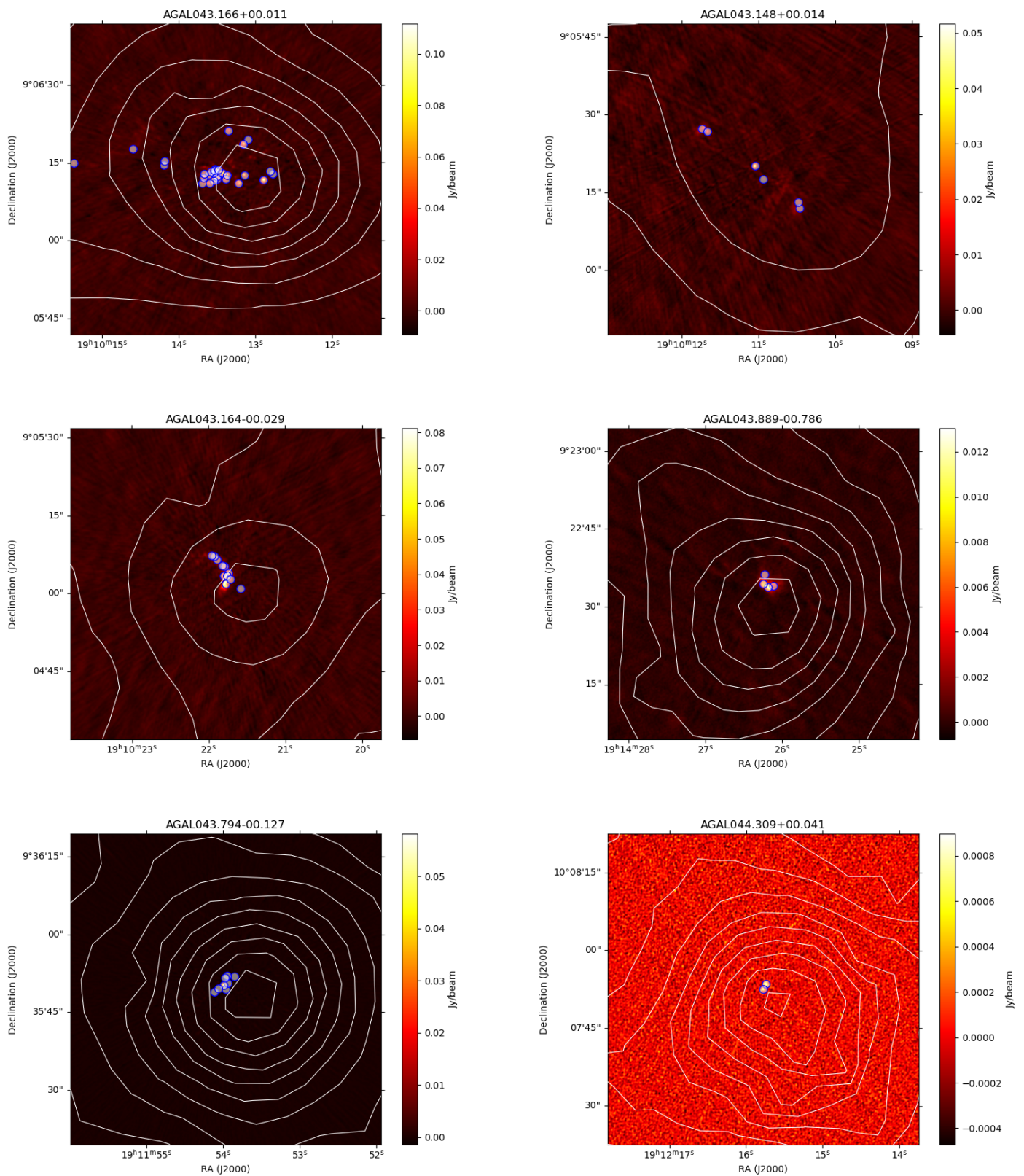
FIGURE 4.1: Continued.
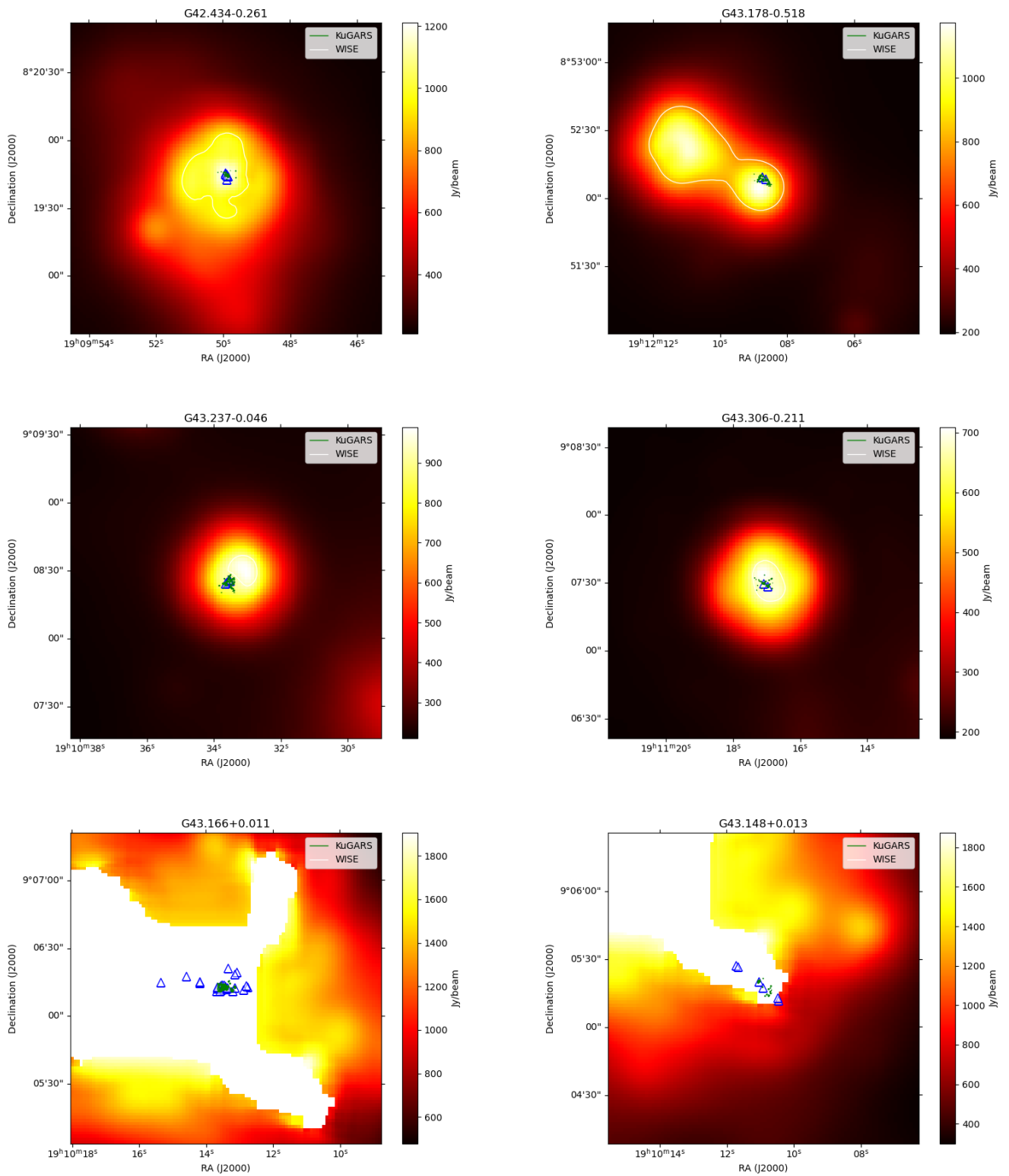
FIGURE 4.2: (a) WISE and KuGARS contours overlaid on the WISE colour-scale. KuGARS sources have been overlaid as triangle markers. Some of the sources are highly saturated at 22μm.
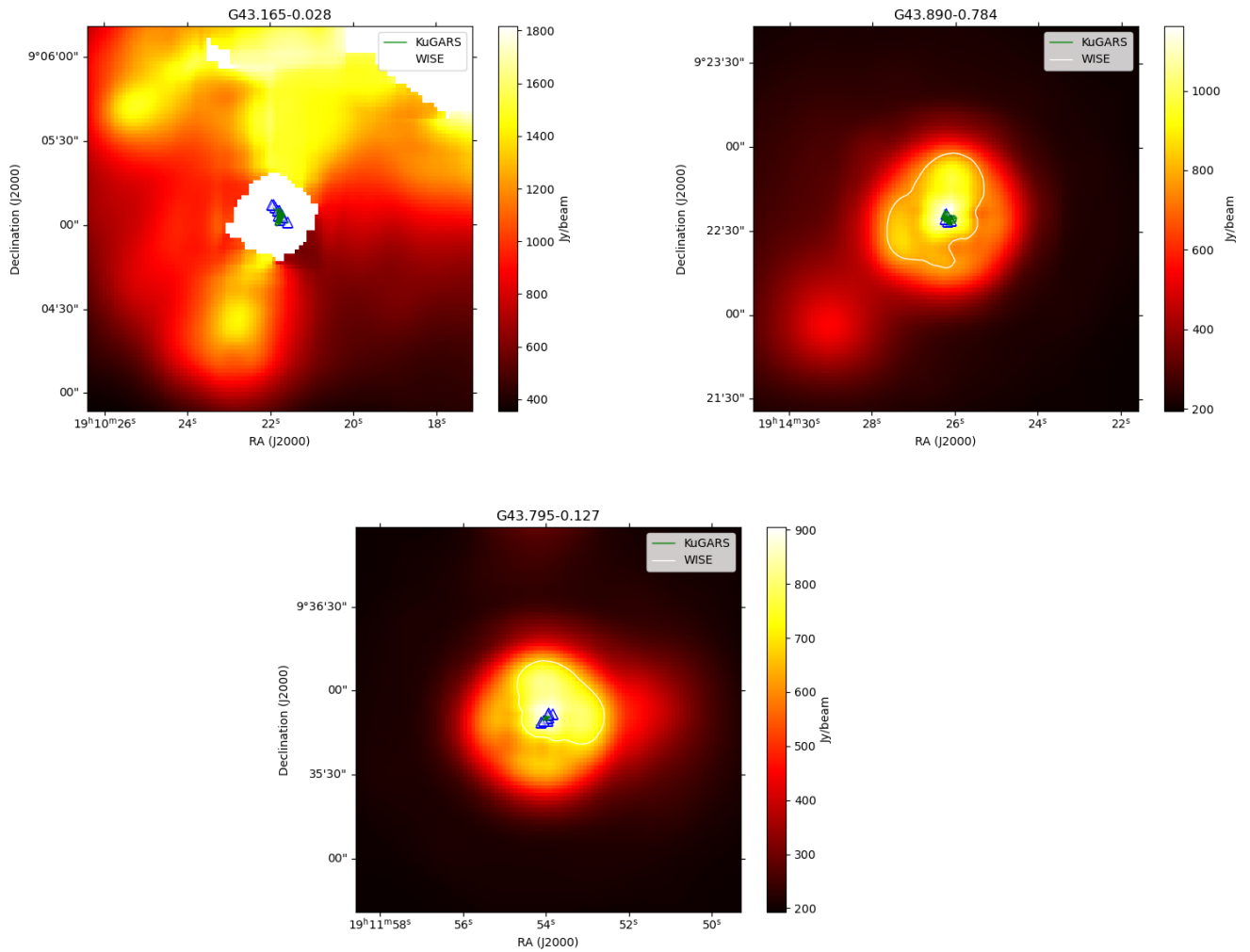
FIGURE 4.2: Continued.

4.3 Physical Properties of the Host Clumps

In this section I will describe the physical properties of the host clumps following the process outlined in Urquhart et al. (2013, 2018). The velocity information used to derive the kinematic properties of the clumps was obtained from studies in the literature. The majority of the estimations of the clump kinematic temperatures made use of studies that carried out targeted observations of the lower excitation states of the ammonia inversion transition (Urquhart et al., 2011; Dunham et al., 2011; Wienen et al., 2012), while the remnant made use of the Schlingman et al. (2011) study of HCO^+ and N_2H^+, as well as targeted observations by Bronfman et al. (1996), Blum et al. (2000), Urquhart et al.

(2009b), Anderson and Bania (2009), and Walsh et al. (2011). The physical properties of the host clumps under discussion are presented in Table 4.1.

4.3.1 Distances

Heliocentric distances are crucial to determining the physical properties of clumps as some properties (e.g. clump mass) vary with distance. The ATLASGAL clump distances were compiled using a combination of maser parallax, spectroscopic and kinematic distances drawn from the literature. In this sample the clump distances range from 4.2 to 11.7 kpc with a mean distance of 7.9 kpc.

4.3.2 Clump Sizes

The clump distances derived from the literature and the observed effective angular radii of the respective clumps were used to determine their physical sizes following the definition in Rosolowsky et al. (2010). They define a catalogue object as being *defined by the assignment algorithm established above which yields a set of pixels with known Galactic coordinates (l_i,b_j) and associated intensities I_j(Jy beam^{-1}).* The clump properties are determined by emission-weighted moments over the coordinate axes of an image and positions in the mask with negative intensity are not included in the calculation. Take, for example, the centroid Galactic longitude and latitude of an object are given as

$$l_{cen} = \frac{\Sigma_j l_j I_j}{\Sigma_j I_j}, \ b_{cen} = \frac{\Sigma_j b_j I_j}{\Sigma_j I_j} \qquad (4.1)$$

Then, the sizes of the objects are determined from the second moments of the emission along the coordinate axes:

$$\sigma_l^2 = \frac{\Sigma_j (l_j - l_{cen})^2 I_j}{\Sigma_j I_j} \qquad (4.2)$$

$$\sigma_b^2 = \frac{\Sigma_j (b_j - b_{cen})^2 I_j}{\Sigma_j I_j} \qquad (4.3)$$

$$\sigma_{lb} = \frac{\Sigma_j (l_j - l_{cen})(b_j - b_{cen}) I_j}{\Sigma_j I_j} \tag{4.4}$$

The principle axes of the flux density distribution are determined by diagonalising the tensor

$$I = \begin{bmatrix} \sigma_l^2 & \sigma_{lb} \\ \sigma_{lb} & \sigma_b^2 \end{bmatrix}. \tag{4.5}$$

This yields the major (σ_{maj}) and minor (σ_{min}) axis dispersions as well as the position angle of the source. However, because the moments are calculated for an emission mask that has been clipped at a positive significance level, the source size estimates will be slightly underestimated consequently, this could result in size estimates that are smaller than the beam size. If we take σ_{bm} to be the rms size of the beam ($\theta_{FWHM}/\sqrt{8ln2}$), and η a factor that relates the rms size of the emission distribution to the angular radius of the object determined, then by projecting the angular radius onto the principal axes of the intensity distribution, it can be calculated as the geometric mean of the deconvolved major and minor axes:

$$\theta_R = \eta \left[(\sigma_{maj}^2 - \sigma_{bm}^2)(\sigma_{min}^2 - \sigma_{bm}^2) \right]^{1/4}. \tag{4.6}$$

The value used for η is chosen based on the true emission of the object and its size relative to the beam.

The calculated clump sizes peak at $\sim$1 pc, but range from 0.1 to 5.8 parsecs with a mean size of 0.72$\pm$0.01 pc. The clumps associated with KuGARS HII region candidates have effective radii ranging from 15 to 79 pc, with a mean value of 39.25 pc, and physical sizes between 0.18 and 1.28 pc, with a mean value of 0.48 pc.

4.3.3   Dust Temperature and Bolometric Luminosity

Urquhart et al. (2013) derived the dust temperatures of the clumps using a greybody fit to the submillimetre dust emission. The fit gave temperatures between 10 and 40 K

with a peak at ∼16 K. The temperatures in the KuGARS associated sample of clumps lie in the range 22.46 to 34.90 K.

TABLE 4.1: Derived parameters of the ATLASGAL host clumps.

Name ATLASGAL	RA (°) J2000	Dec (°) J2000	Major arcsecs	Minor arcsecs	Peak flux Jy beam^{-1}	Int flux Jy	Temp. K	Log(N_{H_2}) cm^{-2}	R_{eff} pc	D kpc	Radius pc	Log($\Sigma(R)$) M$_\odot$	Log(M$_{clump}$) M$_\odot$	Log(L_{bol}) L$_\odot$
AGAL041.741+00.097	286.815	7.878	10	10	1.12	3.25	29.57	22.21	15	11.7	0.57	2.07	3.15	4.62
AGAL043.889-00.786	288.611	9.375	31	20	3.73	26.45	22.46	22.9	55	4.4	0.3	2.68	3.38	4.4
AGAL043.179-00.519	288.038	8.87	27	18	4.15	21.36	23.32	22.92	49	8.5	0.5	2.66	3.83	4.97
AGAL042.108-00.447	287.473	7.953	16	14	1.16	6.0	25.96	22.3	29	3.4	0.3	2.19	2.42	3.69
AGAL042.434-00.261	287.458	8.328	14	10	1.55	8.97	30.05	22.34	20	4.4	0.2	2.45	2.74	4.0
AGAL043.306-00.212	287.822	9.124	13	11	3.57	7.95	26.55	22.78	22	4.2	0.18	2.51	2.71	4.08
AGAL043.794-00.127	287.974	9.596	13	12	6.36	13.83	34.9	22.88	22	6.0	0.24	2.62	3.12	5.08
AGAL043.166+00.011	287.556	9.103	39	29	62.19	319.98	33.29	23.89	79	11.1	0.54	3.62	5.04	6.91
AGAL043.164-00.029	287.591	9.083	30	22	13.51	86.15	31.17	23.27	58	11.1	0.48	3.07	4.5	6.21
AGAL043.236-00.047	287.641	9.138	21	17	4.46	18.83	25.3	22.9	41	11.1	0.63	2.65	3.96	5.14
AGAL043.148+00.014	287.545	9.089	21	18	5.76	48.87	31.19	22.89	43	11.1	1.27	2.87	4.26	5.93
AGAL044.309+00.041	288.065	10.13	21	15	2.51	12.23	23.51	22.7	38	8.1	0.53	2.5	3.54	4.52

4.4 Physical Properties of the Embedded Radio Sources

There are 82 sources in the KuGARS catalogue embedded in an ATLASGAL molecular clump. Without an unresolved, low frequency counterpart corresponding only to one KuGARS source, I am unable to fit an SED to all but 4 of the 82 radio sources. However, if I assume the radio continuum emission detected has been emitted by homogeneous optically thin HII regions, I can calculate their physical parameters. For this, I have used the methods outlined in Mezger and Henderson (1967), Rubin (1968), and Sánchez-Monge et al. (2013). The physical parameters calculated through these formalisms are presented in Table 4.2 and Appendix A.

4.4.1 Angular Size

The angular size is calculated from the deconvolved major and minor axes:

$$angular\_size = \sqrt{\theta_a \times \theta_b} \qquad (4.7)$$

Where, θ_a is the semi major axis and θ_b is the semi minor axis.

4.4.2 Emission Measure

The emission measure (EM) calculation makes use of integrated flux density and the angular diameter:

$$EM\left[\frac{pc}{cm^6}\right] = 1.7 \times 10^7 \left(S_\nu \nu^{0.1} T_e^{0.35} \theta_s^{-2}\right) \tag{4.8}$$

Where,

S_ν (in *Jy*) is the radio continuum integrated flux density

ν (in *GHz*) is the observing frequency

T_e is the electron temperature assumed to be $10^4 K$

θ_s (in *arcsecs*) is the angular diameter of the source

4.4.3 Electron Density

The electron density calculation also makes use of the integrated flux density and angular diameter, but also relies on the heliocentric distance, and is presented as follows:

$$n_e[cm^{-3}] = 2.3 \times 10^6 \left(\frac{S_\nu^{0.5} \nu^{0.05} T_e^{0.175}}{d^{0.5} \theta_s^{1.5}}\right) \tag{4.9}$$

Where,

S_ν, ν, T_e, θ_s are as defined above and,

d (pc) is the kinematic distance

4.4.4 Ionised Mass

The mass of ionized gas is calculated assuming a spherical homogeneous distribution as follows:

$$M_i[M_\odot] = 3.5 \times 10^{-12} \left(S_\nu^{0.5} \nu^{0.05} T_e^{0.175} d^{2.5} \theta_s^{1.5}\right) \tag{4.10}$$

Where,

$M_\odot$ is the mass of the sun and S_ν, ν, T_e, θ_s, d are as defined above.

4.4.5 Lyman Continuum Flux

The calculation of the Lyman continuum Flux (in *photons s^{-1}*) was dependent on the integrated flux density and the kinematic distance, the equation is presented as follows:

$$N_{Ly}[s^{-1}] = 8.9 \times 10^{40} \left(S_\nu \nu^{0.1} T_e^{-0.45} d^2 \right) \qquad (4.11)$$

Where,

S_ν, ν, T_e, d are as defined above.

4.4.6 In-band Spectral Indices

The in-band spectral indices ($\alpha; S_\nu \propto \nu^\alpha$) were determined using 4 sub-band data points. The 32 continuum spectral windows were sub-divided into 4 groups of 8 spectral windows centred on the following frequencies: band1 at 14.44 GHz; band2 at 15.46 GHz; band3 at 16.44 GHz; band4 at 17.46 GHz. A goal of KuGARS was to measure the SEDs, however, in practice this proved to be more difficult than first thought. I attempted to measure SEDs using the 4 KuGARS subbands and CORNISH at 5 GHz, but the analysis was too difficult to implement because of the difference in angular resolution between CORNISH and KuGARS. Very few sources had the same number of counterparts, and there was very little intermediate frequency data between CORNISH and KuGARS making it difficult to properly constrain the SEDs. I discuss this in further detail in § 4.5, but base my statistical lifetime analysis on emission measure.

TABLE 4.2: Excerpt of the derived parameters of the KuGARS sources embedded in molecular clumps. The parameters are derived using 4 sub-band data points, each containing 8 continuum spectral windows centred at 14.44, 15.46, 16.44, and 17.46 GHz. The first column is the source identifier giving the Galactic source name in the full KuGARS compact source catalogue. The next four columns give the observed flux densities and their respective errors. Columns 6 and 7 are the spectral index and its error. In column 8, the electron density is given in units of $10^4 cm^{-3}$ and in column 9 the emission measure in units of $10^6 cm^{-6}$. Columns 10 and 11 are the turnover frequency in GHz and the physical diameter in parsecs. The ionised mass in units of $10^{-3} M_\odot$ is given in column 12, the Lyman alpha flux in units of photons s^{-1} is given in column 13, and the angular size in arcseconds is given in the final column. A complete table of the candidate HII regions is given in Appendix A

Source Galactic name	Peak Flux (mJy beam^{-1})	error	Integrated Flux (mJy)	error	α	α_{err}	n_e ($10^4 cm^{-3}$)	EM ($10^6 pc\,cm^{-6}$)	$\nu_{turnover}$ (GHz)	Diameter (pc)	M_{HII} ($10^{-3} M_\odot$)	N_{Ly} (photons s^{-1})	Angular size (arcsec)
G041.7417+00.0974	2.0	0.15	19.65	1.44	-1.71	0.6	1.14	6.4	1.73	0.075	44.7	3.18e+47	1.32
G041.7420+00.0974	1.45	0.15	6.36	0.64	-5.3	0.81	1.18	4.6	1.48	0.05	13.7	1.01e+47	0.88
G041.7419+00.0972	0.82	0.15	14.02	2.52	-2.5	0.72	0.63	2.6	1.12	0.099	56.8	2.23e+47	1.74
G041.7419+00.0971	0.77	0.15	3.43	0.65	-1.45	1.21	0.91	2.8	1.16	0.05	10.8	6.17e+46	0.88
G041.7419+00.0970	1.18	0.15	11.1	1.38	-3.98	0.97	0.88	3.7	1.33	0.073	32.2	1.77e+47	1.29
G041.7412+00.0974	1.1	0.15	15.41	2.05	-1.9	0.7	0.78	3.6	1.32	0.089	52.0	2.54e+47	1.57
G042.1093-00.4470	0.78	0.13	0.92	0.15	-2.23	0.25	2.22	2.5	1.1	0.008	0.1	1.24e+45	0.46
G042.1091-00.4468	1.33	0.13	5.95	0.57	-2.62	0.61	2.08	4.2	1.41	0.015	0.6	7.99e+45	0.89
G042.4341-00.2607	0.63	0.16	0.63	0.16	3.06	0.37	2.47	3.6	1.32	0.009	0.2	2.62e+45	0.42
G042.4349-00.2605	0.6	0.15	1.06	0.26	2.14	2.86	1.76	2.4	1.09	0.012	0.3	3.06e+45	0.56
G042.4348-00.2604	0.63	0.15	0.97	0.22	-0.49	1.58	1.78	2.3	1.07	0.011	0.2	2.53e+45	0.52
G042.4348-00.2606	0.86	0.15	4.38	0.75	-2.49	0.57	1.42	2.7	1.15	0.02	1.1	9.85e+45	0.95
G042.4344-00.2604	1.72	0.15	5.59	0.48	-1.8	0.8	2.25	5.4	1.6	0.016	0.9	1.26e+46	0.76
G042.4346-00.2605	1.6	0.15	4.64	0.42	-2.45	0.35	2.23	5.1	1.54	0.015	0.7	1.04e+46	0.72
G043.1781-00.5180	0.94	0.14	0.95	0.14	-0.9	0.65	1.6	3.0	1.2	0.017	0.8	7.94e+45	0.42
G043.1777-00.5178	0.88	0.14	0.89	0.14	-1.64	1.02	1.6	3.0	1.19	0.017	0.8	7.91e+45	0.42
G043.1683+00.0085	4.56	1.12	13.5	3.33	-0.34	3.96	2.36	14.4	2.54	0.039	13.1	1.93e+47	0.72
G043.1657-00.0281	11.19	1.74	329.02	51.01	-1.95	0.78	2.09	35.4	3.9	0.123	361.2	4.71e+48	2.28
G043.1662-00.0283	10.68	1.74	77.76	12.63	-4.06	2.77	2.89	33.8	3.81	0.061	61.7	1.11e+48	1.13
G043.1663+00.0107	44.51	2.16	97.05	4.71	-1.4	1.04	8.6	163.7	8.08	0.033	30.1	1.62e+48	0.62
G043.1458+00.0141	6.14	0.55	64.76	5.79	-5.68	1.16	2.0	19.4	2.93	0.073	74.3	9.27e+47	1.36
G043.1665+00.0108	34.16	2.16	159.78	10.1	-2.23	0.37	5.77	108.0	6.63	0.049	63.4	2.29e+48	0.91
G043.1664+00.0105	52.69	2.16	223.68	9.17	-1.78	0.99	7.35	166.6	8.15	0.047	69.8	3.2e+48	0.87
G043.1489+00.0130	49.08	0.82	84.44	1.42	-1.11	0.47	9.09	162.3	8.05	0.03	22.3	1.26e+48	0.55
G043.1684+00.0125	33.73	0.96	122.19	3.49	-1.47	1.23	5.31	119.0	5.71	0.042	52.7	1.75e+48	0.8
G043.1664-00.0283	8.0	1.74	24.2	5.25	-2.06	1.14	3.28	28.0	3.49	0.039	18.7	3.84e+47	0.73
G043.1520+00.0114	12.74	0.36	144.57	4.05	-2.68	2.77	3.0	45.4	4.39	0.076	124.5	2.33e+48	1.41
G043.1685+00.0086	11.3	1.12	29.72	2.96	-5.08	0.28	3.83	35.7	3.92	0.037	17.8	4.26e+47	0.68
G043.1667+00.0104	15.46	2.16	105.0	14.67	-3.63	2.45	3.54	48.9	4.55	0.059	68.0	1.5e+48	1.09
G043.1669+00.0108	26.97	2.16	164.31	13.16	-4.19	1.14	4.8	85.3	5.92	0.056	78.4	2.35e+48	1.04

4.5 SEDs of a Subsample

At 14 GHz, KuGARS has an imaging resolution of 0″.42 while at 5 GHz, CORNISH has an imaging resolution of 1″.5. This means CORNISH sources may be resolved into multiple components in KuGARS, making the derivation of their SEDs a complex task. I

have, therefore, isolated the CORNISH sources that break into more than one KuGARS source and kept only those with a single 14 GHz counterpart.

Sources and contours from both surveys were overlaid on maps of the KuGARS colourscale (Fig. 4.3) to determine, by visual inspection, which CORNISH sources are broken up in KuGARS. I eliminated nearly all the CORNISH sources because they were resolved into multiple components in KuGARS. I applied a further filter to the remaining COR-NISH sources that took into account the difference in flux densities of the corresponding sources - CORNISH sources that were much bigger than their KuGARS counterpart had excess emission due to the difference in uv-coverage between CORNISH and KuGARS. The disparity in flux densities meant they could not be used. This left four sources that I was able to use in the SED fitting.

In the SED fits shown in Fig. 4.4, the 5 GHz points all lie below the turnover frequency, i.e., they are in the optically thick regime. Conversely, the KuGARS points are all located in the optically thin regime. Clearly, these HII regions are optically thick at 5 GHz and optically thin at 14 GHz. Thus, it is likely that the optically thin approximation used in the calculations of the physical parameters of the KuGARS sources in § 4.4 works, from this subsample of 4. In their physical properties, this subsample of 4 appear to be HII regions in transition between HC and UC HII regions. They have diameters greater than 0.03 pc and less than 0.1 pc, the typical sizes of HC and UC HII regions, respectively. Thus they must be between the UC and HC stages in their evolution as defined by Kurtz (2005a). The presence of the 5 GHz points in the optically thick regime implies that the optically thin approximations for the physical properties of UC HII regions as derived from CORNISH are not secure in all cases, particularly for these high ($> 10^8$ pc cm^{-6}) EM objects.

However, the SEDs will not be discussed further because of the fact that I can only make fits for a limited number of the sources and that the fit is constrained highly by the CORNISH point. And, I did not find any appropriate angular resolution data between CORNISH and KuGARS. Thus, the SEDs will not form part of my further analysis.
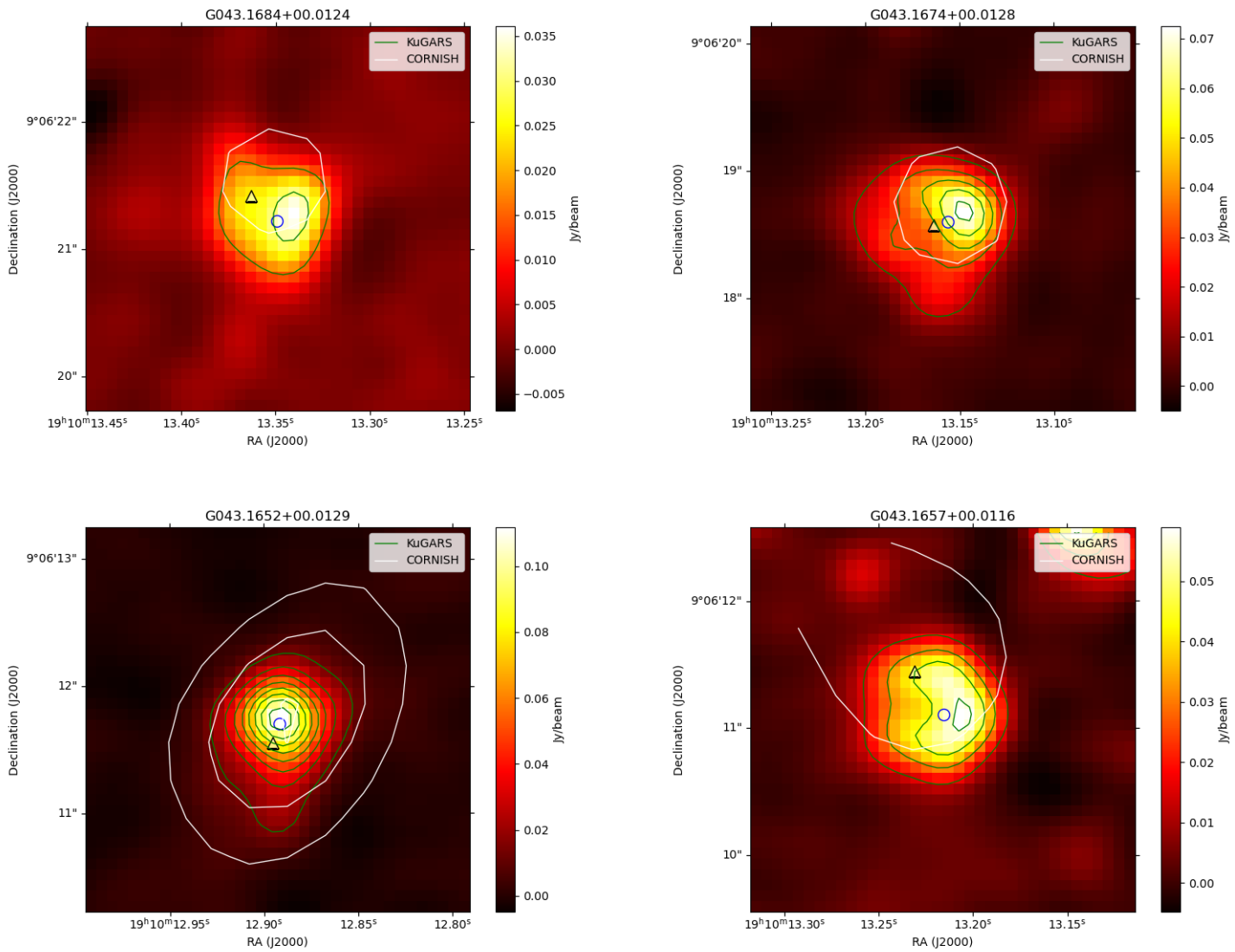
FIGURE 4.3: CORNISH and KuGARS contours overlaid on the KuGARS full-band colourscale, in white and green, respectively. The relevant CORNISH and KuGARS sources have been shown as black triangles and blue circles, respectively.
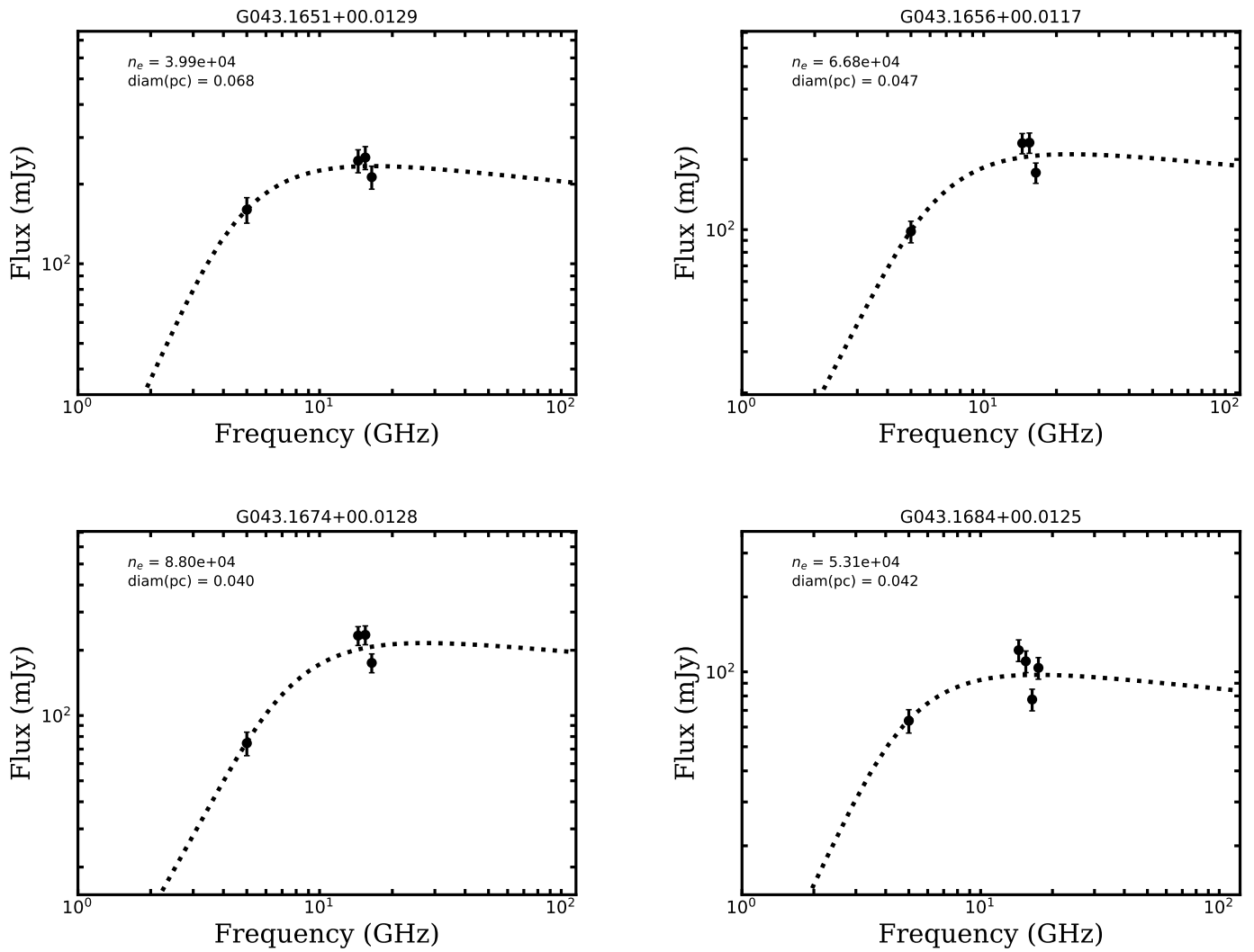
FIGURE 4.4: Candidate HII region models constructed with four KuGARS bands and one CORNISH band.

TABLE 4.3: Physical properties derived from SED fits on the radio sources.

Source name	Source index	RA (°) J2000	Dec (°) J2000	Spectral index	n_e $(10^4 cm^{-3})$	Diameter (pc)	EM $(10^6$ pc cm$^{-6})$	$u_{turnover}$ (GHz)	M_{HII} $(10^{-3}M_\odot)$	N_{Ly} (photons s^{-1})	Angular size (arcsecs)
'G043.1684+00.0125'	513430	287.556	9.106	-1.47	5.31	0.04	119.03	5.71	52.74	1.75e+48	0.8
'G043.1674+00.0128'	514391	287.555	9.105	-1.96	8.8	0.04	309.43	9.0	61.74	3.4e+48	0.84
'G043.1651+00.0129'	514470	287.554	9.103	-1.0	3.99	0.07	108.85	5.47	145.79	3.64e+48	0.64
'G043.1656+00.0117'	514480	287.555	9.103	-1.97	6.68	0.05	211.25	7.5	81.44	3.4e+48	0.84

4.6   Statistical Lifetime

The Strömgren theory is the relation between the radius of a spherical region of ionized hydrogen around an OB star, the concentration of gas in the region, and the spectral class of the OB star (Gershberg and Pronik, 1959). This relation takes the form

$$S_0 = U(S_p)n^{-2/3}, \tag{4.12}$$

where S_0 and n are the radius and density of the region, respectively, and S_p is the spectral class of the exciting star. The region of ionized hydrogen around the star, known as a strömgren sphere, possesses the conditions to host an HII region and its radius, known as the Strömgren radius, is the distance within which the OB star's ultraviolet radiation can keep hydrogen ionised. HII regions have widely been assumed to follow the Strömgren theory, wherein the star ionises the gas around it and the rapid and extreme increase in temperature makes the ionised gas over pressured with respect to its surroundings, thus it expands with time. In this assumption the expanding UC HII regions are pictured as roughly spherically symmetric and given that they expand with time, being very small means they are also young. However, Wood and Churchwell (1989b) show that at high angular resolution ($< 1''$), the morphology of HII regions is more dynamic than implied by only the Strömgren theory. They present five HII region morphologies that differ significantly from the Strömgren sphere model. Because of the sample size (75) of their identified UC HII regions, and the small size of the region of the Galactic Plane over which it was observed, Wood and Churchwell (1989b) find it likely that the lifetime of UC HII regions is longer than previously thought. They predict that UC HII regions must survive longer than their sound crossing times. To estimate the average lifetime of an UC HII region produced by an OB star embedded in a molecular core, they assume a typical UC HII region for simplicity. Here, a typical UC HII region is defined as having an n_e of $\sim 5 \times 10^4$ cm^{-3}, a radius of ~ 0.05 pc, and is ionised by a ZAMS O6 star with a N_{Ly} of 1.2×10^{49} *photons* s^{-1} (Panagia, 1973). They find that the dust within the HII absorbs between 50 and 90%, of the UV photons interacting with the gas. They assume 10^5 cm^{-3} and 25 K for the density and temperature of the ambient gas (Wood et al., 1987; Henkel et al., 1987).

An O star that turns on its UV illumination while still embedded in a molecular cloud forms an ionisation front which expands rapidly to fill an initial Strömgren sphere (Wood and Churchwell, 1989b). This expansion begins with a high velocity that is only sustained during the initial expansion, and will decrease to less than the sound speed as the volume of the sphere and therefore gas that must be kept ionised increases. This will happen in a time

$$t = \sim 4(n_0 \beta)^{-1}, \tag{4.13}$$

where n_0 and β are the density of the ambient medium and recombination coefficient ($\sim 3 \times 10^{-13}$ cm^3 s^{-1}), respectively (Dyson and Williams, 1980). Wood and Churchwell (1989b) give the radius, r_i, of the initial Strömgren sphere as

$$r_i = \left(\frac{3N_c^*}{4\pi n_e n_H \beta} \right)^{1/3} \tag{4.14}$$

which is ~ 0.051 pc for a typical UC HII region without dust. Using the aforementioned assumptions, they show that the relation between the initial and final Strömgren spheres is related by

$$r_f = \left(\frac{2T_e}{T_0} \right)^{2/3} r_i, \tag{4.15}$$

which, assuming typical values of $T_e = 10^4$ K and $T_0 = 25$ K, gives $r_f = 86r_i$. And the radius of the HII region as a function of time, assuming a strong shock approximation is given by

$$r(t) = ri \left(1 + \frac{7c_i t}{4r_i} \right)^{4/7}, \tag{4.16}$$

where c_i is the sound speed in the ionized gas (~ 10 km s^{-1}). With this, they predict that it takes $\sim 3 \times 10^6$ yr for an HII region to reach pressure equilibrium, which is roughly the main-sequence liftime of an O6 star with mass loss (2.4×10^6 yr: Maeder and Meynet 1987). When it achieves equilibrium, the HII region will have a physical diameter of $\sim$ 2 pc, and an angular diameter of ~ 1 pc, at a heliocentric distance of 7 kpc. Therefore,

it will no longer be classified as ultracompact and having a diameter greater than $10''$ means it would be undetectable in their survey. Wood and Churchwell (1989b) estimate the time required to fill a sphere $10''$ in diameter at a distance of 7 kpc as $\sim 4 \times 10^4$ yr which corresponds to $\sim 1.7\%$ of an O6 star's main-sequence lifetime. However, this contradicts the logical length of time within which an UC HII region is detectable in their survey as it limits the detectable UC HII regions in the entire Galaxy to 290, while this survey detects 75 over a very small portion of the Galactic Plane. They suggest that the time it takes an HII region's diameter to expand beyond $10''$ must be longer than the time required for it to expand against the density of the ambient medium, therefore, there must exist mechanisms that inhibit their expansion (c.f. Wood and Churchwell 1989b). Ultimately, finding a larger number of UC HII regions than expected in an incomplete sample of a small portion of the Galactic Plane means the lifetime UC HII regions coincides with a significant fraction of the main-sequence lifetime of the ionising stars.

Hypercompact (HC) HII regions are presumably the object class the immediately precedes the ultracompact stage of HII regions. These objects are typically 10 times smaller and a 100 times denser than UC HII regions (Kurtz, 2005a). In a similar manner to the fractional lifetime of UC HII regions with respect to the main-sequence lifetime of the ionising star, I will discuss and estimate the average lifetime of HC HII regions with respect to the lifetime of UC HII regions.

4.6.1 Statistical Lifetime of HC HII regions

The lifetime of HII regions spent in the HC stage can be determined by comparing them to the number of UC HII regions present at the same time. This comparison is based on the assumption that UC and HC HII regions are the same object at different stages in time. Since the evolution proceeds from the HC to the UC stage, taking the ratio of the number of HII regions in the HC stage to the those in the UC stage will give the fraction of the UC HII lifetime that is spent in the HC stage. Therefore, the statistical lifetime of a HC HII region is given by

$$lifetime_{HC\ HIIs} = \frac{Number\ of\ HC\ HIIs}{Number\ of\ UC\ HIIs}. \tag{4.17}$$

The key thing here, is determining the number of HC HII regions against the number of UC HII regions. Because the physical properties of an HII region change as it evolves, they can be used to determine where it is in its evolution. The most ideal parameter for this is the spectral index. Kurtz (2005a) shows a distinction between the SEDs of HC and UC HII regions, with HC HII regions having a steep positive spectrum (ν^2) and UC HII regions portraying a near flat spectrum ($\nu^{-0.1}$). I have derived spectral indices for the 82 KuGARS sources embedded in a molecular clump (see Table 4.2). However, by removing sources with a large error in spectral index ($> \pm 1$), the number of sources in the sample was reduced to 45. Furthermore, large source sizes (> 2 beams) result in unreliable spectral indices. Applying this constraint to the sample leaves very few eligible sources. Removing sources with sizes > 2 beams (0.84 arcesecs) leaves only 16 sources and placing a tighter constraint of limiting source sizes to < 1.2 beams (0.5 arcsecs) leaves only 5 sources in the sample. Obviously, applying these constraints and reducing the sample size makes using in-band spectral indices for the statistical lifetime calculation unreliable. The emission measure, which does not depend on the sources being unresolved, is the other defining quality of a HC HII region compared to an UC HII region. This is a measure that can be calculated for the full sample so I chose to do it this way. Yang et al. (2021) use HII regions from their own data in tandem with CORNISH UC HII regions from Kalcheva et al. (2018) to map the evolution of HII regions using their physical parameters: n_e, diameter, N_{Ly}, and EM. They show a clear evolutionary trend in n_e, diameter, and EM that agrees with the classical theoretical models presented in Mezger and Henderson (1967) and Dyson et al. (1995) that point to the expansion of an HII region over time resulting in a gradual increase in diameter while n_e and EM gradually decrease. They, however, find no distinct correlation between these evolutionary trends and N_{Ly} which they suggest is due to more luminous HII regions expanding rapidly in their earliest stages, but slowing down later and appearing more like less luminous HII regions.
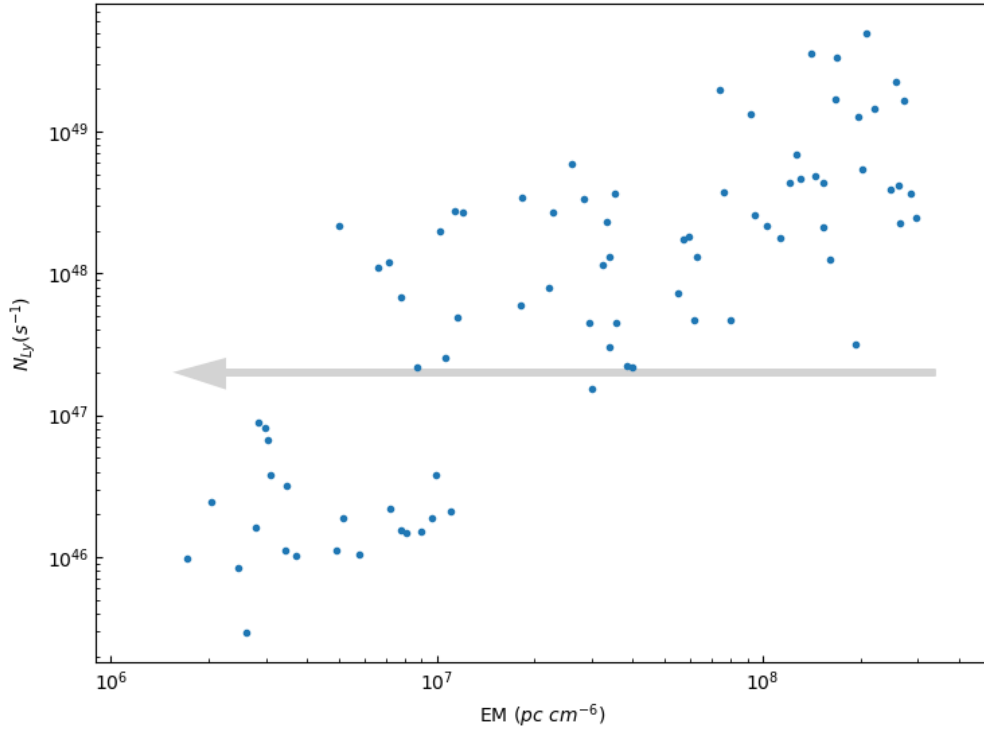
FIGURE 4.5: Evolution of an HII region perceived through emission measure and Lyman flux. The grey arrow indicates the direction of evolution with respect to emission measure.

Fig. 4.5 is a plot of N_{Ly} as a function of EM. The classical theoretical models in Mezger and Henderson (1967); Dyson et al. (1995), tell us to expect EM to decrease with evolution of an HII region. The direction of evolution in Fig. 4.5 is indicated by the grey arrow, showing the EM as reducing with time. However, there is no obvious correlation between N_{Ly} and the evolution of the HII regions, which is consistent with the results seen in Yang et al. (2021). We see some spread in the N_{Ly}, but this is expected because, even though we generally expect a similar evolutionary pattern with HII regions, the HII regions will have been formed by stars of different spectral type ($\geq$ B0.5) thus have different 'starting points' and evolutionary paths. Table 4.4 shows the stars that powered these candidate HII regions following the description in Panagia (1973). Note that the Lyman continuum photon values given in this table are average values and while there is no quantitative estimate of the expected dispersion from the average values for B-type stars, Panagia (1973) find the data indicates a similar dispersion as for O-type stars: a logarithmic dispersion of ± 0.28 from the average.

There is no visible break in the distribution shown in Fig. 4.5. It shows the HII region evolution as continuous rather than as perfectly distinguishable stages. This gives every indication that in the evolution of HII regions, the supposed boundaries are contiguous with no fixed point separating the respective evolutionary stages. The demarcation between young HII regions with high EM and more evolved HII regions with lower EM is clearly a sliding scale. Therefore, based on the radio properties derived from the SEDs of young HII regions in Yang et al. (2021), I have picked 10^8 pc cm^{-6} as an arbitrary dividing line between the stages of evolution on which to base the statistical lifetime. In this sample of KuGARS sources, there are 24 sources with EM $\geq 10^8$ pc cm^{-6}, 32 sources with $10^7 \leq$ EM$< 10^8$ pc cm^{-6}, and 26 sources with EM $< 10^7$. The ratio of high EM to low EM objects is 24/58, thus the time an HII region spends in high EM is $\sim$41% of its lifetime in the UC phase. It is important to note, however, that because this is a continuous spectrum with no sharp transition, estimated lifetime can vary based on the choice of boundary between stages of evolution. Clearly, this analysis puts into question the need for multiple classifications and implies that these are in fact, the same object.

TABLE 4.4: Distribution of spectral classification of KuGARS candidate HII regions, following fluxes of Lyman continuum photons assigned to each spectral type in Panagia (1973)

Spectral type	$log(N_{Ly})$ ZAMS	Source count	Spectral type	$log(N_{Ly})$ ZAMS	Source count	Spectral type	$log(N_{Ly})$ ZAMS	Source count
O4	49.93	0	O7	48.62	6	O9.5	47.84	5
O5	49.62	1	O7.5	48.51	7	B0	47.36	10
O5.5	49.63	2	O8	48.35	7	B0.5	46.23	15
O6	49.08	7	O8.5	48.21	7	B1	45.29	11
O6.5	48.82	1	O9	48.08	3	B2	44.65	0

4.7 Summary

i). Reliably identifying young HII regions requires aligning emission in the radio, IR, and sub-mm regimes. By applying this technique to the sources in the KuGARS catalogue in tandem with ATLASGAL 850 μm and WISE 22μm data, I have identified 82 radio continuum sources as potential young HII regions. The host

clump distances range from 4.2 to 11.7 kpc with an average of 7.9 kpc. The physical properties of the HII regions were determined using the formalisms in Mezger and Henderson (1967), Rubin (1968), and Sánchez-Monge et al. (2013), with the assumption that the detected radio continuum emission was emitted by homogeneous, optically thin HII regions.

ii). The four sub-bands of the KuGARS images were used to determine in-band spectral indices. The sub-band catalogues were also used to fit SEDs by combining them with CORNISH 5 GHz data. However this was only successful for a subsample of 4 sources becasue the difference in the resolution of the surveys ($0.42''$ & $1''5$) meant the majority of CORNISH sources were resolved into 2 or more components in KuGARS.

From the SED fits, the HII regions are all optically thick at 5 GHz and optically thin at 14 GHz, thus justifying the optically thin approximation used to derive their physical parameters. The diameters of the sources in the subsample are greater than 0.03 pc and less than 0.1 pc, the typical sizes of HC and UC HII regions respectively. This means that they are in transition between the UC and HC HII region stages of their evolution.

iii). In a similar manner to the statistical lifetime estimates Wood and Churchwell (1989b) used for UC HII regions with respect to their ionising stars, I have estimated the lifetime of HC HII regions as a fraction of the lifetime an HII region spends in the UC phase. The ideal physical parameter for identifying objects in either stage of evolution, and placing a boundary between them, is spectral index. However, I was unable to use this because many of the sources are resolved and have unreliable spectral indices. Instead, I used EM which is another defining quality of a HC HII region compared to an UC HII region. The evolutionary trend perceived through EM shows no observable boundaries depicting the edges of the respective evolutionary stages. Therefore 10^8 *pc cm*$^{-6}$ was chosen as an arbitrary dividing line between the stages of evolution. This gives a high to low emission measure ratio of 24/58. Thus the time an HII region spends in high EM is $\sim$41% of its lifetime in the UC phase.

iv). Evidently, both spectral index and EM trends put into question the need for multiple classifications in the evolution of an HII region. The evolutionary trend

is gradual and continuous with no sharp transition, making it impossible to define a fixed boundary. With no clear dividing line in any of the physical parameters, the evolutionary trends between HC and UC HII regions suggest that these are in fact the same object.

Chapter 5

A search for radio counterparts to possible star-forming clumps found with SASSy

The advent of the 21st Century came with a significant increase in surveys of the Galactic Plane (e.g. Drew et al. 2005; Lucas et al. 2008; Churchwell et al. 2009; Schuller et al. 2009; Molinari et al. 2010; Aguirre et al. 2011; Hoare et al. 2012; Barentsen et al. 2014; Moore et al. 2015; Medina et al. 2019; Brunthaler et al. 2021; Goedhart et al. in prep; Thompson et al. in prep) covering a range of wavelengths from the visible to the radio with angular resolutions of $\sim$1-30$''$. These multi-wavelength, multi-resolution surveys have considerably impacted our understanding of Galactic star formation. They led to the compilation of the largest sample of massive star-forming clumps yet, which includes a fraction of all embedded massive stars in the Galaxy (Urquhart et al., 2013, 2014a,c). We also see the most complete catalogue of compact and ultracompact HII regions presented in Djordjevic et al. (2019), constructed by combining data from these surveys. We cannot understand the birth of massive stars without first understanding the environments in which they are born. Unlike studies of extragalactic star formation, for which we are limited to studying global properties, in the Milky Way we are able to examine sub-processes such as feedback and the environmental dependence of star formation (Kennicutt and Evans, 2012; Urquhart et al., 2014b). Thus, on local scales we are able to probe the finer details and develop a more comprehensive understanding

of star formation. Therefore, these statistically significant samples of molecular clumps and HII regions are vital for understanding the birth of massive stars.
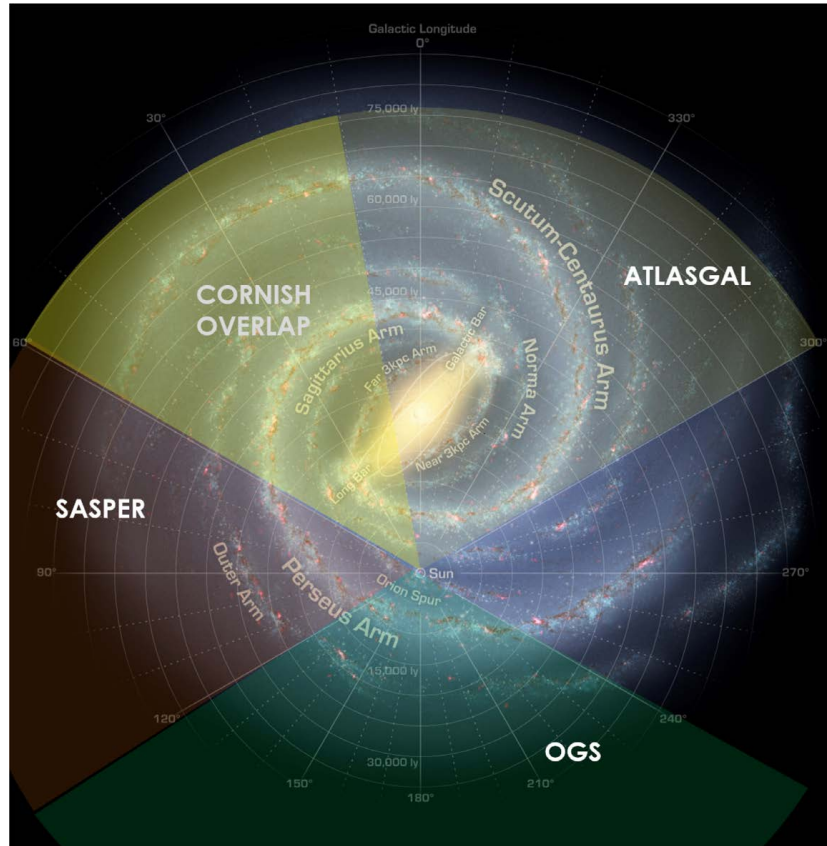
FIGURE 5.1: A schematic of the Milky Way showing the coverage of some Galactic plane surveys [courtesy of Djordjevic et al. 2019]. The gold shading indicates the ATLASGAL survey, and also shows the CORNISH region which overlaps ATLASGAL from $10° \leq l \leq 60°$. The SASSy regions, SASSy-Perseus (SASPER) and SASSy-Outer-Galaxy-Survey (OGS) are shown in red and green, respectively. The background image is an artist's impression of the Galactic plane and includes generic points of reference such as larger spiral arms and their names, location of the Sun, and the Galactic bar. To remain consistent with work by Urquhart et al. (2013, 2014c); Djordjevic et al. (2019), the value of $R_{GC} = 8.5$ kpc has been adopted for the distance of the Sun from the Galactic Centre and radius of the solar circle.

The aforementioned surveys of the Galactic Plane have largely been focused on the Inner Galaxy, with only a few in the recent past focusing on the Outer Galaxy. The Inner Galaxy (see Fig. 5.1) has higher source densities and easier detections, making it more sought after than the Outer Galaxy. Furthermore, the Outer Galaxy requires a larger latitude range because of the shape of the HI layer which is severely warped, and whose flare thickness increases with increasing distance from the Galactic centre (c.f. Wouterloot et al. (1990) and the references therein). The SCUBA-2 Ambitious Sky Survey (SASSy: Thompson et al., in prep) was the first widefield-continuum survey in the

submillimetre to thoroughly observe the Outer Galaxy. SASSy is an 850 μm continuum survey of the Outer Galaxy covering the region $120° \leq l \leq 240°$ and $|b| \leq 2.9°$. The survey was purposed towards being the Outer Galaxy complement to Inner Galaxy surveys (ATLASGAL & JPS), provide a long wavelength matched resolution counterpart to the *Herschel* Hi-GAL survey, and identify cold "starless" cores. The final, post calibration, post imaging maps have a beam FWHM of $15''.2$. A catalogue containing 1171 sources is presented in Thompson et al. (in prep).

Unlike observations of Inner Galactic clumps (Urquhart et al., 2013), the highest column density clumps in SASSy do not appear to yet show evidence of massive star formation (MSF). However, it may in fact be the case that there is star formation occurring in these regions which was missed due to a lack of complete, contiguous, uniform surveys in the Outer Galaxy. The inner Galaxy is well surveyed by studies such as ATLASGAL, CORNISH, and GLOSTAR but no such study exits for the Outer Galaxy. Finding radio continuum emission embedded in these clumps will be an indication of possible HII regions. Consequently, this has potential to improve our understanding of the rate and prevalence of MSF in the Outer Galaxy.

In § 5.1, I present the source selection process for the clumps used in this column density limited sample. The observations of the radio targets are then described in § 5.1.1. In § 5.2, I briefly present the data reduction and imaging of the radio observations. The individual steps of the cataloguing process, which comprised source detection followed by completeness and false positive rate simulations, are then outlined in § 5.3. I visually inspected 78 clumps overlaid on radio images to identify clump radio associations in § 5.4 and found a total of 28 radio sources associated with 9 clumps. Using the procedures outlined in the Appendices of Rodriguez et al. (1989) and Anglada et al. (1998), I estimated the number of expected background sources to be $\langle N \rangle \simeq 0.11$ in a single clump or $\langle N \rangle \simeq 9$ in the full sample of 78 clumps. In § 5.5 I cross-reference the clump positions with objects in the SIMBAD database to examine the nature of the clumps and possibly identify radio sources previously associated with them. § 5.6 presents the physical properties of the host clumps and § 5.7 the physical properties of the embedded radio sources. In § 5.8 I discuss the high column density clumps in the sample that have no radio associations, in § 5.9 I discuss the results, and in § 5.10 I summarise the main results and provide possible angles for future work.

5.1 Source Selection
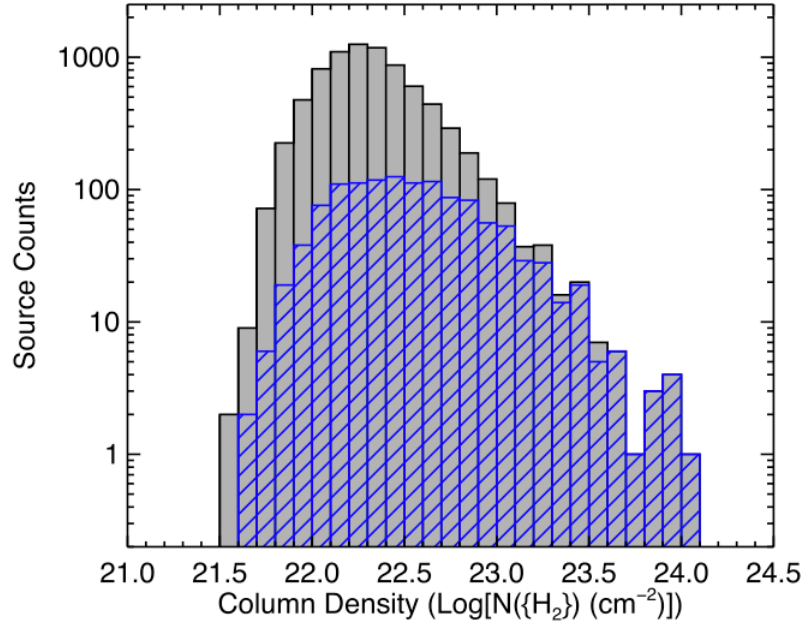
FIGURE 5.2: ATLASGAL peak column density distribution for the whole sample (grey) and the massive star formation subsample (blue). The bin size used is 0.1 dex.

Urquhart et al. (2013) and Urquhart et al. (2014c) show that clumps with high column densities ($> 10^{23} cm^{-2}$) have a near 100% likelihood of hosting massive star formation, and MSF tracers such as young HII regions. Owing to this hypothesis, Djordjevic et al. (2019) calculated the column densities of all the sources in the SASSy catalogue and crossmatched them with all known (and potential) MSF tracers in the RMS catalogue, as well as objects in the literature that fall within the SASSy region. They found a large percentage of the higher column density SASSy clumps ($> 10^{23} cm^{-2}$) without a known counterpart in the radio regime. This potentially opposes the assumption that the percentage of high column density clumps with ongoing MSF is $\sim$100%. It implies that this either is not the case or the observational record of radio counterparts, and thus MSF tracers, is incomplete. Radio observations were carried out on the Very Large Array (VLA) to address this question. The radio targets were observed in the regions of SASSy clumps that are currently not associated with a known star formation tracer with $\log N_{H_2} > 22 cm^{-2}$. The presence of radio emission, or lack thereof, will serve to answer the question on whether the percentage of high column density clumps hosting star formation is indeed at $\sim$100%.

5.1.1 Observations

These VLA observations were carried out to facilitate a study aimed at addressing the question of missing massive star formation in the Outer Galaxy - a search for radio counterparts to SASSy clumps whose properties are consistent with star-forming clumps but have not as yet been shown to have ongoing star formation. The observations were designed to target the regions of 78 SASSy sources of a column density $(\log N_{H_2} > 22 cm^{-2})$ selected sample with the aim to identify embedded MSF using the same techniques as Urquhart et al. (2013). The observations were carried out in the C configuration of the VLA, in C-band (FWHM$\sim 3{''}.5$): observing at 6 GHz allowed for the simultaneous search of 6.7 GHz methanol maser emission and free-free emission from thermal radio continuum, which is indicative of candidate HII regions. Note, however, that I have not looked at the 6.7 GHz maser data in this work, it will be reduced and analysed in future work. The target areas were split into seven four-hour scheduling blocks, each covering between 38 and 54 fields. The desired sensitivity was driven by the need to detect the 6.7 GHz maser line. This was estimated to have a typical brightness of 60 mJy per 0.1 km/s channel. This sensitivity is comparable to the 6 GHz Multibeam Maser Survey (Green et al., 2009, 2017; Breen et al., 2018). Thus, to reach the required sensitivity, an on source integration time of 5 minutes was used. Each scheduling block took $\sim$4 hours to observe.

5.2 Data Reduction and Imaging

The data were observed in 7 scheduling blocks. Each block comprised multiple fields, each one centred on pre-determined coordinates matching a SASSy clump. Each block was calibrated separately. Similarly, each field was imaged separately as their respective phase centres traced different clumps. Two sets of images were extracted: full-band images where all the spectral windows were combined into a 4 GHz bandwidth, and sub-band images, processed as subsets of the full frequency range. The data were split into 5 sub-bands each containing 6 of the 30 continuum spectral windows covering the frequency ranges: 4.0-4.6, 4.7-5.4, 5.5-6.0, 6.1-6.9, 7.0-7.6 GHz, for bands 1 to 5, respectively. The full-band images provide the highest sensitivity while the sub-band images allow in-band

spectral indices to be measured. The data reduction and imaging was carried out using the NRAO's data reduction package CASA.

5.2.1 Calibration

The data were examined, edited and flagged in CASA using the CASA tasks PLOTMS, PLOTCAL, and FLAGDATA. By inspecting the MS' visibilities to reveal variations in amplitude as a function of time and frequency, RFI was noted and flagged. A priori calibration solutions such as antenna position error corrections, gain curves, atmospheric optical depth and setting the flux density were then applied. A delay calibration solved for antenna based delays, a bandpass calibration solved for the instrumental response of the receiver, and a gain calibration derived solutions for the complex antenna gains. These were individually inspected by plotting the solution tables in the CASA task PLOTCAL. The corrected tables were then applied to the DATA column of the MS using the CASA task APPLYCAL.

5.2.2 Imaging

The images were deconvolved and imaged non-interactively using the CASA task TCLEAN. A total of 292 fields were imaged as full and subband images. However, only 78 fields have been included in this study as the full set contains fields from SASSy Perseus which will not be considered in this study. The full band images comprised all 30 continuum spectral windows across the frequency range, 4.0 to 7.6 GHz. The sub-bands comprised 5 subsets of 6 spectral windows. The clean was carried out non-interactively. First a zero iteration clean was run to produce a "dirty" image, this was then used to measure the global RMS of the image which was then used determine a stopping threshold in the full clean, this was set to 3 times the global RMS. The image size was set to 1024 square pixels, $\sim$ twice the size required to image the fields, in order to avoid aliasing. The cell size was set to $1\rlap{.}''5$, a third the value of the synthesized beam, i.e. 3 pixels per beam. The restoring beam was set to the value of the synthesized beam, $4\rlap{.}''5$ (see § 5.2.2.1). The gridder, deconvolver, and weighting parameters were set to mosaic, hogbom and briggs, respectively. A mosaic is an image of a patch of sky that is made up of more than one observed field; hogbom is a variant of the CLEAN algorithm that operates with a delta function sky model - it is most appropriate for fields of isolated point sources; and briggs

is an implementation of the flexible weighting scheme developed by Dan Briggs[1], essentially a compromise between uniform and natural weighting. The remaining parameters were left to their defaults.

5.2.2.1   Restoring beam

To improve the consistency of the measurement of in-band spectral indices, I used a uniform restoring beam (c.f. § 3.7.3) across the different sub-bands: a circular Gaussian beam. However, to ensure this does not cause any unwarranted problems (e.g. super-resolution), I have measured the beam elongation across all the fields in the observation. Fig. 5.3, shows the elongation ratio centred at ~ 1.4 with a standard deviation of 0.3. The beam elongation varies with declination, these observations having targets at different declination will vary in beam shape. With a large observing bandwidth, the beam in the lowest frequency subband will have a larger FWHM than the highest frequency subband. Therefore, the restoring beam used was the FWHM ($4\rlap{.}''5$) of the lowest frequency in the bandwidth (c.f. § 3.7.3).

---

[1]http://www.aoc.nrao.edu/dissertations/dbriggs/
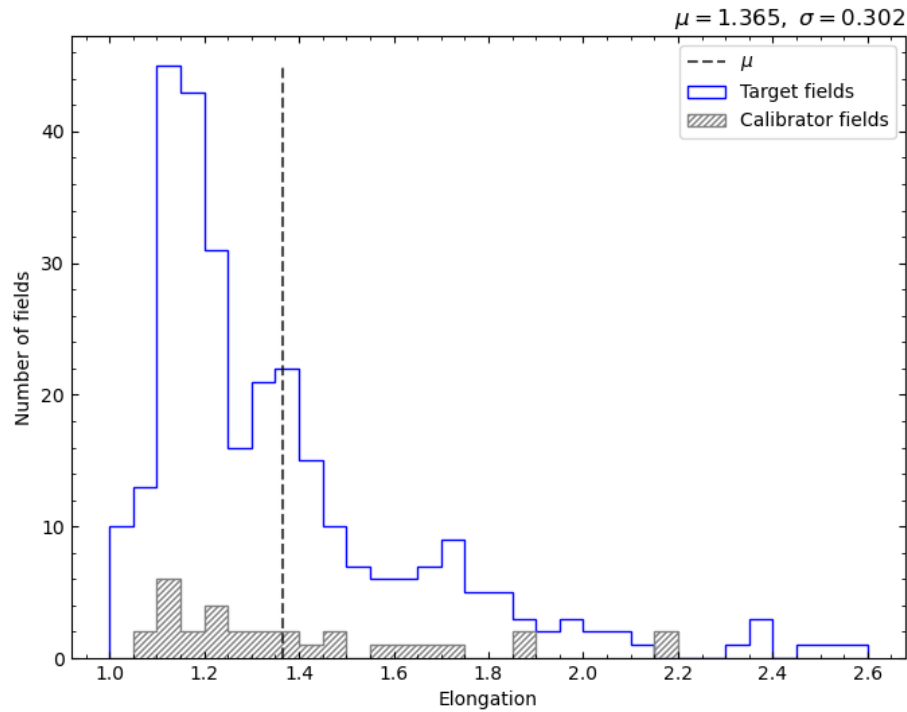
FIGURE 5.3: The beam elongation in all the fields is shown to determine the feasibility of imposing a circular Gaussian beam as the common restoring beam. The mean elongation is 1.365 with a standard deviation of 0.3.

5.3 Cataloguing

The observing strategy used was based on a selection of source positions from clumps that fit the selection criteria as described in § 5.1; thus, the fields are sparsely located and have different noise properties. The RMS values in the images range from 11.9 μJy to 44.7mJy. The majority of the fields have an even distribution of noise, with the value of the RMS being higher in the regions close to a radio source. Some fields lie near a bright radio source positioned on the edge or outside the field of view, consequently causing dominant sidelobes. Images with somewhat centrally located bright sources presumably have no sidelobe interference, while the fields with the weakest sources tend to show a grid-like artefact pattern.
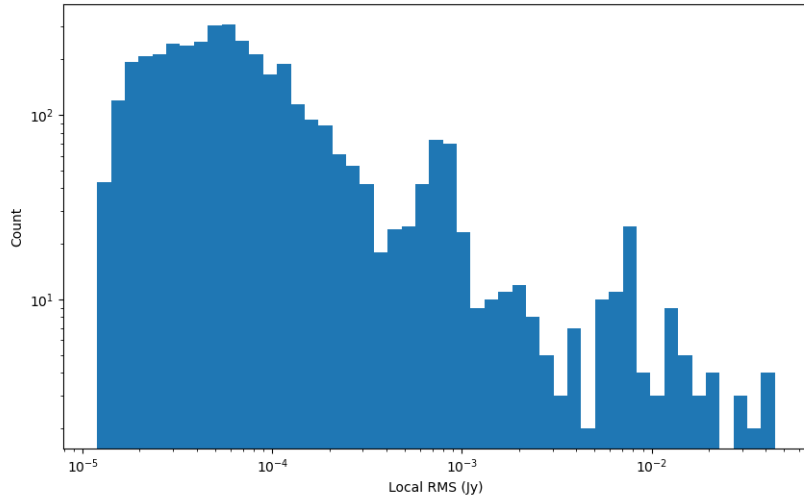
FIGURE 5.4: Distribution of the local RMS across the entire observation. The RMS values range from 11.9 μJy to 44.7mJy.

5.3.1 Source extraction

The source extraction was carried out using the AEGEAN radio source finder, (see § 3.9.1 and § 3.9.1.1). Using the default parameters ($\sigma_{seed} = 5$ and $\sigma_{flood} = 4$), I have extracted 3839 distinct components, from a total of 292 fields in the radio data. The peak flux densities of the detected radio sources range between 69μJy and 2.8Jy and the integrated flux densities between 70μJy and 7Jy. The properties, fidelity, and completeness of the sources in this catalogue are discussed in the following sub-sections.
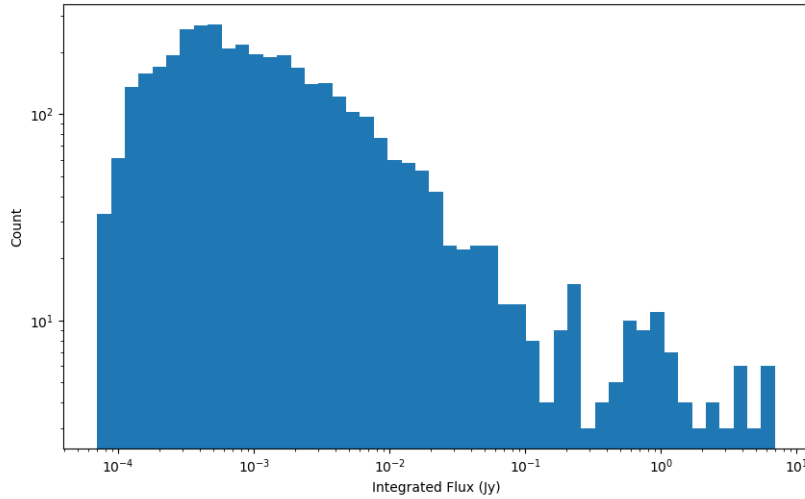
FIGURE 5.5: Distribution the of integrated flux densities of the catalogue sources. There are 3839 sources between 70μJy and 7Jy.

5.3.2 Completeness

The completeness limit shows at what flux density value the catalogue becomes reliable based on some nominal threshold (e.g. 90 or 95% complete) (c.f. § 3.10). I have carried out a completeness limit simulation using a sub-region of field 7 of scheduling block 1. The fields in this data are sparsely populated, containing an average of 13 sources per field. Therefore, source confusion is unlikely and therefore not important, thus I have chosen not to model this in my simulations for simplicity. To do this, I selected a region free of sources and background emission. I repeatedly injected 10000 randomly generated compact Gaussian sources into this region, limiting them to four in each iteration and inserting each source into a separate quadrant from the others. The sources were then extracted using AEGEAN with the same parameters used to extract the real catalogue. All the input sources were concatenated into a single catalogue and the same was done for the AEGEAN detections. The catalogues were then compared to determine the completeness as a function of signal to noise ratio (SNR), by crossmatching the input catalogue with the AEGEAN generated output catalogue and noting the number of sources recovered at the respective SNRs. The detection ratio is the fraction of sources recovered, and therefore represents the completeness of the catalogue. This result is shown in Fig. 5.6, the detection ratio reveals 90% completeness at 6σ and 95% completeness at 7σ.
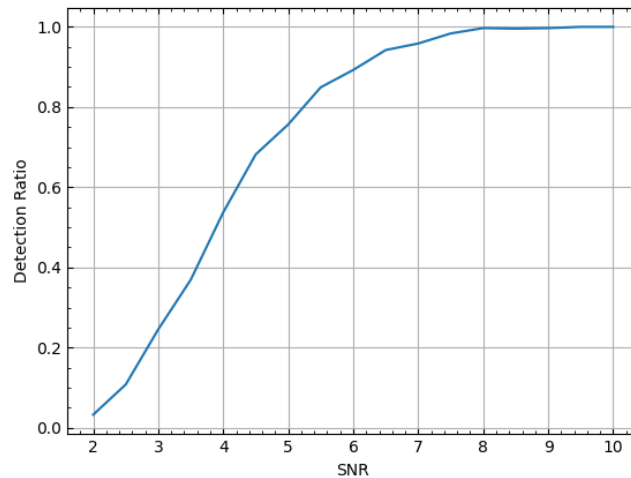
FIGURE 5.6: The completeness limit is shown by the detection ratio as a function of SNR, determined on a sub-region of a representative tile.

At low SNR, source finders have trouble distinguishing between real emission and noise. The noise in the image results in sources falling below the detection threshold and therefore not being detected by the source finder. For this reason, sources with low SNR will be largely unreliable and in many cases go undetected. The completeness limit simulation determines at what value the unreliable detections have been minimised. Fig. 5.7 shows a histogram of source injections that were not detected by the source finder, these non-detections are weighted towards low SNR. The detection ratio is low, which implies the sample has low completeness at SNR below 6σ.

The AEGEAN source finder has been shown to have low false positive and high completeness rates in Hancock et al. (2012). Fig. 5.8 shows a histogram of AEGEAN detections that were not injected into the catalogue. No more than 6 false positives have occurred at any SNR, with the majority only having 2. Figs 5.7 and 5.8 suggest that, in this data, non-detections are more likely to occur than false positives at low SNR.
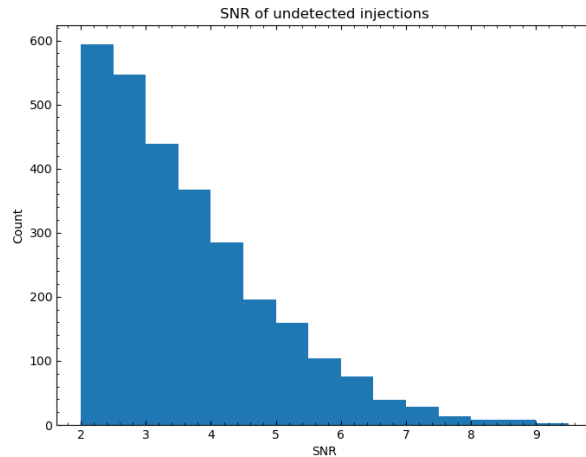
FIGURE 5.7: The distribution of undetected input sources from the completeness is illustrated in a histogram. There is strong evidence that low SNR sources are most likely to go undetected. The number of sources in the histogram monotonically increases as the SNR value tends towards zero.
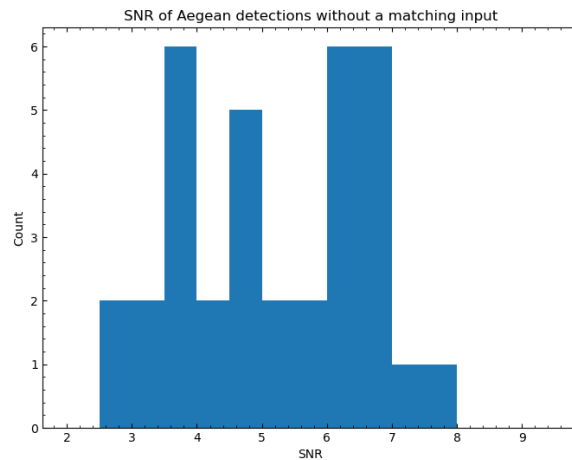
FIGURE 5.8: The distribution of sources in the AEGEAN (output) catalogue that do not have a counterpart in the input catalogue, hence are false positives.

Figs 5.9 and 5.10 illustrate the effect that background noise has on the sources. Positive noise fluctuations result in higher flux densities for low SNR sources, hence causing the so-called 'flux boosting' phenomenon (c.f. § 3.10), while negative bowls will reduce the flux density measured on sources that land on them, or completely negate them. The calculated difference in the injected and detected flux densities peaks around zero but shows some spread in both the positive and negative directions. The positive increase is due to 'flux boosting' and the negative is due to sources landing on negative bowls. Fig 5.10 shows the values generally scattered around the "y = x" line, with a few outliers.

Furthermore, the 'flux boosting' phenomenon is seen in the "y = x" and best fit lines which are positioned apart at low SNR but tend towards each other with increasing SNR.
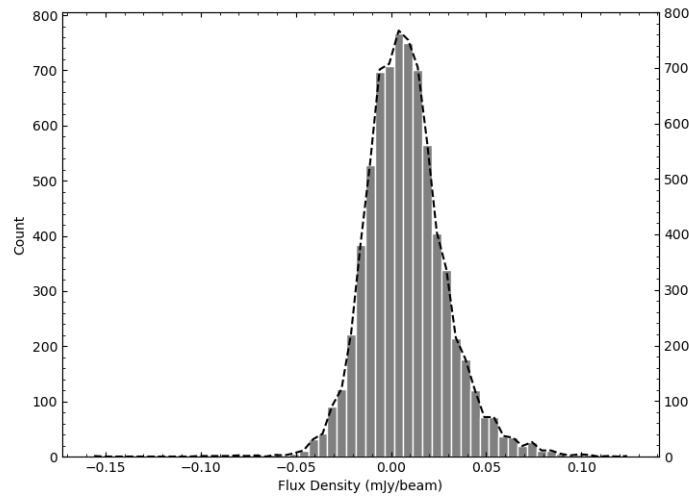
FIGURE 5.9: Difference in the peak flux density values of the detected and injected sources.
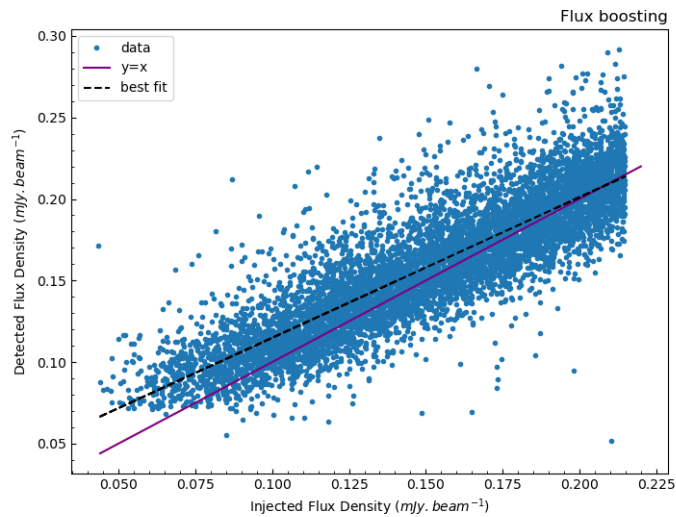
FIGURE 5.10: Illustration of the effect of flux boosting in the simulation. Detected flux density is plotted against the injected flux density. The solid purple line represents the line of equality, and the black dashed line is a best fit of the data: $y = 0.03 + 0.86x$.

5.3.3 False positives

The likely false positive rate was determined by running tests on the images for spurious detections. This was done by multiplying the images by -1 and running the AEGEAN source finder on them using the same configuration used on the standard images. None of the detections in the inverted maps will be real sources as we do not expect to find sources in absorption, thus any detections in the inverted maps will be spurious. There were no detections in 168 inverted fields, while the number of spurious sources in the remaining 124 fields varied from 1 to 51, with an average of ~6 detections in each field. This result is illustrated in Fig. 5.11 - the blue histogram illustrates the detections from the standard tiles and the red histogram illustrates detections from the the inverted tiles. Every observed field has been included in the simulation. Therefore, there are 3839 sources from the standard maps while there are 704 detections seen in the inverted maps. This gives a false positive rate of 18.4%. Of the 704 spurious sources, 538 (76.1%) are below 7σ and 694 (98.2%) are below 14σ. The high SNR spurious detections ($\geq 8\sigma$) are due to non-Gaussian noise as the images were very shallowly cleaned (c.f. § 6.1.3).
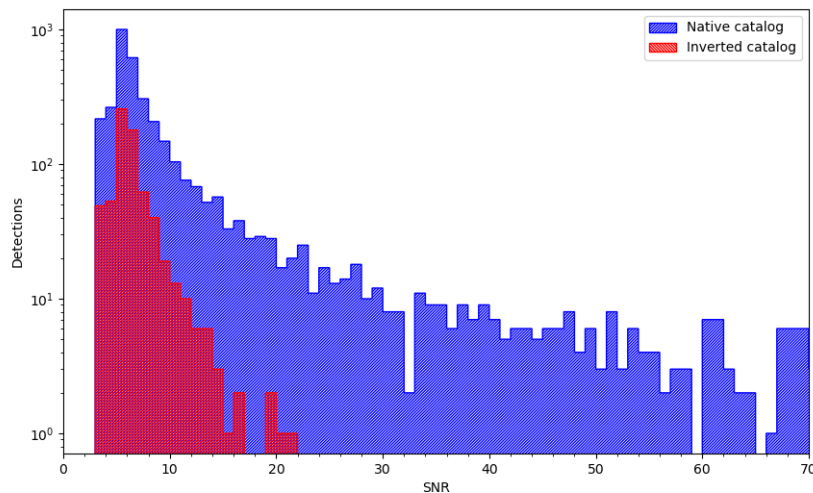
FIGURE 5.11: The likely false positive rate has been determined by running the AEGEAN source finder on 17A-130 maps in their native form (illustrated by the blue histogram) and then inverting these maps and running the source finder on them. The detections from the inverted maps (illustrated by the red histogram) represent false positives as we do not expect to detect sources in absorption. The test has been run on all the tiles. I have determined 704 spurious sources in a pool of 3839, thus giving a false positive rate of 18.4%. Of the 704 spurious sources, 538 (76.4%) are below 7σ, and 694 (98.6%) are below 14σ and 10 have an SNR $> 10\sigma$.

5.4 SASSy-Radio Counterparts

The identification of clumps containing radio emission was done by matching the clump positions against all the extracted compact sources. 78 SASSy clumps were checked against the corresponding fields from the radio observations. The matches were verified by visually inspecting the data in plots that presented the clump and radio emission overlaid on the radio maps as contours. In total, I identified 28 radio sources embedded in 9 clumps (See Tables 5.1 and 5.2).
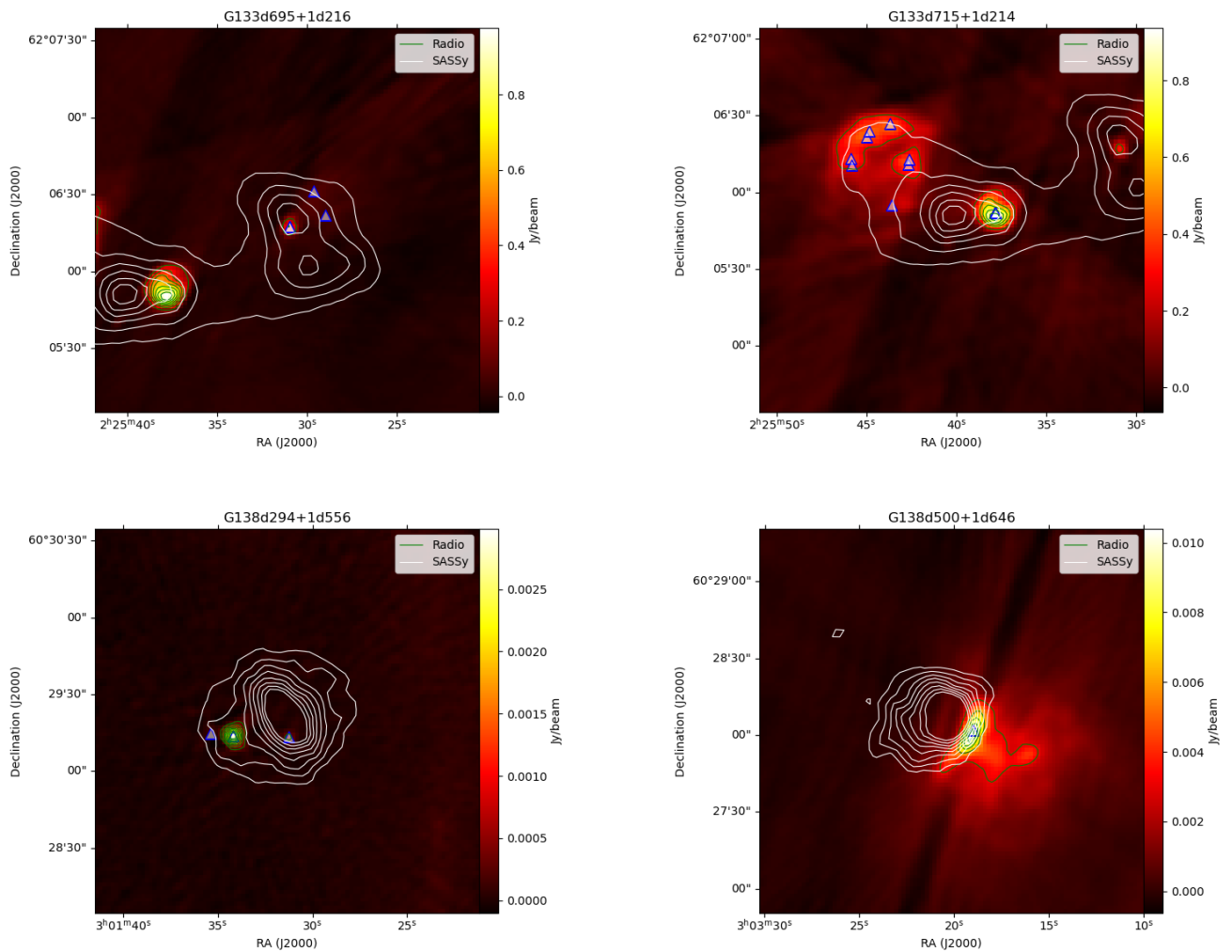
FIGURE 5.12: SASSy clump and radio emission contours overlaid on the radio colour scale. The base contours for the radio and SASSy data, are set at 3 and 2 σ, respectively. The radio contours are plotted in green, the SASSy contours in white, and the radio source markers as blue triangles.
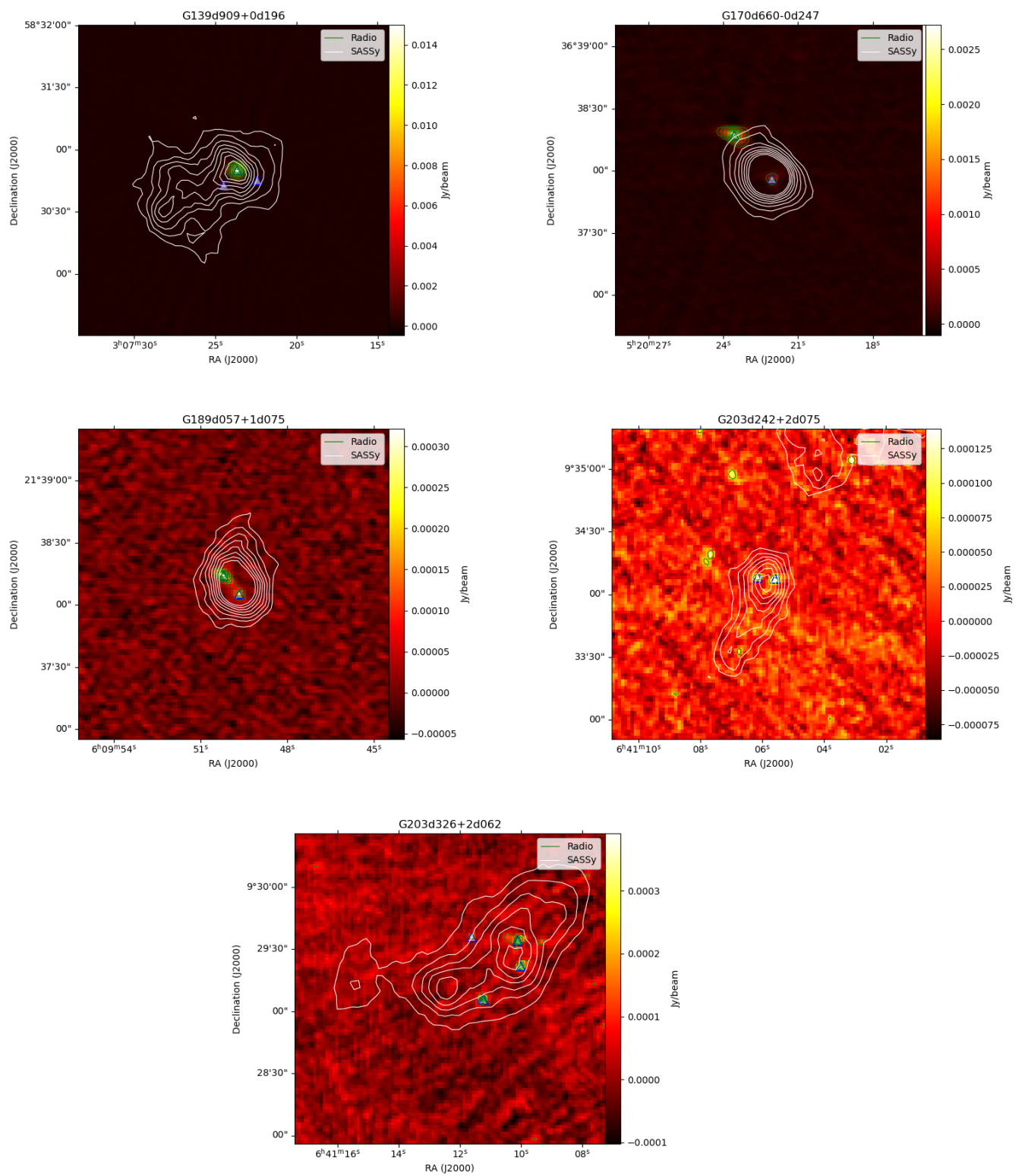
FIGURE 5.12: Continued.

TABLE 5.1: SASSy clumps with embedded radio emission and their nearest SIMBAD association.

Name	SASSy_ID	RA (°)	Dec (°)	Peak Flux Jy beam^{-1}	Int. Flux Jy	Effective Radius arcsecs	Otype
G133.695+1.216	81	36.38	62.11	7.37	31.06	50.22	Radio(mm)
G133.715+1.214	83	36.42	62.1	10.4	79.25	74.3	Radio(mm)
G138.294+1.556	148	45.38	60.49	2.14	9.49	43.58	Candidate_YSO
G138.500+1.646	151	45.83	60.47	1.37	3.86	31.35	Radio(sub-mm)
G139.909+0.196	160	46.85	58.51	1.19	6.85	42.21	Radio
G170.660-0.247	391	80.09	36.63	3.49	6.67	32.25	IR
G189.057+1.075	569	92.46	21.64	1.48	3.77	31.07	MolCld
G203.242+2.075	782	100.27	9.57	1.54	4.69	33.75	Unknown
G203.326+2.062	786	100.3	9.49	4.22	16.98	38.6	Radio(mm)

5.4.1 Background sources

In a visual inspection using contour-overlay plots, I have verified 28 radio sources as collectively being embedded in 9 SASSy clumps. However, there exists the possibility

TABLE 5.2: Observed properties of radio sources embedded in SASSy clumps. The first 3 columns identifiers representing each source's Galactic name, radio ID as generated from the radio data, and the SASSy ID of the natal clump. The fourth and fifth columns are source positions in J2000 RA and Dec, in units of degrees. The sixth through tenth columns are the peak and integrated flux densities and their respective errors. The last four columns are the semi-major and -minor of the FWHM, and their respective errors.

Name Galactic	Source index Radio	SASSy	RA (°)	Dec (°)	Peak flux density mJy beam^{-1}	error	Integrated flux density mJy	error	Major arcsecs	error	Minor arcsecs	error
G133.691+1.215	7030400	81	36.37	62.11	94.41	59.51	595.11	375.18	14.59	0.08	8.75	0.06
G133.691+1.218	7030401	81	36.37	62.11	101.64	59.51	1022.87	604.58	17.5	0.95	11.64	0.7
G133.695+1.215	7040300	81	36.38	62.1	370.1	13.89	589.75	25.81	6.22	0.1	5.19	0.08
G133.710+1.213	7040100	83	36.41	62.1	938.38	15.92	5815.22	117.02	11.34	0.09	11.07	0.08
G133.717+1.222	7040202	83	36.43	62.1	379.12	24.37	6421.5	416.75	20.62	0.17	16.64	0.06
G133.717+1.226	7030201	83	36.43	62.11	346.62	179.82	3511.28	2012.76	23.68	0.9	8.66	2.09
G133.720+1.218	7040203	83	36.43	62.1	120.98	24.37	2350.48	477.08	26.55	0.56	14.82	0.19
G133.720+1.226	7040200	83	36.44	62.11	533.44	24.37	4979.56	231.23	19.63	0.13	9.63	0.05
G133.722+1.224	7030203	83	36.44	62.1	302.57	179.82	4859.15	2953.29	18.3	0.9	17.77	2.09
G133.723+1.224	7040201	83	36.44	62.1	410.75	24.37	4302.97	281.91	14.78	0.39	14.36	0.13
G138.295+1.555	7080400	148	45.38	60.49	0.37	0.02	0.36	0.02	4.74	0.0	4.1	0.0
G138.300+1.558	7080300	148	45.39	60.49	3.18	0.02	4.55	0.03	5.55	0.02	5.22	0.01
G138.302+1.559	7080301	148	45.4	60.49	0.13	0.02	0.63	0.1	27.04	0.01	3.6	0.01
G138.498+1.644	7090100	151	45.83	60.47	8.02	0.32	50.46	2.39	17.37	0.28	7.34	0.14
G139.907+0.194	7131600	160	46.84	58.51	0.27	0.03	0.28	0.03	4.54	-1.0	4.5	-1.0
G139.909+0.197	7131500	160	46.85	58.51	15.84	0.03	20.0	0.04	5.08	0.0	5.03	0.0
G139.911+0.196	7131501	160	46.85	58.51	0.87	0.03	0.69	0.03	4.51	0.0	3.6	0.0
G170.658-0.240	2390400	391	80.1	36.64	2.57	0.01	4.72	0.03	7.8	0.0	4.77	0.0
G170.660-0.247	2390300	391	80.09	36.63	0.62	0.02	0.69	0.02	4.89	0.0	4.62	0.0
G189.056+1.077	5390400	569	92.46	21.64	0.32	0.01	0.52	0.03	6.42	0.12	5.07	0.08
G189.057+1.074	5390401	569	92.46	21.63	0.2	0.01	0.21	0.02	5.05	0.13	4.34	0.09
G203.240+2.075	5162500	782	100.27	9.57	0.15	0.02	0.15	0.02	4.54	-1.0	4.5	-1.0
G203.241+2.077	5162600	782	100.28	9.57	0.12	-1.0	0.12	-1.0	4.55	-1.0	4.5	-1.0
G203.316+2.057	5160400	786	100.29	9.49	0.41	0.07	0.42	0.07	4.54	-1.0	4.5	-1.0
G203.317+2.056	5171900	786	100.29	9.49	0.37	0.03	0.36	0.03	4.8	0.16	4.15	0.12
G203.319+2.054	5171800	786	100.29	9.49	0.31	0.03	0.2	0.02	3.6	0.11	3.6	0.12
G203.319+2.062	5172000	786	100.3	9.49	0.15	0.03	0.15	0.03	4.54	-1.0	4.5	-1.0
G203.326+2.057	5171700	786	100.3	9.48	0.37	0.03	0.25	0.02	3.76	0.12	3.66	0.1

that some or all of these are chance alignments. The number of expected background sources can be estimated via the detectable flux density threshold and the observed field diameter. Using the procedures outlined in the Appendices of Rodriguez et al. (1989) and Anglada et al. (1998), the number of background sources expected in each clump is

$$\langle N \rangle = 1.4 \left[1 - e^{-0.0066\left(\frac{\theta_F}{arcmin}\right)^2} \right] \left(\frac{S_0}{mJy} \right)^{-0.75}, \tag{5.1}$$

where S_0 is the detectable flux density threshold at the center of the field, given in units of mJy and θ_F is the average clump diameter, derived from the clump effective radii. For $S_0 = 0.069$ mJy and $\theta_F = 1\rlap{.}'27$, I expect to detect $\langle N \rangle \simeq 0.11$ background sources in a single clump thus I expect to detect $\langle N \rangle \simeq 9$ background sources in the full sample of 78 clumps.

5.5   SIMBAD-SASSy associations, and distances

By cross-referencing the source positions in the clump sub-catalogue with objects in the SIMBAD database, I have examined the nature of the clumps, identified radio objects previously associated with them, and for all but G170.660-0.246, I have obtained distances from previous studies. I have cross-referenced the SASSy clumps with SIMBAD to understand the nature of the clumps by examining previously observed and classified objects that lie within $30''$ ($\sim$ two beams) of the centre of the clump in question.

5.5.1   G133.695+1.210

This clump is located in the well observed region, W3 (e.g. Ladd et al., 1993; Tieftrunk et al., 1997; Oey et al., 2005; Wang et al., 2012; Merello et al., 2015). Cross referencing G133.695+1.21 with the literature to find objects observed within $30''$ of its centre returned several matches. The majority of the matches have an angular separation $>13''$, one $\sim 4''$, and for two matches the separation is $<1''$. Therefore, I adopt the distance of W3: 1.95±0.04 (Wang et al., 2012; Xu et al., 2006).

Ten of the thirty six objects that fall within the $30''$ constraint are located in two of the high mass star forming regions observed by Wang et al. (2012): SMS2 and SMS3.

There are seven millimetre continuum sources detected in SMS2 and three millimetre continuum sources detected in SMS3. The sources in SMS2 are at different evolutionary stages: three sources are assumed to be at a very early evolutionary stage as they are not associated with either infrared or radio continuum emission, three are predominantly associated with free-free emission from an UC HII region, and one is associated with an HC HII region (Tieftrunk et al., 1997). Further evidence of massive star formation is seen in the outflows detected in the region. However, SMS3 shows no additional evidence of star formation: no outflows are detected and the three sources are not associated with any infrared or radio emission thus implying they are at a very young evolutionary stage (Wang et al., 2012). The sources associated with this clump, detected in Wang et al. (2012) strongly indicate ongoing star formation in this clump. The rest of the SIMBAD associations similarly indicate active star formation from detections that include: stars, YSOs, HII regions, and masers as well as IR, submillimetre, and radio emission.

5.5.2   G133.715+1.214

G133.715+1.214 is located in the same region as G133.695+1.210, and is therefore associated with the same studies and objects. Therefore, I also adopt the distance of W3 for this clump. In SIMBAD, the objects shown as being closest to this clump are SMS1-MM2, a millimetre object in Wang et al. (2012), SMM3 and SMM4, submillimetre objects in Wang et al. (2013), and G133.715+01.215, a maser in Argon et al. (2000). These are located $1.''73$, $1.''81$, $2.''30$, and $2.''32$ from the centre of the clump, respectively. Further out, the clump has more millimetre, submillimetre and maser associations. Other objects within the matching radius include radio sources, YSOs, near/far infrared sources, and HII regions.

5.5.3   G138.294+1.556

G138.294+1.556 is located in the very densely populated and well studied region, W5. Therefore, the SIMBAD search on this region returned multiple associations from multiple studies. The majority of these associations are with sources are from Chauhan et al. (2009) and Deharveng et al. (1997). The closest object is located in BRC 14 (Chauhan et al., 2009) which is associated with the molecular cloud IC 1848A (Deharveng et al., 1997) and thus, both are part of the photoionised cloud, IC 1848 (Thompson et al.,

2004; Matsuyanagi et al., 2006). I therefore adopt the distance of IC 1848, 2.2±0.2kpc (Becker and Fenkart, 1971; Moffat, 1972; Deharveng et al., 1997) as the distance of G138.294+1.556.

The sources within the matching constraints are dominated by YSO candidates (Chauhan et al., 2009) and T-Tauri stars (Deharveng et al., 1997). Also seen among the associations are objects with IR, millimetre and submillimetre emission; masers; molecular clouds; and, at an angular distance of $23\rlap{.}{''}77$, an HII region (Kurtz et al., 1994).

5.5.4   G138.500+1.647

This clump is also located in the W5 star forming complex. However, with 19 matches it has significantly fewer associations within the $30''$ radius. The closest matches are submillimetre sources from Merello et al. (2015) and MacKenzie et al. (2011), and an IR source from Deharveng et al. (2012), respectively. For consistency, I use the distance to W5 adopted for G138.294+1.556, 2.2±0.2kpc, here as well.

The nature of sources associated with G138.500+1.647 includes submillimetre and IR emission (as mentioned in the preceding sentences), millimetre emission, outflow candidates (Ginsburg et al., 2011a), masers (Blair et al., 1980; Braz et al., 1990; Harju et al., 1998), molecular clouds (Niwa et al., 2009; Shimoikura et al., 2018), YSOs/YSO candidates (Cutri et al., 2003; Ojha et al., 2004), an IR star cluster (Bica et al., 2003), an HII region (Bronfman et al., 1996), and a radio source (Condon et al., 1998). The two IR sources detected in Deharveng et al. (2012) are part of a bipolar HII region.

5.5.5   G139.909+0.196

The closest SIMBAD match for this clump is a 1.42 GHz compact radio source, 27P 52 from Green (1989), located $2\rlap{.}{''}39$ from the centre of the clump. This means at least one of the three radio sources in my data embedded in this clump, will have previously been observed. The second closest object, located $\sim 1''$ further out, is a YSO in the AFGL437 cluster (Devine et al., 2008). I therefore assume the distance of this cluster, 2.0±0.5 kpc (Arquilla and Goldsmith, 1984), as the distance of G139.909+0.196.

The SIMBAD objects in this match are dominated by sources (mostly YSOs) from AFGL437, which is assumed to be active in star formation as it contains three IR sources, a bipolar molecular outflow and a reflection nebulosity (Meakin et al., 2005; Devine et al., 2008), thus indicating that this clump has ongoing star formation. Furthermore, the region contains HII regions (Bronfman et al., 1996; Kurtz et al., 2004; Di Francesco et al., 2008; Anderson et al., 2015) and masers (Cesaroni et al., 1988; Palagi et al., 1993; Harju et al., 1998) which emphasises the presence of star formation in the clump.

5.5.6   G170.660-0.246

G170.660-0.246 has one SIMBAD match within the $30''$ matching radius. The source WISE J052022.10+363757.1, which is classified as a mid infrared source in Cutri (2012), is centred $1''25$ from the centre of the clump. This has no previous radio emission associated with it, and similarly has no well studied association from which I can adopt a distance. Therefore, for this clump, I have used the median value of the distances of the other clumps, and therefore assumed the distance of the clump to be 1.975 kpc.

5.5.7   G189.057+1.075

This molecular clump has been previously observed by Shimoikura et al. (2013) during observations carried out toward the HII regions S247, S252, and BFS52. They postulate that star formation is ongoing in this region, since the clump is associated with the cluster CSS3 (Carpenter et al., 1995) which has two YSO candidates, IRAS 06067+2138 and IRAS 0609+2142. Moreover, a water maser has been detected towards IRAS 06067+2138 (Koempe et al., 1989), thus emphasising the evidence of star formation in the region. An IR star cluster (Bica et al., 2003), an HII region (Bronfman et al., 1996) and a maser (Harju et al., 1998) are the other objects closely associated with G189.057+1.075. The centre of the clump reported in Shimoikura et al. (2013) is only $8''54$ away from the centre of G189.057+1.075, thus I follow suit and adopt the distance to S252, reported by Reid et al. (2009) to be 2.1±0.026 kpc, as the distance to this clump.

5.5.8   G203.242+2.075

This clump is located in a well studied region, NGC 2264. Therefore, the match returned associations from several studies (e.g. Girart et al., 2002; Flaccomio et al., 2006; Young et al., 2006; Teixeira et al., 2006; Teixeira et al., 2007; Rapson et al., 2014; Buckle and Richer, 2015; Romine et al., 2016) that have catalogued objects within $30''$ of the clump. The closest object to G203.242+2.075 is part of a discrete cluster of sources located in the star forming core IRAS 12 S1 region of the young cluster NGC 2264 (Young et al., 2006). I therefore assume the distance of NGC 2264, 715 pc (Buckle and Richer, 2015; Morgan et al., 1965), as the distance of this clump.

Previous studies have predominantly classified objects associated with this clump as star formation tracers (or candidates). Within the $30''$ radius used to cross reference this clump with objects in other studies, the classifications include YSOs, or YSO candidates, pre-main sequence stars, star clusters, T-Tauri stars, X-ray emission, submillimetre, and millimetre emission, as well as one radio source. The radio source, labelled VLA 9 in Girart et al. (2002), was detected in 3.6 cm sub arcsecond resolution maps where it appeared to be embedded in a dense core (Wolf-Chase et al., 1995) and is therefore considered a candidate for the driving source of a molecular outflow. VLA 9 is located $\sim 29''$ from the centre of the clump whereas the radio source in my data is positioned $4\rlap{.}''35$ from the centre of the clump thus presenting a new radio association to G203.242+2.075.

5.5.9   G203.326+2.062

Like G203.242+2.075, the molecular clump G203.326+2.062 is located in NGC 2264, and therefore is associated with objects from many of the same studies. The closest object, centred $1\rlap{.}''02$ away from the clump, is a millimetre object, MMS 3 (Ward-Thompson et al., 2000; Schreyer et al., 2003), that is one of five emission peaks that make up a ridge (NGC 2264 MMS) of bright submillimetre and millimetre emission around IRS 1. In fact, MMS 3 is classified as a molecular clump and must therefore be the same object as G203.326+2.062. Here as well, I therefore assume the distance of NGC 2264, 715 pc, as the distance of this molecular clump.

The objects seen within the $30''$ matching radius are, again, indicative of star formation. MMS 3 is shown to have an outflow centred on it by Ward-Thompson et al. (2000) who

suggest that it may already have formed a YSO at its centre and may in fact be a high mass equivalent of a Class 0 protostar. In observations covering the frequency ranges of 336.0-347.3 GHz and 348.0-359.3 GHz, Watanabe et al. (2017) have also detected molecular outflows associated with two objects, CMM3A and CMM3B, that are within the matching radius, thus showing further evidence of active star formation. Furthermore, they have detected six continuum peaks around these objects, four of which are also located within the radius of interest. CMM3D has infrared emission associated with it and is therefore likely to be a low-mass Class I or Class II protostar. CMM3F may be a low-mass protostellar or prestellar source as it has no infrared counterparts. Even though the final two peaks, CMM3G and H have no derived parameters shown in Watanabe et al. (2017), they are noted as being close to the outflow lobe B1 of Saruwatari et al. (2011). There are several other YSO, mm, and submm associations (e.g. Cutri et al., 2003; Flaccomio et al., 2006) but I also find radio sources within the applied constraints. There are three radio sources in Reipurth et al. (2004) within $17''$ of the clump's centre. Moreover, the aforementioned radio sources are closely associated with MMS 3. VLA 6/7 are embedded in the MMS 3 clump, albeit off centre while VLA 5 is located just outside of it's FWHM. VLA 6 is unresolved and corresponds to the 'very red' and embedded source IRS D, in a cluster of near-infrared sources centred on IRAS 22343+7501 (Meehan et al., 1998). And VLA7, which is also noted as corresponding to one of the sources in the small cluster (IRS A), is a small subarcsecond radio jet.

5.6 Clump Properties

Here I present the physical properties of the molecular clumps identified as having embedded radio emission in § 5.4. The calculations of the physical parameters are largely dependent on the dust temperature, distances, sizes, integrated and peak flux densities of the sources. The majority of these parameters are extracted during the source finding process. The distances, however, are assumed according to the discussion in § 5.5. As there are currently no temperatures available for the SASSy clumps, I have adopted the mean temperature used in Djordjevic et al. (2019), which, for consistency, assumes an average dust temperature from those calculated in Urquhart et al. (2018).

5.6.1 Clump Effective Radius

The effective radii of the clumps has been derived using the submillimetre area extracted during the source finding. The area, which is recorded in pixel units has been converted to arcseconds and used in the effective radius calculation which uses the approximation presented by Rosolowsky et al. (2010):

$$R_{eff} = \sqrt{\frac{A}{\pi}} \qquad (5.2)$$

Where,

A is the area of the clump in arcseconds, calculated by: pixel-size^2×Submm_Vol

5.6.2 Clump Mass

The clump masses have been estimated using the approach outlined in Hildebrand (1983) which works with the assumption that if the dust temperature is constant and the emission is optically thin, the total clump mass varies directly with the integrated submillimetre flux density. This gives the relation:

$$M_{clump} = \frac{S_\nu D^2 R}{B_\nu(T_{dust})\kappa_\nu}, \qquad (5.3)$$

Where,

D is the heliocentric distance in units of m,

S_ν is the integrated flux density in units of $Wm^{-2}Hz^{-1}$ (SI for Jansky),

R is the gas-to-dust mass ratio, assumed to be 100 (Draine et al., 2007),

κ_ν is the dust absorption coefficient, in units of m^2Kg^{-1} (Schuller et al., 2009),

B_ν is the Planck function with $T_{dust} = 27K$, in units of $Wm^{-2}sr^{-1}Hz^{-1}$.

This gives the clump mass in kilograms, and dividing this result by the mass of the sun gives the result in solar masses, which I have used to present the clump masses in this study.

5.6.3 Column Density

The peak column densities are estimated from the peak submillimetre flux densities of the clumps using the relation:

$$N_{H_2} = \frac{S_\nu R}{B_\nu(T_{dust})\Omega\kappa_\nu\mu m_H} \tag{5.4}$$

where,

S_ν is the peak submillimetre flux density in units of $Wm^{-2}Hz^{-1}$ (SI for Jansky),

μ is the mean molecular weight of the gas, assumed to be 2.8 (Kauffmann et al., 2008),

m_H is the mass of hydrogen,

Ω is the beam solid angle in steradians,

B_ν, R, and κ_ν are as defined in Eqn. 5.3.

TABLE 5.3: Derived properties of the host molecular clumps. The first column gives the Galactic name of each clump; columns 2 and 3 are the peak and integrated flux densities; column 4 is the clump area in units of arcseconds derived from the source finder measurement of the clump size; columns 5 and 6 are the clump mass and the log of the clump mass, respectively; columns 8 (N_{H_2}) and 9 are the column density and log column density, respectively; column 10 is the effective radius of the clump and column 11 is the heliocentric distance.

Name	RA	Dec	Peak flux	Int flux	Clump Area	M_{clump}	Log M_{clump}	(N_{H_2})	Log(N_{H_2})	R_{eff}	D
	(°)	(°)	Jy beam^{-1}	Jy	arcsec^2	M$_\odot$	M$_\odot$	cm^{-2}	cm^{-2}	arcsecs	pc
G133.695+1.216	36.38	62.105	7.37	31.06	71310.0	408.0	2.61	1.84e+23	23.3	150.66	1950
G133.715+1.214	36.418	62.097	10.4	79.25	156101.0	1040.0	3.02	2.6e+23	23.4	222.91	1950
G138.294+1.556	45.38	60.489	2.14	9.49	53699.0	158.0	2.2	5.36e+22	22.7	130.74	2200
G138.500+1.646	45.834	60.468	1.37	3.86	27783.0	64.0	1.81	3.43e+22	22.5	94.04	2200
G139.909+0.196	46.849	58.513	1.19	6.85	50374.0	95.0	1.98	2.97e+22	22.5	126.63	2000
G170.660-0.247	80.092	36.632	3.49	6.67	29399.0	90.0	1.95	8.71e+22	22.9	96.74	1975
G189.057+1.075	92.458	21.636	1.48	3.77	27294.0	57.0	1.76	3.69e+22	22.6	93.21	2100
G203.242+2.075	100.274	9.568	1.54	4.69	32215.0	8.0	0.92	3.86e+22	22.6	101.26	715
G203.326+2.062	100.301	9.486	4.22	16.98	42137.0	30.0	1.48	1.06e+23	23.0	115.81	715
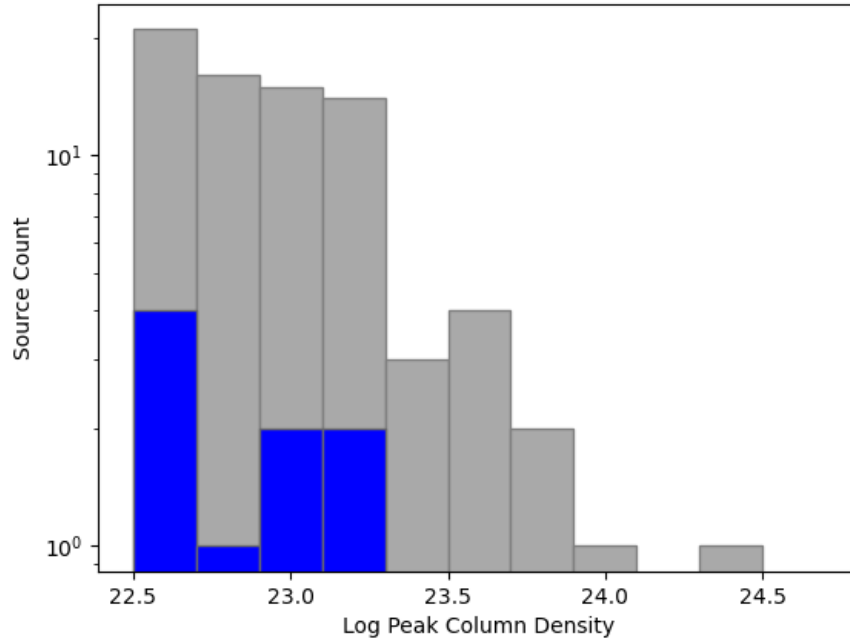
FIGURE 5.13: Column densities of the full sample of 78 SASSy clumps (in grey) and the sub-sample of SASSy clumps with embedded radio emission (in blue).

5.7 HII Region Properties

The physical parameters of the HII regions embedded in the the molecular clumps are derived using parameters extracted during the source finding as well as the heliocentric distances determined for the respective clumps in which they are embedded.

5.7.1 Lyman Continuum Flux

The dividing line between the optically thick and thin regimes of thermal bremsstrahlung is at the turnover frequency, where the optical depth, $\tau = 1$ (Kurtz, 2005a). Therefore, objects will be observable in the optically thin regime, and will go unseen in the optically thick regime. The Lyman continuum flux (N_{Ly}) can be derived from the radio continuum if we assume the HII regions detected are in photoionisation equilibrium and optically thin (Carpenter et al., 1990). If the assumption is not valid, the derived value of N_{Ly} represents a lower limit to the true value. With this assumption, we can define the Lyman continuum flux of an optically thin HII region as:

$$N_{Ly} = 9 \times 10^{43} \left(\frac{S_\nu}{mJy} \right) \left(\frac{D}{kpc} \right)^2 \left(\frac{\nu}{5GHz} \right)^{0.1} photons \ s^{-1} \tag{5.5}$$

where,

S_ν is the radio (*5GHz*) integrated flux density in *mJy*,

D is the heliocentric distance in *kpc*,

ν is the frequency in units of *5GHz*, i.e. $\nu = 1$,

5.8 Clumps with $Log(N_{H_2}) > 23 \ cm^{-2}$ but no radio detections

There are 69 clumps in this sample of 78 that have no embedded radio emission, and 30 of these have $Log(N_{H_2}) > 23 \ cm^{-2}$ (see Fig. 5.13). I have cross-referenced these clumps with the SIMBAD database to investigate their nature through associated objects. G137.897+1.464 is associated with 3 SIMBAD sources: 2 YSO candidates (Cutri et al., 2003), and a star (Gaia Collaboration et al., 2018). G223.889-3.035 has a variable star embedded in it towards the edge of its effective radius (Heinze et al., 2018). The remaining clumps have no matches within a search radius equal to their effective radius. Thus these high column density clumps have no radio emission associated with them, both in previous studies and in this one.

I have measured the 3σ upper limits of the flux density in the regions of the radio observations associated with each clump from which I have set an upper limit to the Lyman flux of any massive star present. For this I have assumed an upper limit of 5 kpc to the distance of the clumps. This gives $N_{Ly} \lesssim 10^{45} s^{-1}$ for all the clumps. For an HII region powered by a B0.5 star, we expect $N_{Ly} \gtrsim 10^{46} s^{-1}$ (Panagia, 1973). Therefore, there will be no HII regions present in these clumps.

TABLE 5.4: Derived properties of the candidate HII regions. Column 1 gives the Galactic name of each radio source; column 2 gives the source Id - an integer number formed by combining the scheduling block and field ids with the source finder island and source Ids; columns 3 and 4 are the peak and integrated flux density; columns 5 and 6 give the lyman flux and log lyman flux, respectively; and column 7 gives the heliocentric distance - the same distance as the host clumps.

Name	Radio ID	SASSy ID	RA	Dec	Peak Flux	Int Flux	N_{Ly}	Log(N_{Ly})	D
			(°)	(°)	mJy beam^{-1}	mJy	photons s^{-1}	photons s^{-1}	kpc
G133.691+1.215	7030400	81	36.371	62.106	94.41	595.11	2.04e+47	47.3	1.95
G133.691+1.218	7030401	81	36.373	62.109	101.64	1022.87	3.5e+47	47.5	1.95
G133.695+1.215	7040300	81	36.379	62.105	370.1	589.75	2.02e+47	47.3	1.95
G133.710+1.213	7040100	83	36.408	62.098	938.38	5815.22	1.99e+48	48.3	1.95
G133.717+1.222	7040202	83	36.428	62.104	379.12	6421.5	2.2e+48	48.3	1.95
G133.717+1.226	7030201	83	36.432	62.107	346.62	3511.28	1.2e+48	48.1	1.95
G133.720+1.218	7040203	83	36.432	62.099	120.98	2350.48	8.04e+47	47.9	1.95
G133.720+1.226	7040200	83	36.437	62.107	533.44	4979.56	1.7e+48	48.2	1.95
G133.722+1.224	7030203	83	36.441	62.104	302.57	4859.15	1.66e+48	48.2	1.95
G133.723+1.224	7040201	83	36.441	62.103	410.75	4302.97	1.47e+48	48.2	1.95
G138.295+1.555	7080400	148	45.38	60.487	0.37	0.36	1.56e+44	44.2	2.2
G138.300+1.558	7080300	148	45.392	60.487	3.18	4.55	1.98e+45	45.3	2.2
G138.302+1.559	7080301	148	45.397	60.487	0.13	0.63	2.77e+44	44.4	2.2
G138.498+1.644	7090100	151	45.829	60.467	8.02	50.46	2.2e+46	46.3	2.2
G139.907+0.194	7131600	160	46.843	58.513	0.27	0.28	9.92e+43	44.0	2.0
G139.909+0.197	7131500	160	46.849	58.514	15.84	20.0	7.2e+45	45.9	2.0
G139.911+0.196	7131501	160	46.852	58.512	0.87	0.69	2.5e+44	44.4	2.0
G170.658-0.240	2390400	391	80.098	36.638	2.57	4.72	1.66e+45	45.2	1.975
G170.660-0.247	2390300	391	80.092	36.632	0.62	0.69	2.43e+44	44.4	1.975
G189.056+1.077	5390400	569	92.459	21.637	0.32	0.52	2.07e+44	44.3	2.1
G189.057+1.074	5390401	569	92.457	21.635	0.2	0.21	8.44e+43	43.9	2.1
G203.240+2.075	5162500	782	100.273	9.569	0.15	0.15	6.86e+42	42.8	0.715
G203.241+2.077	5162600	782	100.276	9.569	0.12	0.12	5.49e+42	42.7	0.715
G203.316+2.057	5160400	786	100.292	9.493	0.41	0.42	1.93e+43	43.3	0.715
G203.317+2.056	5171900	786	100.292	9.493	0.37	0.36	1.66e+43	43.2	0.715
G203.319+2.054	5171800	786	100.292	9.489	0.31	0.2	9.22e+42	43.0	0.715
G203.319+2.062	5172000	786	100.298	9.493	0.15	0.15	6.97e+42	42.8	0.715
G203.326+2.057	5171700	786	100.297	9.485	0.37	0.25	1.16e+43	43.1	0.715

TABLE 5.5: Upper limit estimations of clumps without radio detections.

Name	Clump Area arcsecs^2	M$_{clump}$ M$_\odot$	N$_{H_2}$ cm^{-2}	Log(N$_{H_2}$) cm^{-2}	3σ upper limit $_{radio}$ mJy beam^{-1}	N$_{Ly}$ photons s^{-1}	Log(N$_{Ly}$) photons s^{-1}
G119.646-0.247	1698.0	199.0	3.18e+23	23.5	0.127	2.86e+44	44.46
G120.209-3.117	2403.0	105.0	1.43e+23	23.2	0.175	3.94e+44	44.6
G124.016-3.273	2861.0	136.0	1.19e+23	23.1	0.176	3.96e+44	44.6
G127.272-2.865	4227.0	1403.0	2.32e+24	24.4	0.103	2.32e+44	44.37
G131.372-2.901	3098.0	644.0	6.66e+23	23.8	0.571	1.28e+45	45.11
G137.170-3.009	2097.0	395.0	4.74e+23	23.7	0.38	8.55e+44	44.93
G137.897+1.464	2862.0	133.0	1.71e+23	23.2	0.174	3.92e+44	44.59
G139.615-2.699	2647.0	144.0	2.07e+23	23.3	0.135	3.04e+44	44.48
G145.888-2.813	1253.0	59.0	1.19e+23	23.1	0.116	2.61e+44	44.42
G146.213+2.386	3943.0	222.0	9.83e+22	23.0	0.0989	2.23e+44	44.35
G149.534-1.891	2743.0	215.0	3.68e+23	23.6	0.112	2.52e+44	44.4
G149.921-1.820	2353.0	175.0	2.55e+23	23.4	0.146	3.28e+44	44.52
G150.352-1.347	2649.0	100.0	1.45e+23	23.2	2.86	6.44e+45	45.81
G151.348-1.971	1942.0	75.0	1.1e+23	23.0	0.218	4.91e+44	44.69
G156.120-2.857	3061.0	476.0	3.1e+23	23.5	0.325	7.31e+44	44.86
G157.806-1.352	2105.0	82.0	1.1e+23	23.0	0.1	2.25e+44	44.35
G162.381+2.860	2982.0	223.0	3.29e+23	23.5	1.03	2.32e+45	45.37
G162.411+2.894	2579.0	80.0	1.11e+23	23.0	0.255	5.74e+44	44.76
G165.689+3.183	1271.0	74.0	1.09e+23	23.0	0.109	2.45e+44	44.39
G179.180+1.163	2558.0	135.0	1.2e+23	23.1	0.533	1.2e+45	45.08
G183.126+2.575	1119.0	82.0	1.5e+23	23.2	0.112	2.52e+44	44.4
G190.675-3.188	2228.0	134.0	1.81e+23	23.3	0.292	6.57e+44	44.82
G201.168+1.673	4211.0	4353.0	8.84e+24	24.9	0.121	2.72e+44	44.43
G207.789-2.757	1881.0	89.0	1.26e+23	23.1	0.117	2.63e+44	44.42
G216.085-2.868	1795.0	99.0	1.34e+23	23.1	0.191	4.3e+44	44.63
G218.293+2.740	2381.0	102.0	1.36e+23	23.1	0.395	8.89e+44	44.95
G222.713+3.024	1617.0	94.0	1.12e+23	23.1	0.314	7.06e+44	44.85
G223.889-3.035	3595.0	100.0	1.19e+23	23.1	0.15	3.37e+44	44.53
G230.506-0.872	2717.0	583.0	9.17e+23	24.0	0.147	3.31e+44	44.52
G240.536+1.172	3202.0	129.0	1.16e+23	23.1	1.78	4.01e+45	45.6

5.9 Discussion

I have looked at 78 SASSy clumps and only found 28 radio sources embedded in 9 clumps. The column densities of these clumps are between $10^{22.5}$ *cm*$^{-2}$ and $10^{23.4}$ *cm*$^{-2}$. However, the radio emission embedded in the clumps have $N_{Ly} \lesssim 10^{45}$ *s*$^{-1}$. Of the 9 clumps with embedded radio emission, all but 2 (G139.909+0.196 and G170.660-0.247) are located in already known sites of massive star formation; thus, the radio sources detected here are not new discoveries. To conclusively rule out the presence of HII regions in the clumps where no embedded radio emission was detected, I have determined the likelihood that massive stars are present using the upper limit to the radio. I have found that despite their high column densities, the upper limits I have determined for the N_{Ly} fall below what we expect for an HII region powered by a B0.5 star.
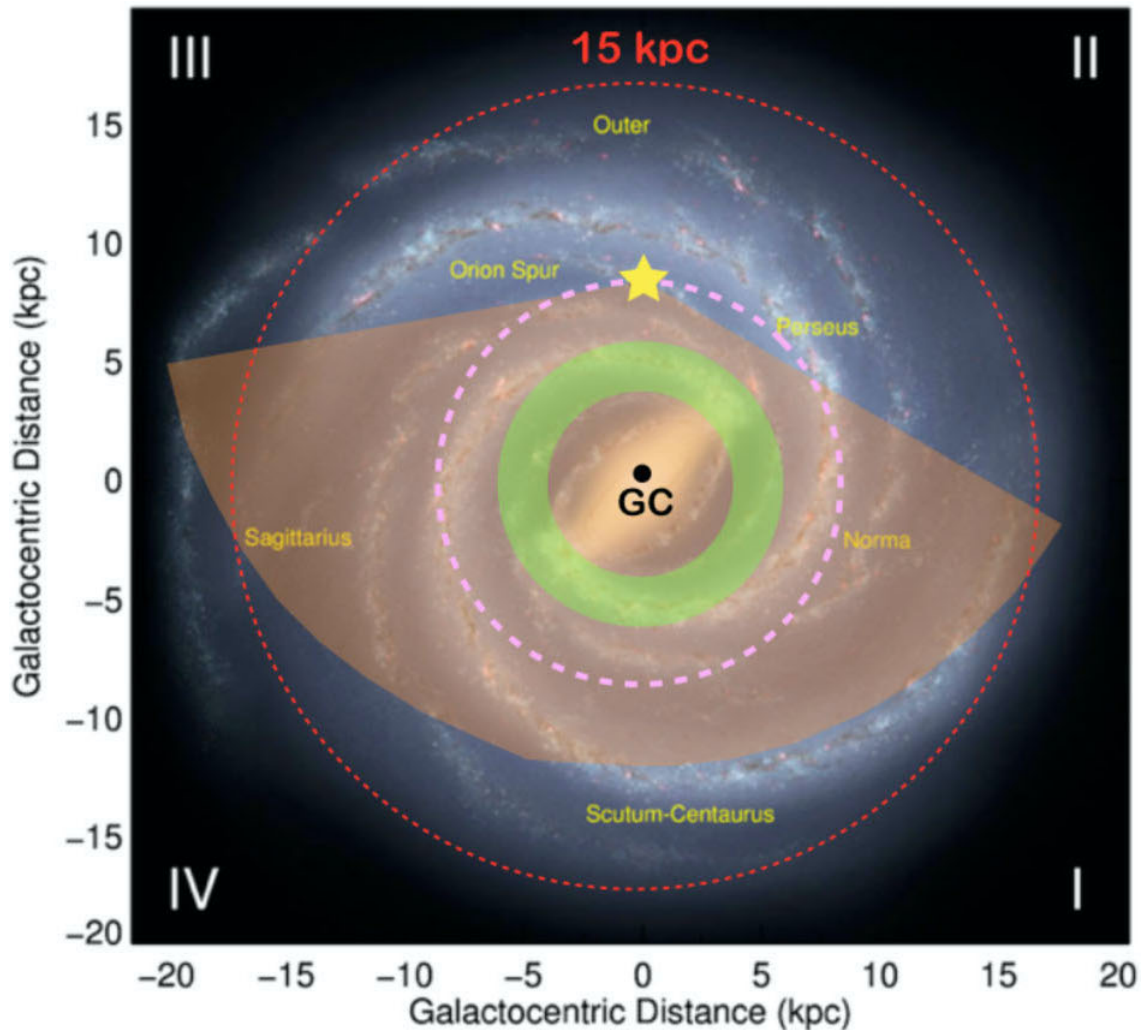
FIGURE 5.14: Overview of the coverage of the Galactic mid-plane provided by the ATLASGAL survey. [courtesy of Urquhart et al. 2018]. The background is an artist's impression of how the Milky Way would appear to an external observer looking down from the Northern Galactic Pole [courtesy of NASA/JPL-Caltech/R. Hurt (SSC/Caltech)]. The yellow star indicates the position of the Sun, while the orange shaded region shows the coverage of the survey out to a heliocentric distance of 20 kpc. The Solar circle and the 5 kpc molecular ring are shown by the pink dashed line and the light green band centred on the Galactic Centre.

The results imply that not all high column density clumps in the Outer Galaxy have ongoing massive star formation. It however raises the questions: Why and how do the clumps have high column densities without hosting high mass star formation? One possibility is that they are forming low mass stars, another is that they actually are forming massive stars, but the massive star formation is at a very early stage and there is no radio emission to detect yet. This would, however, be detectable in the MIR or at $70\mu m$. Table 5.6 illustrates this using the 9 clumps that have radio emission embedded in them. The last four columns show their $70\mu m$ and MIR brightness: Y indicates they

are IR bright, N means they are IR quiet, and those marked with X have not been observed at these wavelengths. The full table can be found in Appendix: C. Table 5.6 shows that 7 clumps are bright in at least one of the three wavelengths - G189.057+1.075 and G203.242+2.075 are weak in the MIR but have not been observed at 70 μm. This means these clumps are either hosting early massive star formation or forming low mass stars.

Heliocentric distances are crucial to determining the physical properties of dense clumps. The distances used in this analysis were assumed based on associations in the literature (c.f. § 5.5). Fig. 5.14 shows an overview of the Galactic mid-plane coverage in the ATLASGAL survey. The SASSy Outer Galaxy clumps are closer than the ATLASGAL clumps. Thus small clumps in the Outer Galaxy are subject to beam dilution, resulting in higher measurements of column density. Hence, the phenomenon of high column density clumps is caused by beam dilution on small clumps. Future studies will need to determine accurate distances in order to conclusively determine what processes are taking place in these clumps.

TABLE 5.6: SASSy clump brightness at $70\mu m$ and in the MIR. The first five columns are the clump names in Galactic coordinates; the clump coordinates in J2000 - sexagesimal and degrees, respectively. The last four columns represent the clump brightness in $70\mu m$, MSX, WISE, and MIR (which is representative of MSX and WISE). Y indicates they are IR bright, N means they are IR quiet, and those marked with X have not been observed.

Name	SASSy ID	RA (°)	Dec (°)	$70\mu m_{Bright}$	MSX_{Bright}	$WISE_{Bright}$	MIR_{Bright}
G133.695+1.216	81	36.38	62.105	Y	Y	N	Y
G133.715+1.214	83	36.418	62.097	Y	Y	N	Y
G138.294+1.556	148	45.38	60.489	Y	Y	Y	Y
G138.500+1.646	151	45.834	60.468	Y	Y	Y	Y
G139.909+0.196	160	46.849	58.513	Y	Y	Y	Y
G170.660-0.247	391	80.092	36.632	Y	N	N	N
G189.057+1.075	569	92.458	21.636	X	N	N	N
G203.242+2.075	782	100.274	9.568	X	N	N	N
G203.326+2.062	786	100.301	9.486	X	N	Y	Y

5.10   Summary

i). I have searched 78 high column density clumps in the Outer Galaxy for evidence of massive star formation and only found a handful of examples. Moreover, at least half of these are in already known sites of massive star formation. Their low N_{Ly} values suggest they are not UC HII regions. This implies that there are no unknown UC HII regions in the Outer Galaxy.

ii). The radio observations have revealed embedded radio continuum emission in 9 of the 78 clumps. However, despite the high column densities of the host clumps, the low N_{Ly} flux of the embedded radio sources rules them out as UC HII regions. 7 clumps are bright in either the MIR or at 70 μm thus implying early star formation or low mass star formation.

iii). In the remaining 69 clumps that have no embedded radio emission, I have determined the likelihood of HII regions being present. Using the 3σ upper limit to the radio to set an upper limit to the Lyman flux, thus placing a limit on the mass of any massive stars present rules out any potential embedded HII regions in these clumps. I have assumed an upper limit of 5 kpc to the distance of the clumps which gives $N_{Ly} \lesssim 10^{45} s^{-1}$. This is lower than what we expect for an HII region powered by a B0.5 star (Panagia, 1973).

iv). Future studies can improve on this question by determining distances for all SASSy clumps, carrying out an analysis of clump SEDs using Hi-GAL, thus determining clump masses, temperatures and more accurate N_{H_2}.

Chapter 6

MeerKAT Galactic Plane Survey

The MeerKAT Galactic Plane Survey (MeerKAT-GPS: Goedhart et al. in prep), is an L band survey of the southern Galactic Plane covering roughly half the Galactic Plane from $252° < l < 358°$, $2° < 60°$ and $|b| < 1.5$ down to a nominal depth of $\sim$ 10-30 μJy (cf. § 2.2). In this chapter, I will present a catalogue of compact radio sources extracted from the MeerKAT-GPS images, and highlight some initial survey results with a primary focus on the lifetimes of young HII regions. Compact sources are seen everywhere in the Galactic Plane and represent a wide range of source types and properties. I will identify the portion of the catalogue sources that have previously been detected and discuss their distribution, highlighting their nature and prevalence in the Milky Way.

In § 6.1, I describe the methods used in the development of the MeerKAT-GPS compact source catalogue. I discuss the source detection as well as the tests used to determine the completeness and likely false positive rate of the catalogue. I then present an excerpt of the catalogue and discuss its major statistics in § 6.2. In § 6.3 I explore the nature of the detected sources by cross-matching them with sources in the literature. I show the portion of the catalogue sources that are previously known and classify them by associating them with objects in the SIMBAD database. In § 6.4, I attempt to address the age problem of UC HII regions. By comparing 5 GHz and 1.28 GHz data, I examine the effect that undetected extended emission in higher frequency observations has on the estimates of the lifetimes of UC HII regions. And finally in § 6.5, I summarise my results and present my conclusions.
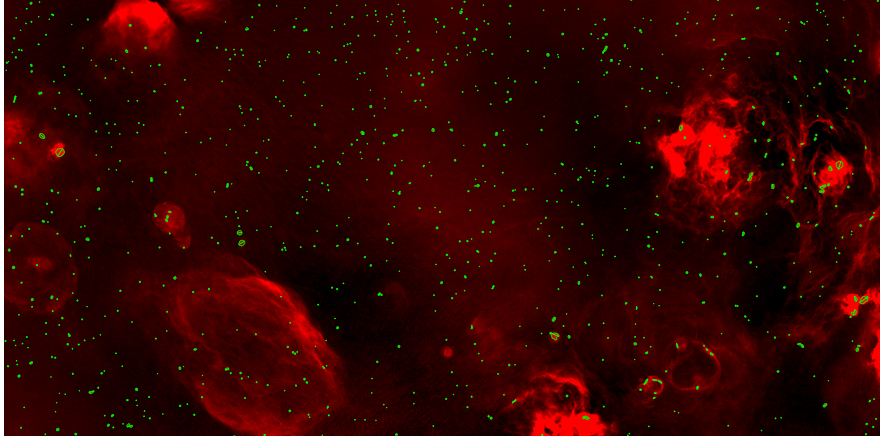
FIGURE 6.1: Cutout from the G321.5+00 MeerKAT-GPS 1.28 GHz zeroth moment tile overlaid with ds9 source regions obtained using the Aegean source finder. Source regions are shown as green polygons.

6.1 Compact Source Catalogue

In 2018, the South African Radio Astronomy Observatory (SARAO) unveiled one of the deepest and highest dynamic range radio images of the Galactic Centre (MeerKAT collaboration 2018). This 1.28 GHz survey of the Galactic Centre (GC) produced mosaic images of the GC from 20 pointings covering 6.5 square degrees with an angular resolution of $4''$. The unveiled image of the GC illustrates the potential of this ground-breaking new radio telescope for wide-area, deep and high fidelity radio interferometry (Heywood et al., 2022). The MeerKAT-GPS was conducted as a natural extension to the GC. This extension also comes with immense potential for new discovery in the Galactic radio population. The survey is over a factor 5 better in angular resolution ($8''$), over an order of magnitude deeper ($1\sigma \sim 10 - 15\mu$Jy), over 6 times larger continuum bandwidth, and with enormously greater uv sampling than previous surveys (e.g. MGPS, Green et al. 1999; SGPS, McClure-Griffiths et al. 2005). An image of a section of the MeerKAT-GPS is shown in Fig. 6.1. The combination of sensitivity, depth and image fidelity reveals the complex structure of the Milky Way with a number of well-resolved HII regions, supernova remnants (SNRs), compact sources, and background radio galaxies. The image is overlaid with ds9 source regions obtained through the source detection process described in § 6.1.1. These regions illustrate the prevalence of the compact sources detectable in the MeerKAT-GPS.

In the following sections, I will present a compact source catalogue created from the 1.28 GHz MeerKAT-GPS images. In § 6.1.1 to § 6.1.3 I will show the method and results of an automated cataloguing process designed to extract point and compact sources from the images and discuss the completeness, likely false positive rate, astrometric accuracy, and flux densities of the catalogue sources.

6.1.1 Source detection

The compact sources were extracted from the MeerKAT-GPS images using the AEGEAN (Hancock et al., 2012) source finder. BANE was used for background estimation and AEGEAN for the source extraction, while set to the default parameters ($\sigma_{seed} = 5$ and $\sigma_{flood} = 4$: c.f. § 3.9.1 and § 3.9.1.1). I have extracted 490790 distinct components with a signal-to-noise ratio $\geqslant 5\sigma$ from 58 fields. The RMS values in these fields ranges from 7.26 μJy to 62 mJy (Fig. 6.2) and the integrated flux densities of the extracted sources range from 20 μJy to 27 Jy (Fig. 6.3). The highest mean noise values are coincident with the brightest sources in the catalogue. Sources with a high flux density drive up both local and global RMS. Consequently, the brightest source, as well as the highest global and local RMS are all from the same field, $l = 291.5$. The global RMS in each field has been listed in Table 6.1, the RMS values range from 0.41 mJy to 7.0 mJy.
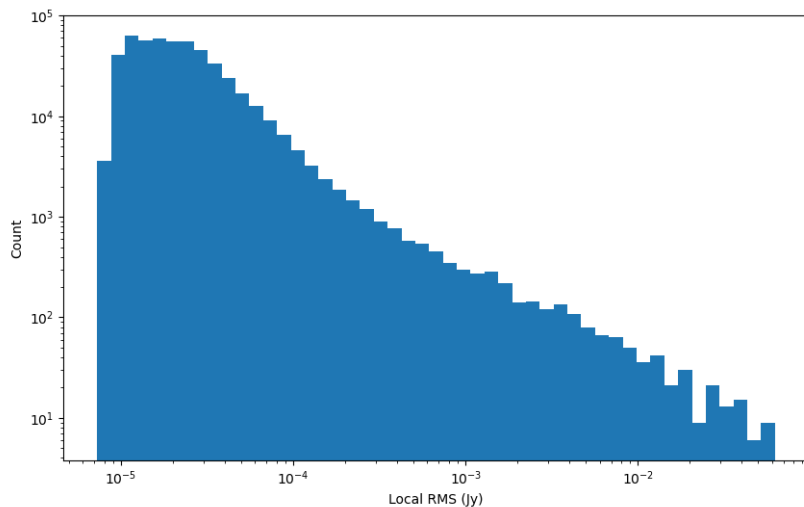
FIGURE 6.2: Noise distribution across the MeerKAT-GPS survey determined through the local RMS of the individual source detections. The RMS values are spread across the range 7.26 μJy to 62 mJy.
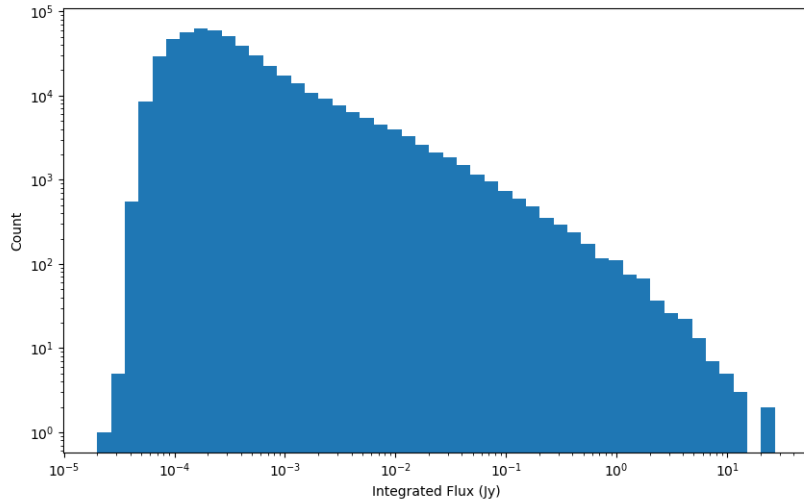
FIGURE 6.3: Histogram of the compact source catalogue integrated flux densities. There are ∼490k sources above 5σ between 20 μJy and 27 Jy.

TABLE 6.1: MeerKAT field RMS distribution

Field Centre Gal. Longitude (°)	Global RMS (mJy beam^{-1})	Field Centre Gal. Longitude (°)	Global RMS (mJy beam^{-1})	Field Centre Gal. Longitude (°)	Global RMS (mJy beam^{-1})
2.5	0.82	59.5	0.46	306.5	4.04
5.5	1.32	252.5	0.7	309.5	1.05
8.5	1.06	255.5	1.06	312.5	0.92
11.5	2.44	258.5	0.47	315.5	1.44
14.5	6.61	261.5	0.49	318.5	1.22
17.5	1.14	264.5	0.55	321.5	2.05
20.5	1.38	267.5	4.47	324.5	0.81
23.5	1.21	270.5	0.84	327.5	2.86
26.5	1.27	273.5	1.31	330.5	1.58
29.5	2.38	276.5	0.8	333.5	3.23
32.5	1.49	279.5	0.58	336.5	1.88
35.5	1.59	282.5	1.47	339.5	1.67
38.5	0.91	285.5	3.35	342.5	0.84
41.5	0.83	288.5	1.65	345.5	2.09
44.5	2.43	291.5	7.06	348.5	2.79
47.5	1.03	294.5	0.96	351.5	3.17
50.5	3.42	297.5	1.93	354.5	2.8
53.5	0.61	300.5	1.21	357.5	1.26
56.5	0.41	300.5	1.22		
57.5	0.49	303.5	0.72		

6.1.2 Completeness

The survey, having been observed along the Galactic plane, will have varying noise and background properties, as seen in § 6.1.1. Therefore, the completeness in the various tiles will also vary. I have run completeness tests on six tiles representing different

Galactic longitudes in the survey following the method outlined in § 3.10. To achieve this, I injected randomly generated point sources into the respective tiles and ran the source finder on the artificial source infused tiles. I then compared the input and output source catalogues, and measured the detection ratio as a function of the flux density. The combined results are shown in Fig. 6.4. As expected, the plot shows varying completeness. Note that $l = 002.5$, which is closest to the GC has the lowest completeness. I wrote the simulation to include regions with pre-existing sources and background emission, hence the test includes source recovery affected by background noise and source confusion. $l = 002.5$, being close to the GC, will be one of the most crowded regions in the survey. In the following sub-sections, I will outline in detail, the parameters used in the simulation as well as the results of the test.

6.1.2.1 Detection ratio

The completeness of the MeerKAT-GPS compact source catalogue has been estimated by repeatedly injecting compact artificial sources into 6 representative tiles. The tiles were selected to possess a wide range of background and noise properties, thus adequately representing the full survey. The global RMS in these tiles ranged from 0.41 to 7.06 mJy beam^{-1}, the RMS in fields $l = 2.5$ and $l = 291.5$, respectively. The global RMS of the other fields included in the simulation as well as the rest of the survey tiles are listed in Table 6.1. The peak flux densities of the artificial sources were randomly generated within the range 0.02 and 5 *mJy beam*$^{-1}$. The source positions, also randomly generated, were restricted to the central 80% of the respective tiles to avoid edge effects. Obviously the central 80%, in which the sources were injected, contained pre-existing sources and background emission. Therefore, the simulation tests source recovery as a function of source confusion. However, to avoid source contamination, the source finder was run on the images before and after artificial source infusion to identify and remove real sources from the test.
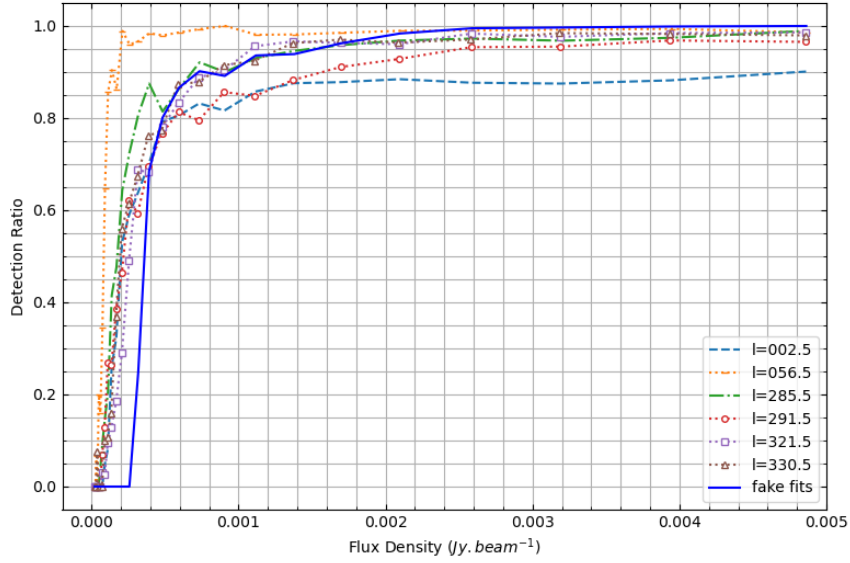
FIGURE 6.4: Survey completeness shown by the detection ratio as a function of flux density from six representative tiles and a synthetic FITS image.

The fraction of recovered sources is $\sim 90\%$ for sources with peak flux densities $\geq$ 2.4 *mJy beam*$^{-1}$ in the tile centred on $l = 2.5°$. The RMS in this tile (0.82 *mJy beam*$^{-1}$) lies on the lower end of survey mean noise values. However, this tile being located close to the GC, is one of the most crowded in the survey. Consequently, source crowding has adversely affected the recovery rate. In $l = 56.5°$, the fraction is $\sim 95\%$ for sources with peak flux densities ≥ 0.2 *mJy beam*$^{-1}$ and $\sim 99\%$ for sources with flux densities ≥ 0.59 *mJy beam*$^{-1}$. The tile centred on $l = 56.5°$, which has the lowest global RMS (0.41 *mJy beam*$^{-1}$) in the survey, has the highest completeness rate. This is in agreement with our expectations since source detection is difficult for faint sources around the noise limit (Coppin et al., 2006). The tiles centred on $l = 285.5°$, 321.5°, and 330.5° have a fraction of $\sim 95\%$ for sources with peak flux densities $\gtrsim 1.3$ *mJy beam*$^{-1}$ and $\sim 99\%$ for flux densities $\gtrsim 3.2$ *mJy beam*$^{-1}$. The fraction of recovered sources in the tile centred on $l = 291.5°$, which has the highest global and local RMS, is $\sim 95\%$ for sources with peak flux densities ≥ 2.4 *mJy beam*$^{-1}$ and $\sim 99\%$ for sources with flux densities ≥ 4.4 *mJy beam*$^{-1}$.

6.1.2.2 Synthetic FITS image

The fraction of recovered sources in tiles $l = 2.5°$ and $291.5°$ show that both source crowding and RMS significantly affect completeness. To better understand the effect of background noise and source crowding in the MeerKAT-GPS images, I have created a synthetic image and run the same completeness test on it. Running the completeness test on a synthetic FITS image reveals how the dynamic variation in noise and background emission in the data affects the completeness of the catalogue. The synthetic image was generated in PYTHON by editing a MeerKAT FITS image and replacing the data with randomly generated noise with a scale of 10μJy. In a similar manner to the real image completeness tests, the synthetic image was repeatedly injected with compact gaussian sources. Again, using the same parameters as the true source detection, AEGEAN was used to detect the injected sources. The detection ratio was then determined as a function of peak flux density. The synthetic image simulation reaches 95% completeness at roughly 1.4 *mJy beam*$^{-1}$ and 99% completeness at roughly 2.53 *mJy beam*$^{-1}$. The synthetic image reaches 95% completeness at a similar flux density to the average tile used in the simulation, but reaches 99% completeness at a lower flux density than all except $l = 56.5°$, which has the lowest mean noise in the survey. Note that, the synthetic tile test has no dips in the fraction after achieving 99% completeness while there are instances where this occurs in the real image simulations. The synthetic image was created with randomly generated Gaussian noise, but contains no pre-existing sources. Therefore, it follows that it has similar completeness to the average real image simulation at low flux density but behaves significantly better at high flux density where the real image simulations are affected by source confusion. The depth and sensitivity in the MeerKAT-GPS means the images have high amounts of background emission and thus also have a significant amount of source confusion. The synthetic image, which lacks the same dynamic noise limitation that the MeerKAT images possess, is affected by noise only at low flux density. At higher values, it reaches and maintains a $\sim$100% completeness rate. At high SNR, the noise threshold is far lower than the injected source flux densities and therefore does not affect the source recovery.

6.1.3 False positives

I have quantified the likely false positive rate by running the Aegean source finder on fifteen of the zeroth moment 1.28 GHz MeerKAT maps and then inverting these maps and running the source finder on the inverted maps. The detections from the inverted maps represent false positives as we do not expect to detect 1.28 GHz continuum sources in absorption. This estimate is illustrated in Fig. 6.5; the blue histogram illustrates the detections from the native tiles (i.e. before inversion) and the red histogram illustrates the detections from the inverted tiles. The fifteen tiles used here have 109866 sources in the non-inverted images while 716 spurious sources were detected in the inverted images, therefore giving a false positive rate of 0.65%. Of the 716 spurious sources, 95% are below 14σ and 73% below 7σ. Fig. 6.5 shows isolated occurrences of false positives in high SNR upto $\sim27\sigma$, these occur because the noise is highly non-Gaussian as the images are very shallowly cleaned and contain negative bowls (see Fig. 6.6). The negative bowls appear as bright sources in the inverted maps due to the inversion, thus will not be detected in the native maps.
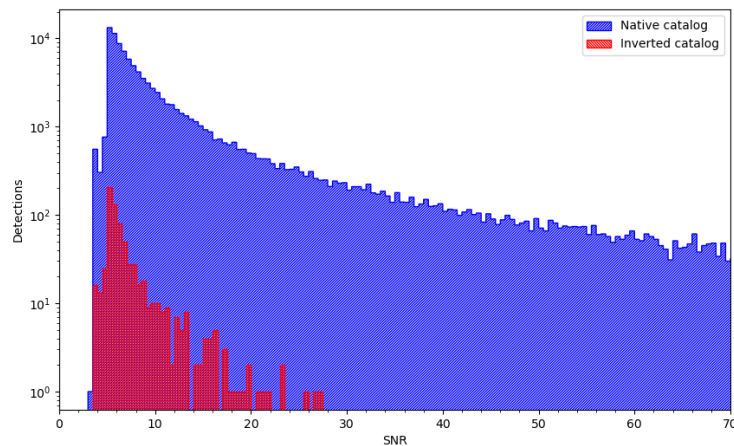
FIGURE 6.5: The likely false positive rate has been determined by running the Aegean source finder on the zeroth moment 1.28 GHz MeerKAT maps (illustrated by the blue histogram) and then inverting these maps and running the source finder on them. The detections from the inverted maps (illustrated by the red histogram) represent false positives as we do not expect to detect sources in absorption. Using a subset (15 tiles) of the full survey I determined 716 spurious sources in a pool of 109866, thus giving a false positive rate of 0.65%. Of the 716 spurious sources, 524 (73%) are below 7σ, and 682 (95%) are below 14σ.
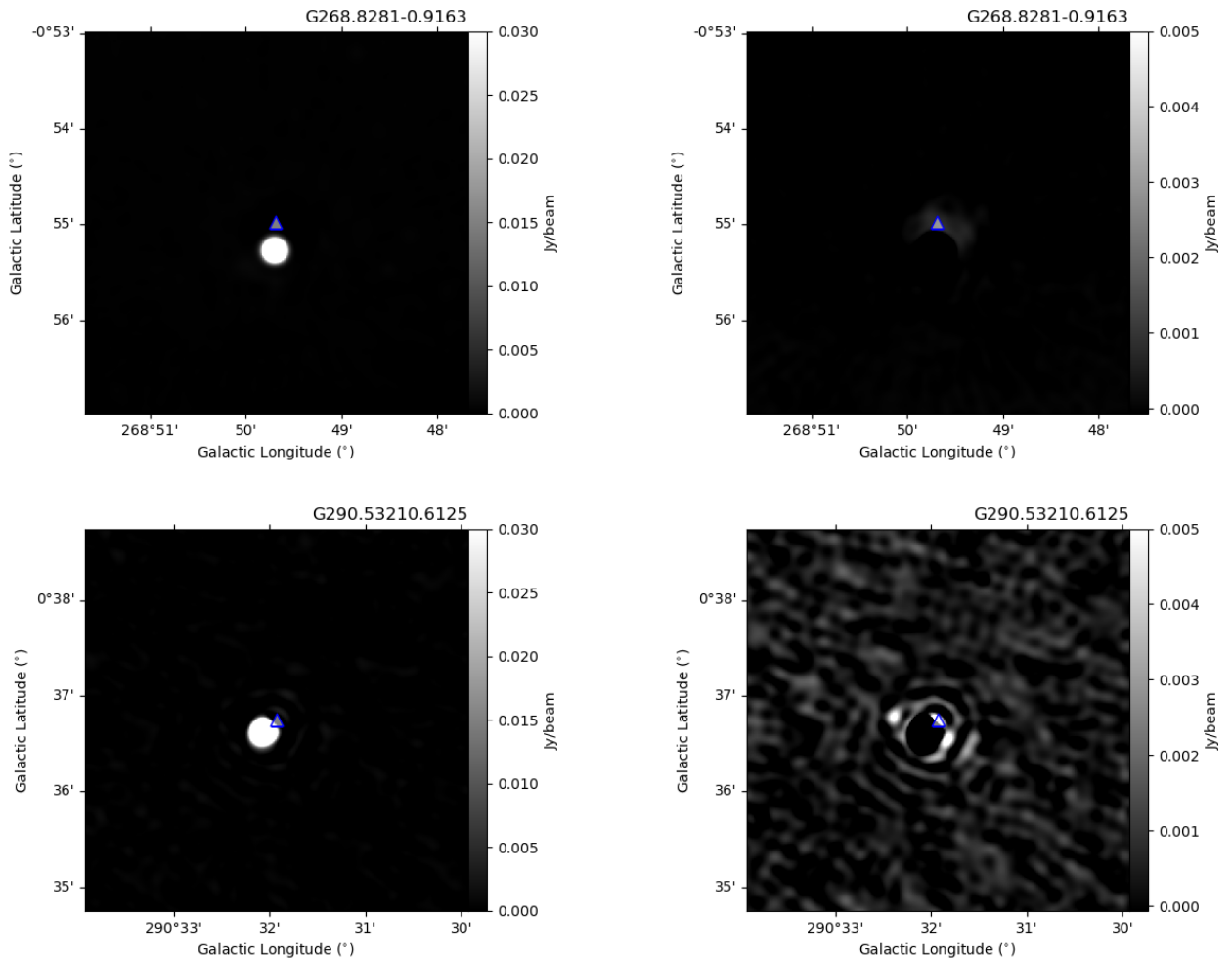
FIGURE 6.6: Examples of the negative bowls responsible for the isolated occurrences of high SNR detections in the inverted maps. Each row of images represents the same tile as a pair of standard and inverted maps. The images to the left show the source around which the negative bowls occurred, the images to the right show the negative bowls, made visible by the inverted maps. In both sets of images the blue triangles are source markers of the negative bowls.

6.2 The Catalogue

The MeerKAT-GPS catalogue contains 490790 sources, with a signal-to-noise $\geqslant 5\sigma$, extracted as described in § 6.1.1. An excerpt of the catalogue[1] is shown in Table 6.2. The data in these tables were extracted from images created from data cubes by calculating the zeroth moment (c.f. 2.2.1). The high sensitivity of the MeerkAT-GPS has produced high dynamic range images, thus some compact sources are part of larger complexes

---

[1]The full catalogue, which contains roughly half a million sources has not been included in this thesis but can be made available upon request

resolved into multiple components. The catalogue contains a total of 468310 source islands. Of these, 451415 have been detected as single components, 16895 have been detected as an island of 2 or more components, and 3520 as 3 or more.

TABLE 6.2: An excerpt of the MeerKAT-GPS point source catalogue. Column 1 is the source identifier, columns 2 to 5 are the flux densities and their errors. Columns 6, 8, and 10 are the major and minor axes of the FWHM, and the PA, and columns 7, 9 and 11 are their respective errors.

Source Galactic name	Peak flux density mJy beam^{-1}	error	Integrated flux density mJy	error	Major arcsecs	error	Minor arcsecs	error	PA (°)	error
G001.9117-1.3937	10.64	0.21	11.06	0.22	8.21	0.02	8.1	0.02	-76.04	0.95
G001.9654-1.3929	2.39	0.12	2.82	0.15	9.07	0.0	8.33	0.0	-89.59	0.45
G002.0383-1.3834	4.92	0.08	5.14	0.09	8.3	0.01	8.04	0.01	7.04	0.36
G002.0543-1.4148	1.37	0.09	1.49	0.1	9.19	0.07	7.57	0.05	74.88	0.27
G002.3564-1.4146	0.6	0.05	0.58	0.05	7.85	0.06	7.8	0.06	-76.64	9.19
G002.3652-1.3920	0.21	0.04	0.22	0.04	8.44	0.13	7.91	0.1	83.11	2.9
G002.3689-1.3904	2.04	0.04	2.23	0.04	8.53	0.02	8.2	0.01	-76.16	0.34
G002.4102-1.4157	0.26	0.05	0.43	0.08	12.72	0.32	8.45	0.13	-80.66	0.62
G002.4436-1.4076	5.86	0.04	6.43	0.05	8.78	0.0	7.99	0.0	-84.34	0.06
G002.4484-1.4186	0.29	0.05	0.21	0.03	7.14	0.11	6.4	0.08	-77.99	1.09
G002.4624-1.4038	1.34	0.04	1.36	0.04	8.09	0.02	8.06	0.02	-78.42	6.61
G002.4707-1.4243	0.55	0.05	0.67	0.06	9.27	0.04	8.47	0.04	7.34	0.6
G002.5038-1.3882	1.26	0.04	1.3	0.04	8.36	0.0	7.92	0.0	-88.84	0.38
G002.5289-1.4114	0.36	0.04	0.36	0.04	8.15	0.03	7.86	0.04	4.8	2.2
G002.5590-1.3978	1.81	0.04	2.48	0.05	10.88	0.03	8.06	0.02	-69.06	0.05
G002.6429-1.3918	0.35	0.04	0.36	0.04	8.17	0.05	8.1	0.05	-83.13	9.33
G002.6662-1.4199	0.26	0.05	0.34	0.07	10.59	0.16	7.88	0.34	10.77	0.45
G002.7274-1.3843	4.94	0.05	4.97	0.05	8.05	0.0	8.0	0.0	-86.87	0.93
G002.7379-1.3956	4.79	0.05	4.88	0.05	8.08	0.0	8.06	0.0	-81.69	2.81
G002.7393-1.4207	2.63	0.05	4.04	0.08	11.88	0.02	8.27	0.01	79.49	0.05
G002.8070-1.4071	0.33	0.05	0.6	0.1	14.82	1.03	7.9	0.3	-54.29	0.21
G002.8144-1.4218	0.51	0.06	0.69	0.08	9.28	0.01	9.25	0.01	-88.36	22.07
G002.8151-1.4086	0.39	0.06	0.45	0.06	9.24	0.05	7.94	0.04	-85.32	0.82
G002.8725-1.3885	1.14	0.05	1.32	0.06	8.78	0.01	8.46	0.01	-88.1	0.9
G002.9529-1.3829	0.41	0.05	0.62	0.08	11.11	0.22	8.76	0.13	-75.17	0.52
G002.9586-1.4071	0.56	0.06	0.61	0.06	9.36	0.05	7.51	0.04	-82.86	0.39
G003.0148-1.3874	0.36	0.05	0.47	0.07	9.44	0.2	9.06	0.19	-73.48	2.96
G003.1196-1.3900	0.65	0.05	0.79	0.06	9.2	0.04	8.44	0.04	-81.65	0.64
G003.1398-1.3992	1.4	0.05	1.47	0.05	8.37	0.0	8.01	0.0	-89.5	0.56
G003.3253-1.3886	0.37	0.05	0.66	0.1	11.82	0.13	9.6	0.2	10.63	0.47
G003.4514-1.3869	0.19	0.04	0.21	0.04	8.86	0.12	8.07	0.15	8.36	1.52
G003.5038-1.4229	0.66	0.04	0.76	0.05	8.73	0.04	8.42	0.04	10.07	1.15
G003.5449-1.3965	0.49	0.04	0.51	0.04	8.48	0.03	7.89	0.04	8.25	0.65
G003.6078-1.3809	0.23	0.04	0.26	0.06	10.03	0.5	7.26	0.94	-78.63	0.52
G003.6219-1.3846	0.2	0.04	0.2	0.05	7.97	0.82	7.71	0.7	18.98	4.64
G003.6550-1.4026	1.57	0.04	1.95	0.06	9.46	0.09	8.44	0.11	-86.47	0.18
G003.6856-1.3844	0.33	0.04	0.51	0.07	11.4	0.72	8.55	0.43	-1.47	0.23
G003.7397-1.4067	0.33	0.05	0.35	0.07	8.75	0.63	7.96	0.52	17.96	1.16
G003.8166-1.4029	0.77	0.06	0.78	0.07	8.42	0.22	7.65	0.25	-80.51	0.55
G003.8246-1.3947	0.32	0.06	0.52	0.13	10.6	0.92	9.84	1.52	-84.9	2.34
G003.8755-1.4225	0.83	0.06	1.0	0.09	9.03	0.27	8.61	0.29	-83.82	1.14
G003.8982-1.4213	1.7	0.05	4.23	0.14	15.13	0.07	10.53	0.11	5.9	0.07
G003.9017-1.4233	3.96	0.05	9.33	0.16	12.97	0.07	11.63	0.11	-82.46	0.11
G004.0277-1.3938	1.2	0.08	1.31	0.09	8.45	0.2	8.26	0.21	-74.58	1.95
G004.0510-1.4141	0.4	0.07	0.59	0.15	10.31	1.33	9.22	0.97	19.28	1.48

6.3 MeerKAT-SIMBAD associations

I have explored the nature of the sources by associating them to previously classified sources in the literature. Using a 10 arcsecond radius, I have crossmatched the catalogue sources with objects listed and classified in the SIMBAD database. Of the ∼497k sources in the MeerKAT-GPS catalogue, the query returned matches and therefore classifications for 13773 (see Table. 6.3), while no matches were found within 10 arcseconds for the remaining sources i.e. ∼97% of the MeerKAT-GPS sources are not identified in SIMBAD. The cross-reference resulted in a total of 116 distinct object types. The object types in SIMBAD are primarily defined with an emphasis on their physical nature rather than on a particular part of the electromagnetic spectrum or location in a particular cluster or galaxy. However, objects are classified based on emission (e.g. Radio, IR, Red, Blue, UV, X or gamma) when their physical nature cannot be conclusively determined. In the following subsection I will examine the nature of these associations more closely.

6.3.1 Matching statistics and classifications

The distribution of classifications, shown in Table 6.3, is dominated by stars and radio sources which account for ∼46% of the classifications. Candidate YSOs, IR sources, Pulsars, Bubbles, YSOs, HII regions, Planetary Nebulae, and Eclipsing Binaries account for the next ∼30%. These 10 object types account for ∼76% of the classifications, while the remaining 106 account for ∼24%. While these object types give an indication of what is detectable in the survey, they represent only ∼2% of the full catalogue, thus it would be unwise to speculate the distribution of object types in the full catalogue based on this.

Fig. 6.7 shows the underlying flux density distribution (grey histogram) overlaid with the flux density distributions of the SIMBAD classified sources (white hatched histogram) and the most dominant class of known objects, stars (black hatched histogram). The flux density distribution of known objects closely follows the underlying distribution at high flux density but falls off at low flux density. This shows that the majority of the brightest sources in the compact source catalogue are previously known while the majority of the unknown detections are of the fainter variety.

TABLE 6.3: Distribution of object types associated with the MeerKAT sources. The associations were achieved by cross matching the MeerKAT-GPS compact source catalogue with the SIMBAD database.

Otype 1	Count 1	Otype 2	Count 2	Otype 3	Count 3	Otype 4	Count 4
Star	3806	RGB*	43	post-AGB*	8		3
Radio	2533	RRLyr	39	PulsV*	8	TTau*	2
Candidate_YSO	789	Cl*	37	Symbiotic*	8	Candidate_SG*	2
IR	617	Candidate_WD*	35	Candidate_C*	7	Candidate_HMXB	2
Pulsar	576	WR*	33	HMXB	7	YellowSG*	2
Bubble	561	gamma	32	SNR	7	Orion_V*	2
YSO	475	C*	30	SB*	7	Blazar	2
HII	434	deltaCep	29	HH	7	gammaBurst	2
PN	352	Radio(cm)	28	Nova	6	Cepheid	2
EB*	320	Candidate_RRLyr	24	Assoc*	6	SG*	2
MIR	259	OpCl	23	SNR?	6	RotV*alf2CVn	2
Radio(sub-mm)	228	AGB*	21	S*	6	gammaDor	2
PN?	207	BlueSG*	21	Candidate_post-AGB*	6	V*?	1
MolCld	180	Candidate_EB*	20	Outflow	6	AGN	1
denseCore	170	Cl*?	20	LPV*	5	low-mass*	1
X	153	multiple_object	17	Possible_G	4	XB	1
Candidate_AGB*	135	**	17	Candidate_RSG*	4	GlCl	1
DkNeb	131	ISM	16	BLLac	4	Transient	1
FIR	126	Mira	15	HB*	4	Candidate_BSG*	1
OH/IR	125	RfNeb	15	PulsV*delSct	4	Candidate_Cepheid	1
EmObj	102	outflow?	15	LMXB	3	Candidate_Symb*	1
V*	99	PulsV*WVir	14	Blazar_Candidate	3	Possible_ClG	1
Galaxy	98	PartofCloud	13	HI	3	Candidate_WR*	1
Maser	90	EllipVar	10	ClG	3	CataclyV*	1
Candidate_LP*	89	Be*	10	RSCVn	3	SFregion	1
Em*	86	RedSG*	9	Eruptive*	3	ComGlob	1
Radio(mm)	82	Unknown	9	Seyfert_1	3	RadioG	1
PM*	75	RotV*	9	HIshell	3	QSO	1
NIR	74	Cloud	8	BYDra	3	Candidate_S*	1

I have found that ∼100% of the sources with flux densities above 10 Jy are known and ∼80% of the sources with flux densities above 100 mJy are known. On the other hand, the unknown detections peak below 1mJy. The histogram of stars, which represent the most dominant class in the classified sample, dominates the lower flux densities, thus representing the majority of known sources detected at low flux density. The underlying

flux density distribution shows a class of objects that peaks with flux densities below a mJy. These might not have been seen in the radio before because previous surveys have only been sensitive to around a mJy.
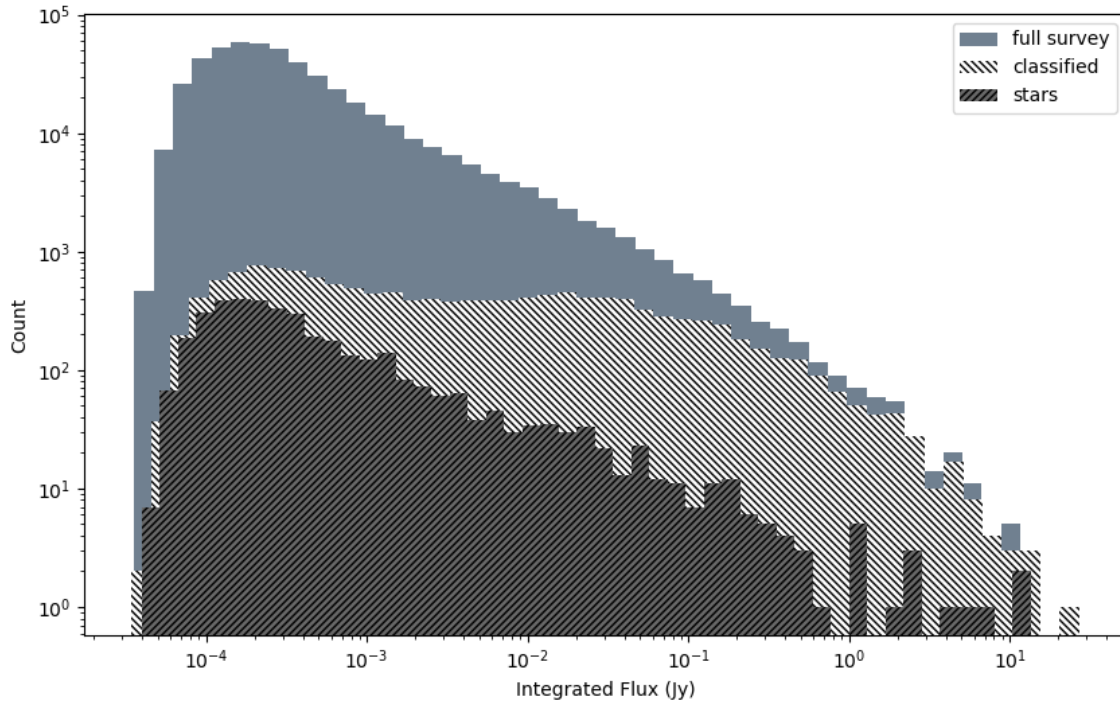
FIGURE 6.7: Integrated flux density distributions of the full survey, the collective SIMBAD classified sources, and the SIMBAD classified stars.

I have selected example sources (see Table 6.4) from the star, galaxy, SNR, PN, and HII region classes to show in Figs. 6.9 to 6.13. The selected sources illustrate the difference in morphology between object types as well as the difference in morphology between objects in the same classification. These have been presented in sections 6.3.1.2 - 6.3.1.6. Many of these sources will have been observed in multiple studies, however I have limited my discussion to their closest associations in SIMBAD.

6.3.1.1 Chance alignments
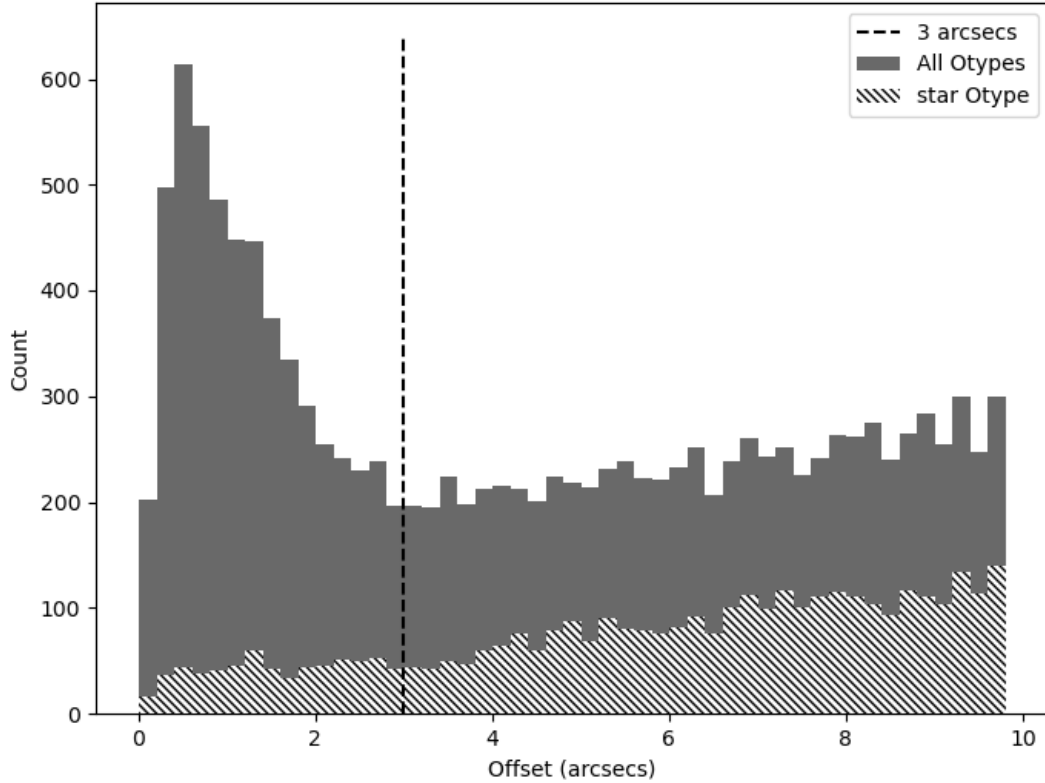
FIGURE 6.8: Positional offset between the MeerKAT-GPS sources and their respective SIMBAD associations. The solid-grey histogram represents the offsets in all the object types. The hatched histogram represents the offsets in the star object type associations.

The histogram in Fig. 6.8 shows the distribution of the angular distance between the MeerKAT-GPS sources and their respective SIMBAD associations. A true statistical association would have seen the histogram peaking around zero, with all the associations clustered around the peak. However, the histogram shows a peak in the distribution near zero that tails off at $\sim 3''$, above which the distribution is nearly flat out to the $10''$ cutoff. Therefore, this population is unlikely to comprise only true associations. There are 5408 associations with angular separation $< 3''$ and 8365 with angular separation $> 3''$. Thus, the majority of these associations are likely to be chance alignments with extragalactic sources along the line of sight. This is particularly true for the star object type, for which there are 3806 associations, of which only 640 have angular separation $< 3''$ and therefore more likely to be real. Increasing the radius in a random sample results in

increasing the number of matches. This behaviour is seen in the large angular distances in Fig. 6.8. Therefore, everything closer than $3''$ is more likely to be a true association, and everything farther than $3''$, a chance alignment.

I have used an extragalactic count at the same frequency to estimate the number of chance alignments expected in this population. At 1.28 GHz, source counts above 50μJy were estimated at about 2200 sources per square degree (Norris et al. 2011 and the references therein). Based on the area of the MeerKAT-GPS, I expect 60% of the sample to be background galaxies.

TABLE 6.4: Some sources from the MeerKAT-GPS catalogue matching SIMBAD star, galaxy, HII region, Planetary Nebulae, and supernova remnant classifications. Matching images are presented in the following subsections.

Source	Observed Flux Density		Nearest SIMBAD ID	Angular Dist.	Otype
Galactic name	Peak (Jy beam^{-1})	Integrated (Jy)			
G251.3719+0.9019	4.31	4.93	2MASX J08143768-3305480	0.64	Galaxy
G255.6242+0.8023	2.23	15.59	2MASX J08255863-3639240	0.91	Galaxy
G256.3912+0.9058	0.81	2.74	ESO 370-15	6.61	Galaxy
G266.1810+0.3253	1.6	1.52	ZOA J085828.676-451630.99	0.52	Galaxy
G006.5521-0.0959	144.77	1775.28	[WC89] 006.55-0.10A	1.13	HII
G008.4323-0.2763	10.19	95.82	HRDS G008.432-00.276	2.81	HII
G007.2535-0.0741	3.38	96.06	HRDS G007.254-00.073	4.41	HII
G021.5026-0.8831	131.2	771.86	RFS 324	9.98	HII
G049.5858-0.3848	73.99	1672.81	[KJB2003] G49.586-0.385	1.66	HII
G338.5911+0.0202	29.81	694.54	IRAS 16378-4612	9.80	HII
G358.5997-0.0583	30.32	42.73	JaSt 37	0.50	PN
G040.3725-0.4761	7.5	28.54	PN A66 53	8.44	PN
G038.9319-0.3857	2.32	45.05	PN HaTr 12	2.48	PN
G029.0782+0.4517	10.66	81.99	PN A66 48	9.11	PN
G310.8739-0.5394	12.37	75.47	GRS G310.80 -00.40	2.95	SNR
G336.9085-0.1624	26.41	418.28	SNR G336.9-00.2	1.22	SNR
G274.0142-1.1425	81.59	259.02	SNR G274.0-01.1	3.61	SNR
G011.9452-0.0368	208.1	803.26	SNR G012.0-00.1	1.22	SNR
G307.5991-0.3806	4.81	4.52	Gaia EDR3 5865264307889498240	4.25	Star
G038.1276+0.5338	2.96	3.06	TYC 457-92-1	9.54	Star
G050.0015+1.1149	4.95	5.25	Gaia DR2 4320874165090587008	4.92	Star
G267.2925+0.3886	2.76	2.91	TYC 8165-861-1	9.36	Star
G298.5362-0.0602	4.42	4.98	TYC 8978-2300-1	0.63	Star
G348.1881+0.6032	9.69	10.96	2MASS J17113985-3826078	7.41	Star

6.3.1.2 Stars

Stars are among the most compact sources I will detect in the survey. According to the small portion of classified sources presented in Table 6.3, they are also likely to be the most prevalent object in the MeerKAT-GPS catalogue. I therefore expect to see them presented in a wide array of configurations. In Fig. 6.9, I show stars in this catalogue that have been identified through previous studies recorded in the literature. G038.1276+0.5338, G267.2925+0.3886, and G298.5362-0.0602 are presented in the Tycho-2 catalogue (Høg et al., 2000) which contains 2.5 million of the brightest stars. G050.0015+1.1149, G307.5991-0.3806 are presented in Gaia DR 2 (Gaia Collaboration et al., 2018), and G348.1881+0.6032 in the 2MASS All Sky Catalogue of point sources (Cutri et al., 2003).

G267.2925+0.3886 (left image in the middle row of Fig. 6.9) is identified in SIMBAD as a star, however, its morphology is more consistent with a galaxy.
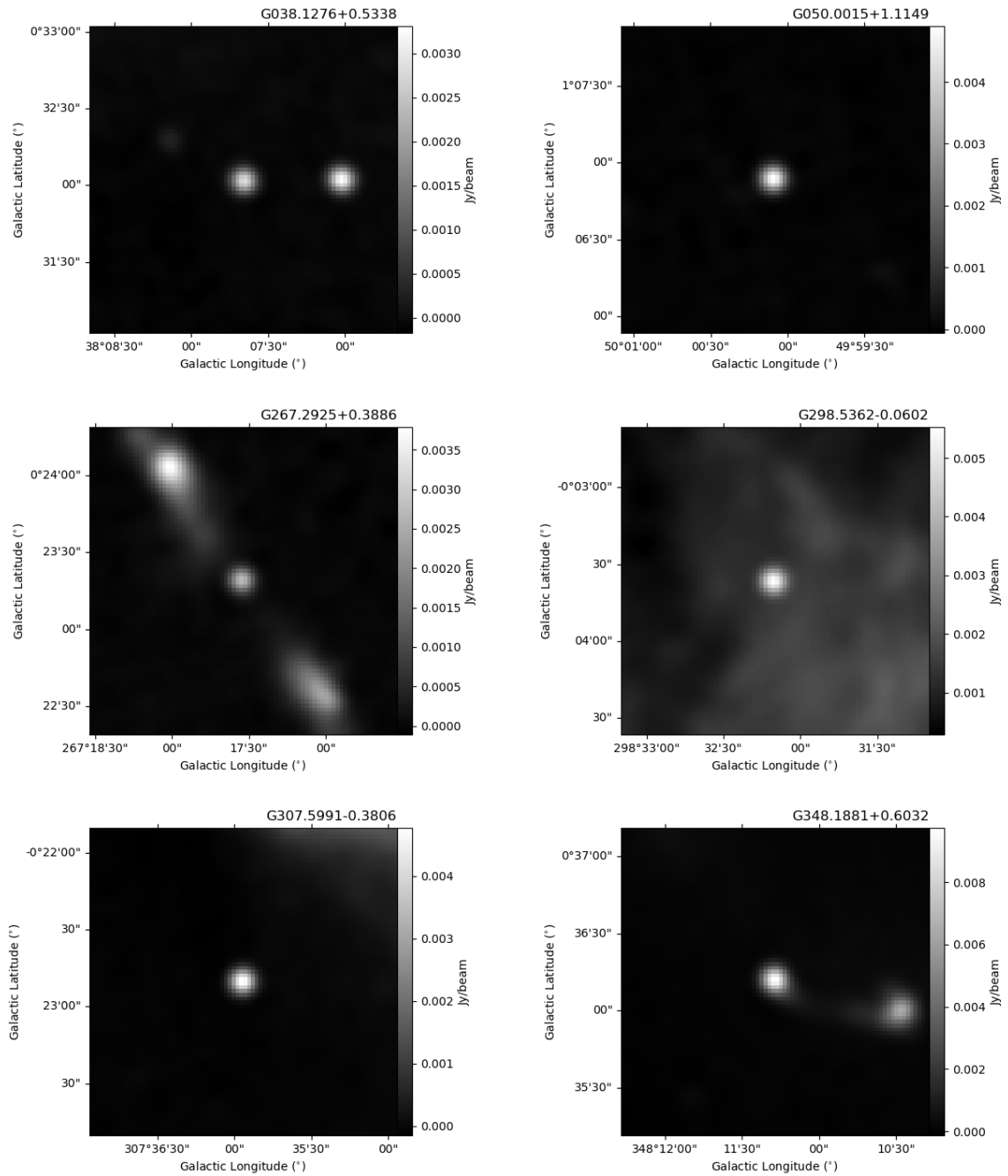
FIGURE 6.9: Example images of sources in MeerKAT associated with stars in the SIMBAD database.

6.3.1.3 Galaxies

Among the sources the survey is sensitive to are background galaxies. In the crossmatch with the SIMBAD database, I have found 98 sources matching a listed galaxy. Fig. 6.10 shows a few examples of the galaxies detected in the MeerKAT-GPS. G251.3719+0.9019,

G255.6242+0.8023, and G256.3912+0.9058 were observed in the Two Micron All Sky Survey (2MASS: Skrutskie et al. 2006) and G266.1810+0.3253 in Said et al. (2016)
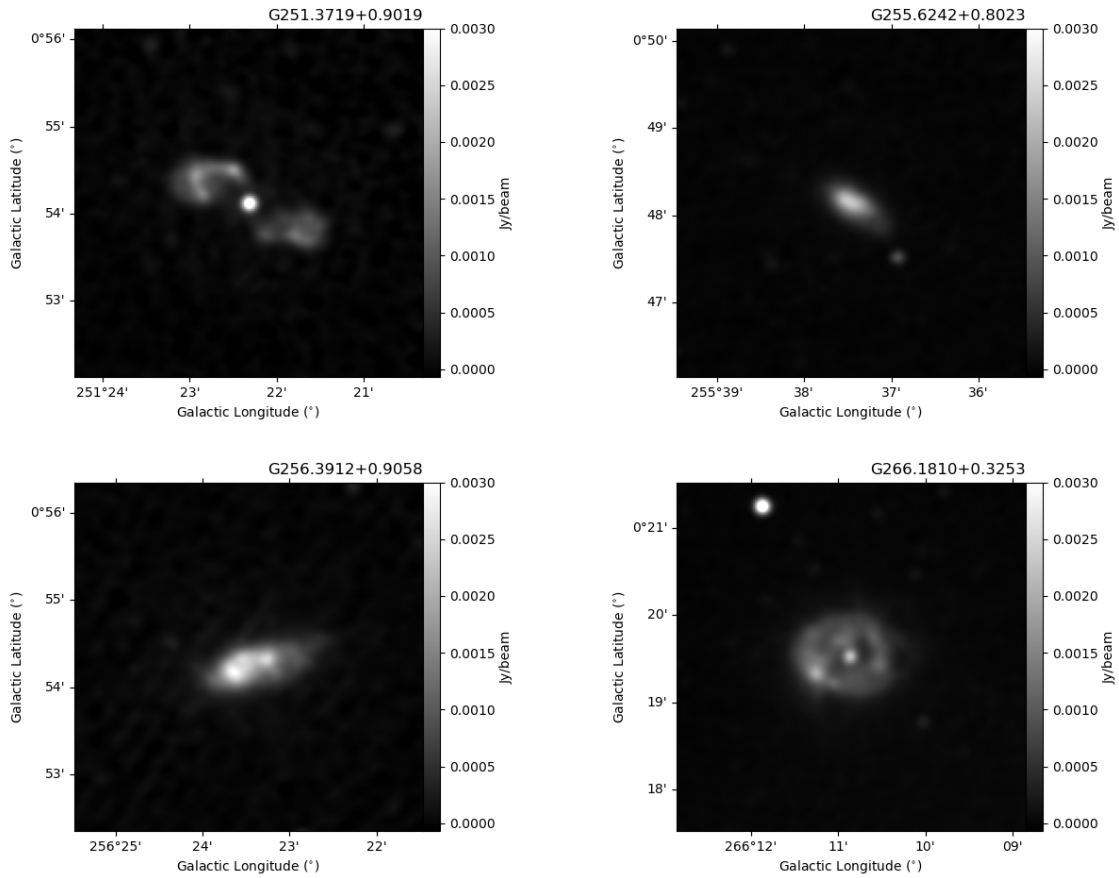
FIGURE 6.10: Example images of sources in MeerKAT associated with galaxies in the SIMBAD database.

6.3.1.4 Supernova remnants

The supernova remnant (SNR) class was not as prevalent in the search as the aforementioned classes. The source detection here was aimed at identifying compact sources, therefore because most SNRs are extended it follows that very few have been extracted. With the constraints used, I have found 7 SNRs and 6 candidate SNRs. The images in Fig. 6.11 are example imges of the SNR morphologies detectable in this survey drawn from the pool of classified SNRs in Table 6.10: G011.9452-0.0368, G274.0142-1.1425, and G336.9085-0.1624 are presented in Green (1984) and G310.8739-0.5394 in Andersen et al. (2011).
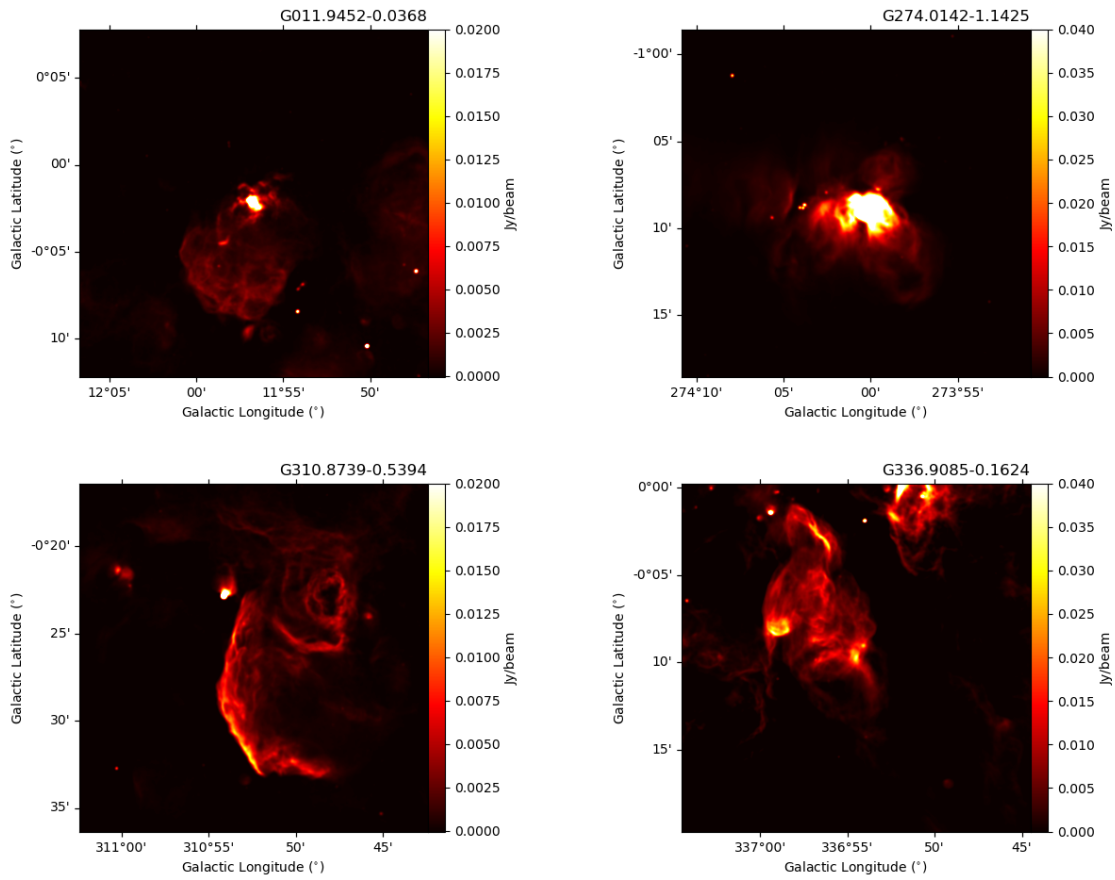
FIGURE 6.11: Example images of sources in MeerKAT associated with SNRs in the SIMBAD database.

6.3.1.5 Planetary Nebulae

The planetary nebulae (PN) class is one of the more prevalent matches between the MeerKAT-GPS and the SIMBAD database - 352 MeerKAT sources were found to be associated with PN in the literature. Fig. 6.12 shows example PN images of sources identified in the match. In the literature, these sources have been seen presented and discussed in Cutri et al. (2003) who present G358.5997-0.0583, Abell (1966) who present G040.3725-0.4761 and G029.0782+0.4517, and in Hartl and Tritton (1985) who present G038.9319-0.3857.
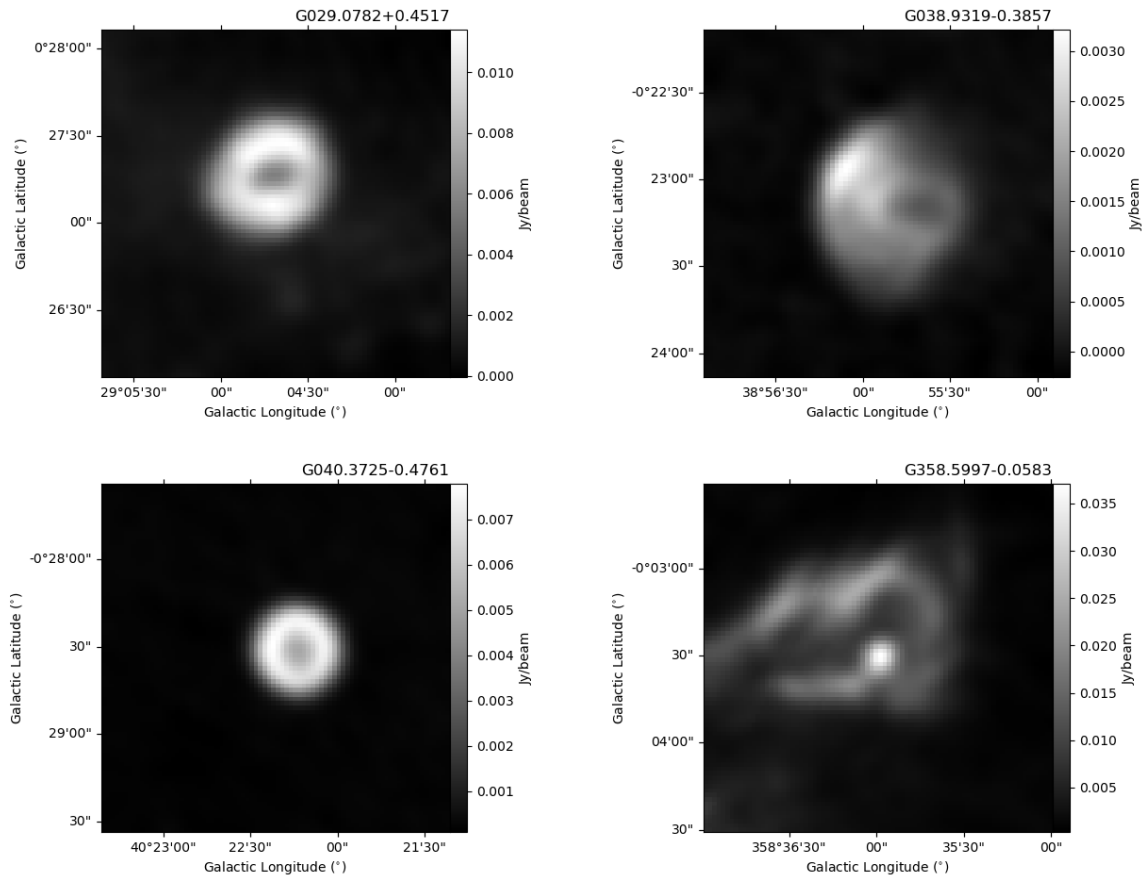
FIGURE 6.12: Example images of sources in MeerKAT associated with Planetary Nebulae in the SIMBAD database.

6.3.1.6 HII regions

The crossmatch between SIMBAD and the compact source catalogue associated 434 classified HII regions with MeerKAT-GPS sources. Examples of these sources are shown in Fig. 6.13. These have been chosen to highlight the different morphologies of the HII regions detected in the survey. G006.5521-0.0959 is an HII region complex in Wood and Churchwell (1989b); G007.2535-0.0741 and G008.4323-0.2763 are presented in Anderson et al. (2011); G021.5026-0.8831 is an HII region in Reich et al. (1984); G049.5858-0.3848 is an HII region in Kolpak et al. (2003); and G338.5911+0.0202 is an HII region in Porras et al. (2003).
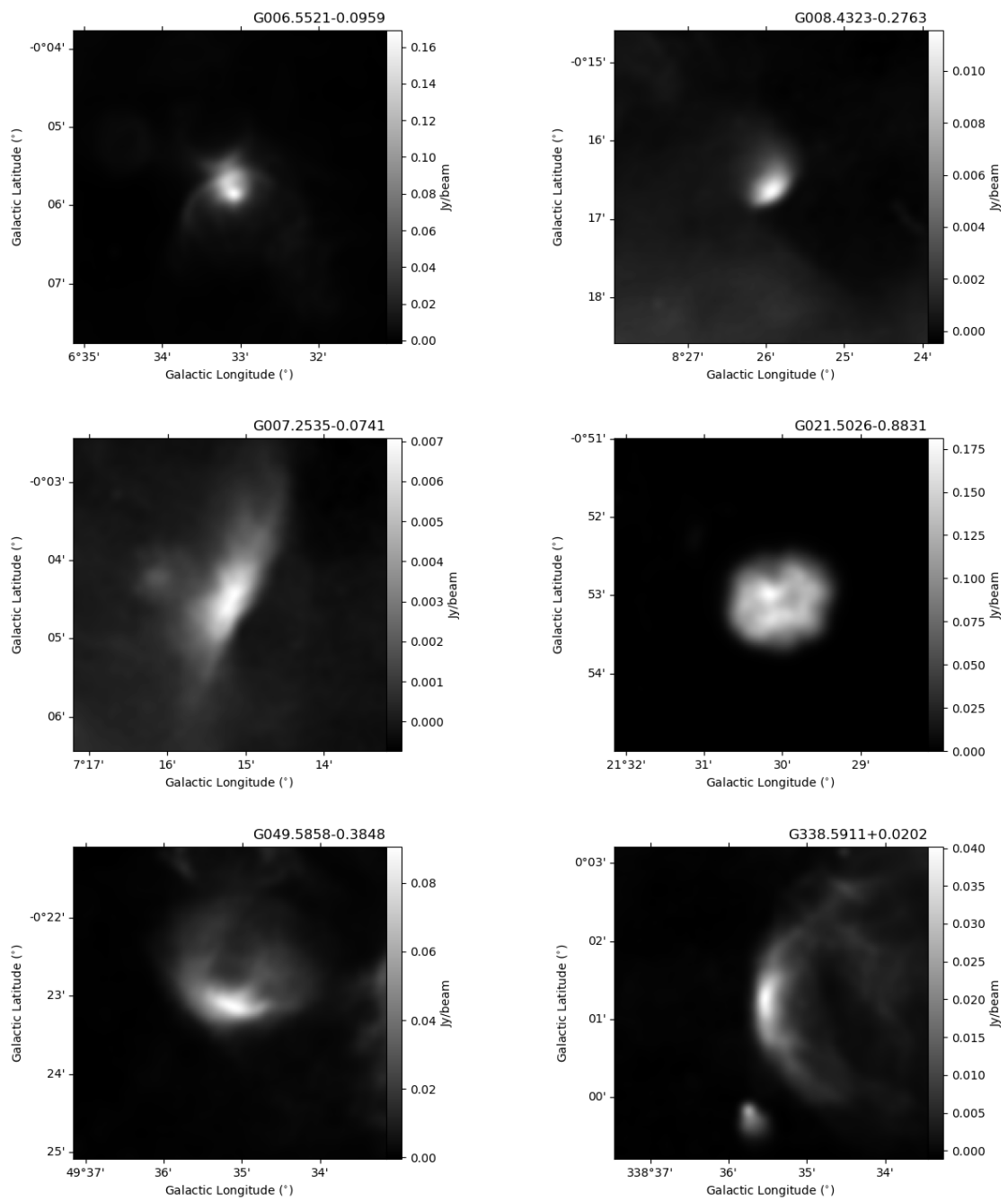
FIGURE 6.13: Example images of sources in MeerKAT associated with HII regions in the SIMBAD database.

6.4 Extended envelopes/halos around Ultracompact HII regions

Ultracompact (UC) HII regions can be defined as small, dense, ionised regions (Kim and Koo, 2001) and can be characterised as having electron densities $\gtrsim 10^4$ cm^{-3}, emission measures $\gtrsim 10^7$ pc cm^{-6}, and diameters $\gtrsim 0.1$ pc (Wood and Churchwell, 1989b).

Wood and Churchwell (1989b) present evidence that the UC HII region phase of a massive star overlaps significantly with its main-sequence lifetime. They find that the total number of UC HII regions in their (incomplete) sample of the Galactic Plane is inconsistent with the lifetime of an UC HII region ($< 3 \times 10^4$ years), which is the length of time it would take a typical object to expand to angular scales undetectable by the VLA. The evidence presented in Wood and Churchwell (1989b) is indicative of some mechanism placing constraints on the expansion of the HII region (e.g. infall of surrounding material or star motion) thus suggesting that their typically small size may not necessarily mean that UC HII regions are extremely young. Kim and Koo (2001) suggest that the small sizes of UC HII regions may be due to the insensitivity of baselines of a certain range to structures that exceed a particular angular scale. They base this on the Koo et al. (1996) VLA D array observations in which a known UC HII region was found to be an HII region complex containing sub structures of varying scales, including an ultracompact core, a compact core and an extended halo. This implies that the UC HII region may actually be older than 10^4 years.

Kim and Koo (2001) looked at 16 known UC HII regions to find associated extended emission. For this they carried out targeted 21 cm radio continuum observations, using the VLA (DnC array), towards these 16 objects. This sample of UC HII regions was drawn from the Wood and Churchwell (1989b) catalogue and comprises objects with simple morphology and large ($\gtrsim 10$) ratios of single-dish to VLA flux densities. They detected extended emission toward all 16 sources, embodying one to several compact components and an extended envelope. By computing the single dish to VLA flux density ratios of UC HII regions in other studies, they found that it is not uncommon for UC HII regions to be associated with extended emission. Their study shows the observed UC HII regions existing as ultracompact cores of more extended HII regions, thus implying their actual ages far exceed their dynamical age ($\lesssim 10^4$ yr). They present

a simple model that supports the coexistence of ultracompact, compact and extended components and places their lifetime at $> 10^5$ yr, effectively providing a solution to the age problem. This model explains how structures with different length scales can coexist for a long time by combining the champagne flow model with the hierarchical structure of massive star-forming regions. It suggests that the density-diameter relationship of HII regions ($n_e \propto D^{-1}$) is a result of hierarchical structure.

Kurtz et al. (1999) carried out a 3.6 cm radio continuum survey, using the VLA (D array), to search for extended emission around UC HII regions. They looked at 15 randomly selected UC HII regions and found extended emission in 12 of the 15 fields. This sample is drawn from the sources detected at 3.6 cm (using the VLA in B array) of the Kurtz et al. (1994) observations towards 59 *IRAS* sources that have densities ≥ 1000 Jy at 100 μm and far-IR colours consistent with UC HII regions as outlined in the Wood and Churchwell (1989a) criteria. Of the 12 objects associated with extended emission, they find it likely that 8 are directly connected to the ultracompact emission. This result has important implications because the presence of extended emission is relevant to the "age problem" for ultracompact HII regions (Wood and Churchwell, 1989b). A direct connection to extended emission means the current definition of UC HII regions was based on an incomplete picture and implies the definition needs to be reconsidered to account for and include these less dense, more extended regions to the picture (Kurtz et al., 1999)

While the Kim and Koo (2001) and Kurtz et al. (1999) studies were highly successful in finding extended emission associated with the UC HII regions in their samples, their studies were both quite possibly biased. In both cases the samples were drawn from the Wood and Churchwell (1989a) survey whose target list was a selection of strong compact sources from previous single dish surveys, and Kurtz et al. (1994) which includes only fields with 100 μm flux densities greater than 1000 Jy - a sample representing the brightest 20% of IRAS-selected UC HII region candidates (Wood and Churchwell, 1989a) and the brightest 40% of IRAS and radio continuum selected candidates (Becker et al., 1994). Moreover, Kurtz et al. (1999) note this bias and suggest that looking into the problem using a survey without this bias would be worthwhile.

This study improves on the question because Kim and Koo (2001), and Kurtz et al. (1999) were limited in the number of UC HII regions that they could observe using the

VLA (DnC and D array, respectively), and their hypotheses are based on a samples of 16 and 15 UC HII regions, respectively. The MeerKAT-GPS provides a much larger sample on which to test this. Therefore, in a similar manner, I have looked at HII regions observed at 5 GHz and compared them to their counterparts in the 1.28 GHz MeerKAT-GPS survey in search for extended emission that would not have been seen in the 5 GHz observations but are visible at 1.28 GHz.

6.4.1 MeerKAT-GPS associations with UC HII region samples from Urquhart et al. 2013 and Djordjevic et al. 2019

Using the catalogues presented in Urquhart et al. (2013) and Djordjevic et al. (2019), I crossmatched the MeerKAT-GPS sources against known UC HII region samples and found 375 matches. However, 25 sources in the UC HII region samples have no diameter listed, thus reducing the eligible matches to 350. The observed parameters in these samples are derived from the RMS survey (Urquhart et al., 2007, 2009a) which comprises observations from the CORNISH survey as well as targeted observations carried out on the Australia Telescope Compact Array (ATCA) and the Very Large Array (VLA). The synthesized beam in all of these 5 GHz observations is comparable at $\sim 1''\!.5$ and the MeerKAT-GPS, observed at 1.28 GHz, has a resolution of $8''$. The MeerKAT-GPS has much better uv coverage than ATCA and the VLA, and is therefore better at detecting and showing the largest angular scales. Comparing the sizes of UC HII regions in Urquhart et al. (2013) and Djordjevic et al. (2019) with their counterparts in the MeerKAT-GPS will highlight any extended emission present, thus giving support to the hypothesis that the UC HII region is considerably older than 10^4 years. A direct comparison shows that the angular diameters of the MeerKAT-GPS sources are predominantly larger than those in the 5 GHz samples (Fig. 6.14: top). I have, however, taken into account the disparity in beam sizes and convolved the 5 GHz sources with an $8''$ beam to match the resolutions. I have assumed a simple convolution of the $8''$ Gaussian beam using the relation $\Theta_{obs}^2 = \Theta_{beam}^2 + \Theta_{source}^2$. This has resulted in an increase in the 5 GHz angular diameters thus shifting the comparisons shown in Fig. 6.14 closer to the line of equality. However, as seen in Fig. 6.14: bottom, the comparison still shows the MeerKAT-GPS sources as being larger. Of the 350 matches, 133 have a diameter at least 20% larger, and 32 have a diameter at least twice that of their RMS counterpart (see Fig. 6.15).
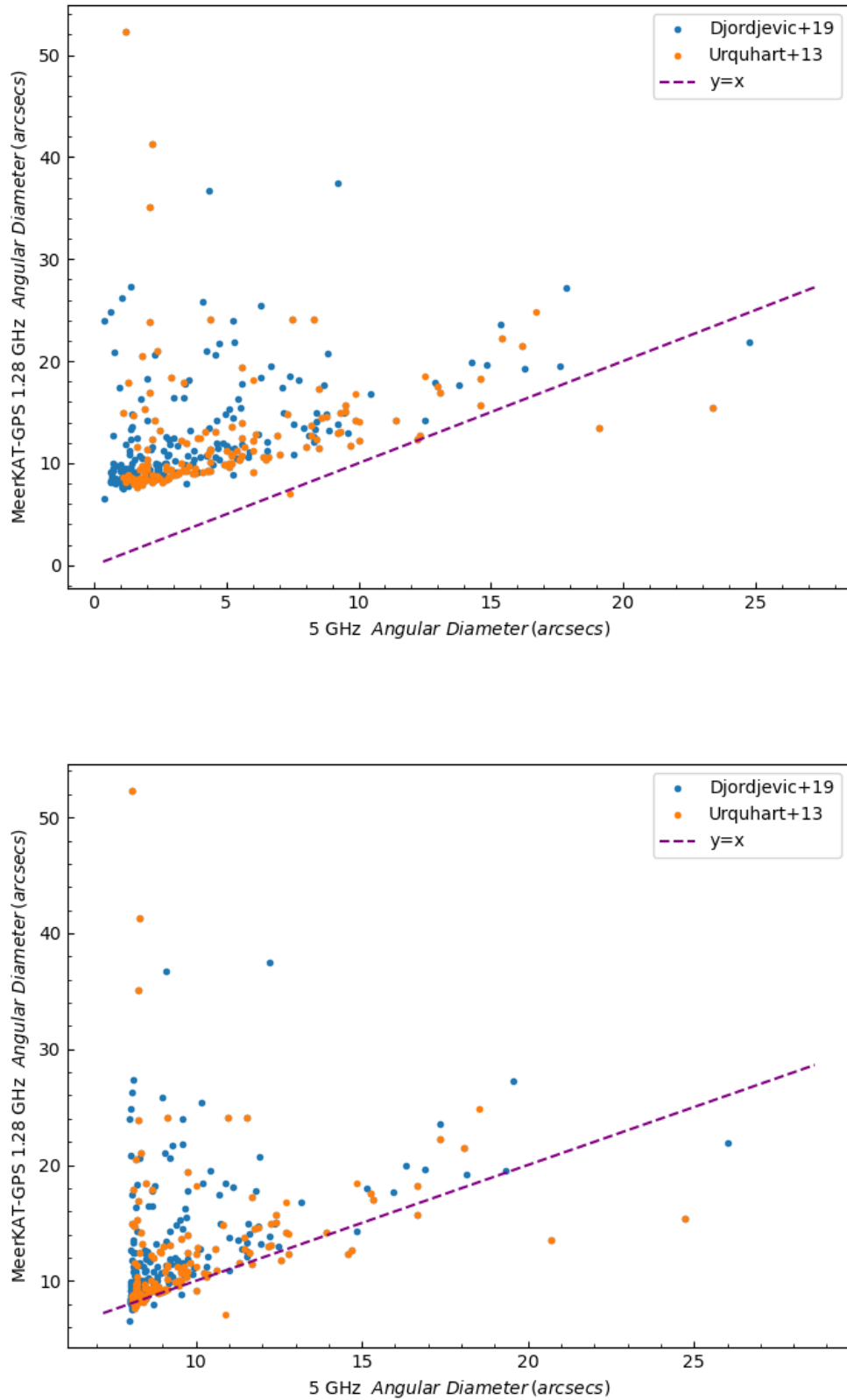
FIGURE 6.14: Comparison of angular diameter between MeerKAT-GPS sources and the Urquhart et al. (2013) and Djordjevic et al. (2019) UC HII region samples. The purple dashed line is the line of equality. The top shows the comparison with the 5 GHz sources at their native resolution, and on the bottom is a comparison with the 5 GHz sources convolved to MeerKAT's 8″ beam.
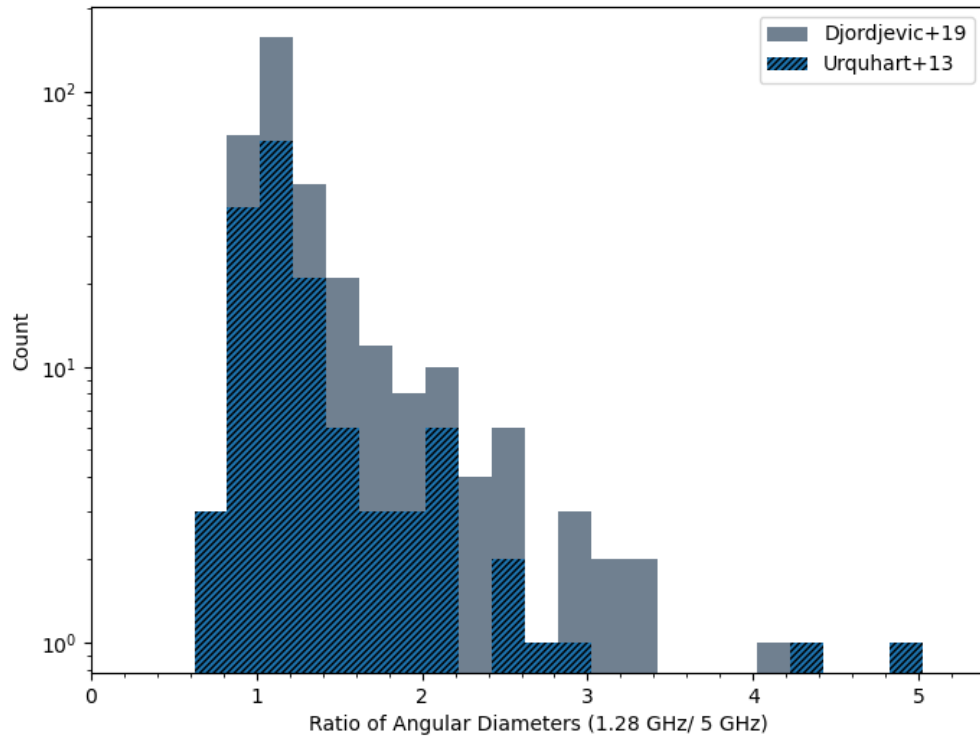
FIGURE 6.15: Histogram of the ratio of the MeerKAT-GPS sizes to the corrected RMS sizes. The plot shows the distribution of the size ratio of 350 1.28 GHz sources to their 5 GHz counterpart. Of the 350 pairs, 133 are at least 20% larger, and 32 are at least double in size.

6.4.2 Contour plots of MeerKAT-GPS & 5 GHz UC HII regions

I have randomly selected 10 HII regions from the Urquhart et al. (2013), Djordjevic et al. (2019) 5 GHz UC HII region samples to shows as images and highlight associated extended emission. Images of the UC HII regions are presented as 1.28 and 5 GHz contour plots overlaid on the MeerKAT-GPS colour-scale in Fig. 6.16.
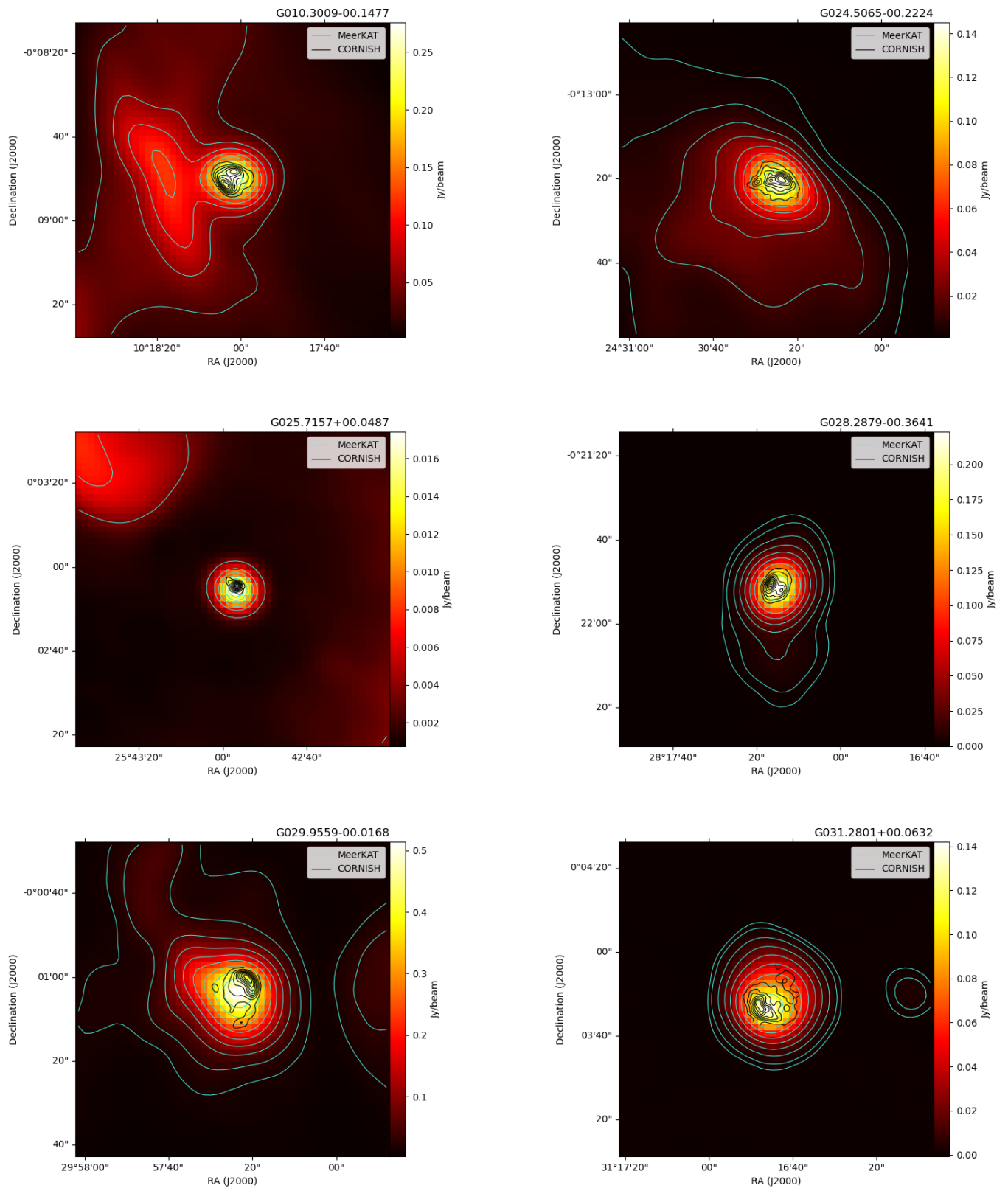
FIGURE 6.16: Contour plots of MeerKAT-GPS sources and 5 GHz UC HII regions Urquhart et al. (2013), Djordjevic et al. (2019) overlaid on the MeerKAT-GPS colour scale.
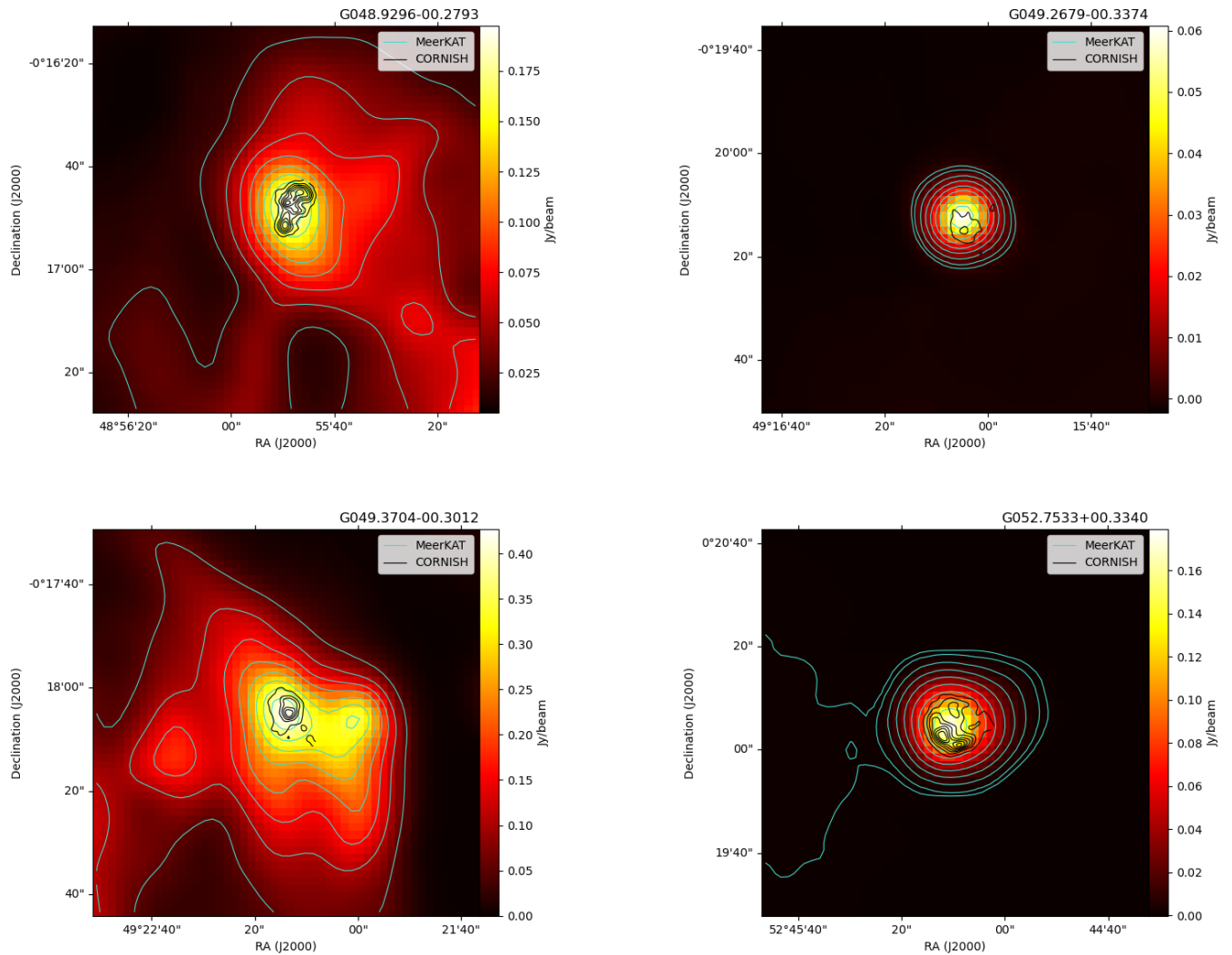
FIGURE 6.16: Continued.

In all of the examples I have shown, the 5 GHz emission is embedded in the more extended 1.28 GHz emission and coincides with its peak. The colour scale (1.28 GHz) shows varied component-envelope configurations. G049.2679-00.3374, G031.2801+00.0632, and G049.2679-00.3374 have simple spherical morphologies. In fact, it is more than likely that for sources like G049.2679-00.3374, there is a resolution effect: MeerKAT-GPS sees an unresolved source and at 5 GHz the source is resolved. However, this is accounted for in the beam correction. G028.2879-00.3641 and G052.7533+00.3340 are elongated and are likely to be accelerating in the direction opposing their tails. G010.3009-00.1477, G024.5065-00.2224, G029.9559-00.0168, G048.9296-00.2793, and G049.3704-00.3012 have complex morphologies portraying the three part configuration of structures with different length scales whose coexistence Kim and Koo (2001) resolved with

their champagne flow-hierarchical structure model. These sources have an ultracompact component coinciding with the UC HII region contours, a compact component and extended halos. Kurtz et al. (1999) determine which ultracompact components are likely to be directly connected to the extended emission associated with them by analysing their morphologies. Here, being directly connected means the same source of ionised gas is responsible for both classes of emission. They argue that a continuous unbroken structure from the UC HII region to the extended emission means it is likely that they are directly connected. However, if anywhere in the structure of emission it falls off to near zero, it is unlikely they are directly connected. The halos in my sample all appear to be seamless structures of emission thus, following the Kurtz et al. (1999) treatment, these are directly connected to the ultracompact components they encompass. While G049.3704-00.3012 coincides with a single UC HII region from the 5 GHz sample, the 1.28 GHz emission shows it as having two peaks. The stronger peak coincides with the 5 GHz contour and is therefore the more likely tracer of the star maintaining the ionisation of the region. Evidently, this subsample predicts a wide range of component configurations and indicates the expected range of morphologies in the full sample.

Kim and Koo (2001) show through 11cm single-dish to VLA (S_{SD}/S_{VLA}) flux density ratios that most known UC HII regions are associated with extended emission. They determine flux density ratios for 30 UC HII regions from Wood and Churchwell (1989b) and find 70% of them with ratios greater than 5, with the caveat that these ratios might be underestimated since UC HII regions are optically thick at 11 cm. They also predict a bias in the results as a consequence of the selection effects in the Wood and Churchwell (1989b) survey. They followed this up with flux density ratios of 22 simple UC HII regions from Kurtz et al. (1994) and obtained a similar result. The flux density ratios of the 12 (of 15) sources in Kurtz et al. (1999) with extended emission were $\gtrsim 10$ for $\sim 80\%$ of the 12. However, it is worth noting that these are all samples that are affected by the biases discussed in § 6.4. In Fig. 6.15, I show the distribution of the ratio of the angular diameters of MeerKAT-GPS sources to corrected angular diameters of RMS UC HII regions. In Fig. 6.17, I show the distribution of the flux density ratios of MeerKAT-GPS to RMS. About a third of the sources are at least 20% larger than previously thought, and about a third of the sources have flux densities at least twice their previous values. Therefore this study, which is unaffected by the aforementioned biases, estimates a less extreme number ($\sim 1/3$) of UC HII regions as being directly connected to extended
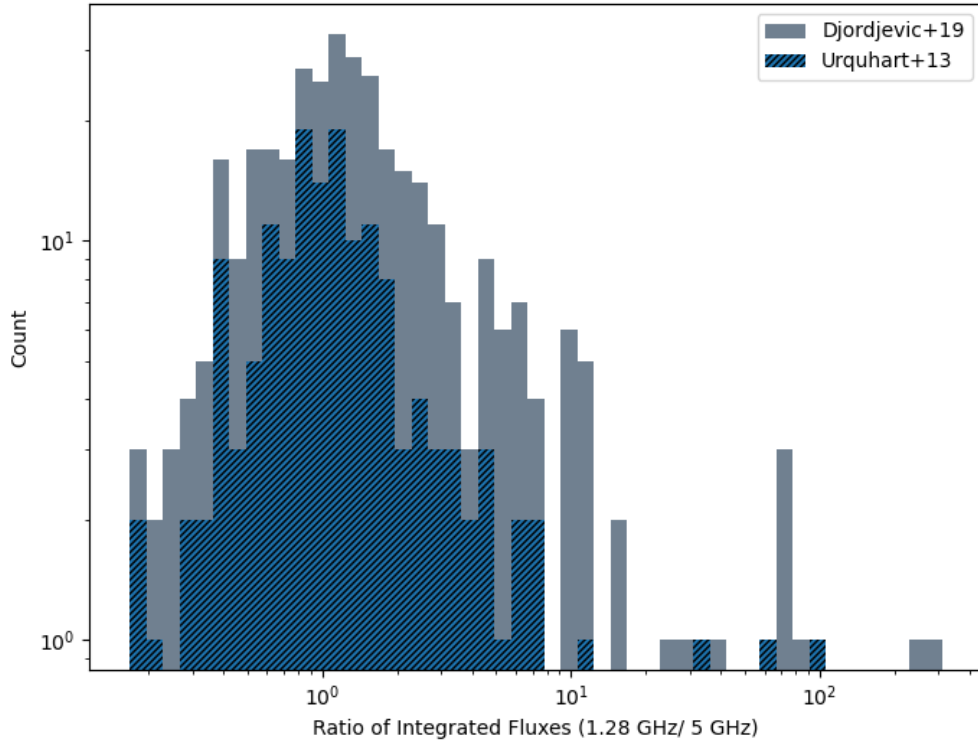
FIGURE 6.17: Distribution of flux density ratios of 350 1.28 GHz sources to their 5 GHz counterpart. Of the 350 pairs, 181 are at least 20% larger, and 96 are at least double in flux density.

emission.

6.5 Summary

i). I have presented a compact source catalogue created from the 1.28 GHz MeerKAT-GPS images and the method used to develop it. The catalogue contains 490790 compact sources, with a signal-to-noise ratio of 5σ or greater. The completeness simulations, carried out on 6 representative tiles, recovered $\sim 90\%$ of the sources with peak flux densities ≥ 2.4 *mJy beam^{-1}*, and $\sim 95\%$ of the sources with peak flux densities ≥ 0.2 *mJy beam^{-1}* in the least and most complete tiles, respectively. Fifteen representative tiles were used to estimate the likely false positive rate, where 716 spurious sources were found in a pool of 109866, thus giving a false positive rate of $\sim 0.65\%$.

ii). I explored the nature of the sources in the 1.28 GHz MeerKAT-GPS compact source catalogue, by associating them with sources in the literature. The SIMBAD database provided 13773 classifications ($\sim 2\%$ of the catalogue) with a total of 116 distinct object types. The flux density distributions of the survey and the known sources showed that the percentage of known sources is $\sim 100\%$ for sources with flux densities above 10 Jy, and $\sim 80\%$ for sources with flux densities above 100 mJy. Therefore, the population of unknown sources is dominated by fainter emission.

iii). The flux densities at the two frequencies presented here are broadly comparable. I identified extended emission in some of the sources, thus supporting the hypotheses of Kim and Koo (2001) and Kurtz et al. (1999). However, I have determined a less extreme estimate for the number of UC HII regions associated with extended halos - I have found this to be around a 1/3 as opposed to $\sim 8/10$ in Kim and Koo (2001); Kurtz et al. (1999). Clearly, there is evidence that some of the UC HII regions are older based on the extended halos I found. But extended halos do not solve the problem for all HII regions because part of my sample has flux density/size ratios of ~ 1. This implies that some HII regions will be as old as the standard estimates say they are, around 10^5 years, while some will be older. A third of the UC HII regions have extended components, this means a third are older than the age in Wood and Churchwell (1989b). Therefore since most UC HII regions do not have extended components, we cannot rely entirely on extended components to explain the large number of observed UC HII regions.

Chapter 7

Conclusions

The overall goal of this thesis was to study young HII regions, looking for their earliest components in order to understand how they form and evolve. This was in order to understand the environments and conditions in which massive stars are born. In KuGARS my aim was to detect and identify HC HII regions. In SASSy, my aim was to find radio counterparts to molecular clumps that showed potential for massive star formation in the Outer Galaxy. In MeerKAT-GPS, my aim was to look for extended emission around UC HII regions and attempt to address the "age problem". Technological advancements in radio interferometers have made it possible to investigate these topics in ways that were previously impossible. In the following sections I present a summary of the technical and science results of each chapter followed by the main conclusions and lastly potential for future work.

7.1 Summary

In Chapter 3 I detailed the data reduction process involved in the KuGARS survey, showing the methods I have developed to circumvent the hurdles presented by the large volume of data. The imaging process outlined shows the steps taken on subsets of the data to build a robust imaging method which was later applied to the full dataset. The size of the data meant imaging a complete scheduling block as a single map was untenable, thus each block was subdivided into 18 overlapping cutouts. The imaging strategy was also designed to take into account the science goals, which include measuring SEDS.

Therefore, a common restoring beam was imposed on the output images. For this, a circular Gaussian beam was used. This was not done without caution. The feasibility of imposing such a beam was verified through analysing the beams of the calibrators to determine the degree of elongation present in the observations. This was found to be ~1.3. Furthermore, to avoid the effects of super resolution, the beam was restored to the resolution of the lowest frequency. Using a compact radio source finder, AEGEAN, I have detected 1238 sources in the $4° \times 2°$ region covered in the survey. The source flux densities range from 246 $\mu Jy\ beam^{-1}$ to 0.279 $Jy\ beam^{-1}$ and 0.214 mJy to 0.796 Jy for peak and integrated flux densities, respectively. Their mean noise ranges from 45.6 $\mu Jy\ beam^{-1}$ to 4.78 $mJy\ beam^{-1}$. The fidelity of this catalogue was tested through completeness simulations run on a subset of the data. This revealed that the catalogue is 95% complete at 7σ or higher in all but the second scheduling block which is 95% complete at 8σ or higher.

In Chapter 4 I analysed and interpreted the continuum data from KuGARS. The main focus in this chapter was to detect and identify HC HII regions. This was coupled with the goal to estimate their statistical lifetime. Reliably identifying young HII regions requires aligning emission in the radio, IR, and sub-mm regimes. By applying this technique to the sources in the KuGARS catalogue in tandem with ATLASGAL 850 μm and WISE 22μm data, I identified 82 radio continuum sources as potential young HII regions. The physical properties of the HII regions were then determined using the formalisms in Mezger and Henderson (1967), Rubin (1968), and Sánchez-Monge et al. (2013), with the assumption that the detected radio continuum emission was emitted by homogeneous, optically thin HII regions. SED fits to in-band spectral indices, showed that the HII regions are all optically thick at 5 GHz and optically thin at 14 GHz, thus justifying the optically thin approximation used to derive their physical parameters. The diameters of these sources are greater than 0.03 pc and less than 0.1 pc, the typical sizes of HC and UC HII regions, respectively. This means that they are in transition between the UC and HC HII region stages of their evolution. In a similar manner to the statistical lifetime estimates Wood and Churchwell (1989b) used for UC HII regions with respect to their ionising stars, I have estimated the lifetime of HC HII regions as a fraction of the lifetime an HII region spends in the UC phase. The ideal physical parameter for identifying objects in either stage of evolution and placing a boundary between them is spectral index. However, I was unable to use this because many of

the sources are resolved and have unreliable spectral indices. Instead, I used EM which is another defining quality of a HC HII region compared to an UC HII region. The evolutionary trend perceived through EM shows no observable boundaries depicting the edges of the respective evolutionary stages. Therefore 10^8 *pc cm^{-6}* was chosen as an arbitrary dividing line between the stages of evolution. This gives a high to low emission measure ratio of 24/58. Thus the time an HII region spends in high EM is ∼41% of its lifetime in the UC phase. Evidently, both spectral index and EM trends put into question the need for multiple classifications in the evolution of an HII region. The evolutionary trend is gradual and continuous with no sharp transition, making it impossible to define a fixed boundary. With no clear dividing line in any of the physical parameters the evolutionary trends between HC and UC HII regions suggest that these are in fact the same object.

In Chapter 5 I explored the prevalence of massive star formation in the Outer Galaxy. To do this I searched 78 high column density clumps in the Outer Galaxy for evidence of massive star formation. Targeted observations aimed at detecting radio emission embedded in the 78 clumps were carried out in the C-configuration of the VLA, in C-band (central frequency of 6 GHz). Radio emission was detected in 9 of the 78 clumps. However, despite the high column densities of the host clumps, the low N_{Ly} flux of the embedded radio sources rules them out as UC HII regions. This implies there are no unknown UC HII regions in the Outer Galaxy. In the clumps associated with radio emission, I found that 7 are bright in either the MIR or at 70 μm thus implying early or low mass star formation. In the 69 with no associated radio emission, I determined the likelihood of HII regions being present. Using the 3σ upper limit to the radio to set an upper limit to the Lyman flux, thus placing a limit on the mass of any massive stars present, rules out any potential embedded HII regions in these clumps. I have assumed an upper limit of 5 kpc to the distance of the clumps which gives $N_{Ly} \lesssim 10^{45} s^{-1}$. This is lower than expected for an HII region powered by a B0.5 star (Panagia, 1973).

In Chapter 6 I presented the process and results in the development of a compact source catalogue created from the 1.28 GHz MeerKAT-GPS images. The catalogue contains 490790 compact sources, with a signal-to-noise ratio of 5σ or greater. The completeness simulations, carried out on 6 representative tiles, recovered ∼90% of the sources with peak flux densities ≥ 2.4 *mJy beam^{-1}*, and ∼95% of the sources with peak flux densities ≥ 0.2 *mJy beam^{-1}* in the least and most complete tiles, respectively. Fifteen

representative tiles were used to estimate the likely false positive rate, where 716 spurious sources were found in a pool of 109866, thus giving a false positive rate of $\sim 0.65\%$. I explored the nature of the sources in the catalogue, by associating them with sources in the literature. The SIMBAD database provided 13773 classifications ($\sim 2\%$ of the catalogue) with a total of 116 distinct object types. The flux density distributions of the survey and the known sources showed that the percentage of known sources is $\sim 100\%$ for sources with flux densities above 10 Jy, and $\sim 80\%$ for sources with flux densities above 100 mJy. Therefore, the population of unknown sources is dominated by fainter emission. The results in this work agree with the hypotheses presented in Kim and Koo (2001) and Kurtz et al. (1999): a significant population of UC HII regions is associated with extended emission. However, I determined a less extreme estimate for the number of UC HII regions associated with extended halos - I found this to be around a 1/3 as opposed to $\sim 8/10$ in Kim and Koo (2001); Kurtz et al. (1999). I have not seen a lot of extended halos and I have not seen a large number of extreme flux density ratios in my sample. These results imply that extended emission around UC HII regions, by itself, cannot fully explain the lifetime problem, which the smaller samples of Kurtz et al. (1999) and Kim and Koo (2001) suggested.

7.2   Main Conclusions

In the KuGARS project, analogously to the statistical lifetime of a HC HII region, I have estimated the time an HII region spends in high EM and found this to be around 41% its lifetime in the UC phase and is therefore of the order 10^4 years. The results strongly suggest that young HII regions have a continuous evolutionary trend. There are no visible boundaries between the standard classes that have previously been thought to represent entirely different objects. Instead, it is likely that HC and UC HII regions are the same object simply evolving into a larger less dense region with time.

The SASSy project rules out unknown massive star formation in the Outer Galaxy. In my search for HII regions to associate with high column density clumps in the Outer Galaxy, I have found very few and none that are not previously known. I therefore conclude that massive star formation in the Outer Galaxy is not as prevalent as in the Inner Galaxy.

The MeerKAT project has provided an unbiased perspective on the 'age problem' of UC HII regions. Previous studies, carried out on samples subject to selection biases, estimated ($\sim 80\%$) of UC HII regions have extended emission around them. In this unbiased-unlimited sample, I have determined a lower estimate. I have found only $\sim$1/3 of UC HII regions have extended emission. While the presence of extended halos implies a longer lifespan than the dynamical age of an UC HII region, this only provides a partial solution. I have looked at a much larger sample and have not found as many extended sources as previous authors. Thus we cannot rely entirely on extended components to solve the lifetime problem.

7.3 Future Work

7.3.1 KuGARS

The science I can carry out with these observations extends beyond HC HII regions and I expect to detect much more than just these objects. As Fig. 2.3 shows, I will also detect UC HII regions (although I am likely to resolve out more extended compact HII regions - it may, however, be possible to use lower limits on their flux densities). Moreover, in this very work, some of the objects in the HII region sample are well into the UC stage of their evolution. By combining these observations with GLOSTAR 5 GHz continuum I will also be able to accurately measure their spectral indices, which are poorly constrained (Urquhart et al., 2013), as well as the spectral indices of the many radio galaxies I will detect. There are also more than 40 OB stars within the survey region, including the clusters GLIMPSE19 and 20 (Mercer et al., 2005), of which the latter contains 3 OB stars and an early WC star (Messineo et al., 2009). Many lie within $\sim$2.5 kpc and so I will be able to constrain their mass loss via stellar winds and also identify colliding wind binaries. Towards bright and compact continuum sources I expect to observe recombination lines in emission (with typical line-continuum ratios towards all detected UC/HC HII regions with flux densities >50 mJy) and also absorption from the 14.4 GHz H_2CO line. For the latter I will combine my data with the GLOSTAR detections of the 4.8 GHz line to obtain the H_2 volume density around these objects (Ginsburg et al., 2011b). Finally, I have obtained a simultaneous survey of 12.2 GHz CH_3OH and 13.4 GHz excited OH masers, in a bid to reveal their relationship to the

star-forming regions traced by the HII regions. For OH, I will be able to measure the Zeeman splitting for all masers brighter than 1 Jy, enabling the measurement of the magnetic field around massive YSOs on sub-arcsec scales, complementing the MAGMO survey (Green et al., 2012).

7.3.2 SASSy

The radio observations carried out to find cm complements to the 850 μm SASSy clumps were carried out in the C configuration of the VLA, in C-band (FWHM$\sim 3''.5$): observing at 6 GHz allowed for the simultaneous search of 6.7 GHz methanol maser emission and free-free emission from thermal radio continuum, which implies the presence of HII regions. The target areas were split into seven four-hour scheduling blocks. The desired sensitivity was driven by the need to detect the 6.7 GHz maser line. This was estimated to have a typical brightness of 60 mJy per 0.1 km/s channel. This sensitivity is comparable to the 6 GHz Multibeam Maser Survey (Green et al., 2009, 2017; Breen et al., 2018). Thus, to reach the required sensitivity, an on source integration time of 5 minutes was used. Each scheduling block took $\sim$4 hours to observe. The next step in this study will be to reduce the spectral line data, detect and analyse the 6.7 GHz maser emission. This provides an additional star formation tracer. There exists the possibility I will trace clumps that host masers but not UC HII regions - clumps that, potentially, are at an earlier stage. This is uncharted territory as there has not been a maser survey in the Outer Galaxy. By definition all masers are associated with molecular clumps, therefore, this is the best way to make a column density limited survey for masers.

7.3.3 MeerKAT

Having come to the same conclusion as the hypotheses in Kim and Koo (2001) and Kurtz et al. (1999), albeit with less extreme estimates, I can delve deeper into the analysis of the three component ensemble of ultracompact, compact and extended components. I can compute the sizes in the MeerKAT data to determine which objects are actually ultracompact. By resolving the UC HII region emission, the RMS samples may have underestimated their sizes and erroneously classified them as ultracompact. The examples in Fig. 6.16 show that the extended halos are likely, at least in these images, to be

directly connected to the UC HII region. This assumption was made by visually inspecting the images. By computing the N_{Ly} for the UC HII region as well as the extended halo I can determine whether or not they are powered by the same source. Similarly, calculating their velocities will tell me if a single ionising source is driving them.

The classifications used in this study were made through associations with SIMBAD, which is a catalogue of catalogues. For a more complete and detailed classification I will employ the use of the source catalogue of the desired object types. For example, in my search for stars, I will use optical and near-IR catalogues to associate radio sources with stars in optical and near-IR catalogues. These can then be classified based on their optical to near-IR colours. I will determine mulitwavelength counterparts for all the sources in the MeerKAT catalogue. There have been a large number of previous Galactic Plane surveys. I will use these observations to attempt to identify the objects in the MeerKAT catalogue.

Appendix A

KuGARS' Candidate HII region catalogue

The errors of the dominant parameters have been listed as individual table columns, and the typical errors in the remaining parameters are as follows: error in distance = 500 pc; error in $N_{Ly} = 0.17 \times 10^{46}$ cm^{-3}; error in EM $= 3.4 \times 10^6$ pc cm^{-6}; error in $M_{HII} = 0.2 \times 10^{-3}$ $M_{\odot}$; and error in angular size = 0.04 arcsecs.

Source Galactic name	Peak Flux (mJy beam^{-1})	error	Integrated Flux (mJy)	error	α	α_{err}	n_e ($10^4 cm^{-3}$)	EM ($10^6 pc\,cm^{-6}$)	$\nu_{turnover}$ (GHz)	Diameter (pc)	M$_{HII}$ ($10^{-3}M_\odot$)	N$_{Ly}$ (photons s^{-1})	Angular size (arcsec)
G041.7417+00.0974	2.0	0.15	19.65	1.44	-1.71	0.6	1.14	6.4	1.73	0.075	44.7	3.18e+47	1.32
G041.7420+00.0974	1.45	0.15	6.36	0.64	-5.3	0.81	1.18	4.6	1.48	0.05	13.7	1.01e+47	0.88
G041.7419+00.0972	0.82	0.15	14.02	2.52	-2.5	0.72	0.63	2.6	1.12	0.099	56.8	2.23e+47	1.74
G041.7419+00.0971	0.77	0.15	3.43	0.65	-1.45	1.21	0.91	2.8	1.16	0.05	10.8	6.17e+46	0.88
G041.7419+00.0970	1.18	0.15	11.1	1.38	-3.98	0.97	0.88	3.7	1.33	0.073	32.2	1.77e+47	1.29
G041.7412+00.0974	1.1	0.15	15.41	2.05	-1.9	0.7	0.78	3.6	1.32	0.089	52.0	2.54e+47	1.57
G042.1093-00.4470	0.78	0.13	0.92	0.15	-2.23	0.25	2.22	2.5	1.1	0.008	0.1	1.24e+45	0.46
G042.1091-00.4468	1.33	0.13	5.95	0.57	-2.62	0.61	2.08	4.2	1.41	0.015	0.6	7.99e+45	0.89
G042.4341-00.2607	0.63	0.16	0.63	0.16	3.06	0.37	2.47	3.6	1.32	0.009	0.2	2.62e+45	0.42
G042.4349-00.2605	0.6	0.15	1.06	0.26	2.14	2.86	1.76	2.4	1.09	0.012	0.3	3.06e+45	0.56
G042.4348-00.2604	0.63	0.15	0.97	0.22	-0.49	1.58	1.78	2.3	1.07	0.011	0.2	2.53e+45	0.52
G042.4348-00.2606	0.86	0.15	4.38	0.75	-2.49	0.57	1.42	2.7	1.15	0.02	1.1	9.85e+45	0.95
G042.4344-00.2604	1.72	0.15	5.59	0.48	-1.8	0.8	2.25	5.4	1.6	0.016	0.9	1.26e+46	0.76
G042.4346-00.2605	1.6	0.15	4.64	0.42	-2.45	0.35	2.23	5.1	1.54	0.015	0.7	1.04e+46	0.72
G043.1781-00.5180	0.94	0.14	0.95	0.14	-0.9	0.65	1.6	3.0	1.2	0.017	0.8	7.94e+45	0.42
G043.1777-00.5178	0.88	0.14	0.89	0.14	-1.64	1.02	1.6	3.0	1.19	0.017	0.8	7.91e+45	0.42
G043.1683+00.0085	4.56	1.12	13.5	3.33	-0.34	3.96	2.36	14.4	2.54	0.039	13.1	1.93e+47	0.72
G043.1657-00.0281	11.19	1.74	329.02	51.01	-1.95	0.78	2.09	35.4	3.9	0.123	361.2	4.71e+48	2.28
G043.1662-00.0283	10.68	1.74	77.76	12.63	-4.06	2.77	2.89	33.8	3.81	0.061	61.7	1.11e+48	1.13
G043.1663+00.0107	44.51	2.16	97.05	4.71	-1.4	1.04	8.6	163.7	8.08	0.033	30.1	1.62e+48	0.62
G043.1458+00.0141	6.14	0.55	64.76	5.79	-5.68	1.16	2.0	19.4	2.93	0.073	74.3	9.27e+47	1.36
G043.1665+00.0108	34.16	2.16	159.78	10.1	-2.23	0.37	5.77	108.0	6.63	0.049	63.4	2.29e+48	0.91
G043.1664+00.0105	52.69	2.16	223.68	9.17	-1.78	0.99	7.35	166.6	8.15	0.047	69.8	3.2e+48	0.87
G043.1489+00.0130	49.08	0.82	84.44	1.42	-1.11	0.47	9.09	162.3	8.05	0.03	22.3	1.26e+48	0.55
G043.1684+00.0125	33.73	0.96	122.19	3.49	-1.47	1.23	5.31	119.0	5.71	0.042	52.7	1.75e+48	0.8
G043.1664-00.0283	8.0	1.74	24.2	5.25	-2.06	1.14	3.28	28.0	3.49	0.039	18.7	3.84e+47	0.73
G043.1520+00.0114	12.74	0.36	144.57	4.05	-2.68	2.77	3.0	45.4	4.39	0.076	124.5	2.33e+48	1.41
G043.1685+00.0086	11.3	1.12	29.72	2.96	-5.08	0.28	3.83	35.7	3.92	0.037	17.8	4.26e+47	0.68
G043.1667+00.0104	15.46	2.16	105.0	14.67	-3.63	2.45	3.54	48.9	4.55	0.059	68.0	1.5e+48	1.09
G043.1669+00.0108	26.97	2.16	164.31	13.16	-4.19	1.14	4.8	85.3	5.92	0.056	78.4	2.35e+48	1.04

Source Galactic name	Peak Flux (mJy beam^{-1})	error	Integrated Flux (mJy)	error	α	α_{err}	n_e ($10^4 cm^{-3}$)	EM ($10^6 pc\,cm^{-6}$)	$v_{turnover}$ (GHz)	Diameter (pc)	M_{HII} ($10^{-3}M_\odot$)	N_{Ly} (photons s^{-1})	Angular size (arcsec)
G043.1667+00.0107	14.85	2.16	36.15	5.26	3.25	1.89	5.81	78.8	5.71	0.035	23.9	8.69e+47	0.66
G043.1518+00.0116	15.8	0.36	51.91	1.17	-4.47	1.82	4.29	49.9	4.59	0.041	27.7	7.43e+47	0.76
G043.1707+00.0043	23.14	1.02	29.82	1.32	-0.61	0.1	6.56	73.2	5.51	0.026	10.4	4.27e+47	0.48
G043.1665+00.0111	79.73	2.16	206.94	5.61	0.01	0.14	10.41	261.3	10.1	0.036	47.2	3.07e+48	0.68
G043.1674+00.0132	8.24	2.05	8.33	2.07	1.29	1.91	4.52	30.8	3.65	0.023	5.0	1.41e+47	0.42
G043.1674+00.0128	58.82	2.05	233.72	8.14	-1.96	1.44	8.8	309.4	9.0	0.04	61.7	3.4e+48	0.84
G043.2374-00.0454	2.53	0.43	5.49	0.92	-4.08	2.29	1.9	8.0	1.92	0.033	6.6	7.86e+46	0.62
G043.1665-00.0284	11.69	1.22	47.33	4.93	0.31	0.62	3.6	39.0	4.08	0.045	31.8	7.15e+47	0.85
G043.1652+00.0135	3.57	1.09	5.61	1.72	7.43	2.76	4.46	37.3	4.0	0.028	9.5	2.65e+47	0.53
G043.1651+00.0129	104.91	1.27	245.22	2.97	-1.0	0.93	3.99	108.9	5.47	0.068	145.8	3.64e+48	0.64
G043.2373-00.0456	5.13	0.43	11.81	0.98	-0.88	0.08	2.67	16.2	2.69	0.034	10.1	1.69e+47	0.64
G043.1462+00.0142	5.95	0.59	44.35	4.4	-1.84	0.71	2.15	18.8	2.89	0.062	47.4	6.35e+47	1.15
G043.2373-00.0452	3.65	0.43	13.98	1.63	-2.08	0.71	1.99	11.6	2.29	0.044	16.1	2e+47	0.82
G043.1658-00.0282	6.85	1.22	177.7	31.59	-4.29	1.31	1.68	21.6	3.08	0.115	241.8	2.54e+48	2.14
G043.2376-00.0453	2.39	0.43	5.08	0.91	-0.33	0.77	1.86	7.6	1.87	0.033	6.3	7.28e+46	0.61
G043.2372-00.0459	18.56	0.43	31.98	0.73	-1.65	0.41	5.46	58.7	4.96	0.03	13.4	4.58e+47	0.55
G043.1652-00.0281	29.48	1.22	229.41	9.47	-0.32	0.39	4.72	93.2	6.18	0.063	111.3	3.29e+48	1.17
G043.1654+00.0134	3.35	1.09	10.99	3.58	3.1	2.22	2.53	17.3	2.77	0.041	16.3	2.57e+47	0.76
G043.1661+00.0111	40.81	3.17	133.08	10.35	-6.65	2.87	6.91	129.0	7.22	0.041	44.2	1.91e+48	0.76
G043.3059-00.2110	1.76	0.08	5.04	0.23	-3.34	0.53	2.41	5.6	1.62	0.014	0.7	1.03e+46	0.71
G043.1665+00.0099	15.78	3.17	80.09	16.1	-2.23	2.99	4.11	57.1	4.9	0.051	51.1	1.31e+48	0.95
G043.1648-00.0285	50.4	1.22	687.39	16.6	-2.78	2.06	5.39	160.8	8.01	0.083	294.9	9.93e+48	1.55
G043.1656+00.0117	58.56	1.56	234.73	6.25	-1.97	1.42	6.68	211.2	7.5	0.047	81.4	3.4e+48	0.84
G043.1668+00.0106	24.53	3.17	279.67	36.17	-0.94	0.49	3.92	77.6	5.66	0.076	163.7	4.01e+48	1.42
G043.1659+00.0121	63.35	1.96	121.52	3.77	0.06	0.8	10.32	221.0	9.32	0.031	29.8	1.92e+48	0.58
G043.1642-00.0279	8.92	1.62	11.52	2.1	-2.49	2.16	4.16	29.4	3.57	0.026	6.6	1.72e+47	0.48
G043.1668+00.0101	40.65	3.17	144.57	11.28	-2.33	1.3	6.74	128.5	7.2	0.043	49.1	2.07e+48	0.79
G043.3064-00.2113	1.53	0.08	4.99	0.25	-3.79	1.05	2.17	4.8	1.51	0.015	0.8	1.02e+46	0.76
G043.1699+00.0075	6.61	0.81	40.76	4.98	3.26	0.79	2.92	31.6	3.69	0.056	48.5	8.83e+47	1.04
G043.1668+00.0108	37.82	3.17	79.65	6.68	-3.89	1.34	7.42	119.6	6.96	0.033	24.6	1.14e+48	0.61

Source Galactic name	Peak Flux (mJy beam^{-1})	error	Integrated Flux (mJy)	error	α	α_{err}	n_e ($10^4 cm^{-3}$)	EM ($10^6 pc\,cm^{-6}$)	$\nu_{turnover}$ (GHz)	Diameter (pc)	M$_{HII}$ ($10^{-3}M_\odot$)	N$_{Ly}$ (photons s^{-1})	Angular size (arcsec)
G043.1652-00.0284	42.57	1.22	152.7	4.37	-1.14	0.11	6.89	134.6	7.36	0.043	50.8	2.19e+48	0.8
G043.1668+00.0110	28.29	3.17	62.5	7.01	-2.61	inf	6.34	89.4	6.06	0.034	22.6	8.95e+47	0.62
G043.1652-00.0282	12.53	1.22	17.03	1.65	-1.9	0.3	4.76	39.6	4.11	0.026	8.2	2.44e+47	0.49
G043.1481+00.0131	5.76	1.22	5.52	1.17	2.58	2.44	4.46	29.2	3.56	0.022	4.5	1.27e+47	0.41
G043.1663+00.0103	39.91	3.17	185.45	14.74	-2.38	0.89	6.25	126.2	7.14	0.049	68.0	2.66e+48	0.91
G043.1663+00.0113	89.88	3.17	136.47	4.82	-0.5	0.34	12.46	286.7	10.55	0.028	25.3	1.97e+48	0.52
G043.1649-00.0281	23.27	1.22	42.21	2.21	1.12	0.87	6.52	85.7	5.94	0.03	17.3	7.04e+47	0.57
G043.1669+00.0102	18.45	3.17	51.45	8.85	0.88	0.02	5.14	66.2	5.25	0.038	26.0	8.36e+47	0.7
G043.8893-00.7837	3.57	0.07	119.78	2.37	-2.22	0.41	1.81	11.3	2.26	0.052	23.8	2.7e+47	2.43
G043.8893-00.7840	9.13	0.07	42.38	0.33	-2.74	0.91	4.75	28.9	3.54	0.019	3.2	9.54e+46	0.9
G043.8896-00.7842	6.4	0.07	51.92	0.57	-2.65	0.59	3.46	20.2	2.99	0.026	5.4	1.17e+47	1.2
G043.8900-00.7839	1.72	0.07	53.79	2.22	-0.2	0.45	1.28	5.4	1.6	0.05	15.2	1.21e+47	2.35
G043.7955-00.1265	-0.19	0.23	-0.24	0.29	-2.11	inf	3.3	9.9	2.12	0.014	0.8	1.63e+46	0.47
G043.7951-00.1273	1.33	0.22	1.97	0.33	1.46	1.22	2.54	6.4	1.72	0.015	0.8	1.25e+46	0.51
G043.7953-00.1270	2.03	0.22	2.83	0.31	-1.17	1.04	2.81	7.6	1.87	0.014	0.8	1.4e+46	0.5
G043.7954-00.1273	59.09	0.22	71.27	0.27	-1.51	0.64	14.76	193.8	8.76	0.013	3.4	3.09e+47	0.46
G043.7957-00.1269	0.49	0.21	0.81	0.35	-0.41	inf	2.94	9.0	2.03	0.016	1.1	1.97e+46	0.54
G043.7957-00.1270	-0.13	0.21	-0.13	0.2	4.2	inf	2.88	6.5	1.74	0.012	0.5	8.17e+45	0.41
G043.7953-00.1279	1.02	0.24	1.26	0.3	3.44	1.23	2.66	6.4	1.72	0.014	0.6	1.04e+46	0.47
G043.7953-00.1276	2.91	0.26	3.04	0.27	-2.96	1.31	3.45	9.8	2.12	0.012	0.6	1.36e+46	0.43
G044.3103+00.0409	0.8	0.06	2.88	0.21	-0.37	0.47	1.11	2.5	1.11	0.031	3.2	2.2e+46	0.8
G044.3101+00.0407	0.8	0.06	1.03	0.08	0.01	1.16	1.63	3.3	1.26	0.019	1.0	1.03e+46	0.48

Appendix B

The full KuGARS compact source catalogue

Source Galactic name	Source Index	RA J2000	Dec J2000	Observed flux density				Major (arcsec)		Minor (arcsec)		PA (°)		flags	aux_flags
				Peak (mJy beam^{-1})		Integrated (mJy)									
					error		error		error		error		error		
G41.3819+0.9995	1115600	19:03:21.27	+07:58:24.31	0.44	0.07	0.45	0.07	0.42	-1.0	0.42	-1.0	-0.02	-1.0	4	0
G41.4069+0.8575	1113300	19:03:54.65	+07:55:50.24	0.44	0.07	0.44	0.09	0.44	0.03	0.41	0.04	85.05	2.11	0	0
G41.4399+0.7174	1111700	19:04:28.47	+07:53:44.56	0.36	0.06	0.36	0.06	0.42	-1.0	0.42	-1.0	0.02	-1.0	4	0
G41.4399+0.7174	1122100	19:04:28.47	+07:53:44.57	0.35	0.06	0.35	0.06	0.42	-1.0	0.42	-1.0	-0.04	-1.0	4	0
G41.4648+0.6454	1121500	19:04:46.74	+07:53:05.22	0.51	0.09	0.52	0.09	0.42	-1.0	0.42	-1.0	-0.03	-1.0	4	0
G41.4660+0.8363	1115500	19:04:05.76	+07:58:24.30	0.37	0.07	0.37	0.07	0.42	-1.0	0.42	-1.0	0.0	-1.0	4	0
G41.4821+0.7994	1210600	19:04:15.50	+07:58:15.04	0.59	0.1	0.59	0.1	0.42	-1.0	0.42	-1.0	0.0	-1.0	4	0
G41.4887+0.7239	1125300	19:04:32.49	+07:56:31.26	0.38	0.06	0.38	0.07	0.42	-1.0	0.42	-1.0	-0.03	-1.0	4	0
G41.5001+0.8378	1211600	19:04:09.23	+08:00:15.81	0.36	0.06	0.37	0.06	0.42	-1.0	0.42	-1.0	-0.0	-1.0	4	0
G41.5017+0.7481	1126200	19:04:28.73	+07:57:53.05	1.53	0.28	1.55	0.28	0.42	-1.0	0.42	-1.0	-0.04	-1.0	4	0
G41.5253+0.7612	1211000	19:04:28.52	+07:59:30.15	0.33	0.06	0.33	0.06	0.42	-1.0	0.42	-1.0	0.01	-1.0	4	0
G41.5388+0.7819	1212300	19:04:25.57	+08:00:47.55	0.37	0.07	0.37	0.07	0.42	-1.0	0.42	-1.0	0.01	-1.0	4	0
G41.5435+0.6084	1125100	19:05:03.46	+07:56:15.78	0.39	0.06	0.4	0.06	0.42	-1.0	0.42	-1.0	-0.02	-1.0	4	0
G41.5531+0.7312	1211400	19:04:38.09	+08:00:09.41	0.4	0.07	0.4	0.07	0.42	-1.0	0.42	-1.0	0.02	-1.0	4	0
G41.5531+0.7312	1222100	19:04:38.09	+08:00:09.42	0.46	0.08	0.46	0.08	0.42	-1.0	0.42	-1.0	-0.04	-1.0	4	0
G41.5898+0.5563	1220100	19:05:19.82	+07:57:17.94	1.65	0.26	1.66	0.26	0.42	-1.0	0.42	-1.0	-0.01	-1.0	4	0
G41.6126+0.3431	1130300	19:06:08.25	+07:52:38.16	1.63	0.15	3.28	0.36	0.89	0.05	0.4	0.01	-18.95	0.04	0	0
G41.6126+0.3431	1120800	19:06:08.25	+07:52:38.17	1.65	0.15	3.34	0.38	0.89	0.05	0.4	0.01	-16.54	0.04	0	0
G41.6484+0.5114	1221600	19:05:36.01	+07:59:10.94	0.41	0.07	0.41	0.07	0.42	-1.0	0.42	-1.0	-0.0	-1.0	4	0
G41.6567+0.6664	1311000	19:05:03.55	+08:03:53.85	0.43	0.08	0.44	0.08	0.42	-1.0	0.42	-1.0	0.02	-1.0	4	0
G41.6604+0.4413	1126100	19:05:52.44	+07:57:53.52	1.04	0.07	1.82	0.13	0.8	0.02	0.39	0.01	-34.92	0.04	0	0
G41.6604+0.4413	1220800	19:05:52.44	+07:57:53.51	1.16	0.11	1.32	0.15	0.49	0.02	0.41	0.02	-13.72	0.34	0	0
G41.6621+0.6576	1321600	19:05:06.05	+08:03:56.29	0.55	0.09	0.56	0.1	0.42	-1.0	0.42	-1.0	-0.03	-1.0	4	0
G41.6651+1.0062	2111600	19:03:51.26	+08:13:41.53	0.25	0.04	0.25	0.04	0.42	-1.0	0.42	-1.0	-0.03	-1.0	4	0
G41.6777+0.4478	1221500	19:05:52.96	+07:58:59.70	0.39	0.06	0.45	0.1	0.48	0.04	0.43	0.06	87.52	1.78	0	0
G41.6777+0.4478	1127100	19:05:52.96	+07:58:59.71	0.36	0.06	0.37	0.06	0.42	-1.0	0.42	-1.0	0.01	-1.0	4	0
G41.6812+0.5526	1224000	19:05:30.78	+08:02:04.21	0.39	0.07	0.39	0.07	0.42	-1.0	0.42	-1.0	-0.01	-1.0	4	0
G41.6943+0.6924	1325400	19:05:02.13	+08:06:37.09	0.4	0.07	0.41	0.07	0.42	-1.0	0.42	-1.0	-0.03	-1.0	4	0
G41.7103+0.3914	1135400	19:06:08.72	+07:59:10.66	0.52	0.09	0.53	0.09	0.42	-1.0	0.42	-1.0	-0.03	-1.0	4	0
G41.7342+0.2057	1132400	19:06:51.37	+07:55:19.69	0.4	0.07	0.4	0.07	0.42	-1.0	0.42	-1.0	-0.01	-1.0	4	0
G41.7412+0.0974	1130403	19:07:15.44	+07:52:42.61	1.28	0.44	17.84	6.2	2.38	0.1	1.04	0.05	-82.31	0.92	0	1
G41.7417+0.0974	1130400	19:07:15.49	+07:52:44.27	2.28	0.44	22.44	4.68	1.44	0.1	1.21	0.05	1.37	0.36	0	0
G41.7419+0.0970	1130404	19:07:15.60	+07:52:44.10	0.97	0.44	9.14	4.18	1.43	0.1	1.16	0.05	8.84	0.35	0	1
G41.7419+0.0971	1130401	19:07:15.57	+07:52:44.30	0.93	0.44	4.13	1.95	1.23	0.04	0.64	0.02	-25.96	0.26	0	1
G41.7419+0.0972	1130402	19:07:15.55	+07:52:44.49	0.92	0.44	15.85	7.53	3.9	0.07	0.78	0.04	47.56	0.18	0	1

Source Galactic name	Source Index	RA J2000	Dec J2000	Observed flux density Peak (mJy beam^{-1})	error	Integrated (mJy)	error	Major (arcsec)	error	Minor (arcsec)	error	PA (°)	error	flags	aux_flags
G41.7420+0.0974	1130405	19:07:15.52	+07:52:45.23	0.95	0.44	4.16	1.97	1.14	0.1	0.68	0.05	85.37	0.72	0	1
G41.7453+0.7212	1314800	19:05:01.60	+08:10:07.77	0.38	0.07	0.39	0.07	0.42	-1.0	0.42	-1.0	0.02	-1.0	4	0
G41.7453+0.7212	1327900	19:05:01.60	+08:10:07.77	0.38	0.06	0.39	0.07	0.42	-1.0	0.42	-1.0	-0.03	-1.0	4	0
G41.7563+0.9086	2210800	19:04:22.45	+08:15:52.07	0.67	0.12	0.68	0.12	0.42	-1.0	0.42	-1.0	-0.02	-1.0	4	0
G41.7649+0.5241	1226800	19:05:46.24	+08:05:44.67	2.34	0.22	3.36	0.39	0.6	0.02	0.42	0.03	-81.89	0.25	0	0
G41.7649+0.5246	1226900	19:05:46.13	+08:05:45.41	5.05	0.25	4.04	0.23	0.41	0.01	0.35	0.01	-14.38	0.18	0	0
G41.7650+0.5246	1323300	19:05:46.13	+08:05:45.67	4.94	0.13	4.73	0.14	0.49	0.01	0.35	0.0	-11.93	0.04	0	0
G41.7650+0.5247	1226901	19:05:46.13	+08:05:45.94	1.75	0.25	1.27	0.18	0.38	0.01	0.34	0.01	-29.21	0.19	0	0
G41.7651+0.5245	1227000	19:05:46.18	+08:05:45.87	1.8	0.25	1.43	0.23	0.42	0.03	0.34	0.02	20.84	0.39	0	0
G41.7651+0.5248	1323500	19:05:46.10	+08:05:46.48	0.95	0.13	1.04	0.2	0.57	0.07	0.34	0.02	2.06	0.12	0	0
G41.7871+0.4879	1227300	19:05:56.50	+08:05:55.82	1.92	0.28	4.8	1.26	0.83	0.05	0.53	0.11	77.79	0.47	0	0
G41.7871+0.4884	1227400	19:05:56.39	+08:05:56.65	4.87	0.31	5.14	0.37	0.5	0.01	0.37	0.01	-16.6	0.1	0	0
G41.7872+0.4882	1323801	19:05:56.45	+08:05:56.71	0.88	0.14	0.79	0.13	0.41	0.0	0.39	0.0	-65.11	0.06	0	0
G41.7872+0.4884	1323800	19:05:56.40	+08:05:56.87	6.03	0.14	6.03	0.16	0.48	0.0	0.37	0.0	-15.13	0.05	0	0
G41.7873+0.4883	1227500	19:05:56.44	+08:05:57.07	2.06	0.32	1.72	0.32	0.44	0.04	0.34	0.02	24.56	0.37	0	0
G41.7873+0.4887	1324100	19:05:56.36	+08:05:57.69	0.91	0.14	1.25	0.26	0.7	0.09	0.35	0.02	0.88	0.08	0	0
G41.8011+0.1601	1134500	19:07:08.62	+07:57:38.12	0.41	0.07	0.41	0.07	0.42	-1.0	0.42	-1.0	0.0	-1.0	4	0
G41.8277+0.5610	2120600	19:05:45.30	+08:10:06.35	1.09	0.19	1.1	0.19	0.42	-1.0	0.42	-1.0	-0.01	-1.0	4	0
G41.8384+0.6609	2123400	19:05:24.95	+08:13:25.62	1.13	0.17	1.14	0.18	0.42	-1.0	0.42	-1.0	-0.03	-1.0	4	0
G41.8440+0.9063	2214300	19:04:32.69	+08:20:29.10	0.45	0.08	0.46	0.08	0.42	-1.0	0.42	-1.0	-0.01	-1.0	4	0
G41.8543+0.3985	1333900	19:06:23.24	+08:07:02.54	0.93	0.17	0.94	0.17	0.42	-1.0	0.42	-1.0	-0.04	-1.0	4	0
G41.8554+0.3593	1324300	19:06:31.80	+08:06:01.39	0.4	0.07	0.41	0.07	0.42	-1.0	0.42	-1.0	0.02	-1.0	4	0
G41.8623+0.6658	2112200	19:05:26.55	+08:14:50.29	0.47	0.08	0.48	0.09	0.42	-1.0	0.42	-1.0	0.03	-1.0	4	0
G41.8702-0.0360	1132700	19:07:58.53	+07:55:53.84	1.32	0.24	1.33	0.24	0.42	-1.0	0.42	-1.0	0.03	-1.0	4	0
G41.8711+0.1013	1232600	19:07:29.09	+07:59:44.20	0.34	0.06	0.34	0.06	0.42	-1.0	0.42	-1.0	0.01	-1.0	4	0
G41.8731+0.6397	2124600	19:05:33.40	+08:14:41.75	0.86	0.08	0.86	0.09	0.46	0.02	0.38	0.01	11.22	0.28	0	0
G41.8741+0.2424	1237300	19:06:59.06	+08:03:47.61	0.43	0.07	0.44	0.07	0.42	-1.0	0.42	-1.0	-0.01	-1.0	4	0
G41.8908+0.2136	1331500	19:07:07.12	+08:03:53.34	0.4	0.07	0.4	0.07	0.42	-1.0	0.42	-1.0	-0.01	-1.0	4	0
G41.8917+0.4034	1335600	19:06:26.34	+08:09:10.44	1.79	0.32	1.81	0.32	0.42	-1.0	0.42	-1.0	-0.04	-1.0	4	0
G41.9006+0.2482	1239800	19:07:00.75	+08:05:21.87	0.71	0.12	0.71	0.12	0.42	-1.0	0.42	-1.0	-0.01	-1.0	4	0
G41.9059-0.2279	1140300	19:08:43.76	+07:52:29.64	1.16	0.2	1.17	0.2	0.42	-1.0	0.42	-1.0	0.0	-1.0	4	0
G41.9097-0.0274	1241000	19:08:01.08	+07:58:14.51	0.59	0.1	0.6	0.11	0.42	-1.0	0.42	-1.0	-0.03	-1.0	4	0
G41.9098-0.0274	1231000	19:08:01.08	+07:58:14.53	0.63	0.11	0.64	0.11	0.42	-1.0	0.42	-1.0	0.03	-1.0	4	0
G41.9118+0.0868	1234200	19:07:36.74	+08:01:30.46	0.59	0.09	0.48	0.09	0.4	0.02	0.36	0.03	-78.97	1.17	0	0
G41.9121+0.0866	1234300	19:07:36.81	+08:01:31.03	0.57	0.09	0.57	0.09	0.42	-1.0	0.42	-1.0	0.01	-1.0	4	0

Source Galactic name	Source Index	RA J2000	Dec J2000	Observed flux density				Major (arcsec)		Minor (arcsec)		PA (°)		flags	aux_flags
				Peak (mJy beam^{-1})	error	Integrated (mJy)	error		error		error		error		
G41.9122+0.0867	1234400	19:07:36.81	+08:01:31.61	0.97	0.1	0.89	0.11	0.44	0.02	0.37	0.01	-21.45	0.38	0	0
G41.9123+0.0866	1234402	19:07:36.85	+08:01:31.63	0.42	0.1	0.44	0.11	0.53	0.02	0.35	0.02	-88.25	0.65	0	0
G41.9124+0.0869	1234500	19:07:36.77	+08:01:32.37	0.5	0.09	0.51	0.09	0.42	-1.0	0.42	-1.0	0.01	-1.0	4	0
G41.9125+0.0866	1234401	19:07:36.86	+08:01:32.11	0.56	0.1	0.84	0.16	0.54	0.02	0.49	0.02	-8.97	0.39	0	0
G41.9213+0.4205	2121500	19:06:25.96	+08:11:13.17	0.53	0.09	0.53	0.09	0.42	-1.0	0.42	-1.0	0.01	-1.0	4	0
G41.9233+0.7282	2213300	19:05:19.92	+08:19:48.43	1.04	0.09	1.28	0.13	0.55	0.02	0.39	0.01	10.94	0.12	0	0
G41.9233+0.7282	2223900	19:05:19.92	+08:19:48.47	0.93	0.1	1.09	0.15	0.5	0.03	0.41	0.02	-1.67	0.32	0	0
G41.9308+0.5761	2125600	19:05:53.50	+08:16:00.97	0.61	0.09	0.81	0.17	0.55	0.07	0.43	0.04	3.5	0.41	0	0
G41.9399-0.2778	1140700	19:08:58.31	+07:52:55.42	0.79	0.1	1.01	0.15	0.51	0.03	0.44	0.02	-18.27	0.58	0	0
G41.9399-0.2782	1140600	19:08:58.38	+07:52:54.98	1.25	0.1	1.4	0.13	0.52	0.02	0.38	0.01	-12.72	0.13	0	0
G41.9401-0.2780	1140800	19:08:58.36	+07:52:55.68	0.78	0.1	0.84	0.14	0.5	0.05	0.38	0.02	7.08	0.25	0	0
G41.9446-0.1168	1147300	19:08:24.20	+07:57:37.60	0.36	0.06	0.36	0.06	0.42	-1.0	0.42	-1.0	-0.01	-1.0	4	0
G41.9560+0.4717	2124200	19:06:18.82	+08:14:29.03	0.59	0.1	0.59	0.1	0.42	-1.0	0.42	-1.0	0.01	-1.0	4	0
G41.9598+0.1461	12310000	19:07:29.34	+08:05:41.85	0.73	0.13	0.73	0.13	0.42	-1.0	0.42	-1.0	0.01	-1.0	4	0
G41.9606+0.0559	1236600	19:07:48.84	+08:03:14.97	0.42	0.07	0.42	0.07	0.42	-1.0	0.42	-1.0	0.02	-1.0	4	0
G41.9621+0.6704	2320200	19:05:36.69	+08:20:16.99	2.18	0.38	2.2	0.39	0.42	-1.0	0.42	-1.0	-0.03	-1.0	4	0
G41.9724+0.8972	2314700	19:04:48.95	+08:27:04.56	0.55	0.09	0.54	0.11	0.43	0.03	0.41	0.04	-84.29	3.02	0	0
G42.0040+0.2439	2131200	19:07:13.22	+08:10:45.12	1.25	0.11	1.14	0.11	0.4	0.01	0.4	0.01	-88.67	8.92	0	0
G42.0040+0.2439	1337600	19:07:13.22	+08:10:45.28	0.85	0.14	0.86	0.14	0.42	-1.0	0.42	-1.0	-0.01	-1.0	4	0
G42.0190+0.4775	2222600	19:06:24.58	+08:17:59.80	0.49	0.08	0.49	0.08	0.42	-1.0	0.42	-1.0	0.0	-1.0	4	0
G42.0221-0.1488	1243700	19:08:39.75	+08:00:52.26	0.39	0.07	0.39	0.07	0.42	-1.0	0.42	-1.0	-0.0	-1.0	4	0
G42.0261-0.3517	1152300	19:09:23.83	+07:55:28.15	0.32	0.06	0.32	0.06	0.42	-1.0	0.42	-1.0	-0.03	-1.0	4	0
G42.0275-0.3347	1145000	19:09:20.31	+07:56:00.76	0.4	0.07	0.41	0.07	0.42	-1.0	0.42	-1.0	0.03	-1.0	4	0
G42.0280+0.9268	3113100	19:04:48.75	+08:30:51.55	1.52	0.06	1.94	0.09	0.51	0.01	0.44	0.01	-1.18	0.19	0	0
G42.0284-0.3519	1144200	19:09:24.12	+07:55:35.30	0.37	0.05	0.37	0.05	0.42	-1.0	0.42	-1.0	0.03	-1.0	4	0
G42.0284-0.3519	1152600	19:09:24.12	+07:55:35.30	0.36	0.06	0.33	0.07	0.44	0.03	0.37	0.04	-84.7	0.92	0	0
G42.0304+0.3622	2125100	19:06:50.69	+08:15:25.70	0.55	0.09	0.55	0.09	0.42	-1.0	0.42	-1.0	0.02	-1.0	4	0
G42.0315+0.9569	3114200	19:04:42.64	+08:31:52.30	0.32	0.06	0.32	0.06	0.42	-1.0	0.42	-1.0	-0.02	-1.0	4	0
G42.0358+0.0290	1333400	19:08:03.01	+08:06:30.75	0.38	0.06	0.39	0.06	0.42	-1.0	0.42	-1.0	0.02	-1.0	4	0
G42.0358+0.0290	1342300	19:08:03.01	+08:06:30.73	0.38	0.06	0.38	0.06	0.42	-1.0	0.42	-1.0	-0.03	-1.0	4	0
G42.0360+0.3509	2135300	19:06:53.75	+08:15:24.57	0.97	0.09	0.82	0.09	0.39	0.01	0.38	0.01	-7.25	1.58	0	0
G42.0360+0.3509	2125000	19:06:53.75	+08:15:24.57	0.97	0.09	0.81	0.09	0.39	0.01	0.37	0.01	-16.0	1.09	0	0
G42.0374+0.3024	2123900	19:07:04.34	+08:14:09.11	2.04	0.36	2.06	0.36	0.42	-1.0	0.42	-1.0	0.03	-1.0	4	0
G42.0380+0.0203	1333300	19:08:05.13	+08:06:23.65	0.39	0.07	0.4	0.07	0.42	-1.0	0.42	-1.0	0.02	-1.0	4	0
G42.0384-0.3145	1146600	19:09:17.21	+07:57:09.31	0.33	0.06	0.33	0.06	0.42	-1.0	0.42	-1.0	0.02	-1.0	4	0

Source Galactic name	Source Index	RA J2000	Dec J2000	Observed flux density				Major (arcsec)		Minor (arcsec)		PA (°)		flags	aux_flags
				Peak (mJy beam^{-1})	error	Integrated (mJy)	error		error		error		error		
G42.0384-0.3145	1155400	19:09:17.21	+07:57:09.29	0.33	0.06	0.33	0.06	0.42	-1.0	0.42	-1.0	-0.03	-1.0	4	0
G42.0406+0.6838	2313500	19:05:42.55	+08:24:50.23	0.51	0.08	0.52	0.09	0.42	-1.0	0.42	-1.0	0.03	-1.0	4	0
G42.0406+0.6838	2325500	19:05:42.55	+08:24:50.25	0.51	0.09	0.51	0.09	0.42	-1.0	0.42	-1.0	-0.03	-1.0	4	0
G42.0456-0.1101	1246200	19:08:34.03	+08:03:11.44	0.4	0.07	0.41	0.07	0.42	-1.0	0.42	-1.0	-0.01	-1.0	4	0
G42.0476+0.7262	2326700	19:05:34.19	+08:26:22.66	0.56	0.1	0.57	0.1	0.42	-1.0	0.42	-1.0	-0.04	-1.0	4	0
G42.0493+0.8530	3111900	19:05:07.03	+08:29:57.50	2.91	0.07	2.97	0.08	0.43	0.0	0.42	0.0	1.53	0.47	0	0
G42.0497+0.8532	3112001	19:05:07.04	+08:29:59.04	1.58	0.07	1.47	0.07	0.42	0.0	0.39	0.0	1.55	0.11	0	0
G42.0499+0.8532	3112000	19:05:07.06	+08:30:00.02	3.17	0.07	3.57	0.09	0.47	0.0	0.42	0.0	-0.15	0.11	0	0
G42.0574+0.9300	3114900	19:04:51.35	+08:32:30.79	0.33	0.06	0.34	0.06	0.42	-1.0	0.42	-1.0	-0.01	-1.0	4	0
G42.0640+0.6124	2324600	19:06:00.53	+08:24:07.03	0.48	0.09	0.49	0.09	0.42	-1.0	0.42	-1.0	-0.02	-1.0	4	0
G42.0740+0.5235	2227000	19:06:20.82	+08:22:11.98	0.45	0.08	0.46	0.08	0.42	-1.0	0.42	-1.0	0.0	-1.0	4	0
G42.0783+0.5084	2225801	19:06:24.53	+08:22:00.73	1.0	0.18	1.93	0.35	1.01	0.0	0.34	0.0	52.3	0.36	0	0
G42.0783+0.5084	2321901	19:06:24.53	+08:22:00.79	1.31	0.14	1.66	0.18	0.66	0.0	0.34	0.0	54.79	0.44	0	0
G42.0785+0.5084	2321900	19:06:24.57	+08:22:01.37	6.52	0.14	7.66	0.2	0.46	0.0	0.45	0.0	-83.63	0.45	0	0
G42.0785+0.5084	2225800	19:06:24.57	+08:22:01.37	6.38	0.18	7.51	0.24	0.46	0.0	0.45	0.0	-87.93	0.51	0	0
G42.0787+0.5089	2322300	19:06:24.48	+08:22:02.69	0.78	0.14	0.79	0.14	0.42	-1.0	0.42	-1.0	-0.0	-1.0	4	0
G42.0788+0.5081	2322100	19:06:24.64	+08:22:01.73	0.91	0.14	0.91	0.14	0.42	-1.0	0.42	-1.0	-0.0	-1.0	4	0
G42.0788+0.5081	2226100	19:06:24.64	+08:22:01.74	0.84	0.14	0.85	0.15	0.42	-1.0	0.42	-1.0	0.0	-1.0	4	0
G42.0792-0.5663	1150500	19:10:15.89	+07:52:21.12	1.12	0.2	1.13	0.21	0.42	-1.0	0.42	-1.0	0.0	-1.0	4	0
G42.0833-0.3378	1242000	19:09:27.21	+07:58:53.86	0.47	0.08	0.47	0.08	0.42	-1.0	0.42	-1.0	0.02	-1.0	4	0
G42.0833-0.3378	1251900	19:09:27.21	+07:58:53.86	0.47	0.08	0.47	0.08	0.42	-1.0	0.42	-1.0	-0.03	-1.0	4	0
G42.0884+0.3925	2233200	19:06:50.62	+08:19:21.25	1.15	0.16	1.26	0.21	0.45	0.03	0.43	0.03	1.27	1.64	0	0
G42.0884+0.3925	2223700	19:06:50.62	+08:19:21.28	1.16	0.1	1.2	0.11	0.5	0.02	0.37	0.01	14.45	0.14	0	0
G42.0891+0.9747	3212400	19:04:45.21	+08:35:25.82	0.27	0.05	0.28	0.05	0.42	-1.0	0.42	-1.0	-0.03	-1.0	4	0
G42.0922+0.6849	2328200	19:05:48.05	+08:27:36.98	0.48	0.08	0.49	0.09	0.42	-1.0	0.42	-1.0	-0.03	-1.0	4	0
G42.0928-0.2976	1158600	19:09:19.63	+08:00:31.07	0.79	0.13	0.8	0.13	0.42	-1.0	0.42	-1.0	-0.03	-1.0	4	0
G42.0929-0.4298	1154100	19:09:48.08	+07:56:51.60	0.93	0.15	0.94	0.15	0.42	-1.0	0.42	-1.0	-0.01	-1.0	4	0
G42.0930-0.4304	1153904	19:09:48.21	+07:56:51.31	0.9	0.15	1.01	0.17	0.59	0.01	0.34	0.0	-43.79	0.05	0	0
G42.0931-0.4301	1153900	19:09:48.17	+07:56:51.93	5.6	0.15	6.66	0.2	0.54	0.01	0.39	0.0	-27.78	0.05	0	0
G42.0932-0.4297	1154600	19:09:48.09	+07:56:52.87	1.05	0.15	1.53	0.32	0.56	0.03	0.46	0.06	-85.97	0.98	0	0
G42.0933-0.4298	1154601	19:09:48.12	+07:56:53.09	0.87	0.15	0.72	0.19	0.4	0.03	0.37	0.06	3.55	0.74	0	0
G42.0933-0.4301	1153901	19:09:48.18	+07:56:52.52	3.66	0.15	3.25	0.15	0.42	0.01	0.38	0.0	21.39	0.06	0	0
G42.0933-0.4303	1153902	19:09:48.22	+07:56:52.36	1.61	0.15	1.89	0.18	0.47	0.01	0.44	0.0	-11.88	0.06	0	0
G42.0934-0.4300	1153903	19:09:48.17	+07:56:53.17	0.94	0.15	0.76	0.12	0.43	0.01	0.34	0.0	-24.41	0.05	0	0
G42.0934-0.4306	1154300	19:09:48.30	+07:56:52.02	0.91	0.16	0.92	0.16	0.42	-1.0	0.42	-1.0	-0.01	-1.0	4	0

Source Galactic name	Source Index	RA J2000	Dec J2000	Peak (mJy beam^{-1})	error	Integrated (mJy)	error	Major (arcsec)	error	Minor (arcsec)	error	PA (°)	error	flags	aux_flags
G42.0935-0.4305	1154500	19:09:48.30	+07:56:52.60	1.19	0.16	0.94	0.14	0.38	0.02	0.37	0.02	15.67	2.37	0	0
G42.0939-0.4803	1152400	19:09:59.03	+07:55:31.08	0.43	0.07	0.43	0.07	0.42	-1.0	0.42	-1.0	-0.0	-1.0	4	0
G42.1014+0.8817	3210600	19:05:06.65	+08:33:31.61	0.53	0.09	0.54	0.09	0.42	-1.0	0.42	-1.0	-0.01	-1.0	4	0
G42.1025+0.9869	3213100	19:04:44.07	+08:36:28.87	0.3	0.05	0.3	0.05	0.42	-1.0	0.42	-1.0	-0.03	-1.0	4	0
G42.1091-0.4468	1155600	19:09:53.55	+07:57:15.42	1.12	0.07	5.0	0.4	1.0	0.04	0.79	0.03	-6.35	0.17	0	0
G42.1093-0.4470	1155601	19:09:53.60	+07:57:15.79	0.6	0.07	0.71	0.11	0.47	0.04	0.44	0.03	82.14	0.23	0	0
G42.1156+0.8733	3211200	19:05:10.03	+08:34:03.16	0.34	0.06	0.35	0.06	0.42	-1.0	0.42	-1.0	-0.01	-1.0	4	0
G42.1163+0.7413	3121800	19:05:38.58	+08:30:27.40	1.02	0.18	1.03	0.18	0.42	-1.0	0.42	-1.0	-0.04	-1.0	4	0
G42.1167+0.0819	2132900	19:08:00.66	+08:12:17.17	0.63	0.1	0.64	0.1	0.42	-1.0	0.42	-1.0	0.01	-1.0	4	0
G42.1244+0.9872	3214100	19:04:46.46	+08:37:39.61	0.33	0.05	0.33	0.05	0.42	-1.0	0.42	-1.0	-0.02	-1.0	4	0
G42.1281+0.2045	2136100	19:07:35.55	+08:16:16.77	0.49	0.09	0.49	0.09	0.42	-1.0	0.42	-1.0	-0.0	-1.0	4	0
G42.1311-0.4871	1250200	19:10:04.66	+07:57:18.49	1.6	0.26	1.62	0.26	0.42	-1.0	0.42	-1.0	-0.01	-1.0	4	0
G42.1315-0.1357	1343200	19:08:49.15	+08:07:03.39	0.4	0.07	0.41	0.07	0.42	-1.0	0.42	-1.0	-0.01	-1.0	4	0
G42.1408+0.3844	2331500	19:06:58.22	+08:21:55.36	0.62	0.11	0.62	0.11	0.42	-1.0	0.42	-1.0	-0.04	-1.0	4	0
G42.1422+0.3624	2235300	19:07:03.11	+08:21:23.23	0.46	0.08	0.47	0.08	0.42	-1.0	0.42	-1.0	-0.03	-1.0	4	0
G42.1434+1.0360	3312800	19:04:38.05	+08:40:00.76	0.44	0.08	0.45	0.08	0.42	-1.0	0.42	-1.0	-0.04	-1.0	4	0
G42.1453+0.4118	2323300	19:06:52.83	+08:22:54.85	0.46	0.08	0.46	0.08	0.42	-1.0	0.42	-1.0	0.01	-1.0	4	0
G42.1492-0.1080	1344200	19:08:45.16	+08:08:45.82	0.45	0.08	0.46	0.08	0.42	-1.0	0.42	-1.0	-0.01	-1.0	4	0
G42.1609+0.2972	2234700	19:07:19.23	+08:20:35.03	0.44	0.07	0.45	0.08	0.42	-1.0	0.42	-1.0	-0.02	-1.0	4	0
G42.1634+0.9683	3215600	19:04:54.88	+08:39:13.08	0.3	0.05	0.31	0.05	0.42	-1.0	0.42	-1.0	-0.02	-1.0	4	0
G42.1634+0.9683	3312100	19:04:54.88	+08:39:13.11	0.32	0.06	0.33	0.06	0.42	-1.0	0.42	-1.0	-0.03	-1.0	4	0
G42.1671+0.3027	2225000	19:07:18.76	+08:21:04.04	2.02	0.36	2.04	0.36	0.42	-1.0	0.42	-1.0	0.04	-1.0	4	0
G42.1709+0.0360	2143500	19:08:16.59	+08:13:54.06	1.25	0.19	1.23	0.22	0.49	0.04	0.35	0.02	-24.61	0.28	0	0
G42.1709+0.0360	2134000	19:08:16.59	+08:13:54.06	1.48	0.17	1.34	0.17	0.43	0.02	0.37	0.02	-10.62	0.45	0	0
G42.1735+0.1157	2230800	19:07:59.72	+08:16:14.61	0.66	0.11	0.67	0.11	0.42	-1.0	0.42	-1.0	0.0	-1.0	4	0
G42.1774-0.4555	1253400	19:10:03.05	+08:00:39.04	0.36	0.07	0.37	0.07	0.42	-1.0	0.42	-1.0	-0.01	-1.0	4	0
G42.1776+0.9731	3216200	19:04:55.41	+08:40:06.28	0.34	0.06	0.35	0.06	0.42	-1.0	0.42	-1.0	-0.02	-1.0	4	0
G42.1776+0.9731	3313000	19:04:55.41	+08:40:06.28	0.3	0.05	0.31	0.05	0.42	-1.0	0.42	-1.0	-0.03	-1.0	4	0
G42.1850-0.1191	2140500	19:08:51.55	+08:10:21.72	0.95	0.17	0.96	0.17	0.42	-1.0	0.42	-1.0	-0.01	-1.0	4	0
G42.1855-0.4587	1159200	19:10:04.66	+08:00:59.49	1.57	0.28	1.58	0.28	0.42	-1.0	0.42	-1.0	-0.0	-1.0	4	0
G42.1863+0.2189	2233700	19:07:38.95	+08:19:46.55	0.41	0.07	0.41	0.07	0.42	-1.0	0.42	-1.0	-0.01	-1.0	4	0
G42.1867+0.0079	2143600	19:08:24.41	+08:13:57.93	0.84	0.15	0.84	0.15	0.42	-1.0	0.42	-1.0	-0.03	-1.0	4	0
G42.1919+0.4198	2326300	19:06:56.29	+08:25:37.38	0.49	0.08	0.49	0.09	0.42	-1.0	0.42	-1.0	0.02	-1.0	4	0
G42.2015+0.3415	2333300	19:07:14.23	+08:23:58.02	0.44	0.08	0.45	0.08	0.42	-1.0	0.42	-1.0	-0.03	-1.0	4	0
G42.2030-0.6248	1155900	19:10:42.31	+07:57:19.44	0.39	0.06	0.4	0.06	0.42	-1.0	0.42	-1.0	0.02	-1.0	4	0

Source Galactic name	Source Index	RA J2000	Dec J2000	Peak (mJy beam^{-1})	error	Integrated (mJy)	error	Major (arcsec)	error	Minor (arcsec)	error	PA (°)	error	flags	aux_flags
G42.2031-0.4839	1254100	19:10:12.05	+08:01:13.93	0.46	0.07	0.46	0.07	0.42	-1.0	0.42	-1.0	-0.0	-1.0	4	0
G42.2047+0.0528	2230700	19:08:16.76	+08:16:10.09	0.56	0.1	0.57	0.1	0.42	-1.0	0.42	-1.0	0.01	-1.0	4	0
G42.2067-0.6516	1153700	19:10:48.47	+07:56:46.49	0.39	0.06	0.39	0.06	0.42	-1.0	0.42	-1.0	0.02	-1.0	4	0
G42.2067-0.6516	1163000	19:10:48.47	+07:56:46.48	0.41	0.06	0.42	0.06	0.42	-1.0	0.42	-1.0	-0.03	-1.0	4	0
G42.2113-0.6316	1156300	19:10:44.71	+07:57:34.48	0.4	0.07	0.41	0.07	0.42	-1.0	0.42	-1.0	0.02	-1.0	4	0
G42.2196+0.8967	3216400	19:05:16.58	+08:40:14.57	0.41	0.06	0.42	0.08	0.44	0.04	0.41	0.03	15.28	2.11	0	0
G42.2196+0.8967	3313200	19:05:16.58	+08:40:14.57	0.38	0.05	0.35	0.06	0.42	0.03	0.39	0.03	89.88	1.77	0	0
G42.2202+0.6678	3210900	19:06:06.01	+08:33:57.87	0.6	0.06	0.54	0.06	0.43	0.01	0.37	0.02	86.75	0.56	0	0
G42.2202+0.6678	3125400	19:06:06.01	+08:33:57.87	0.61	0.06	0.52	0.06	0.42	0.01	0.36	0.02	-89.22	0.42	0	0
G42.2202+0.6678	3115700	19:06:06.01	+08:33:57.88	0.6	0.06	0.51	0.06	0.42	0.01	0.36	0.02	87.96	0.44	0	0
G42.2202+0.6678	3221400	19:06:06.01	+08:33:57.88	0.6	0.06	0.54	0.06	0.42	0.01	0.37	0.02	-89.92	0.57	0	0
G42.2227-0.7345	1162200	19:11:08.10	+07:55:19.67	0.34	0.06	0.35	0.06	0.42	-1.0	0.42	-1.0	-0.02	-1.0	4	0
G42.2232-0.4069	1256900	19:09:57.72	+08:04:25.97	0.44	0.08	0.45	0.08	0.42	-1.0	0.42	-1.0	-0.01	-1.0	4	0
G42.2237+0.8595	3215800	19:05:25.06	+08:39:26.23	0.3	0.05	0.3	0.05	0.42	-1.0	0.42	-1.0	-0.0	-1.0	4	0
G42.2237+0.8595	3312200	19:05:25.06	+08:39:26.21	0.31	0.05	0.31	0.05	0.42	-1.0	0.42	-1.0	-0.01	-1.0	4	0
G42.2295-0.0230	2144400	19:08:35.84	+08:15:23.42	0.6	0.09	0.56	0.1	0.46	0.04	0.36	0.02	-3.96	0.32	0	0
G42.2295-0.0230	2135200	19:08:35.84	+08:15:23.37	0.62	0.1	0.62	0.1	0.42	-1.0	0.42	-1.0	0.03	-1.0	4	0
G42.2347-0.8388	1160400	19:11:31.84	+07:53:04.46	0.53	0.09	0.54	0.1	0.42	-1.0	0.42	-1.0	-0.0	-1.0	4	0
G42.2349+0.9781	3316000	19:05:00.73	+08:43:17.81	0.3	0.05	0.3	0.05	0.42	-1.0	0.42	-1.0	-0.02	-1.0	4	0
G42.2351+0.6745	3211800	19:06:06.22	+08:34:56.86	0.29	0.05	0.29	0.05	0.42	-1.0	0.42	-1.0	0.03	-1.0	4	0
G42.2445+0.9350	3315400	19:05:11.10	+08:42:37.48	0.38	0.05	0.37	0.06	0.42	0.03	0.4	0.03	-17.06	1.82	0	0
G42.2464+0.3071	2326100	19:07:26.65	+08:25:24.94	1.35	0.24	1.36	0.24	0.42	-1.0	0.42	-1.0	0.03	-1.0	4	0
G42.2471-0.1883	2141900	19:09:13.37	+08:11:45.49	1.13	0.09	1.14	0.1	0.47	0.02	0.38	0.01	-13.86	0.2	0	0
G42.2489+0.0538	2147200	19:08:21.48	+08:18:32.75	2.0	0.36	2.02	0.36	0.42	-1.0	0.42	-1.0	-0.03	-1.0	4	0
G42.2496-0.1778	2142700	19:09:11.41	+08:12:10.77	0.7	0.12	0.71	0.12	0.42	-1.0	0.42	-1.0	-0.0	-1.0	4	0
G42.2552-0.6292	1252900	19:10:49.11	+07:59:58.36	0.4	0.06	0.4	0.07	0.42	-1.0	0.42	-1.0	0.02	-1.0	4	0
G42.2568+0.3222	2337100	19:07:24.57	+08:26:23.09	0.58	0.09	0.59	0.09	0.42	-1.0	0.42	-1.0	-0.02	-1.0	4	0
G42.2568+0.3222	2326800	19:07:24.58	+08:26:23.08	0.6	0.1	0.6	0.1	0.42	-1.0	0.42	-1.0	0.03	-1.0	4	0
G42.2672+0.7159	3224400	19:06:00.88	+08:37:47.68	0.29	0.05	0.29	0.05	0.42	-1.0	0.42	-1.0	-0.04	-1.0	4	0
G42.2761+0.6587	3213500	19:06:14.19	+08:36:41.90	0.46	0.08	0.46	0.08	0.42	-1.0	0.42	-1.0	0.03	-1.0	4	0
G42.2774+0.1078	2235600	19:08:13.04	+08:21:33.56	0.46	0.08	0.46	0.08	0.42	-1.0	0.42	-1.0	0.01	-1.0	4	0
G42.2803-0.2475	2142300	19:09:29.82	+08:11:53.12	1.35	0.1	1.43	0.12	0.46	0.01	0.41	0.01	8.96	0.44	0	0
G42.2824+0.1936	2333600	19:07:55.12	+08:24:11.74	0.9	0.12	0.81	0.13	0.45	0.03	0.35	0.02	19.03	0.28	0	0
G42.2827+0.1936	2333700	19:07:55.15	+08:24:12.86	3.96	0.12	3.54	0.12	0.4	0.01	0.4	0.0	9.32	2.01	0	0
G42.2827+0.1938	2333800	19:07:55.10	+08:24:12.94	0.7	0.12	0.7	0.12	0.42	-1.0	0.42	-1.0	-0.01	-1.0	4	0

Source Galactic name	Source Index	RA J2000	Dec J2000	Observed flux density				Major (arcsec)		Minor (arcsec)		PA (°)		flags	aux_flags
				Peak (mJy beam^{-1})	error	Integrated (mJy)	error		error		error		error		
G42.2829+0.1935	2333701	19:07:55.19	+08:24:13.26	1.35	0.12	1.84	0.17	0.64	0.01	0.37	0.0	-89.66	3.47	0	0
G42.2830+0.1937	2333900	19:07:55.17	+08:24:13.87	0.85	0.12	0.91	0.16	0.56	0.05	0.34	0.02	6.63	0.11	0	0
G42.2841-0.2985	2140800	19:09:41.23	+08:10:40.60	0.79	0.14	0.8	0.14	0.42	-1.0	0.42	-1.0	0.02	-1.0	4	0
G42.2880-0.7203	1164500	19:11:12.35	+07:59:11.57	0.39	0.07	0.39	0.07	0.42	-1.0	0.42	-1.0	-0.02	-1.0	4	0
G42.2950+0.8502	3315800	19:05:35.02	+08:42:58.82	0.35	0.06	0.35	0.06	0.42	-1.0	0.42	-1.0	-0.0	-1.0	4	0
G42.2957+0.7124	3312000	19:06:04.81	+08:39:13.25	0.31	0.05	0.31	0.05	0.42	-1.0	0.42	-1.0	0.02	-1.0	4	0
G42.2966+0.9692	4111600	19:05:09.52	+08:46:20.58	0.33	0.06	0.34	0.06	0.42	-1.0	0.42	-1.0	-0.03	-1.0	4	0
G42.3049+0.5519	3222300	19:06:40.43	+08:35:17.06	0.31	0.05	0.31	0.05	0.42	-1.0	0.42	-1.0	-0.01	-1.0	4	0
G42.3108-0.1418	2145300	19:09:10.50	+08:16:25.84	0.53	0.09	0.53	0.09	0.42	-1.0	0.42	-1.0	-0.0	-1.0	4	0
G42.3125+0.5327	3222200	19:06:45.42	+08:35:09.59	0.33	0.05	0.33	0.05	0.42	-1.0	0.42	-1.0	-0.01	-1.0	4	0
G42.3144+0.6679	3321501	19:06:16.50	+08:38:59.25	0.62	0.1	1.17	0.19	0.87	0.0	0.39	0.0	-27.31	1.61	0	0
G42.3144+0.6679	3225801	19:06:16.49	+08:38:59.36	0.52	0.09	0.85	0.14	0.8	0.0	0.36	0.0	-23.19	0.24	0	0
G42.3144+0.6679	3215201	19:06:16.49	+08:38:59.33	0.54	0.08	0.82	0.12	0.7	0.0	0.38	0.0	-23.63	0.34	0	0
G42.3144+0.6679	3311201	19:06:16.49	+08:38:59.25	0.61	0.1	1.23	0.21	0.93	0.0	0.38	0.0	-23.91	0.15	0	0
G42.3144+0.6684	3311500	19:06:16.39	+08:39:00.26	0.54	0.08	0.54	0.08	0.42	-1.0	0.42	-1.0	0.03	-1.0	4	0
G42.3144+0.6684	3321700	19:06:16.39	+08:39:00.26	0.53	0.09	0.54	0.11	0.44	0.03	0.4	0.04	87.91	1.64	0	0
G42.3145+0.6681	3321500	19:06:16.47	+08:38:59.96	3.96	0.1	3.84	0.11	0.41	0.0	0.41	0.0	2.16	2.95	0	0
G42.3145+0.6681	3225800	19:06:16.47	+08:38:59.96	4.31	0.09	4.15	0.09	0.42	0.0	0.41	0.0	9.12	0.46	0	0
G42.3145+0.6681	3215200	19:06:16.47	+08:38:59.96	4.19	0.08	4.05	0.09	0.42	0.0	0.41	0.0	6.57	0.56	0	0
G42.3145+0.6681	3311200	19:06:16.47	+08:38:59.96	3.92	0.1	3.77	0.11	0.42	0.0	0.4	0.0	19.03	0.31	0	0
G42.3147+0.6681	3225802	19:06:16.47	+08:39:00.59	0.35	0.09	0.23	0.06	0.35	0.0	0.34	0.0	2.93	0.45	0	0
G42.3147+0.6681	3215202	19:06:16.47	+08:39:00.58	0.37	0.08	0.23	0.05	0.34	0.0	0.34	0.0	8.49	0.57	0	0
G42.3237+0.0992	2333000	19:08:20.07	+08:23:47.00	0.45	0.08	0.46	0.08	0.42	-1.0	0.42	-1.0	0.01	-1.0	4	0
G42.3239+0.7422	3314400	19:06:01.53	+08:41:32.64	0.37	0.05	0.39	0.07	0.46	0.04	0.4	0.02	-14.07	0.58	0	0
G42.3249-0.5838	1352400	19:10:47.15	+08:04:56.77	0.35	0.06	0.35	0.06	0.42	-1.0	0.42	-1.0	0.01	-1.0	4	0
G42.3316-0.4010	2150400	19:10:08.58	+08:10:21.86	0.95	0.13	0.78	0.12	0.39	0.02	0.37	0.02	87.31	3.03	0	0
G42.3316-0.4010	1357600	19:10:08.59	+08:10:21.97	0.78	0.11	0.55	0.09	0.37	0.02	0.34	0.02	-10.31	0.82	0	0
G42.3323+0.9799	4113800	19:05:11.18	+08:48:32.26	0.3	0.04	0.3	0.04	0.42	-1.0	0.42	-1.0	-0.03	-1.0	4	0
G42.3352+0.1327	2335200	19:08:14.13	+08:25:19.58	0.52	0.09	0.53	0.09	0.42	-1.0	0.42	-1.0	0.01	-1.0	4	0
G42.3421+0.2267	3131100	19:07:54.65	+08:28:17.34	1.79	0.1	1.7	0.11	0.45	0.01	0.37	0.01	87.17	0.24	0	0
G42.3421+0.2267	2338800	19:07:54.66	+08:28:17.32	1.18	0.12	1.15	0.14	0.45	0.01	0.38	0.02	-88.33	0.49	0	0
G42.3433-0.7836	1165300	19:11:32.15	+08:00:22.90	1.0	0.16	1.01	0.16	0.42	-1.0	0.42	-1.0	-0.0	-1.0	4	0
G42.3439+0.0508	2343200	19:08:32.74	+08:23:31.63	1.05	0.18	1.06	0.18	0.42	-1.0	0.42	-1.0	-0.04	-1.0	4	0
G42.3463+0.5166	3223500	19:06:52.66	+08:36:30.92	1.29	0.06	1.42	0.07	0.46	0.01	0.42	0.01	-87.16	0.31	0	0
G42.3535+0.5396	3224000	19:06:48.51	+08:37:31.91	0.66	0.06	0.59	0.06	0.42	0.02	0.38	0.01	-12.11	0.51	0	0

Source Galactic name	Source Index	RA J2000	Dec J2000	Peak (mJy beam^{-1})	error	Integrated (mJy)	error	Major (arcsec)	error	Minor (arcsec)	error	PA (°)	error	flags	aux_flags
G42.3562-0.9370	1163100	19:12:06.55	+07:56:48.66	0.38	0.07	0.38	0.07	0.42	-1.0	0.42	-1.0	0.02	-1.0	4	0
G42.3573+0.9354	4114000	19:05:23.58	+08:48:38.80	0.37	0.05	0.34	0.05	0.45	0.03	0.37	0.02	4.94	0.36	0	0
G42.3586-0.4254	1358500	19:10:16.85	+08:11:07.51	1.0	0.17	1.01	0.17	0.42	-1.0	0.42	-1.0	-0.01	-1.0	4	0
G42.3611+0.7021	3314800	19:06:14.33	+08:42:25.37	2.37	0.06	3.19	0.09	0.52	0.01	0.45	0.0	0.41	0.09	0	0
G42.3611+0.7021	3323900	19:06:14.33	+08:42:25.37	2.37	0.06	3.19	0.09	0.52	0.01	0.45	0.0	0.24	0.1	0	0
G42.3614+0.7018	3314900	19:06:14.41	+08:42:25.70	0.51	0.06	0.45	0.06	0.4	0.02	0.39	0.02	1.38	2.08	0	0
G42.3614+0.7018	3324000	19:06:14.41	+08:42:25.70	0.51	0.06	0.44	0.06	0.39	0.02	0.38	0.02	6.77	2.91	0	0
G42.3616+0.7016	3324200	19:06:14.49	+08:42:26.11	0.74	0.06	0.76	0.07	0.44	0.01	0.42	0.02	82.57	1.1	0	0
G42.3616+0.7016	3315100	19:06:14.49	+08:42:26.11	0.74	0.06	0.76	0.07	0.44	0.01	0.41	0.02	82.88	1.02	0	0
G42.3649+0.0797	2335401	19:08:28.86	+08:25:26.34	0.59	0.1	0.4	0.07	0.36	0.01	0.34	0.01	88.8	0.25	0	0
G42.3650+0.0798	2335400	19:08:28.85	+08:25:26.93	2.17	0.1	3.38	0.19	0.56	0.01	0.49	0.01	83.15	0.27	0	0
G42.3653+0.0799	2335500	19:08:28.87	+08:25:27.95	0.69	0.11	0.74	0.15	0.47	0.05	0.4	0.03	-20.94	0.78	0	0
G42.3660+0.3852	3137300	19:07:23.18	+08:33:56.34	0.42	0.07	0.43	0.07	0.42	-1.0	0.42	-1.0	-0.03	-1.0	4	0
G42.3688-0.3709	2152600	19:10:06.28	+08:13:10.84	1.02	0.18	1.03	0.18	0.42	-1.0	0.42	-1.0	-0.02	-1.0	4	0
G42.3715+0.5777	3226600	19:06:42.32	+08:39:32.76	0.36	0.06	0.36	0.06	0.42	-1.0	0.42	-1.0	-0.01	-1.0	4	0
G42.3785+0.6161	3227700	19:06:34.80	+08:40:58.56	0.55	0.1	0.56	0.1	0.42	-1.0	0.42	-1.0	-0.01	-1.0	4	0
G42.3828+0.9845	4119100	19:05:15.82	+08:51:21.48	0.41	0.05	0.43	0.07	0.51	0.02	0.36	0.03	89.23	0.35	0	0
G42.3847+0.9402	4116900	19:05:25.59	+08:50:14.22	0.26	0.05	0.26	0.05	0.42	-1.0	0.42	-1.0	-0.02	-1.0	4	0
G42.3896-0.2255	2242300	19:09:37.34	+08:18:18.79	0.53	0.09	0.53	0.09	0.42	-1.0	0.42	-1.0	0.01	-1.0	4	0
G42.3922+0.0121	2344900	19:08:46.48	+08:25:01.44	0.53	0.09	0.53	0.09	0.42	-1.0	0.42	-1.0	-0.03	-1.0	4	0
G42.3985+0.0941	2337900	19:08:29.53	+08:27:37.71	0.6	0.1	0.6	0.1	0.42	-1.0	0.42	-1.0	0.02	-1.0	4	0
G42.3994+0.1482	3132200	19:08:17.97	+08:29:10.47	0.32	0.06	0.32	0.06	0.42	-1.0	0.42	-1.0	-0.0	-1.0	4	0
G42.4016+1.0408	4212600	19:05:05.76	+08:53:54.38	0.77	0.13	0.78	0.14	0.42	-1.0	0.42	-1.0	-0.04	-1.0	4	0
G42.4030+0.6927	3325700	19:06:21.02	+08:44:23.69	0.35	0.06	0.35	0.06	0.42	-1.0	0.42	-1.0	-0.03	-1.0	4	0
G42.4158-0.5432	2150600	19:10:48.59	+08:10:54.24	0.5	0.09	0.5	0.09	0.42	-1.0	0.42	-1.0	0.0	-1.0	4	0
G42.4278-0.1953	2245800	19:09:35.10	+08:21:11.08	0.5	0.08	0.51	0.08	0.42	-1.0	0.42	-1.0	0.01	-1.0	4	0
G42.4313-0.5430	2151200	19:10:50.29	+08:11:44.08	0.44	0.07	0.45	0.07	0.42	-1.0	0.42	-1.0	0.0	-1.0	4	0
G42.4341-0.2607	2243900	19:09:49.88	+08:19:42.58	0.79	0.14	0.8	0.14	0.42	-1.0	0.42	-1.0	0.02	-1.0	4	0
G42.4344-0.2604	2244001	19:09:49.85	+08:19:44.02	1.6	0.19	5.22	0.93	1.02	0.03	0.56	0.07	-10.24	0.34	0	0
G42.4346-0.2605	2244000	19:09:49.90	+08:19:44.32	1.57	0.19	4.55	0.77	0.77	0.03	0.67	0.07	88.47	0.69	0	0
G42.4348-0.2604	2244004	19:09:49.89	+08:19:45.10	0.65	0.19	0.99	0.34	0.65	0.03	0.42	0.07	87.42	0.93	0	0
G42.4348-0.2606	2244002	19:09:49.94	+08:19:44.83	0.88	0.19	4.51	1.05	1.11	0.03	0.81	0.07	-16.47	0.46	0	0
G42.4349-0.2605	2244003	19:09:49.93	+08:19:45.41	0.57	0.19	1.01	0.38	0.74	0.03	0.42	0.07	-78.04	0.97	0	0
G42.4374-0.7009	1363700	19:11:24.92	+08:07:41.03	0.37	0.06	0.37	0.07	0.42	-1.0	0.42	-1.0	-0.02	-1.0	4	0
G42.4409+0.6947	3326800	19:06:24.83	+08:46:28.19	0.75	0.14	0.76	0.14	0.42	-1.0	0.42	-1.0	-0.03	-1.0	4	0

Source Galactic name	Source Index	RA J2000	Dec J2000	Observed flux density Peak (mJy beam^{-1})	error	Integrated (mJy)	error	Major (arcsec)	error	Minor (arcsec)	error	PA (°)	error	flags	aux_flags
G42.4463-0.3775	2146100	19:10:16.38	+08:17:07.35	2.03	0.36	2.05	0.36	0.42	-1.0	0.42	-1.0	0.04	-1.0	4	0
G42.4557-0.2456	2245900	19:09:49.05	+08:21:16.47	0.47	0.08	0.47	0.08	0.42	-1.0	0.42	-1.0	0.01	-1.0	4	0
G42.4565+0.6700	3319100	19:06:31.89	+08:46:37.10	1.39	0.24	1.41	0.24	0.42	-1.0	0.42	-1.0	0.04	-1.0	4	0
G42.4585+0.2161	3137400	19:08:09.96	+08:34:11.78	0.96	0.05	1.47	0.09	0.6	0.01	0.45	0.01	-22.78	0.09	0	0
G42.4585+0.2161	3230800	19:08:09.96	+08:34:11.78	1.0	0.05	1.51	0.09	0.59	0.01	0.45	0.01	-20.81	0.1	0	0
G42.4588-0.5833	2151800	19:11:02.04	+08:12:04.87	0.51	0.09	0.51	0.09	0.42	-1.0	0.42	-1.0	0.01	-1.0	4	0
G42.4657+0.2611	3138700	19:08:01.08	+08:35:49.38	0.65	0.12	0.66	0.12	0.42	-1.0	0.42	-1.0	-0.01	-1.0	4	0
G42.4708-0.2910	2255400	19:10:00.51	+08:20:49.12	0.94	0.17	0.95	0.17	0.42	-1.0	0.42	-1.0	-0.03	-1.0	4	0
G42.4718+0.7426	4115600	19:06:17.93	+08:49:26.12	4.95	0.79	6.96	1.52	0.57	0.07	0.44	0.03	25.76	0.57	0	0
G42.4726+0.7421	4115700	19:06:18.15	+08:49:27.94	6.35	0.92	6.04	1.02	0.5	0.04	0.34	0.02	31.1	0.23	0	0
G42.4728+0.7420	4115801	19:06:18.18	+08:49:28.23	7.71	0.92	8.43	1.01	0.51	0.0	0.38	0.0	-32.36	0.36	0	0
G42.4729+0.7421	4115800	19:06:18.15	+08:49:28.84	206.35	0.92	209.93	1.09	0.43	0.0	0.42	0.0	86.92	0.43	0	0
G42.4729+0.7421	4124400	19:06:18.15	+08:49:28.86	278.94	1.71	295.94	2.1	0.45	0.0	0.42	0.0	-89.66	0.07	0	0
G42.4731+0.7420	4116000	19:06:18.20	+08:49:29.44	6.65	0.92	7.09	1.17	0.46	0.03	0.41	0.03	82.11	0.93	0	0
G42.4731+0.7421	4124500	19:06:18.19	+08:49:29.52	12.14	1.75	8.38	1.38	0.35	0.02	0.35	0.02	-7.3	7.0	0	0
G42.4752-0.8816	1361400	19:12:08.00	+08:04:40.77	0.36	0.06	0.36	0.06	0.42	-1.0	0.42	-1.0	0.0	-1.0	4	0
G42.4807+0.9872	4311000	19:05:26.15	+08:56:39.09	0.5	0.08	0.5	0.08	0.42	-1.0	0.42	-1.0	-0.03	-1.0	4	0
G42.4867-0.2130	2247700	19:09:45.51	+08:23:49.53	2.07	0.36	2.09	0.36	0.42	-1.0	0.42	-1.0	0.01	-1.0	4	0
G42.4914+0.0115	3133600	19:08:57.70	+08:30:17.53	0.65	0.07	0.55	0.06	0.4	0.01	0.37	0.02	-89.01	1.02	0	0
G42.4914+0.0115	3143600	19:08:57.70	+08:30:17.53	0.65	0.06	0.55	0.06	0.4	0.01	0.37	0.02	-88.81	0.92	0	0
G42.4986+0.3338	3322000	19:07:49.07	+08:39:34.97	0.29	0.05	0.29	0.05	0.42	-1.0	0.42	-1.0	0.03	-1.0	4	0
G42.4986+0.3338	3330700	19:07:49.07	+08:39:34.97	0.3	0.05	0.3	0.05	0.42	-1.0	0.42	-1.0	-0.03	-1.0	4	0
G42.4986+0.3338	3226700	19:07:49.07	+08:39:34.96	0.29	0.05	0.29	0.05	0.42	-1.0	0.42	-1.0	0.03	-1.0	4	0
G42.4986+0.3338	3234900	19:07:49.07	+08:39:34.96	0.29	0.05	0.29	0.05	0.42	-1.0	0.42	-1.0	-0.03	-1.0	4	0
G42.5140-0.5145	2252400	19:10:53.42	+08:16:55.68	1.54	0.09	1.39	0.09	0.41	0.01	0.39	0.01	-0.91	0.69	0	0
G42.5140-0.5145	2155300	19:10:53.42	+08:16:55.68	1.51	0.09	1.37	0.1	0.41	0.01	0.4	0.01	-0.97	1.65	0	0
G42.5183+0.5055	3326100	19:07:14.28	+08:45:22.47	0.39	0.07	0.39	0.07	0.42	-1.0	0.42	-1.0	0.0	-1.0	4	0
G42.5208-0.0207	3144100	19:09:07.93	+08:30:57.88	0.34	0.06	0.34	0.06	0.42	-1.0	0.42	-1.0	-0.03	-1.0	4	0
G42.5266-0.6069	2153800	19:11:14.70	+08:15:02.11	0.47	0.08	0.48	0.08	0.42	-1.0	0.42	-1.0	0.02	-1.0	4	0
G42.5349+0.9272	4312100	19:05:45.14	+08:57:53.18	0.35	0.06	0.35	0.06	0.42	-1.0	0.42	-1.0	-0.02	-1.0	4	0
G42.5417+0.7015	4221400	19:06:34.62	+08:52:01.71	0.33	0.06	0.33	0.06	0.42	-1.0	0.42	-1.0	-0.04	-1.0	4	0
G42.5440-0.6026	2251600	19:11:15.75	+08:16:04.77	1.41	0.13	1.34	0.14	0.42	0.01	0.4	0.02	-89.17	1.45	0	0
G42.5440-0.6026	2154900	19:11:15.75	+08:16:04.80	1.18	0.09	1.04	0.09	0.41	0.01	0.38	0.01	-24.04	0.73	0	0
G42.5524+0.0071	3240400	19:09:05.47	+08:33:25.16	0.56	0.1	0.57	0.1	0.42	-1.0	0.42	-1.0	-0.03	-1.0	4	0
G42.5524+0.0071	3230500	19:09:05.48	+08:33:25.15	0.56	0.1	0.57	0.1	0.42	-1.0	0.42	-1.0	0.02	-1.0	4	0

Source Galactic name	Source Index	RA J2000	Dec J2000	Observed flux density				Major (arcsec)		Minor (arcsec)		PA (°)		flags	aux_flags
				Peak (mJy beam^{-1})	error	Integrated (mJy)	error		error		error		error		
G42.5564-0.2367	2346600	19:09:58.40	+08:26:52.88	0.44	0.08	0.45	0.08	0.42	-1.0	0.42	-1.0	0.01	-1.0	4	0
G42.5573-0.8646	1365500	19:12:13.56	+08:09:30.76	0.53	0.08	0.58	0.13	0.48	0.03	0.41	0.05	87.77	1.09	0	0
G42.5590+0.3098	3332500	19:08:01.00	+08:42:08.40	0.35	0.06	0.35	0.06	0.42	-1.0	0.42	-1.0	-0.02	-1.0	4	0
G42.5602+0.2278	3331000	19:08:18.80	+08:39:56.10	0.33	0.06	0.34	0.06	0.42	-1.0	0.42	-1.0	-0.01	-1.0	4	0
G42.5602+0.2278	3235400	19:08:18.80	+08:39:56.10	0.36	0.05	0.36	0.05	0.42	-1.0	0.42	-1.0	-0.01	-1.0	4	0
G42.5608-0.2201	2347600	19:09:55.33	+08:27:34.59	0.61	0.1	0.62	0.11	0.42	-1.0	0.42	-1.0	0.01	-1.0	4	0
G42.5638+0.6128	4127700	19:06:56.20	+08:50:45.38	0.34	0.05	0.35	0.05	0.42	-1.0	0.42	-1.0	-0.02	-1.0	4	0
G42.5714-0.5643	2254100	19:11:10.57	+08:18:35.91	0.57	0.09	0.58	0.09	0.42	-1.0	0.42	-1.0	0.01	-1.0	4	0
G42.5767-0.1201	3144500	19:09:35.59	+08:31:11.46	0.29	0.05	0.3	0.05	0.42	-1.0	0.42	-1.0	-0.01	-1.0	4	0
G42.5816-0.9711	1363900	19:12:39.17	+08:07:50.82	0.43	0.07	0.44	0.08	0.42	-1.0	0.42	-1.0	0.02	-1.0	4	0
G42.5820-0.6711	2164000	19:11:34.74	+08:16:12.00	0.45	0.08	0.46	0.08	0.42	-1.0	0.42	-1.0	-0.03	-1.0	4	0
G42.5935-0.9315	1365600	19:12:32.00	+08:09:34.76	0.38	0.06	0.38	0.06	0.42	-1.0	0.42	-1.0	0.02	-1.0	4	0
G42.5951-0.3801	2355600	19:10:33.62	+08:24:58.12	0.48	0.09	0.49	0.09	0.42	-1.0	0.42	-1.0	-0.02	-1.0	4	0
G42.6023+0.0056	3138900	19:09:11.37	+08:36:01.98	0.96	0.14	0.97	0.14	0.42	-1.0	0.42	-1.0	0.03	-1.0	4	0
G42.6023+0.0056	3149200	19:09:11.37	+08:36:01.98	0.97	0.15	0.98	0.15	0.42	-1.0	0.42	-1.0	-0.02	-1.0	4	0
G42.6035+0.6557	4212800	19:06:51.38	+08:54:03.36	7.54	0.09	7.38	0.1	0.42	0.0	0.41	0.0	-82.56	0.43	0	0
G42.6035+0.6557	4223300	19:06:51.38	+08:54:03.36	7.88	0.08	7.85	0.09	0.42	0.0	0.42	0.0	-1.02	1.07	0	0
G42.6100+0.2603	3333600	19:08:17.36	+08:43:29.23	0.28	0.05	0.28	0.05	0.42	-1.0	0.42	-1.0	-0.01	-1.0	4	0
G42.6152+0.1517	3331500	19:08:41.34	+08:40:45.48	0.32	0.06	0.32	0.06	0.42	-1.0	0.42	-1.0	0.0	-1.0	4	0
G42.6162+0.8010	4313000	19:06:21.44	+08:58:44.54	0.33	0.06	0.33	0.06	0.42	-1.0	0.42	-1.0	0.0	-1.0	4	0
G42.6176+0.7057	4213700	19:06:42.16	+08:56:11.21	0.54	0.05	0.56	0.06	0.45	0.02	0.4	0.02	3.28	0.56	0	0
G42.6176+0.7057	4225100	19:06:42.16	+08:56:11.21	0.54	0.05	0.54	0.06	0.43	0.02	0.41	0.02	6.43	0.97	0	0
G42.6176+0.7057	4310600	19:06:42.16	+08:56:11.20	0.54	0.09	0.55	0.09	0.42	-1.0	0.42	-1.0	0.02	-1.0	4	0
G42.6176+0.7057	4320600	19:06:42.16	+08:56:11.20	0.54	0.09	0.54	0.09	0.42	-1.0	0.42	-1.0	-0.04	-1.0	4	0
G42.6204-0.7852	2162900	19:12:03.56	+08:15:04.46	0.52	0.09	0.53	0.09	0.42	-1.0	0.42	-1.0	-0.01	-1.0	4	0
G42.6207+0.6079	4222800	19:07:03.62	+08:53:39.17	0.51	0.06	0.49	0.06	0.42	0.02	0.41	0.02	78.82	1.95	0	0
G42.6220+0.5786	41210800	19:07:10.08	+08:52:54.89	0.46	0.08	0.47	0.08	0.42	-1.0	0.42	-1.0	-0.01	-1.0	4	0
G42.6222+0.1801	3332200	19:08:36.01	+08:41:55.07	0.41	0.05	0.37	0.05	0.41	0.02	0.39	0.02	15.09	1.36	0	0
G42.6254+0.7811	4312900	19:06:26.78	+08:58:40.97	0.29	0.05	0.29	0.05	0.42	-1.0	0.42	-1.0	0.01	-1.0	4	0
G42.6277+0.2663	3334200	19:08:18.06	+08:44:35.58	0.32	0.05	0.32	0.05	0.42	-1.0	0.42	-1.0	-0.01	-1.0	4	0
G42.6279-0.5844	2255700	19:11:21.22	+08:21:02.82	0.45	0.08	0.45	0.08	0.42	-1.0	0.42	-1.0	0.02	-1.0	4	0
G42.6306+0.5774	41211000	19:07:11.30	+08:53:20.47	1.06	0.1	1.05	0.12	0.42	0.02	0.41	0.02	-10.2	2.48	0	0
G42.6306+0.5774	4222300	19:07:11.30	+08:53:20.47	1.21	0.06	1.17	0.07	0.42	0.01	0.41	0.01	-89.52	0.95	0	0
G42.6339-0.7156	2253100	19:11:50.12	+08:17:43.57	0.83	0.14	0.84	0.15	0.42	-1.0	0.42	-1.0	0.03	-1.0	4	0
G42.6353+0.0356	3233700	19:09:08.61	+08:38:37.06	0.52	0.06	0.47	0.06	0.41	0.02	0.39	0.02	-89.72	2.07	0	0

Source Galactic name	Source Index	RA J2000	Dec J2000	Observed flux density Peak (mJy beam^{-1})	error	Integrated (mJy)	error	Major (arcsec)	error	Minor (arcsec)	error	PA (°)	error	flags	aux_flags
G42.6353+0.0356	3245000	19:09:08.61	+08:38:37.07	0.5	0.06	0.44	0.06	0.4	0.02	0.38	0.02	88.31	1.94	0	0
G42.6417-0.0328	3232800	19:09:24.06	+08:37:04.19	0.6	0.11	0.61	0.11	0.42	-1.0	0.42	-1.0	0.03	-1.0	4	0
G42.6418-0.7214	2253600	19:11:52.26	+08:17:58.91	1.41	0.24	1.42	0.25	0.42	-1.0	0.42	-1.0	0.03	-1.0	4	0
G42.6431-0.1072	3241700	19:09:40.24	+08:35:05.06	0.35	0.06	0.35	0.06	0.42	-1.0	0.42	-1.0	-0.01	-1.0	4	0
G42.6444-0.0417	3232700	19:09:26.29	+08:36:57.93	1.27	0.23	1.28	0.23	0.42	-1.0	0.42	-1.0	0.04	-1.0	4	0
G42.6458-0.5856	2351900	19:11:23.50	+08:21:58.21	0.64	0.1	0.57	0.1	0.46	0.03	0.34	0.01	49.57	0.4	0	0
G42.6465-0.5852	2352100	19:11:23.50	+08:22:00.98	0.66	0.1	0.67	0.1	0.42	-1.0	0.42	-1.0	0.01	-1.0	4	0
G42.6465-0.5852	2256500	19:11:23.50	+08:22:00.98	0.62	0.1	0.62	0.1	0.42	-1.0	0.42	-1.0	0.02	-1.0	4	0
G42.6465-0.5855	2256400	19:11:23.55	+08:22:00.31	4.11	0.1	4.39	0.12	0.46	0.0	0.41	0.0	-12.23	0.11	0	0
G42.6465-0.5855	2352000	19:11:23.55	+08:22:00.32	3.98	0.1	4.14	0.12	0.46	0.0	0.4	0.0	-9.78	0.09	0	0
G42.6466+0.3078	4121300	19:08:11.23	+08:46:44.60	0.65	0.12	0.66	0.12	0.42	-1.0	0.42	-1.0	0.03	-1.0	4	0
G42.6513+0.2601	3335400	19:08:22.04	+08:45:40.85	0.32	0.06	0.32	0.06	0.42	-1.0	0.42	-1.0	-0.01	-1.0	4	0
G42.6526+0.9453	5111300	19:05:54.36	+09:04:39.41	0.86	0.06	3.08	0.24	0.86	0.02	0.73	0.03	-83.0	0.35	0	0
G42.6534+0.9454	5111401	19:05:54.42	+09:04:42.25	0.71	0.08	0.55	0.06	0.38	0.01	0.36	0.0	80.61	0.65	0	0
G42.6535+0.9455	5111400	19:05:54.42	+09:04:42.89	2.75	0.08	2.71	0.09	0.42	0.01	0.41	0.0	5.92	0.6	0	0
G42.6538-0.7482	2165400	19:11:59.37	+08:17:52.74	0.9	0.16	0.91	0.16	0.42	-1.0	0.42	-1.0	-0.01	-1.0	4	0
G42.6545-1.0124	1366100	19:12:56.23	+08:10:34.48	1.1	0.18	1.11	0.18	0.42	-1.0	0.42	-1.0	0.03	-1.0	4	0
G42.6548-0.9587	2161500	19:12:44.72	+08:12:05.07	0.48	0.08	0.49	0.08	0.42	-1.0	0.42	-1.0	0.02	-1.0	4	0
G42.6549+0.9459	5111500	19:05:54.50	+09:04:47.78	0.46	0.06	0.83	0.16	0.71	0.07	0.45	0.03	29.29	0.24	0	0
G42.6576-0.1343	3147900	19:09:47.69	+08:35:06.22	0.55	0.08	0.38	0.06	0.36	0.02	0.34	0.02	77.34	1.38	0	0
G42.6576-0.1343	3241800	19:09:47.69	+08:35:06.19	0.31	0.06	0.31	0.06	0.42	-1.0	0.42	-1.0	-0.01	-1.0	4	0
G42.6577+0.4617	4220800	19:07:39.29	+08:51:35.20	2.01	0.07	1.91	0.08	0.41	0.01	0.41	0.01	5.56	1.33	0	0
G42.6577+0.4617	4129600	19:07:39.29	+08:51:35.21	1.91	0.06	1.73	0.06	0.4	0.01	0.39	0.0	-0.69	0.83	0	0
G42.6649+0.4266	4220500	19:07:47.66	+08:51:00.16	1.5	0.1	1.37	0.11	0.41	0.01	0.4	0.01	4.44	1.52	0	0
G42.6649+0.4266	4128100	19:07:47.66	+08:51:00.18	1.65	0.06	1.59	0.07	0.42	0.01	0.41	0.01	11.89	0.71	0	0
G42.6682+0.7752	4315100	19:06:32.84	+09:00:48.11	0.34	0.06	0.35	0.06	0.42	-1.0	0.42	-1.0	0.01	-1.0	4	0
G42.6685-0.7019	2264400	19:11:51.06	+08:19:56.69	0.43	0.08	0.44	0.08	0.42	-1.0	0.42	-1.0	-0.02	-1.0	4	0
G42.6699+0.5121	4222600	19:07:29.76	+08:53:37.84	0.36	0.05	0.41	0.08	0.48	0.05	0.42	0.03	-2.54	1.0	0	0
G42.6706+0.3301	4122800	19:08:09.09	+08:48:38.56	0.26	0.05	0.27	0.05	0.42	-1.0	0.42	-1.0	0.03	-1.0	4	0
G42.6706+0.3301	4132900	19:08:09.09	+08:48:38.54	0.26	0.05	0.26	0.05	0.42	-1.0	0.42	-1.0	-0.03	-1.0	4	0
G42.6730+0.3868	4220100	19:07:57.14	+08:50:20.34	1.2	0.21	1.21	0.22	0.42	-1.0	0.42	-1.0	0.01	-1.0	4	0
G42.6730+1.0205	5114200	19:05:40.41	+09:07:48.80	0.29	0.05	0.29	0.05	0.42	-1.0	0.42	-1.0	-0.03	-1.0	4	0
G42.6754-0.0308	3330400	19:09:27.41	+08:38:54.90	0.52	0.09	0.53	0.09	0.42	-1.0	0.42	-1.0	0.03	-1.0	4	0
G42.6759-0.1094	3243700	19:09:44.39	+08:36:45.91	0.33	0.06	0.33	0.06	0.42	-1.0	0.42	-1.0	-0.01	-1.0	4	0
G42.6792+0.2011	3335300	19:08:37.86	+08:45:32.07	0.4	0.07	0.41	0.07	0.42	-1.0	0.42	-1.0	-0.0	-1.0	4	0

Source Galactic name	Source Index	RA J2000	Dec J2000	Observed flux density				Major (arcsec)		Minor (arcsec)		PA (°)		flags	aux_flags
				Peak (mJy beam^{-1})	error	Integrated (mJy)	error		error		error		error		
G42.6982-0.1478	3244000	19:09:55.15	+08:36:53.51	0.99	0.06	0.93	0.06	0.44	0.01	0.38	0.01	-4.76	0.24	0	0
G42.7129+0.3659	4221200	19:08:06.12	+08:51:53.04	0.27	0.05	0.28	0.05	0.42	-1.0	0.42	-1.0	0.02	-1.0	4	0
G42.7131+0.8739	5112600	19:06:16.55	+09:05:54.95	0.59	0.06	0.55	0.06	0.44	0.02	0.37	0.01	-22.07	0.37	0	0
G42.7136-0.5555	2357000	19:11:24.63	+08:26:24.43	0.53	0.09	0.54	0.09	0.42	-1.0	0.42	-1.0	0.01	-1.0	4	0
G42.7259-0.6005	2356300	19:11:35.68	+08:25:48.71	0.54	0.1	0.55	0.1	0.42	-1.0	0.42	-1.0	0.02	-1.0	4	0
G42.7306+0.9215	5210200	19:06:08.20	+09:08:09.62	0.89	0.16	0.9	0.16	0.42	-1.0	0.42	-1.0	-0.02	-1.0	4	0
G42.7325+0.0598	3334000	19:09:14.29	+08:44:27.84	0.3	0.05	0.3	0.05	0.42	-1.0	0.42	-1.0	0.02	-1.0	4	0
G42.7358+0.5008	4321100	19:07:39.59	+08:56:49.68	0.42	0.08	0.42	0.08	0.42	-1.0	0.42	-1.0	-0.0	-1.0	4	0
G42.7369-0.0798	3246200	19:09:44.85	+08:40:49.96	0.46	0.08	0.46	0.08	0.42	-1.0	0.42	-1.0	-0.01	-1.0	4	0
G42.7370+0.0990	3335500	19:09:06.35	+08:45:47.24	0.4	0.07	0.41	0.07	0.42	-1.0	0.42	-1.0	0.02	-1.0	4	0
G42.7395-0.1631	3340700	19:10:03.07	+08:38:39.96	0.57	0.09	0.57	0.09	0.42	-1.0	0.42	-1.0	-0.01	-1.0	4	0
G42.7403-0.1004	3342000	19:09:49.67	+08:40:26.54	0.33	0.06	0.33	0.06	0.42	-1.0	0.42	-1.0	-0.01	-1.0	4	0
G42.7449+0.5031	4225900	19:07:40.10	+08:57:22.87	0.36	0.06	0.36	0.06	0.42	-1.0	0.42	-1.0	0.0	-1.0	4	0
G42.7450-0.5198	2359400	19:11:20.48	+08:29:04.32	1.97	0.35	1.99	0.35	0.42	-1.0	0.42	-1.0	0.01	-1.0	4	0
G42.7455+0.2877	4135200	19:08:26.62	+08:51:27.61	0.27	0.05	0.28	0.05	0.42	-1.0	0.42	-1.0	-0.02	-1.0	4	0
G42.7539-0.0418	3333000	19:09:38.56	+08:42:47.68	1.37	0.23	1.38	0.23	0.42	-1.0	0.42	-1.0	0.04	-1.0	4	0
G42.7549-0.5284	3151200	19:11:23.43	+08:29:21.44	0.45	0.07	0.42	0.08	0.48	0.05	0.34	0.02	8.36	0.21	0	0
G42.7656+0.9255	5116700	19:06:11.27	+09:10:08.11	0.41	0.07	0.42	0.07	0.42	-1.0	0.42	-1.0	-0.01	-1.0	4	0
G42.7684+0.1823	4134200	19:08:51.90	+08:49:45.67	0.4	0.05	0.42	0.06	0.48	0.02	0.39	0.03	87.46	0.49	0	0
G42.7701-0.8970	2264300	19:12:44.41	+08:19:55.62	1.76	0.09	1.86	0.11	0.44	0.01	0.42	0.01	8.18	0.59	0	0
G42.7729-0.3438	3252800	19:10:45.73	+08:35:26.13	0.31	0.05	0.31	0.05	0.42	-1.0	0.42	-1.0	-0.03	-1.0	4	0
G42.7729-0.3438	3242200	19:10:45.73	+08:35:26.13	0.3	0.05	0.31	0.05	0.42	-1.0	0.42	-1.0	0.03	-1.0	4	0
G42.7733-0.3355	3148900	19:10:43.99	+08:35:41.23	0.6	0.11	0.61	0.11	0.42	-1.0	0.42	-1.0	0.03	-1.0	4	0
G42.7736+0.6178	4326900	19:07:18.57	+09:02:04.57	0.33	0.06	0.33	0.06	0.42	-1.0	0.42	-1.0	-0.02	-1.0	4	0
G42.7770+0.4976	4324001	19:07:44.88	+08:58:56.39	0.6	0.07	0.47	0.06	0.41	0.0	0.34	0.0	-32.15	1.11	0	0
G42.7770+0.4978	4324000	19:07:44.82	+08:58:56.48	6.73	0.07	6.79	0.08	0.42	0.0	0.42	0.0	85.05	1.24	0	0
G42.7770+0.4978	4227600	19:07:44.83	+08:58:56.47	5.9	0.13	6.05	0.16	0.44	0.0	0.41	0.0	0.78	0.25	0	0
G42.7783-0.9558	2263100	19:12:57.98	+08:18:43.85	0.48	0.08	0.49	0.08	0.42	-1.0	0.42	-1.0	0.02	-1.0	4	0
G42.7784+0.4629	4322500	19:07:52.53	+08:58:03.19	0.49	0.06	0.41	0.06	0.43	0.03	0.34	0.01	13.9	0.27	0	0
G42.7784+0.4629	4226500	19:07:52.53	+08:58:03.19	0.43	0.07	0.44	0.07	0.42	-1.0	0.42	-1.0	0.01	-1.0	4	0
G42.7834+0.3626	4224500	19:08:14.71	+08:55:32.72	0.26	0.05	0.26	0.05	0.42	-1.0	0.42	-1.0	0.03	-1.0	4	0
G42.7887+0.8345	5115000	19:06:33.48	+09:08:51.25	0.37	0.05	0.37	0.05	0.42	-1.0	0.42	-1.0	0.0	-1.0	4	0
G42.7897+0.5654	4326300	19:07:31.66	+09:01:29.02	0.58	0.05	0.56	0.06	0.42	0.02	0.41	0.02	8.87	1.82	0	0
G42.7965-0.4813	3153900	19:11:17.97	+08:32:52.68	0.43	0.07	0.43	0.08	0.47	0.05	0.37	0.02	20.13	0.42	0	0
G42.8048+1.0349	5217000	19:05:52.01	+09:15:14.21	0.6	0.1	0.6	0.1	0.42	-1.0	0.42	-1.0	-0.03	-1.0	4	0

Source Galactic name	Source Index	RA J2000	Dec J2000	Observed flux density				Major (arcsec)		Minor (arcsec)		PA (°)		flags	aux_flags
				Peak (mJy beam^{-1})	error	Integrated (mJy)	error		error		error		error		
G42.8093-0.4427	3155400	19:11:11.10	+08:34:37.55	0.37	0.07	0.37	0.07	0.42	-1.0	0.42	-1.0	-0.01	-1.0	4	0
G42.8118-0.1875	3343200	19:10:16.44	+08:41:50.31	0.35	0.05	0.36	0.05	0.42	-1.0	0.42	-1.0	0.0	-1.0	4	0
G42.8127+0.4903	4325600	19:07:50.45	+09:00:38.19	0.3	0.05	0.3	0.05	0.42	-1.0	0.42	-1.0	0.0	-1.0	4	0
G42.8224+0.0253	4143200	19:09:31.78	+08:48:17.67	0.42	0.05	0.38	0.05	0.42	0.02	0.38	0.02	-6.76	0.61	0	0
G42.8224+0.0253	4132400	19:09:31.78	+08:48:17.67	0.42	0.05	0.39	0.05	0.42	0.02	0.39	0.02	-7.03	1.31	0	0
G42.8279+0.0202	4132700	19:09:33.49	+08:48:26.75	0.28	0.05	0.28	0.05	0.42	-1.0	0.42	-1.0	0.02	-1.0	4	0
G42.8279+0.0202	4143400	19:09:33.49	+08:48:26.75	0.28	0.05	0.28	0.05	0.42	-1.0	0.42	-1.0	-0.03	-1.0	4	0
G42.8283+0.6969	5124500	19:07:07.61	+09:07:10.35	0.33	0.06	0.33	0.06	0.42	-1.0	0.42	-1.0	-0.04	-1.0	4	0
G42.8312+0.2995	4330600	19:08:33.68	+08:56:20.99	0.58	0.1	0.59	0.1	0.42	-1.0	0.42	-1.0	-0.03	-1.0	4	0
G42.8314-0.6073	3152500	19:11:49.00	+08:31:14.05	0.38	0.06	0.38	0.06	0.42	-1.0	0.42	-1.0	0.02	-1.0	4	0
G42.8354+0.3128	4235400	19:08:31.27	+08:56:56.29	0.32	0.06	0.33	0.06	0.42	-1.0	0.42	-1.0	-0.02	-1.0	4	0
G42.8642-0.1045	3346600	19:10:04.45	+08:46:55.57	1.39	0.23	1.41	0.23	0.42	-1.0	0.42	-1.0	-0.01	-1.0	4	0
G42.8650+1.0027	5312800	19:06:05.68	+09:17:33.58	0.34	0.06	0.35	0.06	0.42	-1.0	0.42	-1.0	-0.03	-1.0	4	0
G42.8666-0.3752	3341300	19:11:03.01	+08:39:32.92	0.56	0.1	0.57	0.1	0.42	-1.0	0.42	-1.0	0.03	-1.0	4	0
G42.8695-0.4368	3254400	19:11:16.59	+08:37:59.88	0.38	0.06	0.38	0.07	0.43	0.04	0.41	0.03	10.77	1.6	0	0
G42.8808-0.0135	4145500	19:09:46.69	+08:50:19.87	0.26	0.04	0.26	0.05	0.42	-1.0	0.42	-1.0	-0.03	-1.0	4	0
G42.8886+0.0921	4137200	19:09:24.81	+08:53:40.11	1.07	0.19	1.08	0.2	0.42	-1.0	0.42	-1.0	0.02	-1.0	4	0
G42.8922-0.1643	3346500	19:10:20.46	+08:46:45.35	1.45	0.24	1.47	0.24	0.42	-1.0	0.42	-1.0	0.01	-1.0	4	0
G42.8936+0.5720	5125101	19:07:41.88	+09:07:12.00	3.19	0.6	4.19	0.86	0.52	0.03	0.45	0.02	-70.68	0.37	0	0
G42.8937+0.5714	5124700	19:07:42.00	+09:07:11.37	3.26	0.54	3.51	0.75	0.45	0.05	0.42	0.04	-12.58	2.0	0	0
G42.8937+0.5719	5125100	19:07:41.90	+09:07:12.35	3.59	0.6	3.25	0.59	0.47	0.03	0.34	0.02	-44.4	0.31	0	0
G42.8939+0.5711	5124800	19:07:42.09	+09:07:11.42	2.96	0.52	2.99	0.52	0.42	-1.0	0.42	-1.0	-0.01	-1.0	4	0
G42.8939+0.5715	5124904	19:07:42.01	+09:07:12.32	3.11	0.7	7.41	1.66	0.7	0.0	0.6	0.0	-75.64	0.12	0	0
G42.8939+0.5717	5124900	19:07:41.97	+09:07:12.40	72.33	0.7	72.47	0.79	0.43	0.0	0.41	0.0	5.11	0.1	0	0
G42.8940+0.5719	5124903	19:07:41.95	+09:07:13.12	3.74	0.7	2.46	0.46	0.34	0.0	0.34	0.0	27.48	0.1	0	0
G42.8940+0.5719	5125400	19:07:41.94	+09:07:13.12	3.68	0.54	2.92	0.5	0.39	0.02	0.36	0.02	-82.62	1.39	0	0
G42.8941+0.5716	5124901	19:07:42.02	+09:07:13.12	7.36	0.7	10.46	0.99	0.56	0.0	0.45	0.0	22.42	0.09	0	0
G42.8943+0.5715	5124902	19:07:42.07	+09:07:13.57	4.35	0.7	5.87	0.94	0.5	0.0	0.48	0.0	20.57	0.1	0	0
G42.8959+0.5736	5126500	19:07:41.77	+09:07:22.09	6.02	0.35	12.65	0.86	0.74	0.02	0.5	0.01	4.86	0.07	0	0
G42.8960+0.0004	4146400	19:09:45.40	+08:51:31.49	0.31	0.05	0.31	0.05	0.42	-1.0	0.42	-1.0	-0.03	-1.0	4	0
G42.9001-0.0965	4144300	19:10:06.74	+08:49:03.53	11.58	0.08	11.57	0.09	0.42	0.0	0.42	0.0	-84.84	0.64	0	0
G42.9023-0.7023	3153300	19:12:17.41	+08:32:22.21	0.3	0.05	0.3	0.05	0.42	-1.0	0.42	-1.0	0.03	-1.0	4	0
G42.9040-0.3805	3257300	19:11:08.35	+08:41:23.64	0.86	0.15	0.87	0.15	0.42	-1.0	0.42	-1.0	-0.02	-1.0	4	0
G42.9060-0.0839	4145000	19:10:04.68	+08:49:43.26	0.95	0.05	0.92	0.06	0.42	0.01	0.4	0.01	-3.2	0.73	0	0
G42.9072+0.6316	51210000	19:07:30.54	+09:09:34.28	0.29	0.05	0.3	0.05	0.42	-1.0	0.42	-1.0	-0.02	-1.0	4	0

Source Galactic name	Source Index	RA J2000	Dec J2000	Observed flux density Peak (mJy beam^{-1})	error	Integrated (mJy)	error	Major (arcsec)	error	Minor (arcsec)	error	PA (°)	error	flags	aux_flags
G42.9101-0.1434	4143100	19:10:17.97	+08:48:17.48	0.33	0.06	0.34	0.06	0.42	-1.0	0.42	-1.0	-0.01	-1.0	4	0
G42.9169-0.1267	4144800	19:10:15.11	+08:49:06.87	0.26	0.05	0.27	0.05	0.42	-1.0	0.42	-1.0	-0.01	-1.0	4	0
G42.9191-0.4461	3351900	19:11:24.15	+08:40:22.50	0.35	0.06	0.35	0.06	0.42	-1.0	0.42	-1.0	-0.01	-1.0	4	0
G42.9211-0.6432	3252200	19:12:06.80	+08:35:00.77	0.33	0.06	0.33	0.06	0.42	-1.0	0.42	-1.0	0.02	-1.0	4	0
G42.9217+0.2118	4236700	19:09:02.72	+08:58:44.53	0.98	0.14	1.07	0.2	0.47	0.05	0.41	0.03	3.77	0.72	0	0
G42.9217+0.2118	4333200	19:09:02.72	+08:58:44.47	0.56	0.05	0.51	0.05	0.44	0.02	0.37	0.01	15.79	0.31	0	0
G42.9220-0.2931	3356800	19:10:51.54	+08:44:46.24	0.64	0.11	0.65	0.11	0.42	-1.0	0.42	-1.0	-0.03	-1.0	4	0
G42.9246+0.6655	5222500	19:07:25.15	+09:11:26.01	0.73	0.06	0.6	0.05	0.41	0.01	0.35	0.01	89.23	0.37	0	0
G42.9246+0.6655	5213000	19:07:25.15	+09:11:26.02	0.72	0.06	0.59	0.05	0.4	0.01	0.36	0.01	86.25	0.48	0	0
G42.9268+0.4011	4329000	19:08:22.47	+09:04:14.80	1.13	0.21	1.14	0.21	0.42	-1.0	0.42	-1.0	0.02	-1.0	4	0
G42.9318+0.4802	5123100	19:08:05.95	+09:06:41.99	0.28	0.05	0.28	0.05	0.42	-1.0	0.42	-1.0	0.0	-1.0	4	0
G42.9339+0.6418	5222200	19:07:31.32	+09:11:16.60	0.29	0.05	0.29	0.05	0.42	-1.0	0.42	-1.0	-0.03	-1.0	4	0
G42.9365-0.4266	3353000	19:11:21.91	+08:41:50.69	0.3	0.05	0.3	0.05	0.42	-1.0	0.42	-1.0	-0.01	-1.0	4	0
G42.9372-0.2630	3346300	19:10:46.77	+08:46:24.97	0.64	0.11	0.64	0.11	0.42	-1.0	0.42	-1.0	0.02	-1.0	4	0
G42.9486-0.5856	3254500	19:11:57.49	+08:38:04.36	0.35	0.05	0.35	0.05	0.42	-1.0	0.42	-1.0	0.02	-1.0	4	0
G42.9488+0.3647	5120900	19:08:32.77	+09:04:25.01	0.34	0.05	0.34	0.05	0.42	-1.0	0.42	-1.0	0.02	-1.0	4	0
G42.9488+0.3647	5132100	19:08:32.77	+09:04:25.00	0.33	0.05	0.34	0.05	0.42	-1.0	0.42	-1.0	-0.04	-1.0	4	0
G42.9489-0.5419	3351200	19:11:48.11	+08:39:18.02	0.31	0.06	0.31	0.06	0.42	-1.0	0.42	-1.0	0.0	-1.0	4	0
G42.9501-0.5986	3254200	19:12:00.45	+08:37:47.69	0.42	0.06	0.41	0.07	0.47	0.03	0.36	0.02	23.96	0.3	0	0
G42.9530-0.5630	3255300	19:11:53.13	+08:38:56.09	0.76	0.06	0.82	0.08	0.44	0.01	0.43	0.02	2.7	7.77	0	0
G42.9530-0.5631	3350500	19:11:53.14	+08:38:56.04	0.84	0.09	0.93	0.11	0.45	0.02	0.43	0.02	-89.9	1.22	0	0
G42.9568-0.5846	3255000	19:11:58.19	+08:38:32.07	0.3	0.05	0.3	0.05	0.42	-1.0	0.42	-1.0	0.02	-1.0	4	0
G42.9600-0.4683	3353300	19:11:33.52	+08:41:56.04	10.0	0.11	9.91	0.13	0.42	0.0	0.42	0.0	-9.66	0.61	0	0
G42.9613-0.5237	3256800	19:11:45.59	+08:40:27.86	0.44	0.08	0.45	0.08	0.42	-1.0	0.42	-1.0	0.01	-1.0	4	0
G42.9634+0.9145	6110200	19:06:35.73	+09:20:22.21	1.18	0.21	1.19	0.21	0.42	-1.0	0.42	-1.0	-0.02	-1.0	4	0
G42.9737+1.0043	6113000	19:06:17.49	+09:23:23.69	2.0	0.05	2.01	0.06	0.43	0.0	0.41	0.0	-9.58	0.4	0	0
G42.9823-0.5683	3351700	19:11:57.55	+08:40:20.65	0.32	0.06	0.33	0.06	0.42	-1.0	0.42	-1.0	0.01	-1.0	4	0
G42.9917-0.9279	3162700	19:13:15.97	+08:30:50.97	0.42	0.05	0.43	0.06	0.47	0.02	0.39	0.02	18.96	0.4	0	0
G42.9919+0.8760	6110500	19:06:47.22	+09:20:49.57	0.77	0.13	0.78	0.14	0.42	-1.0	0.42	-1.0	-0.01	-1.0	4	0
G42.9957+0.8684	5315600	19:06:49.29	+09:20:49.40	0.34	0.06	0.34	0.06	0.42	-1.0	0.42	-1.0	-0.0	-1.0	4	0
G42.9983+0.0131	4331800	19:09:54.13	+08:57:19.32	0.33	0.06	0.33	0.06	0.42	-1.0	0.42	-1.0	0.02	-1.0	4	0
G42.9985+0.0812	4333800	19:09:39.48	+08:59:12.94	0.32	0.06	0.33	0.06	0.42	-1.0	0.42	-1.0	0.01	-1.0	4	0
G43.0017-0.2969	4143900	19:11:01.30	+08:48:54.62	0.42	0.06	0.43	0.08	0.43	0.04	0.42	0.03	6.27	5.18	0	0
G43.0028-0.2978	4144000	19:11:01.63	+08:48:56.35	0.56	0.06	0.55	0.07	0.46	0.02	0.38	0.02	6.67	0.33	0	0
G43.0028-0.2978	4153600	19:11:01.63	+08:48:56.36	0.51	0.08	0.49	0.1	0.48	0.05	0.35	0.02	8.12	0.32	0	0

Source Galactic name	Source Index	RA J2000	Dec J2000	Observed flux density				Major (arcsec)		Minor (arcsec)		PA (°)		flags	aux_flags
				Peak (mJy beam^{-1})	error	Integrated (mJy)	error		error		error		error		
G43.0034-0.2982	4153700	19:11:01.77	+08:48:57.92	3.2	0.07	5.5	0.14	0.58	0.0	0.53	0.01	89.01	0.18	0	0
G43.0034-0.2982	4144100	19:11:01.77	+08:48:57.93	3.23	0.06	5.78	0.12	0.58	0.0	0.54	0.0	87.44	0.18	0	0
G43.0042+0.4949	51211200	19:08:10.89	+09:10:57.74	0.49	0.08	0.5	0.08	0.42	-1.0	0.42	-1.0	0.01	-1.0	4	0
G43.0049-0.1237	4148000	19:10:24.35	+08:53:52.73	1.34	0.23	1.35	0.23	0.42	-1.0	0.42	-1.0	-0.0	-1.0	4	0
G43.0052+0.0594	4333500	19:09:44.92	+08:58:58.21	0.27	0.05	0.28	0.05	0.42	-1.0	0.42	-1.0	0.02	-1.0	4	0
G43.0079-0.6942	3254700	19:12:27.52	+08:38:12.73	0.28	0.05	0.28	0.05	0.42	-1.0	0.42	-1.0	0.03	-1.0	4	0
G43.0087+0.5478	5223500	19:07:59.97	+09:12:39.99	0.34	0.05	0.35	0.05	0.42	-1.0	0.42	-1.0	-0.01	-1.0	4	0
G43.0149-0.1722	4147400	19:10:35.92	+08:53:04.20	0.54	0.09	0.54	0.09	0.42	-1.0	0.42	-1.0	0.01	-1.0	4	0
G43.0214+0.7071	5324500	19:07:27.01	+09:17:44.33	0.5	0.06	0.47	0.06	0.47	0.02	0.36	0.01	-13.1	0.21	0	0
G43.0214+0.7071	5313100	19:07:27.01	+09:17:44.34	0.5	0.06	0.47	0.06	0.47	0.03	0.35	0.01	-13.98	0.2	0	0
G43.0215+0.6779	5323500	19:07:33.33	+09:16:56.39	0.29	0.05	0.3	0.05	0.42	-1.0	0.42	-1.0	-0.03	-1.0	4	0
G43.0233-0.4765	3357100	19:11:42.39	+08:45:04.49	0.36	0.05	0.36	0.06	0.42	-1.0	0.42	-1.0	-0.0	-1.0	4	0
G43.0252-0.1378	4243200	19:10:29.68	+08:54:34.25	0.34	0.06	0.34	0.06	0.42	-1.0	0.42	-1.0	-0.01	-1.0	4	0
G43.0279+0.0573	4335100	19:09:47.93	+09:00:07.06	0.75	0.05	0.68	0.06	0.41	0.01	0.39	0.01	14.17	1.44	0	0
G43.0279-0.7991	3262800	19:12:52.34	+08:36:21.56	1.01	0.06	0.98	0.06	0.45	0.01	0.38	0.01	-16.8	0.18	0	0
G43.0280+0.1400	4337401	19:09:30.11	+09:02:24.94	3.42	1.21	28.94	11.89	1.42	0.28	1.05	0.07	-50.58	0.22	0	1
G43.0281+0.1400	4337400	19:09:30.11	+09:02:25.18	0.89	1.21	17.24	23.43	2.38	0.2	1.43	0.05	-63.57	0.26	0	2
G43.0283+0.1399	4337402	19:09:30.16	+09:02:25.70	3.19	1.21	18.9	10.08	1.17	0.41	0.9	0.11	-19.74	0.17	0	1
G43.0301-0.0767	4341300	19:10:17.05	+08:56:31.32	10.23	0.13	10.45	0.15	0.44	0.0	0.41	0.0	2.24	0.08	0	0
G43.0301-0.0767	4245400	19:10:17.05	+08:56:31.33	9.22	0.08	9.59	0.09	0.44	0.0	0.41	0.0	1.13	0.08	0	0
G43.0301-0.0769	4341400	19:10:17.10	+08:56:31.26	0.81	0.13	0.7	0.14	0.4	0.03	0.38	0.03	-16.12	2.27	0	0
G43.0331+0.5506	5224800	19:08:02.09	+09:14:02.35	0.34	0.05	0.35	0.05	0.42	-1.0	0.42	-1.0	-0.01	-1.0	4	0
G43.0350-0.0313	4332600	19:10:07.83	+08:58:02.57	1.24	0.1	1.15	0.1	0.41	0.01	0.4	0.01	13.04	1.21	0	0
G43.0350-0.0313	4343600	19:10:07.83	+08:58:02.54	1.23	0.06	1.17	0.07	0.41	0.01	0.4	0.01	9.24	1.86	0	0
G43.0350-0.0314	4236300	19:10:07.83	+08:58:02.56	2.02	0.2	1.88	0.21	0.43	0.01	0.38	0.02	-86.43	0.67	0	0
G43.0350-0.0314	4247200	19:10:07.83	+08:58:02.53	1.35	0.08	1.3	0.09	0.42	0.01	0.4	0.01	-89.21	0.99	0	0
G43.0375+0.1334	5130200	19:09:32.59	+09:02:44.14	1.28	0.23	1.29	0.23	0.42	-1.0	0.42	-1.0	-0.0	-1.0	4	0
G43.0413-0.3290	4155300	19:11:12.66	+08:50:07.55	0.29	0.05	0.29	0.05	0.42	-1.0	0.42	-1.0	-0.03	-1.0	4	0
G43.0475-0.0692	4246600	19:10:17.39	+08:57:39.47	0.69	0.07	0.66	0.07	0.43	0.02	0.39	0.01	-5.67	0.66	0	0
G43.0475-0.0692	4342800	19:10:17.39	+08:57:39.48	0.62	0.06	0.6	0.08	0.42	0.02	0.41	0.02	-85.69	3.58	0	0
G43.0497-0.0659	4343200	19:10:16.92	+08:57:51.86	0.48	0.06	0.42	0.07	0.45	0.03	0.34	0.02	22.97	0.28	0	0
G43.0497-0.0659	4247000	19:10:16.92	+08:57:51.85	0.56	0.07	0.51	0.08	0.4	0.02	0.4	0.02	-78.49	6.57	0	0
G43.0530-0.2588	4147100	19:10:58.85	+08:52:41.82	0.4	0.07	0.41	0.07	0.42	-1.0	0.42	-1.0	0.02	-1.0	4	0
G43.0601-0.2910	4146600	19:11:06.58	+08:52:10.71	0.36	0.06	0.37	0.06	0.42	-1.0	0.42	-1.0	0.02	-1.0	4	0
G43.0609-0.6607	3362000	19:12:26.27	+08:41:57.50	0.28	0.05	0.28	0.05	0.42	-1.0	0.42	-1.0	-0.03	-1.0	4	0

Source Galactic name	Source Index	RA J2000	Dec J2000	Peak (mJy beam^{-1})	error	Integrated (mJy)	error	Major (arcsec)	error	Minor (arcsec)	error	PA (°)	error	flags	aux_flags
G43.0623-0.9135	3261100	19:13:20.83	+08:35:00.36	0.35	0.05	0.35	0.05	0.42	-1.0	0.42	-1.0	0.01	-1.0	4	0
G43.0626-0.9135	3165900	19:13:20.84	+08:35:01.38	1.14	0.06	1.14	0.07	0.46	0.01	0.38	0.01	89.82	0.25	0	0
G43.0626-0.9135	3261300	19:13:20.84	+08:35:01.38	1.26	0.06	1.31	0.07	0.45	0.01	0.41	0.01	-89.82	0.31	0	0
G43.0636-0.7918	3264700	19:12:54.79	+08:38:27.40	0.33	0.06	0.33	0.06	0.42	-1.0	0.42	-1.0	-0.01	-1.0	4	0
G43.0646-0.0419	4334100	19:10:13.42	+08:59:19.49	1.5	0.25	1.51	0.26	0.42	-1.0	0.42	-1.0	0.04	-1.0	4	0
G43.0646-0.4538	4152600	19:11:42.14	+08:47:54.10	0.79	0.05	0.8	0.06	0.44	0.01	0.41	0.01	-12.08	0.55	0	0
G43.0682-0.3495	4146200	19:11:20.10	+08:50:59.15	0.28	0.05	0.28	0.05	0.42	-1.0	0.42	-1.0	0.03	-1.0	4	0
G43.0682-0.3495	4156400	19:11:20.10	+08:50:59.16	0.27	0.05	0.27	0.05	0.42	-1.0	0.42	-1.0	-0.03	-1.0	4	0
G43.0769+0.0417	4348100	19:09:56.78	+09:02:17.92	0.49	0.08	0.49	0.08	0.42	-1.0	0.42	-1.0	-0.04	-1.0	4	0
G43.0769+0.0418	4337200	19:09:56.78	+09:02:17.93	0.48	0.06	0.37	0.06	0.38	0.02	0.36	0.02	-88.65	2.16	0	0
G43.0812-0.9401	3166100	19:13:28.67	+08:35:16.10	0.58	0.09	0.58	0.09	0.42	-1.0	0.42	-1.0	0.02	-1.0	4	0
G43.0819+0.5969	5324800	19:07:57.57	+09:17:54.97	0.55	0.05	0.48	0.05	0.44	0.02	0.35	0.01	-17.05	0.22	0	0
G43.0833-0.3993	4250300	19:11:32.51	+08:50:24.50	1.1	0.19	1.11	0.19	0.42	-1.0	0.42	-1.0	-0.02	-1.0	4	0
G43.0886-0.0114	4347200	19:10:09.53	+09:01:26.75	1.22	0.06	1.26	0.07	0.44	0.01	0.42	0.01	-88.18	0.89	0	0
G43.0886-0.0114	4336200	19:10:09.53	+09:01:26.75	1.2	0.05	1.22	0.06	0.44	0.01	0.41	0.01	89.52	0.63	0	0
G43.0923+0.2411	5137700	19:09:15.52	+09:08:38.12	0.32	0.06	0.32	0.06	0.42	-1.0	0.42	-1.0	-0.01	-1.0	4	0
G43.0929+0.1327	5133400	19:09:38.97	+09:05:40.04	0.31	0.05	0.32	0.05	0.42	-1.0	0.42	-1.0	0.0	-1.0	4	0
G43.0968+0.4190	5320500	19:08:37.62	+09:13:47.72	0.78	0.14	0.79	0.14	0.42	-1.0	0.42	-1.0	0.01	-1.0	4	0
G43.0996-0.9621	3262000	19:13:35.45	+08:35:38.04	1.87	0.05	1.86	0.06	0.44	0.0	0.4	0.01	-89.24	0.22	0	0
G43.0996-0.9621	3166300	19:13:35.45	+08:35:38.04	1.96	0.11	1.88	0.12	0.42	0.01	0.4	0.01	-89.22	0.71	0	0
G43.1004-0.5530	4152000	19:12:07.53	+08:47:02.91	0.32	0.05	0.32	0.05	0.42	-1.0	0.42	-1.0	0.0	-1.0	4	0
G43.1012-0.3161	4147900	19:11:16.62	+08:53:40.28	1.01	0.18	1.02	0.18	0.42	-1.0	0.42	-1.0	0.03	-1.0	4	0
G43.1012-0.3161	4158800	19:11:16.62	+08:53:40.30	0.99	0.18	1.0	0.18	0.42	-1.0	0.42	-1.0	-0.03	-1.0	4	0
G43.1187+0.3212	5223300	19:09:01.19	+09:12:15.37	0.49	0.06	0.5	0.08	0.5	0.02	0.36	0.03	-84.62	0.35	0	0
G43.1187+0.3212	5232600	19:09:01.19	+09:12:15.36	0.49	0.06	0.52	0.07	0.48	0.02	0.39	0.03	-83.95	0.47	0	0
G43.1212-0.4972	4154800	19:11:57.86	+08:49:42.46	0.3	0.05	0.3	0.05	0.42	-1.0	0.42	-1.0	-0.0	-1.0	4	0
G43.1217-0.4514	4156500	19:11:48.04	+08:51:00.27	0.34	0.05	0.35	0.05	0.42	-1.0	0.42	-1.0	-0.01	-1.0	4	0
G43.1231-0.4188	4251700	19:11:41.19	+08:51:59.06	0.69	0.06	0.68	0.07	0.44	0.02	0.39	0.01	-16.29	0.44	0	0
G43.1231-0.4188	4157300	19:11:41.19	+08:51:59.05	0.66	0.06	0.66	0.07	0.44	0.02	0.41	0.01	-13.71	0.78	0	0
G43.1285+0.8708	6211600	19:07:03.63	+09:27:57.68	0.32	0.05	0.33	0.05	0.42	-1.0	0.42	-1.0	-0.01	-1.0	4	0
G43.1307+0.6994	6112900	19:07:40.90	+09:23:20.82	0.31	0.05	0.31	0.05	0.42	-1.0	0.42	-1.0	0.02	-1.0	4	0
G43.1307+0.6994	6122200	19:07:40.90	+09:23:20.81	0.31	0.05	0.31	0.05	0.42	-1.0	0.42	-1.0	-0.04	-1.0	4	0
G43.1319-1.0141	3262300	19:13:50.29	+08:35:54.42	0.44	0.07	0.47	0.09	0.46	0.05	0.41	0.03	8.81	1.07	0	0
G43.1338-0.1935	4344700	19:10:53.86	+08:58:48.37	0.33	0.05	0.33	0.05	0.42	-1.0	0.42	-1.0	0.0	-1.0	4	0
G43.1343-0.5187	4154900	19:12:03.97	+08:49:48.50	0.3	0.05	0.3	0.05	0.42	-1.0	0.42	-1.0	0.0	-1.0	4	0

Source Galactic name	Source Index	RA J2000	Dec J2000	Observed flux density				Major (arcsec)		Minor (arcsec)		PA (°)		flags	aux_flags
				Peak (mJy beam^{-1})	error	Integrated (mJy)	error		error		error		error		
G43.1348-0.2359	4246700	19:11:03.11	+08:57:40.84	0.28	0.05	0.28	0.05	0.42	-1.0	0.42	-1.0	0.02	-1.0	4	0
G43.1348-0.2359	4343000	19:11:03.11	+08:57:40.83	0.27	0.05	0.28	0.05	0.42	-1.0	0.42	-1.0	0.01	-1.0	4	0
G43.1372-0.7760	3362700	19:12:59.67	+08:42:48.48	0.3	0.05	0.31	0.05	0.42	-1.0	0.42	-1.0	-0.01	-1.0	4	0
G43.1426+0.8924	6212500	19:07:00.55	+09:29:18.59	0.33	0.05	0.47	0.09	0.54	0.06	0.47	0.04	12.33	0.91	0	0
G43.1458+0.0141	5143501	19:10:10.46	+09:05:11.90	5.5	6.77	52.5	68.52	1.5	0.62	1.12	0.16	0.93	0.87	0	2
G43.1458+0.0141	5132701	19:10:10.46	+09:05:11.93	5.74	3.97	60.55	45.3	1.57	0.18	1.18	0.31	0.14	1.01	0	1
G43.1462+0.0142	5143500	19:10:10.49	+09:05:13.14	6.65	6.77	49.52	55.62	1.32	0.6	0.99	0.15	15.22	0.9	0	2
G43.1462+0.0142	5132700	19:10:10.49	+09:05:13.17	6.58	3.97	53.81	36.23	1.35	0.17	1.07	0.29	69.14	1.58	0	1
G43.1469+0.1621	5139500	19:09:38.67	+09:09:21.33	1.29	0.23	1.3	0.23	0.42	-1.0	0.42	-1.0	0.0	-1.0	4	0
G43.1469+0.1626	5139900	19:09:38.56	+09:09:22.13	4.21	0.23	4.01	0.26	0.48	0.01	0.35	0.01	-85.2	0.16	0	0
G43.1471+0.1626	51310000	19:09:38.60	+09:09:22.76	13.64	0.23	12.79	0.25	0.41	0.0	0.4	0.0	-10.39	0.5	0	0
G43.1472+0.1624	51310001	19:09:38.64	+09:09:22.81	3.17	0.23	3.2	0.24	0.5	0.0	0.36	0.0	31.71	0.42	0	0
G43.1472+0.1631	51310600	19:09:38.49	+09:09:23.94	1.42	0.22	2.3	0.66	0.7	0.03	0.41	0.1	87.38	0.42	0	0
G43.1474+0.1625	51310500	19:09:38.66	+09:09:23.65	1.5	0.22	1.51	0.22	0.42	-1.0	0.42	-1.0	0.0	-1.0	4	0
G43.1474+0.1625	51310002	19:09:38.66	+09:09:23.66	1.63	0.23	1.05	0.15	0.34	0.0	0.34	0.0	15.12	0.51	0	0
G43.1481+0.0131	5132800	19:10:10.94	+09:05:17.53	8.82	1.13	8.36	1.27	0.42	0.03	0.4	0.02	12.68	1.87	0	0
G43.1481+0.0131	5143600	19:10:10.94	+09:05:17.53	8.83	1.11	8.46	1.27	0.43	0.03	0.4	0.02	13.21	1.26	0	0
G43.1489+0.0130	5132900	19:10:11.05	+09:05:20.10	50.69	0.87	87.22	1.73	0.59	0.0	0.52	0.0	-9.67	0.09	0	0
G43.1489+0.0130	5143700	19:10:11.05	+09:05:20.10	50.57	0.87	86.83	1.74	0.58	0.0	0.52	0.0	-9.22	0.09	0	0
G43.1517+0.0116	5143800	19:10:11.67	+09:05:26.73	15.82	0.84	47.29	2.9	0.84	0.02	0.63	0.01	10.56	0.07	0	0
G43.1518+0.0116	5133000	19:10:11.67	+09:05:26.75	16.44	0.8	54.01	3.04	0.88	0.02	0.66	0.01	11.16	0.07	0	0
G43.1520+0.0114	5143801	19:10:11.73	+09:05:27.20	12.64	0.84	154.05	10.49	1.78	0.02	1.21	0.01	-82.39	0.14	0	0
G43.1520+0.0114	5133001	19:10:11.73	+09:05:27.22	12.77	0.8	144.91	9.38	1.64	0.02	1.22	0.01	-86.24	0.12	0	0
G43.1522-0.7405	3364300	19:12:53.71	+08:44:35.68	0.3	0.05	0.31	0.05	0.42	-1.0	0.42	-1.0	-0.01	-1.0	4	0
G43.1523+0.9375	6214000	19:06:51.88	+09:31:04.05	0.25	0.05	0.26	0.05	0.42	-1.0	0.42	-1.0	-0.02	-1.0	4	0
G43.1599-0.2459	4344400	19:11:08.07	+08:58:44.41	3.32	0.06	3.21	0.06	0.42	0.0	0.41	0.0	89.64	1.04	0	0
G43.1599-0.2459	4248100	19:11:08.08	+08:58:44.41	4.25	0.15	4.02	0.16	0.41	0.01	0.41	0.01	-3.29	10.32	0	0
G43.1622+0.8255	6116400	19:07:17.18	+09:28:30.52	0.45	0.08	0.45	0.08	0.42	-1.0	0.42	-1.0	0.01	-1.0	4	0
G43.1633+0.4407	5325000	19:08:40.41	+09:17:56.14	0.29	0.05	0.29	0.05	0.42	-1.0	0.42	-1.0	0.01	-1.0	4	0
G43.1638+0.2043	51314000	19:09:31.47	+09:11:25.37	1.41	0.24	1.42	0.25	0.42	-1.0	0.42	-1.0	-0.0	-1.0	4	0
G43.1642-0.0279	5143300	19:10:21.58	+09:05:00.93	12.04	1.71	15.54	2.87	0.52	0.05	0.44	0.03	12.48	0.61	0	0
G43.1642-0.0279	5132500	19:10:21.58	+09:05:00.90	12.95	1.86	15.78	2.98	0.49	0.04	0.44	0.04	6.6	1.18	0	0
G43.1648-0.0285	5132400	19:10:21.79	+09:05:01.77	76.88	1.88	796.03	21.82	2.02	0.02	0.9	0.01	-19.38	0.01	0	0
G43.1648-0.0285	5143200	19:10:21.78	+09:05:01.84	48.06	3.03	655.51	43.38	2.15	0.04	1.12	0.01	-32.54	0.02	0	0
G43.1649-0.0281	5143203	19:10:21.72	+09:05:02.79	28.96	3.03	52.53	6.49	0.75	0.04	0.43	0.01	-13.66	0.02	0	0

Source Galactic name	Source Index	RA J2000	Dec J2000	Peak (mJy beam^{-1})	error	Integrated (mJy)	error	Major (arcsec)	error	Minor (arcsec)	error	PA (°)	error	flags	aux_flags
G43.1649-0.0281	5132402	19:10:21.72	+09:05:02.83	35.78	1.88	92.13	5.43	0.9	0.02	0.5	0.01	-13.06	0.01	0	0
G43.1649-0.0285	5143201	19:10:21.79	+09:05:01.95	35.07	3.03	164.02	14.98	1.74	0.04	0.47	0.01	-38.21	0.02	0	0
G43.1651+0.0129	5134700	19:10:12.89	+09:06:11.70	110.74	1.85	261.0	5.07	0.68	0.0	0.61	0.0	-5.5	0.11	0	0
G43.1651+0.0129	5145300	19:10:12.89	+09:06:11.70	111.11	1.84	259.7	5.0	0.67	0.0	0.61	0.0	-4.82	0.11	0	0
G43.1652+0.0135	5145600	19:10:12.77	+09:06:12.91	10.75	2.3	16.88	6.95	0.59	0.05	0.47	0.16	83.85	1.09	0	0
G43.1652-0.0281	5143204	19:10:21.74	+09:05:03.86	29.34	3.03	228.34	24.4	1.65	0.04	0.83	0.01	27.76	0.02	0	0
G43.1652-0.0281	5132403	19:10:21.74	+09:05:03.73	25.01	1.88	209.72	16.18	1.23	0.02	1.21	0.01	71.31	0.01	0	0
G43.1652-0.0282	5143205	19:10:21.76	+09:05:03.45	13.18	3.03	17.92	4.44	0.5	0.05	0.48	0.01	-4.81	0.04	0	0
G43.1652-0.0284	5143202	19:10:21.80	+09:05:03.37	47.26	3.03	169.51	13.13	1.08	0.04	0.59	0.01	24.01	0.02	0	0
G43.1652-0.0284	5132401	19:10:21.81	+09:05:03.36	44.31	1.88	89.16	4.57	0.77	0.02	0.46	0.01	23.44	0.01	0	0
G43.1654+0.0134	5145601	19:10:12.81	+09:06:13.32	10.35	2.3	33.93	13.12	1.19	0.05	0.49	0.15	16.57	0.38	0	0
G43.1656+0.0117	5145200	19:10:13.22	+09:06:11.10	61.07	2.37	244.8	11.21	0.9	0.02	0.79	0.01	-12.6	0.19	0	0
G43.1656+0.0117	5134600	19:10:13.22	+09:06:11.10	61.36	2.41	245.78	11.42	0.9	0.02	0.79	0.01	-12.25	0.19	0	0
G43.1657-0.0281	5143206	19:10:21.79	+09:05:05.36	8.83	3.03	84.84	29.15	1.72	0.04	0.99	0.01	36.7	0.03	0	1
G43.1657-0.0281	5132404	19:10:21.79	+09:05:05.16	15.5	1.88	455.62	55.44	3.55	0.02	1.46	0.01	6.92	0.01	0	0
G43.1658-0.0282	5143207	19:10:21.82	+09:05:05.28	8.87	3.03	230.12	78.55	3.14	0.03	1.46	0.01	51.39	0.03	0	1
G43.1659+0.0121	5145500	19:10:13.14	+09:06:12.64	82.58	2.73	158.41	6.1	0.67	0.01	0.5	0.01	6.93	0.06	0	0
G43.1659+0.0121	5135000	19:10:13.14	+09:06:12.64	82.21	2.77	159.29	6.25	0.68	0.01	0.5	0.01	7.15	0.06	0	0
G43.1661+0.0111	5145409	19:10:13.39	+09:06:11.81	38.24	4.79	124.7	15.88	0.82	0.01	0.7	0.01	-12.03	0.44	0	0
G43.1661+0.0111	5134810	19:10:13.39	+09:06:11.82	37.71	4.74	130.68	16.68	0.83	0.01	0.73	0.01	-10.97	0.29	0	0
G43.1662-0.0283	5132600	19:10:21.89	+09:05:06.46	12.29	1.34	89.5	20.03	1.4	0.19	0.92	0.13	-82.44	0.67	0	0
G43.1662-0.0283	5143209	19:10:21.90	+09:05:06.62	8.32	3.03	40.41	14.82	0.96	0.05	0.89	0.01	-87.57	0.04	0	1
G43.1663+0.0102	5134804	19:10:13.60	+09:06:11.01	41.11	4.74	191.46	22.54	1.39	0.01	0.59	0.01	85.71	0.74	0	0
G43.1663+0.0103	5145405	19:10:13.60	+09:06:11.03	41.96	4.79	194.96	22.68	1.3	0.01	0.63	0.01	84.63	1.02	0	0
G43.1663+0.0107	5145403	19:10:13.50	+09:06:11.82	40.91	4.79	70.08	8.6	0.79	0.01	0.38	0.01	88.39	1.05	0	0
G43.1663+0.0107	5134803	19:10:13.50	+09:06:11.83	41.64	4.74	90.8	10.77	0.91	0.01	0.42	0.01	-88.75	0.69	0	0
G43.1663+0.0113	5145400	19:10:13.37	+09:06:12.66	94.32	4.79	143.22	8.75	0.54	0.01	0.5	0.01	-87.07	0.55	0	0
G43.1663+0.0113	5134800	19:10:13.37	+09:06:12.66	94.52	4.74	144.49	8.74	0.55	0.01	0.49	0.01	-88.91	0.36	0	0
G43.1664+0.0105	5145402	19:10:13.55	+09:06:11.62	54.05	4.79	242.54	22.22	1.35	0.01	0.59	0.01	79.55	1.02	0	0
G43.1664+0.0105	5134802	19:10:13.55	+09:06:11.62	55.97	4.74	237.59	20.93	1.29	0.01	0.58	0.01	85.56	0.7	0	0
G43.1664+0.0108	5145406	19:10:13.49	+09:06:12.32	31.15	4.79	153.95	23.9	1.28	0.01	0.68	0.01	82.69	0.92	0	0
G43.1664-0.0283	5132602	19:10:21.93	+09:05:07.21	8.77	1.34	26.51	9.02	0.92	0.2	0.58	0.13	-83.54	0.69	0	0
G43.1665+0.0099	5145411	19:10:13.69	+09:06:11.10	21.18	4.79	107.51	24.39	1.03	0.01	0.87	0.01	-16.72	0.44	0	0
G43.1665+0.0099	5134813	19:10:13.70	+09:06:10.98	20.1	4.74	42.2	10.03	0.71	0.01	0.52	0.01	-7.44	0.24	0	0
G43.1665+0.0108	5134807	19:10:13.50	+09:06:12.36	32.28	4.74	151.01	22.47	1.42	0.01	0.58	0.01	87.86	0.78	0	0

Source Galactic name	Source Index	RA J2000	Dec J2000	Observed flux density Peak (mJy beam^{-1})	error	Integrated (mJy)	error	Major (arcsec)	error	Minor (arcsec)	error	PA (°)	error	flags	aux_flags
G43.1665+0.0111	5145401	19:10:13.43	+09:06:12.99	84.92	4.79	228.74	14.17	0.74	0.01	0.64	0.01	85.52	0.59	0	0
G43.1665+0.0111	5134801	19:10:13.43	+09:06:12.99	86.34	4.74	224.08	13.65	0.76	0.01	0.6	0.01	89.83	0.4	0	0
G43.1665-0.0284	5143208	19:10:21.96	+09:05:07.32	12.24	3.03	49.58	12.46	1.1	0.05	0.65	0.01	-86.97	0.06	0	0
G43.1665-0.0285	5132601	19:10:21.97	+09:05:07.28	10.24	1.34	28.08	9.79	0.79	0.2	0.61	0.13	-87.81	0.58	0	0
G43.1667+0.0101	5134808	19:10:13.68	+09:06:12.12	39.28	4.74	233.45	28.6	1.58	0.01	0.66	0.01	1.71	0.14	0	0
G43.1667+0.0104	5134814	19:10:13.60	+09:06:12.70	18.69	4.74	126.92	32.26	1.22	0.01	0.98	0.01	-4.82	0.26	0	0
G43.1667+0.0107	5134811	19:10:13.55	+09:06:12.98	16.0	4.74	38.93	11.58	0.67	0.01	0.64	0.01	85.63	0.33	0	0
G43.1668+0.0101	5145407	19:10:13.68	+09:06:12.13	38.94	4.79	138.47	17.34	0.99	0.01	0.63	0.01	-5.07	0.32	0	0
G43.1668+0.0104	5145413	19:10:13.62	+09:06:12.66	13.89	4.79	112.29	38.77	1.44	0.01	0.99	0.01	87.64	0.74	0	1
G43.1668+0.0106	5145410	19:10:13.58	+09:06:13.32	28.18	4.79	321.23	54.8	2.13	0.01	0.94	0.01	14.03	0.24	0	0
G43.1668+0.0106	5134812	19:10:13.57	+09:06:13.10	14.98	4.74	134.57	42.65	2.28	0.01	0.7	0.01	8.34	0.1	0	0
G43.1668+0.0108	5134805	19:10:13.53	+09:06:13.51	28.44	4.74	74.21	12.62	1.12	0.01	0.41	0.01	87.34	0.86	0	0
G43.1668+0.0108	5145404	19:10:13.53	+09:06:13.57	35.95	4.79	75.71	10.33	0.74	0.01	0.5	0.01	-74.45	0.7	0	0
G43.1668+0.0110	5145412	19:10:13.48	+09:06:13.69	21.99	4.79	48.58	10.67	0.64	0.01	0.61	0.01	76.49	0.53	0	0
G43.1669+0.0102	5145408	19:10:13.67	+09:06:12.80	19.7	4.79	54.92	13.43	0.79	0.01	0.62	0.01	-89.79	0.64	0	0
G43.1669+0.0103	5134809	19:10:13.65	+09:06:12.77	18.31	4.74	45.54	11.85	0.71	0.01	0.62	0.01	-83.88	0.37	0	0
G43.1669+0.0108	5134806	19:10:13.53	+09:06:13.73	19.31	4.74	117.67	29.14	2.63	0.01	0.41	0.01	-88.48	2.02	0	0
G43.1674+0.0128	5135700	19:10:13.16	+09:06:18.60	63.32	1.61	251.25	7.43	0.85	0.01	0.83	0.01	-75.29	0.88	0	0
G43.1674+0.0128	5146300	19:10:13.16	+09:06:18.60	63.4	1.6	251.95	7.37	0.85	0.01	0.83	0.01	-73.94	0.95	0	0
G43.1674+0.0132	5135900	19:10:13.09	+09:06:19.48	10.7	1.92	10.8	1.94	0.42	-1.0	0.42	-1.0	0.03	-1.0	4	0
G43.1674+0.0132	5146400	19:10:13.09	+09:06:19.47	10.93	1.93	11.04	1.95	0.42	-1.0	0.42	-1.0	-0.03	-1.0	4	0
G43.1680-0.1352	4347800	19:10:45.13	+09:02:14.49	3.33	0.07	3.02	0.07	0.42	0.0	0.38	0.0	-5.41	0.15	0	0
G43.1683+0.0085	5135301	19:10:14.20	+09:06:14.54	8.1	1.29	24.0	5.77	0.9	0.15	0.58	0.05	-83.83	1.42	0	0
G43.1683+0.0085	5145901	19:10:14.19	+09:06:14.54	7.94	1.29	23.47	5.68	0.96	0.16	0.54	0.04	-85.74	1.16	0	0
G43.1684+0.0125	5136000	19:10:13.35	+09:06:21.22	33.15	1.22	120.11	5.2	0.82	0.01	0.78	0.01	-10.09	0.54	0	0
G43.1684+0.0125	5146500	19:10:13.35	+09:06:21.22	32.81	1.23	119.93	5.31	0.82	0.01	0.78	0.01	-10.33	0.53	0	0
G43.1685+0.0086	5145900	19:10:14.19	+09:06:15.27	9.92	1.29	28.43	6.69	0.8	0.15	0.63	0.04	-17.44	0.54	0	0
G43.1685+0.0086	5135300	19:10:14.19	+09:06:15.28	9.89	1.29	26.01	6.21	0.75	0.14	0.62	0.04	-18.16	0.8	0	0
G43.1691-0.1361	4348000	19:10:45.46	+09:02:16.69	0.74	0.07	0.7	0.07	0.42	0.01	0.4	0.02	87.74	1.03	0	0
G43.1694-0.6111	4154100	19:12:27.80	+08:49:06.50	0.28	0.05	0.28	0.05	0.42	-1.0	0.42	-1.0	0.02	-1.0	4	0
G43.1699+0.0075	5146200	19:10:14.60	+09:06:17.68	10.38	1.26	64.05	14.68	1.07	0.16	1.02	0.13	86.16	3.34	0	0
G43.1699+0.0075	5135600	19:10:14.60	+09:06:17.69	10.27	1.26	62.85	14.36	1.07	0.16	1.01	0.13	87.14	2.88	0	0
G43.1699+0.3077	5235800	19:09:09.84	+09:14:36.52	0.43	0.06	0.51	0.1	0.57	0.06	0.36	0.02	-20.38	0.19	0	0
G43.1699+0.3077	5330800	19:09:09.84	+09:14:36.54	0.5	0.08	0.51	0.08	0.42	-1.0	0.42	-1.0	-0.03	-1.0	4	0
G43.1706+0.0002	5134400	19:10:16.24	+09:06:08.10	4.27	10.55	10.85	27.94	1.03	0.14	0.43	0.3	85.85	0.72	0	2

Source Galactic name	Source Index	RA J2000	Dec J2000	Peak (mJy beam^{-1})	error	Integrated (mJy)	error	Major (arcsec)	error	Minor (arcsec)	error	PA (°)	error	flags	aux_flags
G43.1706+0.0005	5134402	19:10:16.18	+09:06:08.41	5.84	10.55	13.91	26.38	0.77	0.14	0.55	0.3	79.63	0.42	0	2
G43.1706+0.0005	5144901	19:10:16.19	+09:06:08.36	6.61	0.81	19.72	4.99	0.86	0.03	0.61	0.13	82.64	0.31	0	0
G43.1706-0.0004	5134200	19:10:16.36	+09:06:06.89	89.5	0.7	317.9	2.89	0.81	0.0	0.77	0.0	11.58	0.1	0	0
G43.1706-0.0004	5144800	19:10:16.36	+09:06:06.90	89.41	0.72	319.23	2.95	0.82	0.0	0.77	0.0	70.99	0.09	0	0
G43.1707+0.0002	5144900	19:10:16.25	+09:06:08.15	7.53	0.81	26.77	6.72	1.07	0.03	0.59	0.13	79.03	0.38	0	0
G43.1707+0.0002	5134401	19:10:16.25	+09:06:08.25	3.99	10.55	23.51	63.13	1.54	0.14	0.67	0.29	74.01	0.53	0	2
G43.1707+0.0043	5145800	19:10:15.37	+09:06:14.93	25.15	0.88	32.26	1.3	0.48	0.01	0.47	0.01	6.12	1.59	0	0
G43.1707+0.0043	5135200	19:10:15.37	+09:06:14.93	25.0	0.86	32.21	1.27	0.48	0.01	0.47	0.01	9.16	1.2	0	0
G43.1717-0.0003	5134500	19:10:16.46	+09:06:10.58	5.97	0.77	27.17	5.8	1.07	0.14	0.75	0.08	5.93	0.3	0	0
G43.1717-0.0003	5145100	19:10:16.46	+09:06:10.58	6.15	0.85	24.41	6.31	0.95	0.12	0.74	0.13	7.63	0.56	0	0
G43.1722+0.9775	6216000	19:06:45.46	+09:33:14.11	0.3	0.05	0.3	0.05	0.42	-1.0	0.42	-1.0	-0.02	-1.0	4	0
G43.1725-0.6706	4152500	19:12:40.94	+08:47:36.96	0.31	0.05	0.31	0.05	0.42	-1.0	0.42	-1.0	0.03	-1.0	4	0
G43.1725-0.6706	4161400	19:12:40.94	+08:47:36.95	0.31	0.06	0.31	0.06	0.42	-1.0	0.42	-1.0	-0.03	-1.0	4	0
G43.1740-0.3541	4350900	19:11:32.98	+08:56:29.42	0.64	0.08	0.54	0.08	0.4	0.02	0.38	0.02	-89.75	1.5	0	0
G43.1740-0.3541	4341200	19:11:32.98	+08:56:29.42	0.64	0.08	0.54	0.08	0.4	0.02	0.38	0.02	-89.14	1.51	0	0
G43.1740-0.3541	4245300	19:11:32.98	+08:56:29.41	0.7	0.05	0.7	0.06	0.43	0.01	0.41	0.01	-6.44	1.03	0	0
G43.1740-0.3541	4254900	19:11:32.98	+08:56:29.41	0.71	0.05	0.69	0.06	0.43	0.01	0.4	0.01	-7.15	0.79	0	0
G43.1777-0.5178	4252000	19:12:08.65	+08:52:08.50	0.69	0.12	0.7	0.12	0.42	-1.0	0.42	-1.0	-0.0	-1.0	4	0
G43.1781-0.5180	4157800	19:12:08.74	+08:52:09.45	0.67	0.12	0.68	0.12	0.42	-1.0	0.42	-1.0	0.01	-1.0	4	0
G43.1793-0.2927	4344100	19:11:20.33	+08:58:28.40	0.33	0.06	0.33	0.06	0.42	-1.0	0.42	-1.0	0.02	-1.0	4	0
G43.1808+0.3938	5324300	19:08:52.49	+09:17:34.39	0.35	0.06	0.35	0.06	0.42	-1.0	0.42	-1.0	0.02	-1.0	4	0
G43.1848-0.1009	5141500	19:10:39.64	+09:04:05.28	1.21	0.2	1.22	0.2	0.42	-1.0	0.42	-1.0	-0.02	-1.0	4	0
G43.1860-0.0850	5143100	19:10:36.33	+09:04:35.46	1.07	0.19	1.08	0.19	0.42	-1.0	0.42	-1.0	-0.02	-1.0	4	0
G43.1867-0.0901	5142600	19:10:37.52	+09:04:29.34	1.03	0.17	1.04	0.18	0.42	-1.0	0.42	-1.0	-0.02	-1.0	4	0
G43.1898+0.6537	6114200	19:07:57.37	+09:25:14.06	0.39	0.07	0.39	0.07	0.42	-1.0	0.42	-1.0	0.03	-1.0	4	0
G43.1912+0.7799	6116600	19:07:30.29	+09:28:47.65	0.78	0.14	0.79	0.14	0.42	-1.0	0.42	-1.0	0.02	-1.0	4	0
G43.1985+0.7911	6212700	19:07:28.68	+09:29:29.43	2.72	0.05	2.64	0.06	0.42	0.0	0.41	0.0	6.75	0.3	0	0
G43.1986+0.7909	6212701	19:07:28.72	+09:29:29.41	0.31	0.05	0.21	0.04	0.36	0.0	0.34	0.0	-85.41	0.33	0	0
G43.2001+0.0819	51312700	19:10:01.93	+09:09:57.92	0.4	0.07	0.41	0.07	0.42	-1.0	0.42	-1.0	0.02	-1.0	4	0
G43.2009+0.1929	5233500	19:09:38.09	+09:13:04.98	0.33	0.06	0.33	0.06	0.42	-1.0	0.42	-1.0	-0.0	-1.0	4	0
G43.2020+0.6732	6125400	19:07:54.53	+09:26:25.52	0.27	0.05	0.27	0.05	0.42	-1.0	0.42	-1.0	-0.03	-1.0	4	0
G43.2056-0.6058	4156700	19:12:30.73	+08:51:10.88	0.32	0.05	0.33	0.05	0.42	-1.0	0.42	-1.0	0.02	-1.0	4	0
G43.2061-0.3068	4353200	19:11:26.39	+08:59:30.69	0.93	0.05	1.25	0.08	0.5	0.01	0.47	0.01	9.25	0.64	0	0
G43.2061-0.3068	4345300	19:11:26.39	+08:59:30.70	0.93	0.05	1.29	0.08	0.51	0.01	0.48	0.01	14.37	0.66	0	0
G43.2074+0.4346	5326900	19:08:46.68	+09:20:07.06	0.3	0.05	0.31	0.05	0.42	-1.0	0.42	-1.0	0.02	-1.0	4	0

Source Galactic name	Source Index	RA J2000	Dec J2000	Peak (mJy beam^{-1})	error	Integrated (mJy)	error	Major (arcsec)	error	Minor (arcsec)	error	PA (°)	error	flags	aux_flags
G43.2178+0.2638	5236700	19:09:24.70	+09:15:56.71	0.4	0.07	0.4	0.07	0.42	-1.0	0.42	-1.0	-0.01	-1.0	4	0
G43.2178-0.5602	4158300	19:12:22.29	+08:53:05.71	0.52	0.09	0.52	0.09	0.42	-1.0	0.42	-1.0	0.01	-1.0	4	0
G43.2211+0.3766	5335300	19:09:00.71	+09:19:14.55	0.35	0.06	0.35	0.06	0.42	-1.0	0.42	-1.0	-0.04	-1.0	4	0
G43.2271-0.9776	3362100	19:13:53.16	+08:41:58.91	0.61	0.06	0.59	0.07	0.44	0.02	0.38	0.02	11.02	0.46	0	0
G43.2320-0.6475	4157000	19:12:42.67	+08:51:25.54	0.32	0.06	0.32	0.06	0.42	-1.0	0.42	-1.0	0.03	-1.0	4	0
G43.2372-0.0459	5149500	19:10:33.66	+09:08:24.17	17.04	0.47	29.37	0.91	0.55	0.01	0.55	0.01	-2.46	6.17	0	0
G43.2373-0.0452	5149502	19:10:33.52	+09:08:25.45	2.72	0.47	10.41	1.81	0.97	0.01	0.7	0.01	-14.39	4.64	0	0
G43.2373-0.0456	5149501	19:10:33.62	+09:08:24.85	4.74	0.47	10.91	1.09	0.93	0.0	0.44	0.0	-36.05	4.21	0	0
G43.2374-0.0454	5149503	19:10:33.57	+09:08:25.54	2.29	0.47	4.96	1.03	0.77	0.01	0.49	0.01	-11.62	4.1	0	0
G43.2376-0.0453	5149504	19:10:33.57	+09:08:26.19	1.94	0.47	4.12	1.0	0.76	0.01	0.49	0.0	-24.04	4.56	0	0
G43.2425+0.1192	5233900	19:09:58.66	+09:13:15.23	0.73	0.06	0.88	0.08	0.53	0.02	0.4	0.01	-31.43	0.18	0	0
G43.2460-0.2123	5141800	19:11:10.50	+09:04:15.17	0.35	0.06	0.35	0.06	0.42	-1.0	0.42	-1.0	0.0	-1.0	4	0
G43.2511-0.9951	3362600	19:13:59.61	+08:42:46.11	1.88	0.05	2.15	0.07	0.46	0.01	0.44	0.0	2.65	0.46	0	0
G43.2515+0.6467	6222300	19:08:05.80	+09:28:19.63	0.32	0.06	0.33	0.06	0.42	-1.0	0.42	-1.0	-0.03	-1.0	4	0
G43.2538+0.5433	6124100	19:08:28.40	+09:25:35.34	0.49	0.06	0.47	0.06	0.43	0.02	0.39	0.02	6.8	0.81	0	0
G43.2586-0.2808	4348900	19:11:26.70	+09:03:01.54	0.3	0.05	0.3	0.05	0.42	-1.0	0.42	-1.0	0.02	-1.0	4	0
G43.2593+0.8910	6313200	19:07:13.90	+09:35:29.11	0.29	0.05	0.29	0.05	0.42	-1.0	0.42	-1.0	-0.01	-1.0	4	0
G43.2633+0.3181	5335600	19:09:18.07	+09:19:52.01	0.32	0.06	0.32	0.06	0.42	-1.0	0.42	-1.0	-0.03	-1.0	4	0
G43.2633+0.3181	5326700	19:09:18.08	+09:19:51.98	0.35	0.06	0.36	0.06	0.42	-1.0	0.42	-1.0	0.04	-1.0	4	0
G43.2633-0.7343	4260200	19:13:04.87	+08:50:40.49	0.81	0.15	0.82	0.15	0.42	-1.0	0.42	-1.0	-0.02	-1.0	4	0
G43.2722+0.6604	6224300	19:08:05.17	+09:29:48.29	0.3	0.05	0.31	0.05	0.42	-1.0	0.42	-1.0	-0.03	-1.0	4	0
G43.2759+0.9545	6316600	19:07:02.03	+09:38:07.31	0.35	0.06	0.35	0.06	0.42	-1.0	0.42	-1.0	-0.02	-1.0	4	0
G43.2784-0.6233	4253400	19:12:42.68	+08:54:33.95	0.5	0.05	0.47	0.06	0.43	0.02	0.39	0.02	87.03	0.8	0	0
G43.2849-0.4010	4355900	19:11:55.54	+09:01:05.20	0.31	0.05	0.31	0.05	0.42	-1.0	0.42	-1.0	-0.02	-1.0	4	0
G43.2861-0.8052	4163100	19:13:22.69	+08:49:54.84	0.53	0.05	0.49	0.05	0.41	0.02	0.4	0.01	-2.18	1.52	0	0
G43.2886+0.8133	6312500	19:07:33.97	+09:34:54.07	0.31	0.06	0.32	0.06	0.42	-1.0	0.42	-1.0	0.0	-1.0	4	0
G43.2889+0.0080	5233100	19:10:27.84	+09:12:38.57	0.45	0.06	0.39	0.06	0.4	0.02	0.39	0.03	89.3	4.21	0	0
G43.2889+0.0080	5243700	19:10:27.84	+09:12:38.56	0.45	0.06	0.39	0.06	0.39	0.02	0.39	0.03	88.65	4.96	0	0
G43.2895+0.6912	6320600	19:08:00.46	+09:31:34.65	0.54	0.09	0.54	0.09	0.42	-1.0	0.42	-1.0	-0.04	-1.0	4	0
G43.2895+0.6912	6310500	19:08:00.46	+09:31:34.65	0.53	0.09	0.54	0.09	0.42	-1.0	0.42	-1.0	0.02	-1.0	4	0
G43.2912-0.9746	3365000	19:13:59.73	+08:45:28.05	0.41	0.07	0.42	0.07	0.42	-1.0	0.42	-1.0	0.03	-1.0	4	0
G43.2947-0.6454	4262201	19:12:49.27	+08:54:48.89	5.46	0.22	28.58	1.18	1.2	0.01	0.77	0.01	-2.74	0.01	0	0
G43.2947-0.6454	4253701	19:12:49.27	+08:54:48.88	5.84	0.19	30.85	1.06	1.21	0.01	0.77	0.01	-1.47	0.01	0	0
G43.2947-0.6455	4253700	19:12:49.31	+08:54:48.75	5.57	0.19	24.6	0.89	1.17	0.01	0.67	0.01	12.84	0.01	0	0
G43.2947-0.6455	4262200	19:12:49.31	+08:54:48.73	5.27	0.22	23.9	1.03	1.19	0.01	0.67	0.01	14.72	0.01	0	0

Source Galactic name	Source Index	RA J2000	Dec J2000	Peak (mJy beam^{-1})	error	Integrated (mJy)	error	Major (arcsec)	error	Minor (arcsec)	error	PA (°)	error	flags	aux_flags
G43.2962+0.8551	6315000	19:07:25.78	+09:36:27.86	0.28	0.05	0.28	0.05	0.42	-1.0	0.42	-1.0	-0.0	-1.0	4	0
G43.3008+0.8243	6314200	19:07:32.96	+09:35:51.58	18.47	0.11	18.72	0.13	0.42	0.0	0.42	0.0	3.06	3.31	0	0
G43.3038+0.6507	6225800	19:08:10.79	+09:31:13.41	0.34	0.06	0.35	0.06	0.42	-1.0	0.42	-1.0	-0.03	-1.0	4	0
G43.3041+0.0434	5235500	19:10:21.92	+09:14:25.93	0.33	0.06	0.33	0.06	0.42	-1.0	0.42	-1.0	0.02	-1.0	4	0
G43.3059-0.2110	5147700	19:11:16.97	+09:07:28.54	1.3	0.07	3.72	0.23	0.78	0.01	0.65	0.02	84.98	0.24	0	0
G43.3062+0.3170	5337900	19:09:23.12	+09:22:07.38	1.47	0.25	1.48	0.26	0.42	-1.0	0.42	-1.0	-0.02	-1.0	4	0
G43.3064-0.2113	5147900	19:11:17.09	+09:07:29.75	1.11	0.06	3.63	0.29	0.99	0.01	0.58	0.03	-89.46	0.13	0	0
G43.3145+0.4181	6123800	19:09:02.23	+09:25:21.87	0.33	0.06	0.33	0.06	0.42	-1.0	0.42	-1.0	0.02	-1.0	4	0
G43.3150+0.5913	6224700	19:08:24.89	+09:30:10.72	0.27	0.05	0.28	0.05	0.42	-1.0	0.42	-1.0	-0.02	-1.0	4	0
G43.3168+0.6547	6214800	19:08:11.39	+09:32:01.75	0.38	0.06	0.39	0.06	0.42	-1.0	0.42	-1.0	0.04	-1.0	4	0
G43.3222+0.5717	6224500	19:08:29.93	+09:30:01.07	0.32	0.05	0.32	0.05	0.42	-1.0	0.42	-1.0	-0.01	-1.0	4	0
G43.3263-0.2485	5148600	19:11:27.35	+09:07:31.29	0.63	0.07	0.63	0.09	0.49	0.02	0.36	0.03	80.26	0.36	0	0
G43.3263-0.2488	5148000	19:11:27.40	+09:07:30.71	3.02	0.08	2.96	0.09	0.44	0.0	0.4	0.0	-86.01	0.2	0	0
G43.3314-0.9311	4162300	19:13:54.89	+08:48:49.14	0.33	0.05	0.33	0.05	0.42	-1.0	0.42	-1.0	0.01	-1.0	4	0
G43.3369+0.1880	5335800	19:09:54.40	+09:20:11.23	0.38	0.06	0.39	0.06	0.42	-1.0	0.42	-1.0	-0.0	-1.0	4	0
G43.3374+0.9922	7113100	19:07:00.77	+09:42:26.47	0.3	0.05	0.3	0.05	0.42	-1.0	0.42	-1.0	-0.03	-1.0	4	0
G43.3421+0.2242	6130900	19:09:47.19	+09:21:27.91	0.47	0.08	0.47	0.08	0.42	-1.0	0.42	-1.0	-0.02	-1.0	4	0
G43.3527-0.5480	4354800	19:12:34.85	+09:00:36.42	1.93	0.07	1.96	0.08	0.44	0.01	0.41	0.01	-5.68	0.39	0	0
G43.3531-0.5472	4355100	19:12:34.70	+09:00:39.16	7.35	0.07	7.57	0.08	0.43	0.0	0.42	0.0	-1.04	0.32	0	0
G43.3534-0.5472	4355300	19:12:34.74	+09:00:39.84	0.63	0.07	0.44	0.06	0.37	0.02	0.34	0.01	32.28	0.87	0	0
G43.3534-0.5473	4355302	19:12:34.77	+09:00:39.91	0.37	0.07	0.32	0.07	0.45	0.02	0.34	0.01	-72.4	1.14	0	0
G43.3535-0.5471	4355301	19:12:34.73	+09:00:40.27	0.38	0.07	0.25	0.05	0.35	0.02	0.34	0.01	84.79	0.94	0	0
G43.3569-0.6876	4255300	19:13:05.36	+08:56:57.18	1.48	0.06	1.44	0.06	0.42	0.01	0.41	0.01	-88.78	1.95	0	0
G43.3569-0.6876	4264300	19:13:05.36	+08:56:57.18	1.49	0.06	1.44	0.06	0.42	0.01	0.41	0.01	-84.58	1.22	0	0
G43.3569-0.6876	4360800	19:13:05.36	+08:56:57.18	1.48	0.07	1.33	0.08	0.41	0.01	0.39	0.01	89.86	0.8	0	0
G43.3570-0.6876	4351300	19:13:05.36	+08:56:57.18	1.49	0.07	1.33	0.08	0.41	0.01	0.39	0.01	88.25	0.73	0	0
G43.3577+0.4734	6222900	19:08:55.14	+09:29:11.55	0.8	0.05	0.81	0.06	0.45	0.01	0.4	0.01	1.46	0.34	0	0
G43.3654-0.9085	4163900	19:13:53.87	+08:51:15.29	0.31	0.06	0.31	0.06	0.42	-1.0	0.42	-1.0	0.01	-1.0	4	0
G43.3671+0.0883	5334600	19:10:19.32	+09:19:01.87	0.53	0.08	0.47	0.09	0.43	0.02	0.36	0.03	-81.29	0.67	0	0
G43.3673+0.3682	6134300	19:09:18.93	+09:26:47.69	0.29	0.05	0.29	0.05	0.42	-1.0	0.42	-1.0	-0.04	-1.0	4	0
G43.3675+0.0878	5334500	19:10:19.46	+09:19:02.27	2.72	0.08	2.93	0.09	0.52	0.01	0.36	0.0	-20.6	0.04	0	0
G43.3679+0.0878	5335001	19:10:19.51	+09:19:03.66	0.43	0.23	0.45	0.27	0.55	0.04	0.34	0.08	36.75	7.77	0	1
G43.3680+0.0878	5335000	19:10:19.53	+09:19:03.94	0.41	0.23	0.42	0.26	0.43	0.05	0.42	0.1	-82.04	10.89	0	1
G43.3766+0.0014	5343600	19:10:39.12	+09:17:07.72	0.34	0.06	0.35	0.06	0.42	-1.0	0.42	-1.0	-0.03	-1.0	4	0
G43.3766+0.0014	5332400	19:10:39.12	+09:17:07.70	0.34	0.06	0.34	0.06	0.42	-1.0	0.42	-1.0	0.03	-1.0	4	0

Source Galactic name	Source Index	RA J2000	Dec J2000	Observed flux density Peak (mJy beam^{-1})	error	Integrated (mJy)	error	Major (arcsec)	error	Minor (arcsec)	error	PA (°)	error	flags	aux_flags
G43.3858+0.4543	6224600	19:09:02.41	+09:30:09.50	0.34	0.06	0.34	0.06	0.42	-1.0	0.42	-1.0	0.01	-1.0	4	0
G43.3866-0.4692	5151600	19:12:21.66	+09:04:35.90	0.28	0.05	0.28	0.05	0.42	-1.0	0.42	-1.0	-0.01	-1.0	4	0
G43.3869+0.3116	6125100	19:09:33.34	+09:26:16.01	0.46	0.08	0.47	0.08	0.42	-1.0	0.42	-1.0	0.04	-1.0	4	0
G43.3872-0.8164	4262500	19:13:36.51	+08:54:58.64	0.3	0.05	0.31	0.05	0.42	-1.0	0.42	-1.0	-0.0	-1.0	4	0
G43.3896-0.6495	4364000	19:13:00.85	+08:59:44.67	0.31	0.05	0.31	0.05	0.42	-1.0	0.42	-1.0	-0.03	-1.0	4	0
G43.3896-0.6495	4353400	19:13:00.85	+08:59:44.69	0.32	0.05	0.32	0.05	0.42	-1.0	0.42	-1.0	0.03	-1.0	4	0
G43.3930+0.9788	7210800	19:07:09.89	+09:45:01.84	0.27	0.05	0.27	0.05	0.42	-1.0	0.42	-1.0	-0.03	-1.0	4	0
G43.3972-0.5930	4356600	19:12:49.53	+09:01:43.22	0.32	0.06	0.33	0.06	0.42	-1.0	0.42	-1.0	0.02	-1.0	4	0
G43.3979-0.6169	4356000	19:12:54.76	+09:01:05.74	0.46	0.05	0.53	0.08	0.49	0.04	0.41	0.02	12.98	0.42	0	0
G43.3991+0.8951	7113700	19:07:28.67	+09:43:02.82	0.92	0.05	0.98	0.06	0.45	0.01	0.42	0.01	0.58	0.58	0	0
G43.4006+0.5227	6227300	19:08:49.31	+09:32:50.42	0.27	0.05	0.27	0.05	0.42	-1.0	0.42	-1.0	-0.0	-1.0	4	0
G43.4055+0.9942	7211800	19:07:07.95	+09:46:07.36	0.33	0.05	0.34	0.05	0.42	-1.0	0.42	-1.0	-0.03	-1.0	4	0
G43.4066+0.0238	5335400	19:10:37.67	+09:19:20.64	0.3	0.05	0.3	0.05	0.42	-1.0	0.42	-1.0	0.03	-1.0	4	0
G43.4078-0.0230	5333400	19:10:47.88	+09:18:06.75	2.94	0.08	2.99	0.09	0.49	0.01	0.36	0.0	-16.2	0.04	0	0
G43.4078-0.0230	5344600	19:10:47.88	+09:18:06.77	3.03	0.08	3.04	0.09	0.48	0.0	0.37	0.0	-14.98	0.05	0	0
G43.4083-0.0230	5344800	19:10:47.94	+09:18:08.27	0.46	0.08	0.58	0.13	0.48	0.05	0.47	0.05	21.25	14.3	0	0
G43.4093-0.6224	4356300	19:12:57.24	+09:01:32.84	0.32	0.05	0.32	0.05	0.42	-1.0	0.42	-1.0	0.02	-1.0	4	0
G43.4128-0.0814	5343200	19:11:01.03	+09:16:45.57	0.65	0.06	0.52	0.05	0.39	0.01	0.36	0.01	-87.33	0.72	0	0
G43.4146+0.3323	6135900	19:09:31.98	+09:28:19.00	0.42	0.06	0.43	0.06	0.42	-1.0	0.42	-1.0	-0.03	-1.0	4	0
G43.4146+0.3323	6127400	19:09:31.98	+09:28:18.97	0.43	0.07	0.43	0.07	0.42	-1.0	0.42	-1.0	0.04	-1.0	4	0
G43.4269+0.0361	5347300	19:10:37.29	+09:20:45.91	0.35	0.06	0.35	0.06	0.42	-1.0	0.42	-1.0	-0.03	-1.0	4	0
G43.4288-0.2953	51413100	19:11:48.96	+09:11:40.27	1.5	0.24	1.51	0.24	0.42	-1.0	0.42	-1.0	0.03	-1.0	4	0
G43.4288-0.2953	5157200	19:11:48.96	+09:11:40.24	1.52	0.25	1.54	0.25	0.42	-1.0	0.42	-1.0	-0.03	-1.0	4	0
G43.4313-0.8289	4360900	19:13:44.17	+08:56:58.49	1.1	0.07	0.96	0.07	0.4	0.01	0.38	0.01	89.08	1.06	0	0
G43.4313-0.8289	4264400	19:13:44.17	+08:56:58.48	1.04	0.06	0.94	0.06	0.41	0.01	0.39	0.01	-0.41	1.11	0	0
G43.4318+0.3512	6233500	19:09:29.85	+09:29:45.41	0.35	0.06	0.35	0.06	0.42	-1.0	0.42	-1.0	-0.04	-1.0	4	0
G43.4318+0.3512	6224000	19:09:29.85	+09:29:45.40	0.35	0.06	0.36	0.06	0.42	-1.0	0.42	-1.0	0.03	-1.0	4	0
G43.4338+0.9887	7212800	19:07:12.32	+09:47:28.82	0.32	0.05	0.33	0.05	0.42	-1.0	0.42	-1.0	-0.03	-1.0	4	0
G43.4344-0.3570	5156100	19:12:02.88	+09:10:15.38	0.31	0.05	0.32	0.06	0.42	-1.0	0.42	-1.0	-0.02	-1.0	4	0
G43.4359-0.7974	4265200	19:13:37.91	+08:58:05.56	0.34	0.06	0.34	0.06	0.42	-1.0	0.42	-1.0	-0.0	-1.0	4	0
G43.4377-0.6334	4357903	19:13:02.80	+09:02:45.14	0.58	0.11	1.31	0.24	0.86	0.0	0.46	0.0	12.73	0.05	0	0
G43.4379-0.6333	4357902	19:13:02.81	+09:02:45.95	0.43	0.11	0.34	0.09	0.42	0.0	0.34	0.0	36.83	0.08	0	0
G43.4379-0.6334	4366601	19:13:02.82	+09:02:45.62	0.95	0.16	1.56	0.27	0.72	0.0	0.4	0.0	19.42	0.09	0	0
G43.4379-0.6334	4357901	19:13:02.83	+09:02:45.76	0.91	0.11	1.31	0.16	0.6	0.0	0.43	0.0	-0.94	0.06	0	0
G43.4380-0.6333	4366602	19:13:02.81	+09:02:46.02	0.73	0.16	0.55	0.12	0.4	0.0	0.34	0.0	-76.13	0.17	0	0

Source Galactic name	Source Index	RA J2000	Dec J2000	Observed flux density Peak (mJy beam^{-1})	error	Integrated (mJy)	error	Major (arcsec)	error	Minor (arcsec)	error	PA (°)	error	flags	aux_flags
G43.4381-0.6334	5150400	19:13:02.85	+09:02:46.45	6.43	0.2	7.72	0.28	0.5	0.01	0.42	0.01	-0.12	0.1	0	0
G43.4381-0.6334	4357900	19:13:02.85	+09:02:46.43	8.42	0.11	8.28	0.11	0.44	0.0	0.4	0.0	-47.44	0.09	0	0
G43.4381-0.6334	4366600	19:13:02.85	+09:02:46.44	9.98	0.16	9.84	0.19	0.43	0.0	0.4	0.0	-3.09	0.14	0	0
G43.4382-0.6336	4358100	19:13:02.91	+09:02:46.33	0.68	0.11	0.91	0.18	0.5	0.05	0.47	0.03	-13.17	2.13	0	0
G43.4427+0.0722	6131400	19:10:31.28	+09:22:36.58	1.07	0.06	0.97	0.06	0.42	0.01	0.39	0.01	6.16	0.41	0	0
G43.4428+0.0719	6131500	19:10:31.35	+09:22:36.50	0.34	0.05	0.35	0.05	0.42	-1.0	0.42	-1.0	0.01	-1.0	4	0
G43.4448-0.7591	4363900	19:13:30.66	+08:59:38.07	0.32	0.05	0.32	0.05	0.42	-1.0	0.42	-1.0	-0.02	-1.0	4	0
G43.4571+0.2739	6232600	19:09:49.37	+09:28:57.80	5.55	0.08	5.62	0.09	0.42	0.0	0.42	0.0	3.13	1.83	0	0
G43.4571+0.2739	6136500	19:09:49.37	+09:28:57.83	4.33	0.16	4.22	0.17	0.42	0.01	0.41	0.01	89.21	0.67	0	0
G43.4573+0.2979	6223700	19:09:44.20	+09:29:38.26	1.24	0.22	1.25	0.22	0.42	-1.0	0.42	-1.0	0.04	-1.0	4	0
G43.4655-0.6535	5151000	19:13:10.26	+09:03:40.20	0.47	0.08	0.47	0.08	0.42	-1.0	0.42	-1.0	0.02	-1.0	4	0
G43.4655-0.6535	5160700	19:13:10.26	+09:03:40.21	0.47	0.08	0.47	0.08	0.42	-1.0	0.42	-1.0	-0.04	-1.0	4	0
G43.4657+0.7680	7113800	19:08:03.61	+09:43:05.15	0.64	0.05	0.69	0.07	0.44	0.02	0.44	0.02	-2.15	4.75	0	0
G43.4675-0.8621	4265100	19:13:55.39	+08:57:58.43	0.75	0.07	0.65	0.07	0.41	0.02	0.37	0.01	-2.86	0.55	0	0
G43.4675-0.8621	4361700	19:13:55.39	+08:57:58.44	0.72	0.06	0.65	0.06	0.43	0.02	0.37	0.01	1.19	0.31	0	0
G43.4675-0.9215	4360300	19:14:08.17	+08:56:18.98	0.71	0.11	0.65	0.12	0.47	0.05	0.34	0.02	18.03	0.25	0	0
G43.4675-0.9215	4263700	19:14:08.18	+08:56:19.00	0.62	0.05	0.58	0.05	0.44	0.01	0.38	0.01	14.4	0.32	0	0
G43.4681-0.7024	4357300	19:13:21.07	+09:02:26.81	0.28	0.05	0.28	0.05	0.42	-1.0	0.42	-1.0	0.04	-1.0	4	0
G43.4712+0.6328	7121500	19:08:33.43	+09:39:38.66	0.3	0.05	0.3	0.05	0.42	-1.0	0.42	-1.0	-0.03	-1.0	4	0
G43.4717-0.3432	5254300	19:12:04.09	+09:12:37.44	0.31	0.06	0.31	0.06	0.42	-1.0	0.42	-1.0	-0.03	-1.0	4	0
G43.4734+0.4619	6323300	19:09:10.60	+09:35:02.23	3.87	0.07	4.16	0.08	0.45	0.0	0.43	0.0	4.91	0.25	0	0
G43.4735+0.4621	6323301	19:09:10.56	+09:35:02.63	0.38	0.07	0.27	0.05	0.38	0.0	0.34	0.0	-25.67	0.24	0	0
G43.4743+0.3034	6233900	19:09:44.93	+09:30:41.51	0.38	0.06	0.42	0.09	0.45	0.04	0.43	0.04	0.26	4.69	0	0
G43.4744-0.7261	4365800	19:13:26.89	+09:02:07.41	0.3	0.05	0.31	0.05	0.42	-1.0	0.42	-1.0	-0.02	-1.0	4	0
G43.4817-0.8529	4362900	19:13:55.00	+08:58:58.93	0.42	0.05	0.42	0.06	0.46	0.03	0.38	0.02	-1.5	0.39	0	0
G43.4856-1.0040	4262600	19:14:27.97	+08:54:59.03	0.28	0.05	0.28	0.05	0.42	-1.0	0.42	-1.0	0.03	-1.0	4	0
G43.4901+0.3752	6235000	19:09:31.20	+09:33:31.46	0.32	0.06	0.32	0.06	0.42	-1.0	0.42	-1.0	-0.04	-1.0	4	0
G43.4901+0.4316	6323500	19:09:19.02	+09:35:05.26	0.3	0.05	0.3	0.05	0.42	-1.0	0.42	-1.0	0.01	-1.0	4	0
G43.4929+0.1578	6231700	19:10:18.44	+09:27:39.15	0.34	0.06	0.34	0.06	0.42	-1.0	0.42	-1.0	-0.0	-1.0	4	0
G43.4948+0.9016	7213200	19:07:37.98	+09:48:19.48	0.35	0.05	0.28	0.05	0.41	0.02	0.34	0.03	-87.31	0.69	0	0
G43.4961+0.3939	6236000	19:09:27.85	+09:34:21.62	1.2	0.21	1.21	0.21	0.42	-1.0	0.42	-1.0	-0.04	-1.0	4	0
G43.4978-0.3018	5341600	19:11:58.12	+09:15:09.71	0.49	0.06	0.43	0.06	0.4	0.02	0.39	0.02	18.2	2.11	0	0
G43.4978-0.3018	5353000	19:11:58.13	+09:15:09.70	0.41	0.07	0.41	0.07	0.42	-1.0	0.42	-1.0	-0.04	-1.0	4	0
G43.4978-0.3018	5256500	19:11:58.13	+09:15:09.70	0.42	0.06	0.42	0.06	0.42	-1.0	0.42	-1.0	-0.03	-1.0	4	0
G43.4978-0.3018	5246300	19:11:58.12	+09:15:09.72	0.5	0.06	0.47	0.07	0.42	0.03	0.4	0.02	9.24	1.3	0	0

Source Galactic name	Source Index	RA J2000	Dec J2000	Observed flux density				Major (arcsec)		Minor (arcsec)		PA (°)		flags	aux_flags
				Peak (mJy beam^{-1})	error	Integrated (mJy)	error		error		error		error		
G43.4993-0.9543	4264500	19:14:18.82	+08:57:05.47	9.52	0.08	9.43	0.09	0.42	0.0	0.42	0.0	3.03	0.41	0	0
G43.4993-0.9543	4361300	19:14:18.82	+08:57:05.46	9.56	0.09	9.43	0.1	0.42	0.0	0.42	0.0	3.92	0.63	0	0
G43.4994-0.9542	4264501	19:14:18.81	+08:57:06.11	0.67	0.08	0.47	0.06	0.37	0.0	0.34	0.0	4.54	0.38	0	0
G43.4994-0.9542	4361301	19:14:18.81	+08:57:06.10	0.86	0.09	0.57	0.06	0.35	0.0	0.34	0.0	1.68	0.62	0	0
G43.5002-0.6976	5161300	19:13:23.66	+09:04:17.12	0.29	0.05	0.3	0.05	0.42	-1.0	0.42	-1.0	-0.03	-1.0	4	0
G43.5002-0.6976	5151400	19:13:23.66	+09:04:17.12	0.29	0.05	0.29	0.05	0.42	-1.0	0.42	-1.0	0.03	-1.0	4	0
G43.5010-0.3597	5244600	19:12:10.96	+09:13:43.37	1.19	0.06	1.03	0.06	0.39	0.01	0.39	0.01	87.1	1.73	0	0
G43.5010-0.3597	5340200	19:12:10.96	+09:13:43.40	1.23	0.12	1.03	0.12	0.39	0.02	0.37	0.01	14.48	1.25	0	0
G43.5010-0.3597	5254800	19:12:10.96	+09:13:43.38	1.23	0.06	1.05	0.06	0.39	0.01	0.39	0.01	87.39	1.62	0	0
G43.5010-0.3597	5350500	19:12:10.96	+09:13:43.40	1.24	0.12	1.03	0.12	0.39	0.02	0.37	0.01	17.01	1.28	0	0
G43.5087+0.2248	6233800	19:10:05.77	+09:30:21.05	0.32	0.05	0.32	0.05	0.42	-1.0	0.42	-1.0	-0.01	-1.0	4	0
G43.5122-0.8936	4363600	19:14:07.21	+08:59:28.04	0.29	0.05	0.29	0.05	0.42	-1.0	0.42	-1.0	0.01	-1.0	4	0
G43.5123-0.9827	4361000	19:14:26.41	+08:56:59.61	0.41	0.07	0.42	0.07	0.42	-1.0	0.42	-1.0	0.02	-1.0	4	0
G43.5127-0.5672	5154100	19:12:56.98	+09:08:34.78	0.38	0.06	0.38	0.06	0.42	-1.0	0.42	-1.0	0.01	-1.0	4	0
G43.5175+0.9156	7310700	19:07:37.50	+09:49:55.20	0.45	0.07	0.45	0.09	0.43	0.03	0.41	0.04	-86.72	2.26	0	0
G43.5175+0.9156	7214600	19:07:37.50	+09:49:55.21	0.44	0.06	0.4	0.07	0.43	0.02	0.38	0.03	-85.62	0.96	0	0
G43.5192+0.8484	7213100	19:07:52.22	+09:48:09.32	0.55	0.05	0.53	0.05	0.42	0.01	0.4	0.02	-89.36	1.96	0	0
G43.5224-0.3029	5354500	19:12:01.13	+09:16:26.38	0.39	0.07	0.39	0.07	0.42	-1.0	0.42	-1.0	-0.04	-1.0	4	0
G43.5230+0.9593	7311500	19:07:28.65	+09:51:25.28	0.31	0.05	0.31	0.05	0.42	-1.0	0.42	-1.0	-0.03	-1.0	4	0
G43.5290+0.0950	6135400	19:10:36.05	+09:27:50.17	0.33	0.06	0.33	0.06	0.42	-1.0	0.42	-1.0	0.02	-1.0	4	0
G43.5354+0.4764	6326300	19:09:14.44	+09:38:44.22	0.38	0.06	0.39	0.06	0.42	-1.0	0.42	-1.0	0.01	-1.0	4	0
G43.5369+0.8212	7213400	19:08:00.08	+09:48:20.65	0.29	0.05	0.29	0.05	0.42	-1.0	0.42	-1.0	0.0	-1.0	4	0
G43.5374+0.0621	6134900	19:10:44.11	+09:27:22.06	0.28	0.05	0.28	0.05	0.42	-1.0	0.42	-1.0	0.02	-1.0	4	0
G43.5374+0.0621	6231400	19:10:44.11	+09:27:22.07	0.27	0.05	0.27	0.05	0.42	-1.0	0.42	-1.0	0.01	-1.0	4	0
G43.5374+0.7000	7210700	19:08:26.35	+09:45:01.60	0.27	0.05	0.27	0.05	0.42	-1.0	0.42	-1.0	0.02	-1.0	4	0
G43.5405+0.4531	6325800	19:09:20.04	+09:38:21.89	0.32	0.06	0.32	0.06	0.42	-1.0	0.42	-1.0	0.01	-1.0	4	0
G43.5444-0.1101	6142400	19:11:22.04	+09:22:57.85	0.33	0.06	0.33	0.06	0.42	-1.0	0.42	-1.0	-0.01	-1.0	4	0
G43.5468+0.4981	7121900	19:09:11.02	+09:39:56.52	0.45	0.06	0.36	0.06	0.38	0.02	0.37	0.02	-83.31	2.75	0	0
G43.5501+0.6400	7125800	19:08:40.73	+09:44:02.64	0.29	0.05	0.3	0.05	0.42	-1.0	0.42	-1.0	-0.03	-1.0	4	0
G43.5518-0.9975	4362700	19:14:34.03	+08:58:40.85	0.28	0.05	0.28	0.05	0.42	-1.0	0.42	-1.0	0.03	-1.0	4	0
G43.5584+0.8292	7214500	19:08:00.75	+09:49:42.76	0.3	0.05	0.3	0.05	0.42	-1.0	0.42	-1.0	0.0	-1.0	4	0
G43.5603-0.6271	5250900	19:13:15.24	+09:09:26.68	0.3	0.05	0.3	0.05	0.42	-1.0	0.42	-1.0	0.02	-1.0	4	0
G43.5605-0.0345	6133300	19:11:07.53	+09:25:55.11	0.64	0.1	0.65	0.1	0.42	-1.0	0.42	-1.0	0.04	-1.0	4	0
G43.5605-0.0345	6145100	19:11:07.53	+09:25:55.11	0.63	0.06	0.59	0.07	0.45	0.02	0.37	0.01	-4.81	0.29	0	0
G43.5657+0.4155	6326100	19:09:30.98	+09:38:39.89	0.32	0.06	0.33	0.06	0.42	-1.0	0.42	-1.0	0.02	-1.0	4	0

Source Galactic name	Source Index	RA J2000	Dec J2000	Peak (mJy beam^{-1})	error	Integrated (mJy)	error	Major (arcsec)	error	Minor (arcsec)	error	PA (°)	error	flags	aux_flags
G43.5698+0.4873	7122700	19:09:15.93	+09:40:52.13	0.62	0.05	0.64	0.06	0.44	0.01	0.42	0.02	-87.79	1.7	0	0
G43.5720-0.6607	5155100	19:13:23.81	+09:09:07.74	0.3	0.05	0.3	0.05	0.42	-1.0	0.42	-1.0	0.03	-1.0	4	0
G43.5720-0.6607	5164600	19:13:23.81	+09:09:07.74	0.29	0.05	0.29	0.05	0.42	-1.0	0.42	-1.0	-0.03	-1.0	4	0
G43.5760+0.7730	7214200	19:08:14.88	+09:49:05.93	0.28	0.05	0.28	0.05	0.42	-1.0	0.42	-1.0	0.01	-1.0	4	0
G43.5773+0.8284	7311000	19:08:03.05	+09:50:41.88	0.27	0.05	0.28	0.05	0.42	-1.0	0.42	-1.0	-0.0	-1.0	4	0
G43.5791+0.0258	6232200	19:10:56.62	+09:28:34.66	0.37	0.06	0.37	0.07	0.42	-1.0	0.42	-1.0	0.02	-1.0	4	0
G43.5794+0.0261	6148400	19:10:56.58	+09:28:36.27	3.36	0.08	10.08	0.27	0.76	0.01	0.7	0.01	-1.35	0.16	0	0
G43.5794+0.0261	6242500	19:10:56.59	+09:28:36.26	3.85	0.05	11.35	0.17	0.73	0.0	0.71	0.0	4.32	0.33	0	0
G43.5794+0.0261	6232300	19:10:56.59	+09:28:36.26	3.91	0.05	11.55	0.17	0.73	0.0	0.71	0.0	2.57	0.3	0	0
G43.5794+0.0261	6136300	19:10:56.58	+09:28:36.27	3.34	0.08	10.18	0.28	0.77	0.01	0.7	0.01	-0.58	0.15	0	0
G43.5883+0.5624	7125700	19:09:01.78	+09:43:55.84	0.28	0.05	0.29	0.05	0.42	-1.0	0.42	-1.0	-0.01	-1.0	4	0
G43.5963+0.4433	7123000	19:09:28.43	+09:41:03.75	0.26	0.05	0.27	0.05	0.42	-1.0	0.42	-1.0	0.01	-1.0	4	0
G43.5997+1.0208	7315800	19:07:23.94	+09:57:12.30	0.63	0.1	0.63	0.1	0.42	-1.0	0.42	-1.0	-0.03	-1.0	4	0
G43.6024-0.1498	6144200	19:11:37.12	+09:24:56.89	0.32	0.06	0.33	0.06	0.42	-1.0	0.42	-1.0	-0.0	-1.0	4	0
G43.6047-0.7326	5164300	19:13:42.98	+09:08:52.25	0.32	0.05	0.32	0.05	0.42	-1.0	0.42	-1.0	-0.02	-1.0	4	0
G43.6146-0.1106	6240700	19:11:30.03	+09:26:41.14	0.5	0.08	0.5	0.08	0.42	-1.0	0.42	-1.0	-0.02	-1.0	4	0
G43.6154-0.7691	5260200	19:13:52.05	+09:08:25.32	0.9	0.15	0.9	0.15	0.42	-1.0	0.42	-1.0	-0.02	-1.0	4	0
G43.6170-0.2743	6141700	19:12:05.60	+09:22:15.90	0.25	0.05	0.26	0.05	0.42	-1.0	0.42	-1.0	0.02	-1.0	4	0
G43.6238-0.0694	6147900	19:11:22.20	+09:28:19.04	0.5	0.08	0.5	0.08	0.42	-1.0	0.42	-1.0	-0.01	-1.0	4	0
G43.6275+0.9052	7314400	19:07:52.08	+09:55:29.54	0.3	0.05	0.3	0.05	0.42	-1.0	0.42	-1.0	-0.01	-1.0	4	0
G43.6309+0.7949	7312200	19:08:16.31	+09:52:37.81	0.47	0.05	0.47	0.06	0.44	0.02	0.4	0.02	10.04	0.92	0	0
G43.6317-0.4081	5357900	19:12:36.13	+09:19:19.85	0.39	0.06	0.33	0.06	0.45	0.03	0.34	0.02	36.67	0.4	0	0
G43.6328-0.1005	6241700	19:11:29.91	+09:27:56.03	0.32	0.05	0.32	0.06	0.42	-1.0	0.42	-1.0	-0.02	-1.0	4	0
G43.6362-0.1591	6145900	19:11:42.93	+09:26:29.05	0.35	0.05	0.36	0.05	0.42	-1.0	0.42	-1.0	-0.0	-1.0	4	0
G43.6411-0.0029	6330200	19:11:09.79	+09:31:04.94	1.28	0.22	1.29	0.22	0.42	-1.0	0.42	-1.0	0.03	-1.0	4	0
G43.6430-0.7969	5164500	19:14:01.14	+09:09:07.06	0.36	0.06	0.36	0.06	0.42	-1.0	0.42	-1.0	-0.01	-1.0	4	0
G43.6437+0.2397	6334600	19:10:17.72	+09:37:56.68	0.31	0.05	0.31	0.05	0.42	-1.0	0.42	-1.0	-0.01	-1.0	4	0
G43.6465+0.5343	7128500	19:09:14.39	+09:46:15.15	0.48	0.08	0.48	0.08	0.42	-1.0	0.42	-1.0	-0.0	-1.0	4	0
G43.6481+0.4317	7125400	19:09:36.74	+09:43:30.07	0.27	0.05	0.28	0.05	0.42	-1.0	0.42	-1.0	0.01	-1.0	4	0
G43.6533+0.4166	7220200	19:09:40.59	+09:43:21.53	3.81	0.23	3.58	0.24	0.42	0.01	0.39	0.01	-10.24	0.44	0	0
G43.6533+0.4166	7124900	19:09:40.59	+09:43:21.53	3.5	0.06	3.56	0.07	0.43	0.0	0.42	0.0	-8.52	0.35	0	0
G43.6554-0.8278	5260403	19:14:09.20	+09:08:54.60	0.52	0.32	2.24	1.39	0.95	0.06	0.79	0.06	-87.06	10.95	0	1
G43.6555-0.8277	5260401	19:14:09.19	+09:08:55.26	0.56	0.32	1.16	0.68	0.63	0.06	0.58	0.06	-85.68	10.08	0	1
G43.6555-0.8278	5260400	19:14:09.22	+09:08:55.00	0.38	0.32	0.26	0.23	0.35	0.06	0.34	0.06	-86.49	9.34	0	1
G43.6555-0.8278	5164400	19:14:09.21	+09:08:54.95	0.8	0.09	7.28	1.01	1.43	0.04	1.13	0.08	-2.51	0.21	0	0

Source Galactic name	Source Index	RA J2000	Dec J2000	Observed flux density				Major (arcsec)		Minor (arcsec)		PA (°)		flags	aux_flags
				Peak (mJy beam^{-1})	error	Integrated (mJy)	error		error		error		error		
G43.6556-0.8278	5260404	19:14:09.22	+09:08:55.42	0.38	0.32	0.36	0.31	0.41	0.06	0.41	0.06	-6.31	9.1	0	1
G43.6556-0.8279	5260402	19:14:09.25	+09:08:55.10	0.57	0.32	1.79	1.03	0.84	0.06	0.66	0.06	-0.24	7.23	0	1
G43.6556-0.8280	5164401	19:14:09.26	+09:08:55.18	0.43	0.09	2.13	0.51	1.14	0.04	0.78	0.08	-6.45	0.18	0	0
G43.6557-0.8278	5260405	19:14:09.24	+09:08:55.77	0.38	0.32	1.39	1.19	1.46	0.06	0.44	0.06	87.31	26.01	0	1
G43.6599+0.4641	7221600	19:09:31.06	+09:45:01.43	0.31	0.05	0.31	0.06	0.42	-1.0	0.42	-1.0	0.0	-1.0	4	0
G43.6628+0.6389	7321400	19:08:53.61	+09:50:00.91	0.33	0.06	0.34	0.06	0.42	-1.0	0.42	-1.0	-0.03	-1.0	4	0
G43.6629-0.1347	6148300	19:11:40.68	+09:28:34.98	0.66	0.11	0.67	0.11	0.42	-1.0	0.42	-1.0	-0.0	-1.0	4	0
G43.6711+0.6690	7322200	19:08:48.06	+09:51:17.34	0.26	0.05	0.26	0.05	0.42	-1.0	0.42	-1.0	-0.04	-1.0	4	0
G43.6712+0.6690	7311400	19:08:48.06	+09:51:17.34	0.26	0.04	0.26	0.05	0.42	-1.0	0.42	-1.0	0.03	-1.0	4	0
G43.6716-0.6109	5353900	19:13:24.31	+09:15:48.80	0.31	0.05	0.31	0.05	0.42	-1.0	0.42	-1.0	0.02	-1.0	4	0
G43.6766-0.3374	6142900	19:12:25.92	+09:23:40.90	0.31	0.05	0.32	0.06	0.42	-1.0	0.42	-1.0	0.03	-1.0	4	0
G43.6780+0.5113	7223900	19:09:22.91	+09:47:17.44	0.43	0.05	0.39	0.05	0.45	0.03	0.36	0.02	-13.85	0.3	0	0
G43.6784+0.3745	7125600	19:09:52.51	+09:43:31.68	0.29	0.05	0.29	0.05	0.42	-1.0	0.42	-1.0	0.03	-1.0	4	0
G43.6784+0.3745	7134300	19:09:52.51	+09:43:31.69	0.31	0.05	0.26	0.05	0.39	0.03	0.39	0.03	12.55	11.03	0	0
G43.6801-0.8130	5261600	19:14:08.80	+09:10:38.19	0.3	0.05	0.3	0.05	0.42	-1.0	0.42	-1.0	-0.01	-1.0	4	0
G43.6808+0.2464	7131300	19:10:20.44	+09:40:06.53	0.26	0.05	0.27	0.05	0.42	-1.0	0.42	-1.0	-0.02	-1.0	4	0
G43.6811-0.0535	6340900	19:11:25.21	+09:31:48.24	0.4	0.07	0.41	0.07	0.42	-1.0	0.42	-1.0	-0.03	-1.0	4	0
G43.6823-0.4737	5358900	19:12:55.95	+09:20:11.97	0.3	0.05	0.31	0.05	0.42	-1.0	0.42	-1.0	-0.0	-1.0	4	0
G43.6862-0.6553	5361900	19:13:35.54	+09:15:21.21	0.29	0.05	0.3	0.05	0.42	-1.0	0.42	-1.0	-0.04	-1.0	4	0
G43.6927+0.7317	7313100	19:08:36.91	+09:54:10.26	0.3	0.05	0.3	0.05	0.42	-1.0	0.42	-1.0	0.02	-1.0	4	0
G43.7040-0.6545	5266200	19:13:37.36	+09:16:19.36	0.54	0.09	0.54	0.09	0.42	-1.0	0.42	-1.0	-0.03	-1.0	4	0
G43.7093+0.4178	7223300	19:09:46.63	+09:46:22.42	0.41	0.06	0.41	0.07	0.44	0.04	0.4	0.02	11.36	1.04	0	0
G43.7105+0.2558	7132800	19:10:21.74	+09:41:56.98	0.26	0.05	0.26	0.05	0.42	-1.0	0.42	-1.0	-0.02	-1.0	4	0
G43.7192+0.1627	7131100	19:10:42.83	+09:39:49.94	0.38	0.06	0.29	0.05	0.39	0.03	0.35	0.02	2.22	0.7	0	0
G43.7213+0.3971	7128700	19:09:52.44	+09:46:26.28	0.72	0.12	0.72	0.13	0.42	-1.0	0.42	-1.0	0.03	-1.0	4	0
G43.7263-0.8004	5360300	19:14:11.30	+09:13:26.76	1.45	0.25	1.47	0.25	0.42	-1.0	0.42	-1.0	-0.01	-1.0	4	0
G43.7308+0.0972	7130600	19:10:58.28	+09:38:37.97	0.5	0.09	0.5	0.09	0.42	-1.0	0.42	-1.0	0.01	-1.0	4	0
G43.7348-0.2005	6245300	19:12:02.97	+09:30:34.71	0.58	0.05	0.53	0.05	0.43	0.01	0.38	0.02	85.87	0.5	0	0
G43.7374-0.6194	5357000	19:13:33.55	+09:19:04.35	2.66	0.11	5.67	0.27	0.68	0.01	0.55	0.01	-84.88	0.16	0	0
G43.7376-0.6195	5357001	19:13:33.61	+09:19:04.89	1.74	0.11	2.98	0.21	0.64	0.01	0.47	0.01	9.52	0.1	0	0
G43.7376-0.6211	5356400	19:13:33.95	+09:19:02.09	1.26	0.14	1.71	0.21	0.62	0.03	0.38	0.01	31.44	0.12	0	0
G43.7377-0.6207	5356700	19:13:33.88	+09:19:03.16	0.98	0.14	1.04	0.19	0.47	0.03	0.4	0.03	-81.09	0.72	0	0
G43.7378-0.6209	5356502	19:13:33.94	+09:19:03.00	0.82	0.14	1.02	0.18	0.5	0.0	0.44	0.0	28.15	0.1	0	0
G43.7378-0.6211	5356501	19:13:33.98	+09:19:02.76	1.43	0.14	1.55	0.16	0.57	0.0	0.34	0.0	-17.94	0.07	0	0
G43.7379-0.6210	5356500	19:13:33.98	+09:19:03.39	12.35	0.14	11.24	0.15	0.42	0.0	0.39	0.0	-10.18	0.1	0	0

Source Galactic name	Source Index	RA J2000	Dec J2000	Observed flux density				Major (arcsec)		Minor (arcsec)		PA (°)		flags	aux_flags
				Peak (mJy beam^{-1})	error	Integrated (mJy)	error		error		error		error		
G43.7380-0.6213	5356600	19:13:34.04	+09:19:02.99	1.15	0.14	1.3	0.19	0.48	0.02	0.42	0.03	-80.38	0.75	0	0
G43.7382-0.6210	5357200	19:13:34.00	+09:19:04.26	1.62	0.13	1.64	0.16	0.44	0.01	0.41	0.01	13.68	0.89	0	0
G43.7384+0.4998	7226400	19:09:32.18	+09:50:11.25	0.32	0.05	0.32	0.06	0.42	-1.0	0.42	-1.0	0.0	-1.0	4	0
G43.7385-0.7836	5361600	19:14:09.07	+09:14:33.54	0.33	0.06	0.33	0.06	0.42	-1.0	0.42	-1.0	-0.02	-1.0	4	0
G43.7386-0.6234	5356300	19:13:34.57	+09:19:01.58	1.48	0.1	2.11	0.16	0.57	0.02	0.44	0.01	0.68	0.13	0	0
G43.7417-0.8990	5166100	19:14:34.26	+09:11:30.83	1.39	0.24	1.41	0.24	0.42	-1.0	0.42	-1.0	0.02	-1.0	4	0
G43.7451+0.2777	7231400	19:10:20.91	+09:44:23.95	0.36	0.06	0.4	0.09	0.46	0.04	0.43	0.05	89.85	2.5	0	0
G43.7451+0.2777	7135400	19:10:20.91	+09:44:23.94	0.37	0.05	0.38	0.07	0.44	0.03	0.41	0.04	-89.95	1.76	0	0
G43.7463-0.0918	6342700	19:11:40.81	+09:34:12.52	0.28	0.05	0.28	0.05	0.42	-1.0	0.42	-1.0	-0.02	-1.0	4	0
G43.7475+0.8724	8210100	19:08:12.61	+10:00:58.62	1.57	0.25	1.59	0.25	0.42	-1.0	0.42	-1.0	-0.02	-1.0	4	0
G43.7564-0.7930	5361800	19:14:13.10	+09:15:14.81	0.41	0.06	0.41	0.06	0.42	-1.0	0.42	-1.0	-0.01	-1.0	4	0
G43.7564-0.7930	5264900	19:14:13.10	+09:15:14.86	0.4	0.06	0.4	0.06	0.42	-1.0	0.42	-1.0	-0.01	-1.0	4	0
G43.7578+0.2694	7135800	19:10:24.12	+09:44:50.55	0.38	0.06	0.37	0.07	0.43	0.04	0.4	0.03	-10.79	1.47	0	0
G43.7578+0.2694	7231800	19:10:24.12	+09:44:50.57	0.44	0.06	0.45	0.08	0.45	0.03	0.4	0.03	79.2	1.09	0	0
G43.7659-0.9093	5262800	19:14:39.23	+09:12:30.86	0.34	0.06	0.35	0.06	0.42	-1.0	0.42	-1.0	0.01	-1.0	4	0
G43.7662-0.3279	6252500	19:12:33.98	+09:28:42.84	0.28	0.05	0.28	0.05	0.42	-1.0	0.42	-1.0	-0.04	-1.0	4	0
G43.7677+0.3655	7224400	19:10:04.49	+09:48:01.97	0.3	0.05	0.3	0.05	0.42	-1.0	0.42	-1.0	0.03	-1.0	4	0
G43.7677+0.3655	7235300	19:10:04.49	+09:48:01.98	0.31	0.05	0.23	0.04	0.39	0.02	0.34	0.03	-83.8	0.84	0	0
G43.7732+0.2757	7232900	19:10:24.49	+09:45:50.13	0.3	0.05	0.3	0.05	0.42	-1.0	0.42	-1.0	-0.03	-1.0	4	0
G43.7773-0.2384	6340800	19:12:15.93	+09:31:47.20	0.49	0.08	0.5	0.08	0.42	-1.0	0.42	-1.0	0.01	-1.0	4	0
G43.7782+1.0234	8213300	19:07:43.38	+10:06:47.04	0.63	0.08	0.65	0.1	0.45	0.03	0.41	0.02	-2.94	1.07	0	0
G43.7863+1.0080	8213400	19:07:47.62	+10:06:47.22	0.33	0.06	0.33	0.06	0.42	-1.0	0.42	-1.0	-0.03	-1.0	4	0
G43.7879-0.3507	6253200	19:12:41.35	+09:29:13.72	0.95	0.05	1.67	0.09	0.61	0.01	0.51	0.01	-22.36	0.17	0	0
G43.7879-0.3507	6243600	19:12:41.35	+09:29:13.72	0.94	0.04	1.69	0.09	0.62	0.01	0.51	0.01	-23.48	0.15	0	0
G43.7879-0.3507	6158500	19:12:41.35	+09:29:13.80	1.44	0.22	1.45	0.22	0.42	-1.0	0.42	-1.0	-0.02	-1.0	4	0
G43.7879-0.3507	6149300	19:12:41.35	+09:29:13.81	1.36	0.21	1.38	0.21	0.42	-1.0	0.42	-1.0	0.04	-1.0	4	0
G43.7923-0.2868	6257600	19:12:28.07	+09:31:14.59	1.25	0.22	1.27	0.23	0.42	-1.0	0.42	-1.0	-0.04	-1.0	4	0
G43.7943+0.3082	7224200	19:10:19.86	+09:47:51.58	0.44	0.07	0.44	0.07	0.42	-1.0	0.42	-1.0	0.04	-1.0	4	0
G43.7944-0.2241	6246300	19:12:14.78	+09:33:05.58	0.38	0.06	0.38	0.06	0.42	-1.0	0.42	-1.0	0.01	-1.0	4	0
G43.7944-0.2241	6341800	19:12:14.78	+09:33:05.58	0.36	0.05	0.37	0.05	0.42	-1.0	0.42	-1.0	0.01	-1.0	4	0
G43.7951-0.1273	6345302	19:11:53.96	+09:35:49.47	2.45	0.33	3.63	0.49	0.53	0.0	0.49	0.0	22.28	0.07	0	0
G43.7953-0.1270	6345301	19:11:53.94	+09:35:50.55	2.52	0.33	3.52	0.46	0.68	0.0	0.37	0.0	-77.22	0.13	0	0
G43.7953-0.1276	6345400	19:11:54.06	+09:35:49.56	2.43	0.34	2.54	0.46	0.44	0.03	0.42	0.04	88.61	2.38	0	0
G43.7953-0.1279	6345200	19:11:54.12	+09:35:48.90	2.26	0.33	2.78	0.57	0.51	0.03	0.42	0.05	84.96	0.76	0	0
G43.7954-0.1273	6345300	19:11:53.99	+09:35:50.26	56.62	0.33	68.29	0.46	0.47	0.0	0.45	0.0	-89.4	0.08	0	0

Source Galactic name	Source Index	RA J2000	Dec J2000	Peak (mJy beam^{-1})	error	Integrated (mJy)	error	Major (arcsec)	error	Minor (arcsec)	error	PA (°)	error	flags	aux_flags
G43.7955-0.1265	6346100	19:11:53.85	+09:35:51.92	2.07	0.33	2.58	0.56	0.47	0.05	0.46	0.05	83.23	6.88	0	0
G43.7957-0.1269	6345901	19:11:53.95	+09:35:51.99	2.02	0.94	3.34	1.65	0.87	0.04	0.34	0.05	-22.38	3.55	0	1
G43.7957-0.1270	6345900	19:11:53.97	+09:35:51.62	1.99	0.94	1.89	0.95	0.41	0.04	0.4	0.06	85.65	7.75	0	1
G43.7975-0.0935	6348800	19:11:46.94	+09:36:53.11	0.76	0.07	0.72	0.07	0.48	0.02	0.35	0.01	2.52	0.14	0	0
G43.8042-0.0520	63410300	19:11:38.75	+09:38:23.55	0.32	0.05	0.26	0.05	0.43	0.04	0.34	0.02	-0.25	0.43	0	0
G43.8057-0.7209	5358600	19:14:03.14	+09:19:52.47	2.62	0.16	2.16	0.15	0.41	0.01	0.36	0.01	-12.03	0.27	0	0
G43.8057-0.7209	5365500	19:14:03.14	+09:19:52.45	2.58	0.07	2.4	0.08	0.43	0.01	0.38	0.0	-7.78	0.14	0	0
G43.8059-0.7209	5365501	19:14:03.16	+09:19:53.13	2.01	0.07	1.92	0.08	0.42	0.01	0.4	0.0	-9.71	0.15	0	0
G43.8059-0.7209	5358601	19:14:03.16	+09:19:53.15	2.23	0.16	2.03	0.16	0.42	0.01	0.39	0.01	-89.18	0.32	0	0
G43.8066+0.9838	8310600	19:07:55.15	+10:07:11.92	0.59	0.1	0.59	0.11	0.42	-1.0	0.42	-1.0	-0.04	-1.0	4	0
G43.8117+0.9769	8310800	19:07:57.22	+10:07:17.03	0.55	0.09	0.56	0.09	0.42	-1.0	0.42	-1.0	-0.04	-1.0	4	0
G43.8118+0.9769	8214200	19:07:57.23	+10:07:17.10	0.41	0.06	0.38	0.07	0.42	0.03	0.39	0.03	-83.83	1.57	0	0
G43.8120+0.2065	7137500	19:10:43.81	+09:45:58.84	0.42	0.07	0.43	0.07	0.42	-1.0	0.42	-1.0	-0.0	-1.0	4	0
G43.8135+0.8903	8212200	19:08:16.15	+10:04:59.39	0.35	0.06	0.36	0.06	0.42	-1.0	0.42	-1.0	-0.01	-1.0	4	0
G43.8181-0.4924	6156300	19:13:15.31	+09:26:53.81	0.41	0.06	0.66	0.14	0.54	0.06	0.53	0.06	1.37	4.81	0	0
G43.8181-0.4924	6251100	19:13:15.31	+09:26:53.83	0.5	0.07	0.51	0.08	0.42	-1.0	0.42	-1.0	-0.01	-1.0	4	0
G43.8196-0.3661	6255900	19:12:48.24	+09:30:29.29	0.31	0.05	0.31	0.05	0.42	-1.0	0.42	-1.0	-0.03	-1.0	4	0
G43.8223+0.9505	8310500	19:08:04.13	+10:07:07.02	0.56	0.1	0.57	0.1	0.42	-1.0	0.42	-1.0	-0.03	-1.0	4	0
G43.8252-0.6026	6153900	19:13:39.87	+09:24:12.43	0.32	0.06	0.33	0.06	0.42	-1.0	0.42	-1.0	0.02	-1.0	4	0
G43.8314-0.5506	6250300	19:13:29.36	+09:25:59.01	0.77	0.13	0.78	0.13	0.42	-1.0	0.42	-1.0	0.0	-1.0	4	0
G43.8366+1.0002	8215500	19:07:54.96	+10:09:15.27	0.78	0.13	0.79	0.14	0.42	-1.0	0.42	-1.0	-0.03	-1.0	4	0
G43.8372-0.6344	6153500	19:13:48.06	+09:23:57.52	0.37	0.05	0.37	0.05	0.42	-1.0	0.42	-1.0	0.02	-1.0	4	0
G43.8425-0.0308	7142900	19:11:38.48	+09:41:01.45	1.47	0.05	1.33	0.06	0.41	0.01	0.39	0.01	89.53	0.49	0	0
G43.8425-0.0308	7132200	19:11:38.48	+09:41:01.44	1.44	0.07	1.27	0.07	0.41	0.01	0.38	0.01	87.04	0.52	0	0
G43.8448+0.7400	8210700	19:08:52.19	+10:02:29.96	0.35	0.06	0.36	0.06	0.42	-1.0	0.42	-1.0	0.01	-1.0	4	0
G43.8475-0.8139	5365200	19:14:27.89	+09:19:30.34	0.81	0.06	0.69	0.06	0.4	0.01	0.38	0.01	-11.56	0.95	0	0
G43.8538+0.9586	8215400	19:08:05.89	+10:09:01.06	0.71	0.11	0.72	0.11	0.42	-1.0	0.42	-1.0	-0.02	-1.0	4	0
G43.8617-0.4892	6158700	19:13:19.52	+09:29:18.15	1.21	0.21	1.22	0.21	0.42	-1.0	0.42	-1.0	0.0	-1.0	4	0
G43.8623+0.7226	8126300	19:08:57.92	+10:02:56.97	0.54	0.09	0.55	0.1	0.42	-1.0	0.42	-1.0	-0.04	-1.0	4	0
G43.8624+0.0131	7134100	19:11:31.24	+09:43:18.02	0.73	0.06	0.99	0.09	0.56	0.01	0.43	0.02	-76.39	0.24	0	0
G43.8624+0.0131	7145200	19:11:31.24	+09:43:18.02	0.72	0.05	0.97	0.09	0.55	0.01	0.43	0.02	-74.65	0.26	0	0
G43.8626+0.0131	7145201	19:11:31.27	+09:43:18.50	0.36	0.05	0.68	0.11	0.82	0.01	0.4	0.02	25.91	0.13	0	0
G43.8626+0.0131	7134101	19:11:31.27	+09:43:18.52	0.36	0.06	0.67	0.11	0.82	0.01	0.4	0.02	26.54	0.11	0	0
G43.8668+0.7359	8222400	19:08:55.56	+10:03:33.36	1.44	0.26	1.45	0.26	0.42	-1.0	0.42	-1.0	-0.05	-1.0	4	0
G43.8739-0.5367	6157800	19:13:31.15	+09:28:37.56	0.91	0.08	0.88	0.09	0.41	0.02	0.41	0.02	-6.06	11.88	0	0

Source Galactic name	Source Index	RA J2000	Dec J2000	Peak (mJy beam^{-1})	error	Integrated (mJy)	error	Major (arcsec)	error	Minor (arcsec)	error	PA (°)	error	flags	aux_flags
G43.8739-0.5368	6252400	19:13:31.15	+09:28:37.56	1.04	0.05	0.98	0.06	0.41	0.01	0.4	0.01	-74.89	1.08	0	0
G43.8800+0.9814	8313200	19:08:03.91	+10:11:02.68	0.37	0.07	0.38	0.07	0.42	-1.0	0.42	-1.0	-0.03	-1.0	4	0
G43.8812-0.3008	6344900	19:12:41.11	+09:35:34.72	1.27	0.06	1.29	0.07	0.43	0.01	0.41	0.01	-87.32	0.59	0	0
G43.8812-0.3009	6355700	19:12:41.11	+09:35:34.72	1.17	0.07	1.22	0.09	0.47	0.01	0.39	0.01	-83.93	0.29	0	0
G43.8815+0.3921	7325100	19:10:11.53	+09:54:49.52	0.29	0.05	0.29	0.05	0.42	-1.0	0.42	-1.0	0.02	-1.0	4	0
G43.8833+0.1612	7330100	19:11:01.61	+09:48:31.16	1.23	0.22	1.24	0.22	0.42	-1.0	0.42	-1.0	-0.01	-1.0	4	0
G43.8843+0.0429	7136700	19:11:27.29	+09:45:17.56	0.33	0.06	0.33	0.06	0.42	-1.0	0.42	-1.0	0.03	-1.0	4	0
G43.8848+0.7086	8211400	19:09:03.48	+10:03:45.63	0.33	0.06	0.33	0.06	0.42	-1.0	0.42	-1.0	0.02	-1.0	4	0
G43.8890+0.5715	8123700	19:09:33.60	+10:00:11.32	0.63	0.08	0.47	0.07	0.38	0.02	0.34	0.02	-12.3	0.73	0	0
G43.8893-0.7837	6161602	19:14:26.11	+09:22:33.95	3.34	0.34	112.07	11.4	2.56	0.02	2.31	0.02	1.23	0.1	0	0
G43.8893-0.7840	6161600	19:14:26.18	+09:22:33.70	8.31	0.34	38.59	1.89	1.02	0.02	0.8	0.02	15.01	0.09	0	0
G43.8896-0.7842	6161601	19:14:26.25	+09:22:34.39	6.29	0.34	51.02	2.94	1.4	0.02	1.02	0.02	11.56	0.08	0	0
G43.8900-0.7839	6161603	19:14:26.23	+09:22:36.16	2.28	0.34	71.31	10.63	4.07	0.02	1.36	0.02	6.97	0.04	0	0
G43.8909-0.5774	6252000	19:13:41.83	+09:28:24.13	0.31	0.05	0.31	0.05	0.42	-1.0	0.42	-1.0	0.01	-1.0	4	0
G43.8972+0.0782	7233700	19:11:21.12	+09:46:57.33	0.41	0.06	0.4	0.07	0.45	0.03	0.39	0.04	89.79	1.0	0	0
G43.8999+0.7998	8213700	19:08:45.45	+10:07:05.20	0.4	0.06	0.4	0.06	0.42	-1.0	0.42	-1.0	0.01	-1.0	4	0
G43.9043-0.0119	7241500	19:11:41.38	+09:44:50.12	0.31	0.05	0.32	0.05	0.42	-1.0	0.42	-1.0	-0.04	-1.0	4	0
G43.9044-0.0119	7231700	19:11:41.38	+09:44:50.13	0.32	0.05	0.32	0.05	0.42	-1.0	0.42	-1.0	0.03	-1.0	4	0
G43.9044-0.0119	7135700	19:11:41.38	+09:44:50.12	0.25	0.05	0.26	0.05	0.42	-1.0	0.42	-1.0	0.04	-1.0	4	0
G43.9067+0.0777	7234800	19:11:22.29	+09:47:26.98	0.3	0.05	0.3	0.05	0.42	-1.0	0.42	-1.0	0.02	-1.0	4	0
G43.9122+0.0534	7234100	19:11:28.16	+09:47:03.83	0.27	0.05	0.27	0.05	0.42	-1.0	0.42	-1.0	0.02	-1.0	4	0
G43.9135-0.3376	6347500	19:12:52.69	+09:36:16.28	0.32	0.06	0.33	0.06	0.42	-1.0	0.42	-1.0	0.03	-1.0	4	0
G43.9184-0.2047	7141700	19:12:24.57	+09:40:13.68	0.26	0.04	0.26	0.05	0.42	-1.0	0.42	-1.0	0.0	-1.0	4	0
G43.9193-0.4473	62510200	19:13:17.00	+09:33:31.71	0.91	0.16	0.92	0.16	0.42	-1.0	0.42	-1.0	-0.01	-1.0	4	0
G43.9203-0.4790	62510002	19:13:23.94	+09:32:42.16	12.98	672.6	8.4	819.13	0.34	28.06	0.34	0.7	74.15	179.53	0	2
G43.9203-0.4790	62510000	19:13:23.94	+09:32:42.13	5.92	672.6	38.81	5536.47	1.18	101.91	0.98	2.54	-7.4	180.39	0	2
G43.9203-0.4790	62510001	19:13:23.94	+09:32:42.23	16.94	672.6	34.57	1586.05	1.06	24.24	0.34	0.6	-76.36	179.04	0	2
G43.9211-0.4787	6351701	19:13:23.98	+09:32:45.16	4.63	0.66	2.97	0.42	0.34	0.0	0.34	0.0	10.8	0.15	0	0
G43.9213-0.4789	6351700	19:13:24.03	+09:32:45.37	73.94	0.66	73.87	0.77	0.43	0.0	0.41	0.0	-89.36	0.15	0	0
G43.9214-0.4786	6351900	19:13:23.99	+09:32:46.23	4.11	0.61	4.15	0.62	0.42	-1.0	0.42	-1.0	-0.01	-1.0	4	0
G43.9214-0.4786	6351703	19:13:23.99	+09:32:46.24	3.99	0.66	3.95	0.65	0.52	0.0	0.34	0.0	-3.63	0.09	0	0
G43.9215-0.4788	6351702	19:13:24.04	+09:32:46.15	5.03	0.66	7.72	1.02	0.79	0.0	0.34	0.0	32.63	0.08	0	0
G43.9219-0.4788	6352100	19:13:24.08	+09:32:47.75	3.96	0.58	4.0	0.59	0.42	-1.0	0.42	-1.0	-0.01	-1.0	4	0
G43.9221+0.6030	8221600	19:09:30.51	+10:02:49.65	0.41	0.07	0.41	0.07	0.42	-1.0	0.42	-1.0	-0.03	-1.0	4	0
G43.9221+0.6030	8126100	19:09:30.51	+10:02:49.67	0.39	0.07	0.39	0.07	0.42	-1.0	0.42	-1.0	-0.02	-1.0	4	0

Source Galactic name	Source Index	RA J2000	Dec J2000	Observed flux density				Major (arcsec)		Minor (arcsec)		PA (°)		flags	aux_flags
				Peak (mJy beam^{-1})	error	Integrated (mJy)	error		error		error		error		
G43.9228+0.0541	7244600	19:11:29.20	+09:47:38.95	1.18	0.2	1.19	0.21	0.42	-1.0	0.42	-1.0	-0.04	-1.0	4	0
G43.9281-0.2445	7141300	19:12:34.24	+09:39:38.31	0.67	0.05	0.57	0.05	0.39	0.01	0.39	0.01	11.55	12.46	0	0
G43.9305+0.7365	8310400	19:09:02.58	+10:06:58.00	0.57	0.09	0.57	0.09	0.42	-1.0	0.42	-1.0	0.01	-1.0	4	0
G43.9337-0.1615	7143900	19:12:16.96	+09:42:14.61	0.43	0.05	0.43	0.06	0.47	0.03	0.38	0.02	-7.56	0.29	0	0
G43.9345-0.0266	7147000	19:11:47.94	+09:46:01.92	0.48	0.09	0.48	0.09	0.42	-1.0	0.42	-1.0	-0.02	-1.0	4	0
G43.9370+0.7563	8311400	19:08:59.03	+10:07:51.55	0.43	0.08	0.44	0.08	0.42	-1.0	0.42	-1.0	0.01	-1.0	4	0
G43.9402+0.6877	8224300	19:09:14.23	+10:06:07.93	0.36	0.06	0.36	0.06	0.42	-1.0	0.42	-1.0	-0.04	-1.0	4	0
G43.9402+0.6877	8213000	19:09:14.23	+10:06:07.93	0.36	0.06	0.37	0.06	0.42	-1.0	0.42	-1.0	0.03	-1.0	4	0
G43.9435-0.0668	7146800	19:11:57.62	+09:45:23.59	0.34	0.06	0.35	0.06	0.42	-1.0	0.42	-1.0	-0.02	-1.0	4	0
G43.9497+0.0380	7245600	19:11:35.71	+09:48:38.11	0.36	0.06	0.36	0.06	0.42	-1.0	0.42	-1.0	-0.04	-1.0	4	0
G43.9517-0.5287	6352600	19:13:38.20	+09:32:59.27	0.36	0.06	0.37	0.06	0.42	-1.0	0.42	-1.0	0.0	-1.0	4	0
G43.9662-0.6289	6257000	19:14:01.43	+09:30:58.20	0.29	0.05	0.3	0.05	0.42	-1.0	0.42	-1.0	0.02	-1.0	4	0
G43.9678+0.7880	8313000	19:08:55.62	+10:10:22.67	0.35	0.06	0.36	0.06	0.42	-1.0	0.42	-1.0	0.01	-1.0	4	0
G43.9763+0.3599	8122100	19:10:29.17	+09:58:58.59	0.35	0.06	0.36	0.06	0.42	-1.0	0.42	-1.0	0.03	-1.0	4	0
G43.9763+0.3599	8132600	19:10:29.17	+09:58:58.60	0.36	0.06	0.37	0.06	0.42	-1.0	0.42	-1.0	-0.04	-1.0	4	0
G43.9807-0.4398	6356800	19:13:22.30	+09:37:00.24	0.41	0.06	0.46	0.08	0.55	0.06	0.36	0.02	-5.28	0.16	0	0
G43.9820-0.0198	7245700	19:11:51.83	+09:48:44.70	0.27	0.05	0.28	0.05	0.42	-1.0	0.42	-1.0	-0.03	-1.0	4	0
G43.9823-0.0514	7244900	19:11:58.67	+09:47:53.10	3.14	0.05	3.27	0.06	0.44	0.0	0.42	0.0	-8.34	0.35	0	0
G43.9841-0.6825	6255600	19:14:15.01	+09:30:25.43	0.31	0.06	0.32	0.06	0.42	-1.0	0.42	-1.0	0.03	-1.0	4	0
G43.9942+0.7230	8312700	19:09:12.66	+10:09:58.98	0.41	0.07	0.41	0.07	0.42	-1.0	0.42	-1.0	0.02	-1.0	4	0
G43.9979+0.7022	8312500	19:09:17.57	+10:09:36.18	0.31	0.05	0.31	0.05	0.42	-1.0	0.42	-1.0	0.02	-1.0	4	0
G43.9988+0.2518	8131100	19:10:55.05	+09:57:10.75	0.37	0.07	0.37	0.07	0.42	-1.0	0.42	-1.0	-0.02	-1.0	4	0
G43.9990-0.7737	6164900	19:14:36.35	+09:28:40.47	0.91	0.12	0.8	0.12	0.4	0.02	0.39	0.02	-3.98	2.06	0	0
G43.9990-0.7737	6260800	19:14:36.35	+09:28:40.48	0.99	0.05	0.9	0.05	0.41	0.01	0.39	0.01	2.65	1.0	0	0
G44.0025-0.2199	7241200	19:12:37.34	+09:44:16.65	0.39	0.07	0.4	0.07	0.42	-1.0	0.42	-1.0	0.0	-1.0	4	0
G44.0043-0.3136	7153100	19:12:57.74	+09:41:46.09	0.25	0.04	0.25	0.04	0.42	-1.0	0.42	-1.0	-0.04	-1.0	4	0
G44.0236+0.2957	8123000	19:10:48.36	+09:59:42.78	1.58	0.27	1.59	0.28	0.42	-1.0	0.42	-1.0	0.04	-1.0	4	0
G44.0365+0.2448	8132700	19:11:00.81	+09:58:59.21	0.34	0.06	0.34	0.06	0.42	-1.0	0.42	-1.0	-0.02	-1.0	4	0
G44.0376-0.2852	7241300	19:12:55.37	+09:44:19.81	2.38	0.06	2.27	0.07	0.42	0.0	0.4	0.0	-2.27	0.43	0	0
G44.0376-0.2852	7145700	19:12:55.37	+09:44:19.80	2.51	0.05	2.44	0.06	0.42	0.0	0.41	0.0	-1.63	1.3	0	0
G44.0379-0.1247	7245800	19:12:20.76	+09:48:48.29	0.26	0.05	0.26	0.05	0.42	-1.0	0.42	-1.0	-0.01	-1.0	4	0
G44.0389-0.2015	7243500	19:12:37.46	+09:46:43.41	1.0	0.05	0.95	0.05	0.43	0.01	0.4	0.01	89.04	0.47	0	0
G44.0421-0.4979	7150700	19:13:41.77	+09:38:38.94	0.78	0.12	0.79	0.12	0.42	-1.0	0.42	-1.0	-0.01	-1.0	4	0
G44.0422-0.0337	7331700	19:12:01.61	+09:51:33.85	0.72	0.07	0.86	0.1	0.47	0.02	0.45	0.02	-6.73	2.82	0	0
G44.0422-0.0337	7247800	19:12:01.61	+09:51:33.86	0.7	0.09	1.05	0.17	0.53	0.03	0.5	0.04	-88.3	2.13	0	0

Source Galactic name	Source Index	RA J2000	Dec J2000	Observed flux density				Major (arcsec)		Minor (arcsec)		PA (°)		flags	aux_flags
				Peak (mJy beam^{-1})	error	Integrated (mJy)	error		error		error		error		
G44.0422-0.0337	7342600	19:12:01.61	+09:51:33.86	0.68	0.05	0.94	0.09	0.5	0.02	0.48	0.02	89.68	1.37	0	0
G44.0454-0.5262	7150300	19:13:48.24	+09:38:02.13	1.07	0.19	1.08	0.19	0.42	-1.0	0.42	-1.0	-0.0	-1.0	4	0
G44.0464-0.7524	6360800	19:14:37.13	+09:31:47.37	0.48	0.08	0.49	0.09	0.42	-1.0	0.42	-1.0	-0.02	-1.0	4	0
G44.0522+0.0286	7333900	19:11:49.30	+09:53:49.62	0.26	0.05	0.26	0.05	0.42	-1.0	0.42	-1.0	0.03	-1.0	4	0
G44.0522+0.0286	7344700	19:11:49.30	+09:53:49.60	0.27	0.05	0.27	0.05	0.42	-1.0	0.42	-1.0	-0.04	-1.0	4	0
G44.0543-0.0583	7247600	19:12:08.29	+09:51:31.29	1.1	0.1	1.13	0.11	0.45	0.02	0.4	0.01	-0.58	0.44	0	0
G44.0543-0.0583	7342400	19:12:08.29	+09:51:31.34	0.83	0.05	0.82	0.05	0.44	0.01	0.39	0.01	1.71	0.3	0	0
G44.0595-0.6797	62510600	19:14:22.92	+09:34:30.73	0.96	0.17	0.97	0.18	0.42	-1.0	0.42	-1.0	0.04	-1.0	4	0
G44.0606+0.3907	8128100	19:10:31.99	+10:04:19.24	1.43	0.25	1.45	0.25	0.42	-1.0	0.42	-1.0	0.03	-1.0	4	0
G44.0618-0.0926	7342000	19:12:16.55	+09:50:58.08	0.26	0.05	0.26	0.05	0.42	-1.0	0.42	-1.0	-0.02	-1.0	4	0
G44.0628-0.3145	7251900	19:13:04.54	+09:44:51.19	0.29	0.05	0.29	0.05	0.42	-1.0	0.42	-1.0	-0.04	-1.0	4	0
G44.0683-0.9423	6260600	19:15:20.52	+09:27:39.22	1.04	0.06	0.95	0.07	0.4	0.01	0.4	0.01	1.58	3.28	0	0
G44.0683-0.9423	6164500	19:15:20.52	+09:27:39.23	1.02	0.07	0.87	0.07	0.4	0.01	0.38	0.01	-2.73	0.64	0	0
G44.0757+0.3504	8232200	19:10:42.42	+10:04:00.23	3.2	0.07	3.3	0.08	0.43	0.0	0.42	0.0	-0.5	0.54	0	0
G44.0757+0.3504	8127800	19:10:42.42	+10:04:00.20	3.38	0.16	3.39	0.18	0.43	0.01	0.42	0.01	13.1	1.35	0	0
G44.0757+0.3504	8136900	19:10:42.42	+10:04:00.20	3.37	0.16	3.36	0.18	0.42	0.01	0.42	0.01	70.7	1.72	0	0
G44.0757+0.3504	8223000	19:10:42.42	+10:04:00.23	3.2	0.07	3.31	0.08	0.43	0.0	0.42	0.0	-0.24	0.54	0	0
G44.0768-0.9274	6260700	19:15:18.27	+09:28:31.20	0.31	0.05	0.32	0.05	0.42	-1.0	0.42	-1.0	0.01	-1.0	4	0
G44.0802+0.6510	8324300	19:09:37.89	+10:12:34.26	0.39	0.06	0.39	0.06	0.42	-1.0	0.42	-1.0	-0.03	-1.0	4	0
G44.0849-0.8072	6263200	19:14:53.29	+09:32:18.17	0.28	0.05	0.28	0.05	0.42	-1.0	0.42	-1.0	-0.0	-1.0	4	0
G44.0853-0.7020	6355100	19:14:30.66	+09:35:15.69	0.29	0.05	0.29	0.05	0.42	-1.0	0.42	-1.0	0.04	-1.0	4	0
G44.0858+0.1311	8131700	19:11:30.95	+09:58:27.46	0.38	0.06	0.39	0.06	0.42	-1.0	0.42	-1.0	0.0	-1.0	4	0
G44.0897-0.2755	7244300	19:12:59.18	+09:47:22.14	0.27	0.05	0.27	0.05	0.42	-1.0	0.42	-1.0	0.02	-1.0	4	0
G44.0920-0.1487	7247200	19:12:32.07	+09:51:00.95	0.36	0.06	0.36	0.06	0.42	-1.0	0.42	-1.0	0.0	-1.0	4	0
G44.0951-0.4145	7154600	19:13:29.78	+09:43:47.08	0.31	0.05	0.31	0.05	0.42	-1.0	0.42	-1.0	-0.02	-1.0	4	0
G44.0968-0.1108	7248700	19:12:24.42	+09:52:19.68	1.17	0.21	1.18	0.21	0.42	-1.0	0.42	-1.0	-0.01	-1.0	4	0
G44.1005-0.0045	7345900	19:12:01.88	+09:55:28.34	0.29	0.05	0.3	0.05	0.42	-1.0	0.42	-1.0	-0.03	-1.0	4	0
G44.1005-0.1426	7342700	19:12:31.71	+09:51:38.29	0.3	0.05	0.3	0.05	0.42	-1.0	0.42	-1.0	-0.01	-1.0	4	0
G44.1070-0.3964	7252200	19:13:27.21	+09:44:55.40	0.26	0.05	0.26	0.05	0.42	-1.0	0.42	-1.0	-0.03	-1.0	4	0
G44.1121-0.1954	7341900	19:12:44.41	+09:50:47.05	0.46	0.05	0.39	0.05	0.41	0.02	0.36	0.01	20.23	0.51	0	0
G44.1121-0.1954	7247000	19:12:44.41	+09:50:47.06	0.46	0.05	0.36	0.05	0.4	0.02	0.36	0.01	19.1	0.66	0	0
G44.1193-0.4039	7252900	19:13:30.21	+09:45:22.17	0.29	0.05	0.29	0.05	0.42	-1.0	0.42	-1.0	-0.02	-1.0	4	0
G44.1202+0.3946	8320800	19:10:37.86	+10:07:35.89	0.37	0.06	0.38	0.06	0.42	-1.0	0.42	-1.0	0.01	-1.0	4	0
G44.1203-0.0355	8140100	19:12:10.80	+09:55:40.07	1.8	0.28	1.82	0.28	0.42	-1.0	0.42	-1.0	-0.03	-1.0	4	0
G44.1203-0.0355	8130100	19:12:10.80	+09:55:40.06	1.81	0.29	1.83	0.3	0.42	-1.0	0.42	-1.0	0.03	-1.0	4	0

Source Galactic name	Source Index	RA J2000	Dec J2000	Observed flux density				Major (arcsec)		Minor (arcsec)		PA (°)		flags	aux_flags
				Peak (mJy beam^{-1})	error	Integrated (mJy)	error		error		error		error		
G44.1228-0.4219	7155700	19:13:34.51	+09:45:03.30	0.28	0.05	0.29	0.05	0.42	-1.0	0.42	-1.0	-0.01	-1.0	4	0
G44.1485-0.2433	7342300	19:12:58.85	+09:51:23.28	0.27	0.05	0.27	0.05	0.42	-1.0	0.42	-1.0	0.01	-1.0	4	0
G44.1500-0.8967	6263800	19:15:19.94	+09:33:15.78	0.4	0.06	0.4	0.06	0.42	-1.0	0.42	-1.0	0.02	-1.0	4	0
G44.1526+0.1823	8232000	19:11:27.40	+10:03:25.98	0.33	0.06	0.34	0.06	0.42	-1.0	0.42	-1.0	-0.01	-1.0	4	0
G44.1559+0.3412	8331800	19:10:53.43	+10:08:00.90	0.39	0.07	0.4	0.07	0.42	-1.0	0.42	-1.0	-0.04	-1.0	4	0
G44.1566-0.9180	6361900	19:15:25.27	+09:33:01.43	0.29	0.05	0.29	0.05	0.42	-1.0	0.42	-1.0	0.01	-1.0	4	0
G44.1607-0.9288	6361800	19:15:28.06	+09:32:56.30	0.27	0.05	0.28	0.05	0.42	-1.0	0.42	-1.0	0.01	-1.0	4	0
G44.1722-0.5465	7154900	19:14:06.96	+09:44:12.62	0.8	0.05	0.91	0.06	0.45	0.01	0.44	0.01	-88.19	2.14	0	0
G44.1722-0.5465	7251200	19:14:06.96	+09:44:12.60	0.8	0.07	0.89	0.09	0.46	0.02	0.42	0.01	6.94	0.59	0	0
G44.1773-0.2125	7344600	19:12:55.46	+09:53:46.74	0.27	0.05	0.27	0.05	0.42	-1.0	0.42	-1.0	0.01	-1.0	4	0
G44.1803-0.8233	6366000	19:15:07.54	+09:36:55.45	0.31	0.06	0.31	0.06	0.42	-1.0	0.42	-1.0	-0.0	-1.0	4	0
G44.1803-0.9986	6361100	19:15:45.32	+09:32:01.75	0.36	0.06	0.36	0.06	0.42	-1.0	0.42	-1.0	0.02	-1.0	4	0
G44.1890+0.3102	8332500	19:11:03.86	+10:08:55.11	0.45	0.06	0.45	0.07	0.42	-1.0	0.42	-1.0	-0.03	-1.0	4	0
G44.1944+0.3775	8334000	19:10:49.93	+10:11:04.38	0.47	0.08	0.48	0.08	0.42	-1.0	0.42	-1.0	-0.04	-1.0	4	0
G44.1979-0.4510	7255900	19:13:49.26	+09:48:14.11	0.32	0.06	0.32	0.06	0.42	-1.0	0.42	-1.0	-0.01	-1.0	4	0
G44.1986-0.8483	6366400	19:15:15.01	+09:37:11.89	0.5	0.05	0.52	0.06	0.44	0.02	0.42	0.02	-87.06	2.16	0	0
G44.2043-0.4411	7256300	19:13:47.86	+09:48:51.04	0.32	0.05	0.28	0.06	0.42	0.04	0.37	0.03	-7.51	0.79	0	0
G44.2084-0.3094	7354100	19:13:19.88	+09:52:44.17	0.29	0.05	0.29	0.05	0.42	-1.0	0.42	-1.0	-0.04	-1.0	4	0
G44.2084-0.3094	7343600	19:13:19.88	+09:52:44.17	0.28	0.05	0.29	0.05	0.42	-1.0	0.42	-1.0	0.03	-1.0	4	0
G44.2098-0.8513	6366900	19:15:16.92	+09:37:42.58	0.27	0.05	0.27	0.05	0.42	-1.0	0.42	-1.0	0.01	-1.0	4	0
G44.2159-0.5055	7255300	19:14:03.06	+09:47:40.39	1.49	0.05	1.34	0.05	0.42	0.01	0.38	0.0	-1.8	0.23	0	0
G44.2271-0.3171	7355000	19:13:23.67	+09:53:30.69	1.15	0.05	1.13	0.06	0.44	0.01	0.4	0.01	0.26	0.3	0	0
G44.2271-0.3171	7344500	19:13:23.67	+09:53:30.69	1.17	0.05	1.16	0.05	0.44	0.01	0.4	0.01	-0.71	0.28	0	0
G44.2511-0.7022	7164800	19:14:49.45	+09:44:03.58	0.48	0.05	0.42	0.05	0.41	0.02	0.38	0.02	-14.24	1.02	0	0
G44.2511-0.7022	7154700	19:14:49.45	+09:44:03.58	0.47	0.05	0.41	0.05	0.41	0.02	0.37	0.01	-15.56	0.72	0	0
G44.2511-0.7022	7260300	19:14:49.45	+09:44:03.61	0.51	0.07	0.5	0.09	0.42	0.03	0.41	0.03	81.02	7.74	0	0
G44.2511-0.7022	7250900	19:14:49.45	+09:44:03.61	0.51	0.07	0.5	0.09	0.43	0.03	0.41	0.04	82.26	2.68	0	0
G44.2543-0.9342	6367000	19:15:39.83	+09:37:45.43	0.29	0.05	0.3	0.05	0.42	-1.0	0.42	-1.0	0.02	-1.0	4	0
G44.2568+0.1990	8332900	19:11:35.54	+10:09:26.39	0.37	0.06	0.37	0.06	0.42	-1.0	0.42	-1.0	-0.01	-1.0	4	0
G44.2602-0.9980	6365300	19:15:54.23	+09:36:17.33	0.27	0.04	0.27	0.05	0.42	-1.0	0.42	-1.0	0.03	-1.0	4	0
G44.2611+0.1041	8330600	19:11:56.53	+10:07:01.87	0.76	0.12	0.76	0.12	0.42	-1.0	0.42	-1.0	0.01	-1.0	4	0
G44.2611+0.1041	8234000	19:11:56.54	+10:07:02.00	0.8	0.06	1.28	0.1	0.73	0.02	0.39	0.01	28.3	0.05	0	0
G44.2615+0.1042	8234100	19:11:56.57	+10:07:03.46	0.51	0.06	0.61	0.09	0.55	0.04	0.39	0.02	-0.65	0.18	0	0
G44.2661-0.4723	7352700	19:14:01.57	+09:51:15.81	0.26	0.05	0.27	0.05	0.42	-1.0	0.42	-1.0	-0.01	-1.0	4	0
G44.2671-0.9714	6366600	19:15:49.28	+09:37:23.95	0.33	0.05	0.33	0.05	0.42	-1.0	0.42	-1.0	0.03	-1.0	4	0

Source Galactic name	Source Index	RA J2000	Dec J2000	Peak (mJy beam^{-1})	error	Integrated (mJy)	error	Major (arcsec)	error	Minor (arcsec)	error	PA (°)	error	flags	aux_flags
G44.2678-0.6943	7165900	19:14:49.64	+09:45:10.23	0.25	0.04	0.25	0.05	0.42	-1.0	0.42	-1.0	-0.02	-1.0	4	0
G44.2685-0.6374	7254600	19:14:37.45	+09:46:47.54	0.7	0.05	0.7	0.06	0.44	0.01	0.4	0.01	11.57	0.43	0	0
G44.2685-0.6374	7262700	19:14:37.45	+09:46:47.56	0.73	0.09	0.95	0.15	0.56	0.04	0.41	0.02	2.45	0.23	0	0
G44.2739+0.2370	8334300	19:11:29.27	+10:11:24.11	0.34	0.06	0.34	0.06	0.42	-1.0	0.42	-1.0	-0.01	-1.0	4	0
G44.2756-0.3432	7345800	19:13:34.78	+09:55:21.99	0.34	0.06	0.34	0.06	0.42	-1.0	0.42	-1.0	0.04	-1.0	4	0
G44.2756-0.3432	7357100	19:13:34.78	+09:55:21.98	0.33	0.06	0.34	0.06	0.42	-1.0	0.42	-1.0	-0.03	-1.0	4	0
G44.2764-0.6455	7156900	19:14:40.08	+09:46:59.24	1.25	0.19	1.26	0.19	0.42	-1.0	0.42	-1.0	0.03	-1.0	4	0
G44.2764-0.6455	7166800	19:14:40.08	+09:46:59.27	1.26	0.19	1.27	0.19	0.42	-1.0	0.42	-1.0	-0.03	-1.0	4	0
G44.2821-0.7695	7164500	19:15:07.48	+09:43:49.98	0.38	0.05	0.33	0.05	0.4	0.02	0.38	0.02	83.44	2.09	0	0
G44.2884-0.7246	7261600	19:14:58.50	+09:45:25.09	0.36	0.05	0.34	0.06	0.42	0.03	0.39	0.03	-7.04	1.27	0	0
G44.2884-0.7246	7166000	19:14:58.50	+09:45:25.11	0.35	0.05	0.3	0.05	0.41	0.02	0.37	0.03	-89.09	1.35	0	0
G44.2905+0.3029	8337100	19:11:16.89	+10:14:07.01	0.44	0.08	0.45	0.08	0.42	-1.0	0.42	-1.0	-0.02	-1.0	4	0
G44.2911-0.7903	7164300	19:15:12.97	+09:43:43.62	0.33	0.06	0.33	0.06	0.42	-1.0	0.42	-1.0	-0.01	-1.0	4	0
G44.2947-0.6795	7166900	19:14:49.51	+09:47:00.68	1.17	0.21	1.18	0.21	0.42	-1.0	0.42	-1.0	-0.02	-1.0	4	0
G44.2957+0.1561	8333400	19:11:49.21	+10:10:18.83	0.42	0.07	0.43	0.07	0.42	-1.0	0.42	-1.0	-0.0	-1.0	4	0
G44.3053-0.0043	8340200	19:12:24.95	+10:06:22.24	1.54	0.28	1.55	0.28	0.42	-1.0	0.42	-1.0	-0.04	-1.0	4	0
G44.3101+0.0407	8234600	19:12:15.78	+10:07:52.53	0.88	0.07	1.13	0.11	0.54	0.02	0.42	0.01	10.84	0.18	0	0
G44.3101+0.0407	8243500	19:12:15.78	+10:07:52.53	0.92	0.1	1.17	0.15	0.52	0.03	0.43	0.02	9.13	0.3	0	0
G44.3101+0.0407	8341500	19:12:15.77	+10:07:52.54	1.18	0.13	1.44	0.18	0.54	0.03	0.4	0.02	12.71	0.19	0	0
G44.3101+0.0407	8331600	19:12:15.78	+10:07:52.53	0.92	0.08	1.19	0.12	0.54	0.02	0.42	0.01	18.55	0.19	0	0
G44.3103+0.0409	8331700	19:12:15.74	+10:07:53.56	0.85	0.06	2.87	0.26	0.88	0.03	0.67	0.03	4.73	0.15	0	0
G44.3103+0.0409	8341600	19:12:15.74	+10:07:53.54	0.9	0.12	1.87	0.38	0.63	0.06	0.59	0.07	4.57	1.77	0	0
G44.3103+0.0409	8234700	19:12:15.74	+10:07:53.54	0.8	0.06	2.87	0.25	0.91	0.03	0.69	0.02	1.02	0.14	0	0
G44.3103+0.0409	8243600	19:12:15.74	+10:07:53.50	0.82	0.1	1.66	0.26	0.62	0.04	0.58	0.04	-87.34	1.29	0	0
G44.3107-0.4583	7355500	19:14:03.58	+09:54:01.45	0.9	0.06	0.82	0.06	0.41	0.01	0.39	0.01	86.49	0.95	0	0
G44.3237-0.7296	7263000	19:15:03.58	+09:47:09.22	3.39	0.04	7.21	0.12	0.8	0.0	0.47	0.0	-83.81	0.03	0	0
G44.3264-0.8394	7260600	19:15:27.56	+09:44:13.80	0.67	0.09	0.68	0.11	0.44	0.03	0.4	0.02	-19.68	0.95	0	0
G44.3264-0.8395	7165100	19:15:27.56	+09:44:13.77	0.62	0.05	0.58	0.05	0.44	0.01	0.37	0.01	-32.27	0.29	0	0
G44.3397-0.4183	7358400	19:13:58.23	+09:56:40.99	0.4	0.07	0.4	0.07	0.42	-1.0	0.42	-1.0	-0.01	-1.0	4	0
G44.3611-0.7087	7264500	19:15:03.31	+09:49:43.42	0.31	0.05	0.31	0.05	0.42	-1.0	0.42	-1.0	-0.02	-1.0	4	0
G44.3611-0.7087	7257300	19:15:03.31	+09:49:43.42	0.32	0.05	0.32	0.06	0.42	-1.0	0.42	-1.0	0.04	-1.0	4	0
G44.3613-0.6215	7353700	19:14:44.52	+09:52:10.05	0.67	0.04	1.78	0.12	0.69	0.02	0.67	0.02	-79.08	1.42	0	0
G44.3780-0.6139	7354800	19:14:44.76	+09:53:15.89	0.64	0.05	0.72	0.06	0.48	0.02	0.42	0.01	-10.92	0.37	0	0
G44.3933+0.1399	8337600	19:12:03.73	+10:15:03.55	1.16	0.21	1.17	0.21	0.42	-1.0	0.42	-1.0	0.01	-1.0	4	0
G44.3935+0.0602	8335700	19:12:20.97	+10:12:51.22	0.31	0.06	0.32	0.06	0.42	-1.0	0.42	-1.0	0.02	-1.0	4	0

Source Galactic name	Source Index	RA J2000	Dec J2000	Peak (mJy beam^{-1})	error	Integrated (mJy)	error	Major (arcsec)	error	Minor (arcsec)	error	PA (°)	error	flags	aux_flags
G44.3945-0.7002	7259100	19:15:05.26	+09:51:44.22	0.78	0.13	0.78	0.13	0.42	-1.0	0.42	-1.0	0.04	-1.0	4	0
G44.3946-0.7002	7265800	19:15:05.26	+09:51:44.25	0.72	0.12	0.73	0.12	0.42	-1.0	0.42	-1.0	-0.02	-1.0	4	0
G44.3969-0.8290	7263900	19:15:33.31	+09:48:16.10	0.33	0.06	0.34	0.06	0.42	-1.0	0.42	-1.0	-0.0	-1.0	4	0
G44.4024-0.4091	8154600	19:14:03.35	+10:00:16.12	0.48	0.08	0.44	0.09	0.47	0.05	0.34	0.02	-12.18	0.25	0	0
G44.4117-0.6504	7355600	19:14:56.47	+09:54:02.31	0.29	0.05	0.3	0.05	0.42	-1.0	0.42	-1.0	0.03	-1.0	4	0
G44.4117-0.6504	7364800	19:14:56.47	+09:54:02.29	0.3	0.05	0.31	0.05	0.42	-1.0	0.42	-1.0	-0.04	-1.0	4	0
G44.4197-0.6279	7366000	19:14:52.51	+09:55:05.63	1.24	0.21	1.25	0.21	0.42	-1.0	0.42	-1.0	-0.04	-1.0	4	0
G44.4265-0.3172	8157200	19:13:46.24	+10:04:06.56	0.75	0.13	0.76	0.13	0.42	-1.0	0.42	-1.0	-0.03	-1.0	4	0
G44.4435-0.9764	7262500	19:16:10.36	+09:46:37.36	0.31	0.05	0.31	0.05	0.42	-1.0	0.42	-1.0	0.02	-1.0	4	0
G44.4511-0.6181	7359100	19:14:53.95	+09:57:01.77	0.53	0.09	0.53	0.09	0.42	-1.0	0.42	-1.0	0.03	-1.0	4	0
G44.4543-0.8714	7264600	19:15:48.95	+09:50:07.78	0.31	0.05	0.31	0.05	0.42	-1.0	0.42	-1.0	0.01	-1.0	4	0
G44.4606-0.0666	8345300	19:12:55.97	+10:12:53.80	0.43	0.06	0.48	0.09	0.46	0.03	0.43	0.04	-88.43	1.87	0	0
G44.4693-0.3323	8253500	19:13:54.33	+10:05:57.77	0.37	0.07	0.38	0.07	0.42	-1.0	0.42	-1.0	-0.03	-1.0	4	0
G44.4716-0.0443	8346800	19:12:52.38	+10:14:06.07	0.4	0.07	0.41	0.07	0.42	-1.0	0.42	-1.0	-0.02	-1.0	4	0
G44.4750-0.9880	7263700	19:16:16.43	+09:47:58.23	0.31	0.05	0.32	0.06	0.42	-1.0	0.42	-1.0	0.03	-1.0	4	0
G44.4777-0.1810	8343100	19:13:22.61	+10:10:37.46	0.38	0.06	0.38	0.07	0.42	-1.0	0.42	-1.0	0.0	-1.0	4	0
G44.5032-0.9048	7362300	19:16:01.69	+09:51:47.75	0.34	0.06	0.34	0.06	0.42	-1.0	0.42	-1.0	0.01	-1.0	4	0
G44.5066-0.4262	8252700	19:14:18.83	+10:05:19.73	0.35	0.06	0.35	0.06	0.42	-1.0	0.42	-1.0	-0.02	-1.0	4	0
G44.5126-0.1503	8345500	19:13:19.92	+10:13:19.98	0.39	0.07	0.4	0.07	0.42	-1.0	0.42	-1.0	-0.0	-1.0	4	0
G44.5220-1.0270	7360500	19:16:30.17	+09:49:22.51	0.87	0.16	0.88	0.16	0.42	-1.0	0.42	-1.0	0.03	-1.0	4	0
G44.5220-1.0270	7264200	19:16:30.17	+09:49:22.52	0.85	0.15	0.86	0.15	0.42	-1.0	0.42	-1.0	0.04	-1.0	4	0
G44.5292-0.9288	7363000	19:16:09.81	+09:52:30.27	0.26	0.05	0.26	0.05	0.42	-1.0	0.42	-1.0	0.02	-1.0	4	0
G44.5363-0.8525	7365500	19:15:54.16	+09:55:00.82	0.98	0.05	0.95	0.06	0.45	0.01	0.38	0.01	2.55	0.2	0	0
G44.5366-0.8522	7365600	19:15:54.14	+09:55:02.31	1.1	0.05	1.15	0.06	0.47	0.01	0.39	0.01	-4.62	0.13	0	0
G44.5389-0.8219	8160300	19:15:47.86	+09:56:00.54	1.0	0.17	1.01	0.17	0.42	-1.0	0.42	-1.0	-0.01	-1.0	4	0
G44.5393-0.8324	8160100	19:15:50.18	+09:55:44.15	1.65	0.29	1.66	0.29	0.42	-1.0	0.42	-1.0	-0.01	-1.0	4	0
G44.5491-0.5382	8252100	19:14:47.82	+10:04:28.04	0.62	0.06	0.77	0.09	0.58	0.03	0.38	0.01	-3.23	0.1	0	0
G44.5622-0.6038	8156800	19:15:03.47	+10:03:19.98	0.46	0.08	0.47	0.09	0.42	-1.0	0.42	-1.0	0.02	-1.0	4	0
G44.5755-0.9164	7366300	19:16:12.40	+09:55:18.54	0.3	0.05	0.31	0.05	0.42	-1.0	0.42	-1.0	0.02	-1.0	4	0
G44.5810-0.7371	8164300	19:15:34.34	+10:00:36.60	0.34	0.06	0.35	0.06	0.42	-1.0	0.42	-1.0	-0.02	-1.0	4	0
G44.6076-0.5367	8254800	19:14:54.12	+10:07:36.92	0.43	0.06	0.35	0.06	0.4	0.02	0.35	0.03	-89.02	0.85	0	0
G44.6116-0.5808	8254100	19:15:04.11	+10:06:35.72	0.33	0.06	0.33	0.06	0.42	-1.0	0.42	-1.0	0.02	-1.0	4	0
G44.6206-0.7858	8260300	19:15:49.35	+10:01:21.17	0.77	0.14	0.78	0.14	0.42	-1.0	0.42	-1.0	-0.02	-1.0	4	0
G44.6407-0.7931	8261000	19:15:53.21	+10:02:13.12	1.42	0.09	1.94	0.14	0.53	0.01	0.46	0.01	10.69	0.28	0	0
G44.6407-0.7931	8166100	19:15:53.21	+10:02:13.09	1.24	0.07	1.78	0.12	0.52	0.01	0.49	0.01	5.37	0.65	0	0

Source Galactic name	Source Index	RA J2000	Dec J2000	Observed flux density				Major (arcsec)		Minor (arcsec)		PA (°)		flags	aux_flags
				Peak (mJy beam^{-1})	error	Integrated (mJy)	error		error		error		error		
G44.6492-0.5282	8351800	19:14:57.00	+10:10:03.81	0.42	0.07	0.42	0.07	0.42	-1.0	0.42	-1.0	0.0	-1.0	4	0
G44.6493-0.7951	8166301	19:15:54.61	+10:02:37.09	1.63	0.1	5.01	0.31	0.77	0.0	0.7	0.0	-2.82	0.16	0	0
G44.6493-0.7951	8261901	19:15:54.61	+10:02:37.10	1.78	0.12	5.78	0.4	0.79	0.0	0.72	0.0	-4.47	0.2	0	0
G44.6494-0.7952	8261900	19:15:54.65	+10:02:37.25	5.3	0.12	6.85	0.18	0.49	0.0	0.46	0.0	-8.01	0.21	0	0
G44.6494-0.7952	8166300	19:15:54.65	+10:02:37.25	5.12	0.1	6.62	0.15	0.49	0.0	0.46	0.0	-6.59	0.16	0	0
G44.6522-0.4071	8354700	19:14:31.20	+10:13:36.08	0.92	0.07	0.93	0.08	0.45	0.01	0.4	0.01	-11.64	0.42	0	0
G44.6699-0.4962	8353600	19:14:52.44	+10:12:03.21	0.33	0.06	0.34	0.06	0.42	-1.0	0.42	-1.0	-0.0	-1.0	4	0
G44.7549-0.9610	8262800	19:16:42.39	+10:03:35.19	0.33	0.06	0.33	0.06	0.42	-1.0	0.42	-1.0	0.02	-1.0	4	0
G44.7856-0.9147	8360200	19:16:35.90	+10:06:30.58	1.48	0.25	1.49	0.26	0.42	-1.0	0.42	-1.0	0.01	-1.0	4	0
G44.7858-0.7149	8353700	19:15:52.80	+10:12:06.33	0.55	0.09	0.55	0.1	0.42	-1.0	0.42	-1.0	0.04	-1.0	4	0
G44.8218-0.6735	8367000	19:15:47.96	+10:15:10.27	1.52	0.27	1.54	0.27	0.42	-1.0	0.42	-1.0	-0.03	-1.0	4	0
G44.8540-0.7398	8366900	19:16:05.92	+10:15:01.90	1.84	0.27	1.74	0.32	0.45	0.04	0.37	0.02	-15.6	0.54	0	0
G44.9393-0.9303	8366600	19:16:56.72	+10:14:13.65	0.53	0.09	0.53	0.1	0.42	-1.0	0.42	-1.0	0.02	-1.0	4	0

Appendix C

70 μm and MIR as a star formation tracer

Name	RA	Dec	RA (°)	Dec (°)	$70\mu m_{Bright}$	MSX_{Bright}	$WISE_{Bright}$	MIR_{Bright}
G119.646-0.246	00:22:58.230001	+62:26:35.10001	5.743	62.443	X	N	N	N
G120.208-3.117	00:29:53.680000	+59:38:25.50000	7.474	59.64	X	N	N	N
G124.015-3.273	00:59:59.350000	+59:34:50.30001	14.997	59.581	X	N	N	N
G126.823-3.033	01:22:13.510000	+59:36:21.70001	20.556	59.606	X	N	N	N
G127.271-2.864	01:25:54.780000	+59:42:57.50000	21.478	59.716	X	N	N	N
G128.066-1.145	01:34:23.220000	+61:17:50.89999	23.597	61.297	X	N	N	N
G129.708-2.269	01:45:48.380000	+59:53:05.70000	26.452	59.885	X	N	N	N
G131.371-2.901	01:57:21.190000	+58:53:09.90001	29.338	58.886	X	N	N	N
G133.695+1.21	02:25:30.130000	+62:06:00.50001	36.376	62.1	Y	N	N	N
G133.748+1.198	02:25:53.440000	+62:04:10.30000	36.473	62.07	Y	N	Y	Y
G137.170-3.008	02:38:17.360001	+56:52:47.00000	39.572	56.88	X	N	N	N
G137.897+1.464	02:58:19.210001	+60:35:44.40001	44.58	60.596	N	N	N	N
G138.294+1.556	03:01:31.239999	+60:29:18.89999	45.38	60.489	Y	Y	Y	Y
G138.5+1.647	03:03:20.440000	+60:28:06.30000	45.834	60.468	Y	Y	Y	Y
G139.614-2.698	02:55:13.860000	+56:06:36.39999	43.808	56.11	X	N	N	N
G139.909+0.196	03:07:23.790000	+58:30:46.10000	46.849	58.513	Y	Y	Y	Y
G145.888-2.813	03:31:43.950000	+52:45:46.30001	52.933	52.763	X	N	N	N
G146.175+2.453	03:55:31.100000	+56:46:30.40001	58.88	56.775	X	N	N	N
G146.213+2.386	03:55:24.610001	+56:41:56.40000	58.853	56.699	X	N	N	N
G147.252-2.999	03:38:15.610000	+51:48:59.99999	54.565	51.817	X	N	N	N
G147.864+2.833	04:06:31.000000	+55:57:19.90000	61.629	55.956	X	N	N	N
G149.534-1.89	03:54:12.530000	+51:17:14.30000	58.552	51.287	X	N	N	N
G149.809-1.732	03:56:12.580000	+51:13:56.60001	59.052	51.232	X	N	N	N
G149.920-1.82	03:56:23.550000	+51:05:39.90000	59.098	51.094	X	N	N	N
G149.962-1.859	03:56:26.149999	+51:02:13.19999	59.109	51.037	X	N	N	N
G150.351-1.346	04:00:26.490001	+51:10:31.59999	60.11	51.175	X	N	N	N
G150.761-3.044	03:55:29.970001	+49:37:00.10000	58.875	49.617	X	N	N	N
G151.348-1.97	04:02:35.550000	+50:03:02.70000	60.648	50.051	X	N	N	N
G152.344-1.17	04:10:31.860000	+49:58:41.60001	62.633	49.978	X	N	N	N
G156.120-2.857	04:19:52.070000	+46:09:00.29999	64.967	46.15	X	N	N	N
G157.806-1.352	04:32:51.620000	+45:59:15.00001	68.215	45.988	X	N	N	N

Name	RA	Dec	RA (°)	Dec (°)	$70\mu m_{Bright}$	MSX_{Bright}	$WISE_{Bright}$	MIR_{Bright}
G162.381+2.860	05:08:05.940000	+45:09:52.99999	77.025	45.165	X	N	N	N
G162.411+2.894	05:08:21.320000	+45:09:39.60000	77.089	45.161	X	N	N	N
G165.689+3.182	05:20:15.530000	+42:40:10.00001	80.065	42.669	X	N	N	N
G165.771-0.258	05:05:36.720000	+40:34:52.00000	76.403	40.581	N	N	N	N
G170.660-0.246	05:20:22.180000	+36:37:56.29999	80.092	36.632	Y	N	N	N
G170.785+2.531	05:32:19.010000	+38:04:50.20001	83.079	38.081	X	N	N	N
G176.423-0.399	05:35:15.009999	+31:45:21.49999	83.813	31.756	N	N	N	N
G179.179+1.162	05:48:14.140001	+30:14:25.30000	87.059	30.24	X	N	N	N
G183.125+2.574	06:02:52.990000	+27:32:35.89999	90.721	27.543	X	N	N	N
G183.747-0.42	05:52:40.710000	+25:30:25.20000	88.17	25.507	N	N	N	N
G186.703+0.379	06:02:13.500001	+23:20:57.90001	90.556	23.349	N	N	N	N
G187.465+2.163	06:10:38.220000	+23:33:16.30001	92.659	23.555	X	N	N	N
G189.057+1.075	06:09:49.810000	+21:38:09.39999	92.458	21.636	X	N	N	N
G190.675-3.187	05:57:25.140000	+18:07:56.60001	89.355	18.132	X	N	N	N
G194.663-0.223	06:16:22.770000	+16:05:39.50001	94.095	16.094	N	N	N	N
G201.167+1.673	06:35:47.050000	+11:13:35.79999	98.946	11.227	X	N	N	N
G201.71+1.507	06:36:11.920000	+10:40:09.10000	99.05	10.669	X	N	N	N
G202.281-0.218	06:31:02.840001	+09:22:00.00001	97.762	9.367	N	N	N	N
G202.296+2.525	06:40:58.399999	+10:36:50.90001	100.243	10.614	X	N	Y	Y
G203.242+2.075	06:41:05.850000	+09:34:05.00001	100.274	9.568	X	N	N	N
G203.326+2.062	06:41:12.350000	+09:29:11.30000	100.301	9.486	X	N	Y	Y
G203.332+2.073	06:41:15.520000	+09:29:11.69999	100.315	9.487	X	N	N	N
G204.079-3.131	06:23:59.970001	+06:25:20.39999	96.0	6.422	X	N	N	N
G207.491-1.449	06:36:19.390000	+04:10:32.10001	99.081	4.176	N	N	N	N
G207.789-2.756	06:32:12.960001	+03:18:38.50000	98.054	3.311	N	N	N	N
G210.1+2.626	06:55:37.980000	+03:42:59.60000	103.908	3.717	X	N	N	N
G211.104+1.155	06:52:13.340000	+02:09:10.90000	103.056	2.153	X	N	N	N
G211.631+0.909	06:52:18.210000	+01:34:20.59999	103.076	1.572	X	N	N	N

Name	RA	Dec	RA (°)	Dec (°)	$70\mu m_{Bright}$	MSX_{Bright}	WISE_{Bright}	MIR_{Bright}
G216.084-2.867	06:46:57.660000	-04:06:42.49999	101.74	-4.112	N	N	N	N
G218.292+2.740	07:11:00.180000	-03:30:41.79999	107.751	-3.512	X	N	N	N
G219.474-1.172	06:59:13.190000	-06:21:19.40001	104.805	-6.355	N	N	N	N
G219.475+0.338	07:04:37.140000	-05:39:55.90000	106.155	-5.666	N	N	N	N
G219.982+1.341	07:09:08.360000	-05:39:18.10000	107.285	-5.655	X	N	N	N
G220.053-2.5	06:55:31.160000	-07:28:35.00001	103.88	-7.476	X	N	N	N
G222.304+2.896	07:19:00.540000	-06:59:25.20000	109.752	-6.99	X	N	N	N
G222.713+3.023	07:20:14.040000	-07:17:32.70001	110.059	-7.292	X	N	N	N
G223.889-3.034	07:00:39.080000	-11:07:55.19999	105.163	-11.132	X	N	N	N
G226.380-2.765	07:06:16.620000	-13:13:22.80000	106.569	-13.223	X	N	N	N
G228.754+2.717	07:30:43.600000	-12:45:16.89999	112.682	-12.755	X	N	N	N
G230.505-0.871	07:21:06.820000	-15:59:57.80000	110.278	-15.999	X	N	N	N
G232.684-2.905	07:17:50.780000	-18:52:30.80000	109.462	-18.875	X	N	N	N
G232.802+2.627	07:38:29.280000	-16:20:14.19999	114.622	-16.337	X	N	N	N
G232.915+2.862	07:39:34.260000	-16:19:13.80001	114.893	-16.32	X	N	N	N
G233.181-0.012	07:29:35.210000	-17:56:49.50000	112.397	-17.947	N	N	N	N
G234.24+0.419	07:33:19.619999	-18:39:58.69999	113.332	-18.666	X	N	N	N
G240.536+1.171	07:49:30.840001	-23:45:51.30001	117.379	-23.764	X	N	N	N
G241.183+0.598	07:48:47.079999	-24:36:45.59999	117.196	-24.613	X	N	N	N

Bibliography

Abell, G.O., 1966. Properties of Some Old Planetary Nebulae. *ApJ*, 144:259.

Aguirre, J.E., Ginsburg, A.G., Dunham, M.K., et al., 2011. The Bolocam Galactic Plane Survey: Survey Description and Data Reduction. *ApJ*, 192(1):4.

Andersen, M., Rho, J., Reach, W.T., et al., 2011. Dust Processing in Supernova Remnants: Spitzer MIPS Spectral Energy Distribution and Infrared Spectrograph Observations. *ApJ*, 742(1):7.

Anderson, L.D., Armentrout, W.P., Johnstone, B.M., et al., 2015. Finding Distant Galactic HII Regions. *ApJS*, 221:11.

Anderson, L.D. and Bania, T.M., 2009. Resolution of the Distance Ambiguity for Galactic H II Regions. *ApJ*, 690(1):706.

Anderson, L.D., Bania, T.M., Balser, D.S., et al., 2011. The Green Bank Telescope H II Region Discovery Survey. II. The Source Catalog. *ApJ*, 194(2):32.

Anglada, G., Villuendas, E., Estalella, R., et al., 1998. Spectral Indices of Centimeter Continuum Sources in Star-forming Regions: Implications on the Nature of the Outflow Exciting Sources. *ApJ*, 116:2953.

Argon, A.L., Reid, M.J., and Menten, K.M., 2000. Interstellar Hydroxyl Masers in the Galaxy. I. The VLA Survey. *ApJS*, 129:159.

Arquilla, R. and Goldsmith, P.F., 1984. The molecular cloud associated with the infrared source GL 437. *ApJ*, 279:664.

Barentsen, G., Farnhill, H.J., Drew, J.E., et al., 2014. The second data release of the INT Photometric $H\alpha$ Survey of the Northern Galactic Plane (IPHAS DR2). *MNRAS*, 444(4):3230.

Becker, R.H., White, R.L., Helfand, D.J., et al., 1994. A 5 GHz VLA Survey of the Galactic Plane. *ApJ*, 91:347.

Becker, R.H., White, R.L., McLean, B.J., et al., 1990. A 20 Centimeter Survey of Compact Sources in the Northern Galactic Plane. *ApJ*, 358:485.

Becker, W. and Fenkart, R., 1971. A catalogue of galactic star clusters observed in three colours. *A&AS*, 4:241.

Benjamin, R.A., Churchwell, E., Babler, B.L., et al., 2003. GLIMPSE. I. An SIRTF Legacy Project to Map the Inner Galaxy. *PASP*, 115:953.

Bica, E., Dutra, C.M., and Barbuy, B., 2003. A Catalogue of infrared star clusters and stellar groups. *A&A*, 397:177.

Blair, G.N., Dinger, A.S.C., and Dickinson, D.F., 1980. Interstellar and stellar water maser emission. *ApJ*, 85:161.

Blum, R.D., Conti, P.S., and Damineli, A., 2000. The Stellar Content of Obscured Galactic Giant H II Regions. II. W42. *AJ*, 119(4):1860.

Bonnell, I.A., Bate, M.R., and Zinnecker, H., 1998. On the formation of massive stars. *MNRAS*, 298:93.

Borys, C., Chapman, S., Halpern, M., et al., 2003. The Hubble Deep Field North SCUBA Super-map - I. Submillimetre maps, sources and number counts. *MNRAS*, 344(2):385.

Braun, R., 2013. Understanding synthesis imaging dynamic range. *A&A*, 551:A91.

Braz, M.A., Lepine, J.R.D., Sivagnanam, P., et al., 1990. New OH sources associated with young stellar objects. *A&A*, 236:479.

Breen, S.L., Contreras, Y., Ellingsen, S.P., et al., 2018. The 6-GHz Multibeam Maser Survey - III. Comparison between the MMB and HOPS. *MNRAS*, 474(3):3898.

Bronfman, L., Nyman, L.A., and May, J., 1996. A CS(2-1) survey of IRAS point sources with color characteristics of ultra-compact HII regions. *A&A*, 115:81.

Brunthaler, A., Menten, K.M., Dzib, S.A., et al., 2021. A global view on star formation: The GLOSTAR Galactic plane survey. I. Overview and first results for the Galactic longitude range 28° < l < 36°. *A&A*, 651:A85.

Buckle, J.V. and Richer, J.S., 2015. Wide-field SCUBA-2 observations of NGC 2264: submillimetre clumps and filaments. *MNRAS*, 453:2006.

Calabretta, M.R., Staveley-Smith, L., and Barnes, D.G., 2014. A New 1.4 GHz Radio Continuum Map of the Sky South of Declination +25°. *PASA*, 31:e007.

Carpenter, J.M., Snell, R.L., and Schloerb, F.P., 1990. Molecular Clouds Associated with Luminous Far-Infrared Sources in the Outer Galaxy. *ApJ*, 362:147.

Carpenter, J.M., Snell, R.L., and Schloerb, F.P., 1995. Star Formation in the Gemini OB1 Molecular Cloud Complex. *ApJ*, 450:201.

Cesaroni, R., Palagi, F., Felli, M., et al., 1988. A catalogue of H2O maser sources north of delta = -30. *A&AS*, 76:445.

Chauhan, N., Pandey, A.K., Ogura, K., et al., 2009. Triggered star formation and evolution of T-Tauri stars in and around bright-rimmed clouds. *MNRAS*, 396:964.

Churchwell, E., Babler, B.L., Meade, M.R., et al., 2009. The Spitzer/GLIMPSE Surveys: A New View of the Milky Way. *PASP*, 121(877):213.

Condon, J.J., Cotton, W.D., Greisen, E.W., et al., 1998. RThe NRAO VLA Sky Survey. *ApJ*, 115:1693.

Coppin, K., Chapin, E.L., Mortier, A.M.J., et al., 2006. The SCUBA Half-Degree Extragalactic Survey - II. Submillimetre maps, catalogue and number counts. *MNRAS*, 372(4):1621.

Cutri, R.M., 2012. VizieR Online Data Catalog: WISE All-Sky Data Release (Cutri+ 2012). *VizieR*.

Cutri, R.M., Skrutskie, M.F., van Dyk, S., et al., 2003. VizieR Online Data Catalog: 2MASS All-Sky Catalog of Point Sources (Cutri+ 2003). *VizieR*.

Davidson, K. and Harwit, M., 1967. Infrared and Radio Appearance of Cocoon Stars. *ApJ*, 148:443.

De Pree, C.G., Gaume, R.A., Goss, W.M., et al., 1996. The Sagittarius B2 Star-forming Region. III. High-Resolution H52 alpha and H66 alpha Observations of Sagittarius B2 Main. *ApJ*, 464:788.

De Pree, C.G., Mehringer, D.M., and Goss, W.M., 1997. Multifrequency, High-Resolution Radio Recombination Line Observations of the Massive Star-forming Region W49A. *ApJ*, 482(1):307.

De Pree, C.G., Peters, T., Mac Low, M.M., et al., 2014. Flickering of 1.3 cm Sources in Sgr B2: Toward a Solution to the Ultracompact H II Region Lifetime Problem. *ApJ*, 781(2):L36.

De Pree, C.G., Peters, T., Mac Low, M.M., et al., 2015. Evidence of Short Timescale Flux Density Variations of UC HII Regions in Sgr B2 Main and North. *ApJ*, 815(2):123.

De Pree, C.G., Wilner, D.J., and Goss, W.M., 2011. Ionized Gas Kinematics and Morphology in Sgr B2 Main on 1000 AU Scales. *AJ*, 142(5):177.

Deharveng, L., Zavagno, A., Anderson, L.D., et al., 2012. Interstellar matter and star formation in W5-E. A Herschel view. *A&A*, 546:41.

Deharveng, L., Zavagno, A., Cruz-Gonzalez, I., et al., 1997. AFGL 4029: a cluster of massive young stars. *A&A*, 317:459.

Devine, K.E., Churchwell, E.B., Indebetouw, R., et al., 2008. A WIYN Near-Infrared Investigation of Three Massive Star-Forming Regions. *ApJ*, 135:2095.

Di Francesco, J., Johnstone, D., Kirk, H., et al., 2008. The SCUBA Legacy Catalogues: Submillimeter-Continuum Objects Detected by SCUBA. *ApJS*, 175:277.

Dickel, H.R. and Goss, W.M., 1990. VLA Observations of the 6 Centimeter and 2 Centimeter Lines of H 2CO in the Direction of W49. *ApJ*, 351:189.

Djordjevic, J.O., Thompson, M.A., Urquhart, J.S., et al., 2019. Beyond the solar circle - trends in massive star formation between the inner and outer galaxy. *MNRAS*, 487:1057.

Draine, B.T., Dale, D.A., Bendo, G., et al., 2007. Dust Masses, PAH Abundances, and Starlight Intensities in the SINGS Galaxy Sample. *ApJ*, 633,2:866.

Dreher, J.W., Johnston, K.J., Welch, W.J., et al., 1984. Ultracompact structure in the H II region W49N. *ApJ*, 283:632.

Drew, J.E., Lennon, D.J., Greimel, R., et al., 2005. IPHAS: Surveying the North Galactic Plane in Hα. *The Newsletter of the Isaac Newton Group of Telescopes*, 9:3.

Dunham, M.K., Robitaille, T.P., Evans, Neal J., I., et al., 2011. A Mid-infrared Census of Star Formation Activity in Bolocam Galactic Plane Survey Sources. *ApJ*, 731(2):90.

Dyson, J.E. and Williams, D.A., 1980. *Physics of the interstellar medium.* New York: Wiley & Sons.

Dyson, J.E., Williams, R.J.R., and Redman, M.P., 1995. Clumpy Ultra Compact HII Regions - Part One - Fully Supersonic Wind-Blown Models. *MNRAS*, 277:700.

Eddington, A.S., 1913. On a formula for correcting statistics for the effects of a known error of observation. *MNRAS*, 73:359.

Egan, M.P. and Price, S.D., 1996. The MSX Infrared Astometric Catalog. *AJ*, 112:2862.

Egan, M.P., Price, S.D., Kraemer, K.E., et al., 2003. VizieR Online Data Catalog: MSX6C Infrared Point Source Catalog. The Midcourse Space Experiment Point Source Catalog Version 2.3 (October 2003). *VizieR Online Data Catalog*, V/114.

Egan, M.P., Price, S.D., Shipman, R.F., et al., 1999. The MSX Infrared Point Source Catalog, Version 1. 0. In M.D. Bicay, R.M. Cutri, and B.F. Madore, editors, *Astrophysics with Infrared Surveys: A Prelude to SIRTF*, volume 177 of *Astronomical Society of the Pacific Conference Series*, page 404.

Elia, D., Merello, M., Molinari, S., et al., 2021. The Hi-GAL compact source catalogue - II. The 360° catalogue of clump physical properties. *MNRAS*, 504:2742.

Elia, D., Molinari, S., Schisano, E., et al., 2017. The Hi-GAL compact source catalogue - I. The physical properties of the clumps in the inner Galaxy (-71.0° < ℓ < 67.0°). *MNRAS*, 471:100.

Flaccomio, E., Micela, G., and Sciortino, S., 2006. ACIS-I observations of NGC 2264. Membership and X-ray properties of PMS stars. *A&A*, 455:903.

Gaia Collaboration, Brown, A.G.A., Vallenari, A., et al., 2018. Gaia Data Release 2. Summary of the contents and survey properties. *A&A*, 616:A1.

Gaume, R.A., Goss, W.M., Dickel, H.R., et al., 1995. The NGC 7538 IRS 1 Region of Star Formation: Observations of the H66 alpha Recombination Line with a Spatial Resolution of 300 AU. *ApJ*, 438:776.

Gershberg, R.E. and Pronik, V.I., 1959. On the Theory of Stromgren's Zones. *sovast*, 3:876.

Ginsburg, A., Bally, J., and Williams, J.P., 2011a. JCMT HARP CO 3-2 observations of molecular outflows in W5. *MNRAS*, 418:2121.

Ginsburg, A., Darling, J., Battersby, C., et al., 2011b. Galactic H2CO Densitometry. I. Pilot Survey of Ultracompact H II Regions and Methodology. *ApJ*, 736:149.

Girart, J.M., Curiel, S., Rodríguez, L.F., et al., 2002. Radio Continuum Observations towards Optical and Molecular Outflows. *RevMexAA*, 38:169.

Giveon, U., Becker, R.H., Helfand, D.J., et al., 2005. A New Catalog of Radio Compact H II Regions in the Milky Way. *AJ*, 129(1):348.

Goedhart et al., in prep. MeerKAT GPS: The MeerKAT 1.28 GHz Galactic Plane Survey. *MeerKAT*.

Green, A.J., Cram, L.E., Large, M.I., et al., 1999. The Molonglo Galactic Plane Survey. I. Overview and Images. *ApJ*, 122(1):207.

Green, D.A., 1984. Statistical studies of supernova remnants. *MNRAS*, 209:449.

Green, D.A., 1989. The DRAO galactic plane survey. I. l=140, b=0. *A&A*, 78:277.

Green, J.A., Breen, S.L., Fuller, G.A., et al., 2017. The 6-GHz multibeam maser survey - II. Statistical analysis and Galactic distribution of 6668-MHz methanol masers. *MNRAS*, 469(2):1383.

Green, J.A., Caswell, J.L., Fuller, G.A., et al., 2009. The 6-GHz multibeam maser survey - I. Techniques. *MNRAS*, 392(2):783.

Green, J.A., McClure-Griffiths, N.M., Caswell, J.L., et al., 2012. MAGMO: coherent magnetic fields in the star-forming regions of the Carina-Sagittarius spiral arm tangent. *MNRAS*, 425:2530.

Hales, C.A., Murphy, T., Curran, J.R., et al., 2012. BLOBCAT: software to catalogue flood-filled blobs in radio images of total intensity and linear polarization. *MNRAS*, 425:979.

Hancock, P.J., Murphy, T., Gaensler, B.M., et al., 2012. Compact continuum source finding for next generation radio surveys. *MNRAS*, 422:1812.

Hancock, P.J., Trot, C., and Hurley-Walker, N., 2018. Source Finding in the Era of the SKA (Precursors): Aegean 2.0. *PASA*, 35.

Harju, J., Lehtinen, K., Booth, R.S., et al., 1998. A survey of SiO emission towards interstellar masers. I. SiO line characteristics. *A&AS*, 132:211.

Hartl, H. and Tritton, S.B., 1985. New planetary nebulae of low surface brightness detected on UK-Schmidt plates. *A&A*, 145:41.

Heinze, A.N., Tonry, J.L., Denneau, L., et al., 2018. A First Catalog of Variable Stars Measured by the Asteroid Terrestrial-impact Last Alert System (ATLAS). *AJ*, 156(5):241.

Henkel, C., Wilson, T.L., and Mauersberger, R., 1987. A multilevel study of ammonia in star forming regions. II. G 34.3+0.2, a new "hot core". *A&A*, 182:137.

Heywood, I., Rammala, I., Camilo, F., et al., 2022. The 1.28 GHz MeerKAT Galactic Center Mosaic. *ApJ*, 925(2):165.

Hildebrand, R.H., 1983. The determination of cloud masses and dust characteristics from submillimetre thermal emission. *QJRAS*, 24:267.

Hindson, L., Thompson, M.A., Urquhart, J.S., et al., 2012. The G305 star-forming complex: a wide-area radio survey of ultracompact H II regions. *MNRAS*, 421:3418.

Hoare, M.G., Kurtz, S.E., Lizano, S., et al., 2007. Ultracompact Hii Regions and the Early Lives of Massive Stars. In B. Reipurth, D. Jewitt, and K. Keil, editors, *Protostars and Planets V*, page 181.

Hoare, M.G., Lumsden, S.L., Oudmaijer, R.D., et al., 2005. The RMS survey: Massive young stars throughout the galaxy. In R. Cesaroni, M. Felli, E. Churchwell, and M. Walmsley, editors, *Massive Star Birth: A Crossroads of Astrophysics*, volume 227, pages 370–375.

Hoare, M.G., Purcell, C.R., Churchwell, E.B., et al., 2012. The Coordinated Radio and Infrared Survey for High-Mass Star Formation (The CORNISH Survey). I. Survey Design. *PASP*, 124:939.

Høg, E., Fabricius, C., Makarov, V.V., et al., 2000. The Tycho-2 catalogue of the 2.5 million brightest stars. *A&A*, 355:L27.

Hosokawa, T. and Omukai, K., 2009. Evolution of Massive Protostars with High Accretion Rates. *ApJ*, 691(1):823.

Hosokawa, T., Yorke, H.W., and Omukai, K., 2010. Evolution of Massive Protostars Via Disk Accretion. *ApJ*, 721(1):478.

Jonas, J., 2018. The MeerKAT Radio Telescope. *PoS*, MeerKAT2016:001.

Kalcheva, I.E., Hoare, M.G., Urquhart, J.S., et al., 2018. The coordinated radio and infrared survey for high-mass star formation. III. A catalogue of northern ultra-compact H II regions. *A&A*, 615:A103.

Kauffmann, J., Bertoldi, F., Bourke, T.L., et al., 2008. MAMBO mapping of Spitzer c2d small clouds and cores. *A&A*, 487:993.

Kennicutt, R.C. and Evans, N.J., 2012. Star Formation in the Milky Way and Nearby Galaxies. *Annual Review of Astronomy and Astrophysics*, 50:531.

Keto, E., 2002. On the Evolution of Ultracompact H II Regions. *ApJ*, 580(2):980.

Keto, E., 2003. The Formation of Massive Stars by Accretion through Trapped Hypercompact H II Regions. *ApJ*, 599(2):1196.

Kim, K.T. and Koo, B.C., 2001. Radio Continuum and Recombination Line Study of Ultracompact H II Regions with Extended Envelopes. *ApJ*, 549(2):979.

Koempe, C., Baudry, A., Joncas, G., et al., 1989. Multi-line observations and analysis of the Sharpless 247/252 gas complex. *A&A*, 221:295.

Kolpak, M.A., Jackson, J.M., Bania, T.M., et al., 2003. Resolving the Kinematic Distance Ambiguity toward Galactic H II Regions. *ApJ*, 582(2):756.

Koo, B.C., Kim, K.T., Lee, H.G., et al., 1996. The H II Region Complex G5.48-0.24: Radio Continuum, H i, and CO Observations. *ApJ*, 456:662.

Krumholz, M.R., 2016. Notes On Star Formation. *The Open Astrophysics Bookshelf*.

Kuiper, R., Klahr, H., Beuther, H., et al., 2012. A solution to the radiation pressure problem in the formation of massive stars. *arXiv*, page 1211.7064.

Kurtz, S., 2002. Ultracompact H II Regions. *ASP*, 267:81.

Kurtz, S., 2005a. Hypercompact HII Regions. *IAU*, 227:111.

Kurtz, S., 2005b. The Young Massive Star Environment. *IAU*, 231:47.

Kurtz, S., Cesaronoi, R., Churchwell, E., et al., 2000. Hot Molecular Cores and the Earliest Phases of High-Mass Star Formation. *Protostars and Planets*, IV:299.

Kurtz, S., Churchwell, E., and Wood, D.O.S., 1994. Ultracompact H II Regions. II. New High-Resolution Radio Images. *ApJ*, 91:659.

Kurtz, S. and Franco, J., 2002. Ultracompact H II Regions. *RevMexAA(SC)*, 12:16.

Kurtz, S., Hofner, P., and Álvarez, C.V., 2004. A Catalog of CH3OH 70-61 A+ Maser Sources in Massive Star-forming Regions. *ApJS*, 155:149.

Kurtz, S.E., Watson, A.M., Hofner, P., et al., 1999. Ultracompact H II Regions with Extended Radio-Continuum Emission. *ApJ*, 514(1):232.

Ladd, E.F., Deane, J.R., Sanders, D.B., et al., 1993. Luminous Radio-quiet Sources in W3(Main). *ApJ*, 419:186.

Low, F.J. and Aumann, H.H., 1970. Observations of Galactic and Extragalactic Sources Between 50 and 300 Mi-Crons. *ApJ*, 162:L79.

Lucas, P.W., Hoare, M.G., Longmore, A., et al., 2008. The UKIDSS Galactic Plane Survey. *MNRAS*, 391(1):136.

Lumsden, S.L., Hoare, M.G., Oudmaijer, R.D., et al., 2002. The population of the Galactic plane as seen by MSX. *MNRAS*, 336(2):621.

Lumsden, S.l., Hoare, M.G., Urquhart, J.S., et al., 2013. The Red MSX Source Survey: The Massive Young Stellar Population of Our Galaxy. *ApJS*, 208:17.

MacKenzie, T., Braglia, F.G., Gibb, A.G., et al., 2011. A pilot study for the SCUBA-2 'All-Sky' Survey. *MNRAS*, 415:1950.

Maeder, A. and Meynet, G., 1987. Grids of evolutionary models of massive stars with mass loss and overshooting - Properties of Wolf-Rayet stars sensitive to overshooting. *A&A*, 182:243.

Mangum, J., Emerson, D., and Greisen, E., 2000. The On-The-Fly Imaging Technique. *ASP*, 217:179.

Marton, G., Tóth, L.V., Paladini, R., et al., 2016. An all-sky support vector machine selection of WISE YSO candidates. *MNRAS*, 458:3479.

Matsuyanagi, I., Itoh, Y., Sugitani, K., et al., 2006. Sequential Formation of Low-Mass Stars in the BRC 14 Region. *PASJ*, 58:L29.

McClure-Griffiths, N.M., Dickey, J.M., Gaensler, B.M., et al., 2005. The Southern Galactic Plane Survey: H I Observations and Analysis. *ApJ*, 158(2):178.

Meakin, C.A., Hines, D.C., and Thompson, R.I., 2005. Young Stars and Dust in AFGL 437: Hubble Space Telescope NICMOS Polarimetric Imaging of an Outflow Source. *ApJ*, 634:1146.

Medina, S.N.X., Urquhart, J.S., Dzib, S.A., et al., 2019. GLOSTAR: Radio Source Catalog I. 28° < ℓ < 36° and |b| < 1°. *A&A*, 627:A175.

Meehan, L.S.G., Wilking, B.A., Claussen, M.J., et al., 1998. Water Masers in the Circumstellar Environments of Young Stellar Objects. *ApJ*, 115:1599.

Mercer, E.P., Clemens, D.P., et al., et al., 2005. New Star Clusters Discovered in the GLIMPSE Survey. *ApJ*, 635:560.

Merello, M., Evans, Neal J., I., Shirley, Y.L., et al., 2015. The Bolocam Galactic Plane Survey. XI. Temperatures and Substructure of Galactic Clumps Based On 350 M Observations. *ApJS*, 218:29.

Messineo, M., Davies, B., Ivanov, V.D., et al., 2009. Near-Infrared Spectra of Galactic Stellar Clusters Detected on Spitzer/GLIMPSE Images. *ApJ*, 147:471.

Mezger, P.G., Altenhoff, W., Schraml, J., et al., 1967a. A New Class of Compact H II Regions Associated with OH Emission Sources. *ApJ*, 150:L157.

Mezger, P.G. and Henderson, A.P., 1967. Galactic H II Regions. I. Observations of Their Continuum Radiation at the Frequency 5 GHz. *ApJ*, 147:471.

Mezger, P.G., Schraml, J., and Terzian, Y., 1967b. Galactic H II Regions. III. The Nature of the Radio Source W49. *ApJ*, 150:807.

Mill, J.D., O'Neil, R.R., Price, S., et al., 1994. Midcourse space experiment: Introduction to the spacecraft, instruments, and scientific objectives. *Journal of Spacecraft and Rockets*, 31(5):900.

Moffat, A.F.J., 1972. Photmetry of eleven young open star clusters. *A&AS*, 7:355.

Molinari, S., Schisano, E., Elia, D., et al., 2016. Hi-GAL, the Herschel infrared Galactic Plane Survey: photometric maps and compact source catalogues. First data release for the inner Milky Way: $+68° \geq l \geq$ -70°. *A&A*, 591:A149.

Molinari, S., Swinyard, B., Bally, J., et al., 2010. Hi-GAL: The Herschel Infrared Galactic Plane Survey. *PASP*, 122(889):314.

Moore, T.J.T., Plume, R., Thompson, M.A., et al., 2015. The JCMT Plane Survey: early results from the $\ell = 30°$ field. *MNRAS*, 453(4):4264.

Morgan, W.W., Hiltner, W.A., Neff, J.S., et al., 1965. Studies in Spectral Classification. III. The H-R Diagrams of NGC 2244 and NGC 2264. *ApJ*, 142:974.

Murphy, T., Cohen, M., Ekers, R.D., et al., 2010. Ultra- and hyper-compact HII regions at 20 GHz. *MNRAS*, 405(3):1560.

Murphy, T., Mauch, T., Green, A., et al., 2007. The second epoch Molonglo Galactic Plane Survey: compact source catalogue. *MNRAS*, 382:382.

Neugebauer, G. and Garmire, G., 1970. Infrared Observations of the Nebula K3-50. *ApJ*, 161:L91.

Niwa, T., Tachihara, K., Itoh, Y., et al., 2009. Millimeter-wave survey of molecular clouds around the W5-East triggered star-forming region. *A&A*, 500:1119.

Norris, R.P., Hopkins, A.M., Afonso, J., et al., 2011. EMU: Evolutionary Map of the Universe. *PASA*, 28(3):215.

Oey, M.S., Watson, A.M., Kern, K., et al., 2005. Hierarchical Triggering of Star Formation by Superbubbles in W3/W4. *ApJ*, 219:393.

Ojha, D.K., Ghosh, S.K., Kulkarni, V.K., et al., 2004. A study of the Galactic star forming region IRAS 02593+6016/S 201 in infrared and radio wavelengths. *A&A*, 415:1039.

Palagi, F., Cesaroni, R., Comoretto, G., et al., 1993. Classification and statistical properties of galactic H2O masers. *A&A*, 101:153.

Palla, F. and Stahler, S.W., 1993. The Pre-Main-Sequence Evolution of Intermediate-Mass Stars. *ApJ*, 418:414.

Panagia, N., 1973. Some Physical parameters of early-type stars. *AJ*, 78:929.

Pandian, J.D., Goldsmith, P.F., and Deshpande, A.A., 2007. The Arecibo Methanol Maser Galactic Plane Survey. I. Data. *ApJ*, 656:255.

Perley, R.A., 1999. High Dynamic Range Imaging. In G.B. Taylor, C.L. Carilli, and R.A. Perley, editors, *Synthesis Imaging in Radio Astronomy II*, volume 180 of *Astronomical Society of the Pacific Conference Series*, page 275.

Peters, T., Banerjee, R., Klessen, R.S., et al., 2010a. H II Regions: Witnesses to Massive Star Formation. *ApJ*, 711(2):1017.

Peters, T., Klessen, R.S., Mac Low, M.M., et al., 2010b. Limiting Accretion onto Massive Stars by Fragmentation-induced Starvation. *ApJ*, 725(1):134.

Peters, T., Mac Low, M.M., Banerjee, R., et al., 2010c. Understanding Spatial and Spectral Morphologies of Ultracompact H II Regions. *ApJ*, 719(1):831.

Porras, A., Christopher, M., Allen, L., et al., 2003. A Catalog of Young Stellar Groups and Clusters within 1 Kiloparsec of the Sun. *AJ*, 126(4):1916.

Price, S.D., Carey, S.J., and Egan, M.P., 2002. The MSX galactic plane survey submillimeter results. *Advances in Space Research*, 30(9):2027.

Price, S.D., Egan, M.P., Carey, S.J., et al., 2001. Midcourse Space Experiment Survey of the Galactic Plane. *AJ*, 121(5):2819.

Purcell, C.R., Hoare, M. G.and Cotton, W.D., Lumsden, S.L., et al., 2013. The Coordinated Radio and Infrared Survey for High-mass Star Formation. II. Source Catalog. *ApJS*, 205:1 (22pp).

Rapson, V.A., Pipher, J., Gutermuth, R.A., et al., 2014. A Spitzer View of the Giant Molecular Cloud MON OB1 EAST/NGC 2264. *ApJ*, 794.

Reich, W., Fuerst, E., Haslam, C.G.T., et al., 1984. A radio continuum survey of the galactic plane at 11 cm wavelenght. I. The area 357.4 < or = L < or = 76, - 1.5 < or = B < or = 1.5. *A&A Supp.*, 58:197.

Reid, M.J., Menten, K.M., Brunthaler, A., et al., 2009. Trigonometric Parallaxes of Massive Star-Forming Regions. I. S 252 & G232.6+1.0. *ApJ*, 693:397.

Reipurth, B., Rodríguez, L.F., Anglada, G., et al., 2004. Radio Continuum Jets from Protostellar Objects. *ApJ*, 127:1736.

Rodriguez, L.F., Myers, P.C., Cruz-Gonzalez, I., et al., 1989. Radio Continuum Observations of IRAS Sources Associated with Dense Cores. *ApJ*, 347:461.

Romine, G., Feigelson, E.D., Getman, K.V., et al., 2016. Young Stellar Populations in MYStIX Star-forming Regions: Candidate Protostars. *ApJ*, 833.

Rosolowsky, E., Dunham, M.K., Ginsburg, A., et al., 2010. The Bolocam Galactic Plane Survey. II. Catalog of the Image Data. *ApJ*, 188:123.

Rubin, R.H., 1968. A Discussion of the Sizes and Excitation of H II Regions. *ApJ*, 154:391.

Ryle, M. and Downes, D., 1967. High-Resolution Radio Observations of an Intense H II Region in Cygnus X. *ApJ*, 148:L17.

Said, K., Kraan-Korteweg, R.C., Staveley-Smith, L., et al., 2016. NIR Tully-Fisher in the Zone of Avoidance - II. 21 cm H I-line spectra of southern ZOA galaxies. *MNRAS*, 457(3):2366.

Sánchez-Monge, Á., Beltrán, M.T., Cesaroni, R., et al., 2013. Different evolutionary stages in massive star formation. Centimeter continuum and H_2O maser emission with ATCA. *A&A*, 550:A21.

Saruwatari, O., Sakai, N., Liu, S.Y., et al., 2011. Compact Molecular Outflow From NGC 2264 CMM3: A Candidate for Very Young High-mass Protostar. *ApJ*, 729,2.

Schlingman, W.M., Shirley, Y.L., Schenk, D.E., et al., 2011. The Bolocam Galactic Plane Survey. V. HCO$^+$ and N$_2$H$^+$ Spectroscopy of 1.1 mm Dust Continuum Sources. *ApJ*, 195(2):14.

Schreyer, K., Stecklum, B., Linz, H., et al., 2003. NGC 2264 IRS 1: The Central Engine and Its Cavity. *ApJ*, 599:335.

Schuller, F., Menten, K.M., Contreras, Y., et al., 2009. ATLASGAL - The APEX telescope large area survey of the galaxy at 870 m. *A&A*, 504:415.

Sewilo, M., Churchwell, E., Kurtz, S., et al., 2004. Broad Radio Recombination Lines from Hypercompact H II Regions. *ApJ*, 605:285.

Shimoikura, T., Dobashi, K., Nakamura, F., et al., 2018. A Statistical Study of Massive Cluster-forming Clumps. *ApJ*, 855:28.

Shimoikura, T., Dobashi, K., Saito, H., et al., 2013. Molecular Clumps and Infrared Clusters in the S247, S252, and BFS52 Regions. *ApJ*, 768:27.

Sjouwerman, L.O. and Mills, E.A.C., 2013. Galactic kU-band Thermal Survey (GUTS). *arXiv*, 1312.6710.

Skrutskie, M.F., Cutri, R.M., Stiening, R., et al., 2006. The Two Micron All Sky Survey (2MASS). *AJ*, 131(2):1163.

Spitzer, L., 1978. *Physical processes in the interstellar medium.* New York: Wiley.

Stahler, S.W., Palla, F., and Ho, P.T.P., 2000. The Formation of Massive Stars. *Protostars and Planets*, IV:327.

Stahler, S.W., Shu, F.H., and Taam, R.E., 1980a. The evolution of protostars. I - Global formulation and results. *ApJ*, 241:637.

Stahler, S.W., Shu, F.H., and Taam, R.E., 1980b. The evolution of protostars. II - The hydrostatic core. *ApJ*, 242:226.

Strömgren, B., 1939. The Physical State of Interstellar Hydrogen. *ApJ*, 89:526.

Tan, J.C., Beltrán, M.T., Caselli, P., et al., 2014. Massive Star Formation. In H. Beuther, R.S. Klessen, C.P. Dullemond, and T. Henning, editors, *Protostars and Planets VI*, page 149.

Teixeira, P.S., Lada, C.J., Young, E.T., et al., 2006. Identifying Primordial Substructure in NGC 2264. *ApJ*, 636:L45.

Teixeira, P.S., Zapata, L.A., and Lada, C.J., 2007. A Dense Microcluster of Class 0 Protostars in NGC 2264 D-MM1. *ApJ*, 667:L179.

Thompson, A.R., Moran, J.M., and Swenson, George. W., J., 2017. Interferometry and Synthesis in Radio Astronomy, 3rd Edition. *A&A*.

Thompson, M., Goedhart, S., Goedhart, S., et al., 2016. MeerGAL: the MeerKAT Galactic Plane Survey. In *MeerKAT Science: On the Pathway to the SKA*, page 15.

Thompson, M.A., Hatchell, J., Walsh, A.J., et al., 2006. A SCUBA imaging survey of ultracompact HII regions. The environments of massive star formation. *A&A*, 453(3):1003.

Thompson, M.A., White, G.J., Morgan, L.K., et al., 2004. Searching for signs of triggered star formation toward IC 1848. *A&A*, 414:1017.

Thompson et al., in prep. The SCUBA-2 Ambitious Sky Survey: SASSy The Outer Galaxy from $l = 120 to 240$. *MNRAS*.

Tieftrunk, A.R., Gaume, R.A., Claussen, M.J., et al., 1997. The H II/molecular cloud complex W3 revisited: imaging the radio continuum sources using multi-configuration, multi-frequency observations with the VLA.. *A&A*, 318:931.

Urquhart, J.S., Busfield, A.L., Hoare, M.G., et al., 2007. The RMS survey. Radio observations of candidate massive YSOs in the southern hemisphere. *A&A*, 461(1):11.

Urquhart, J.S., Csengeri, T., Wyrowski, F., et al., 2014a. ATLASGAL - Complete compact source catalogue: 280°< < 60°. *A&A*, 568, A41:4.

Urquhart, J.S., Figura, C.C., Moore, T.J.T., et al., 2014b. The RMS survey: galactic distribution of massive star formation. *MNRAS*, 437,2:1791.

Urquhart, J.S., Hoare, M.G., Lumsden, S.L., et al., 2008. The RMS Survey: A Galaxy-wide Sample of Massive Young Stellar Objects. In H. Beuther, H. Linz, and T. Henning, editors, *Massive Star Formation: Observations Confront Theory*, volume 387 of *Astronomical Society of the Pacific Conference Series*, page 381.

Urquhart, J.S., Hoare, M.G., Purcell, C.R., et al., 2009a. The RMS survey. 6 cm continuum VLA observations towards candidate massive YSOs in the northern hemisphere. *A&A*, 501(2):539.

Urquhart, J.S., König, C., Giannetti, A., et al., 2018. ATLASGAL - properties of a complete sample of Galactic clumps. *MNRAS*, 473:1059.

Urquhart, J.S., Moore, T.J.T., Csengeri, T., et al., 2014c. ATLASGAL - towards a complete sample of massive star forming clumps. *MNRAS*, 443, 2:1555.

Urquhart, J.S., Morgan, L.K., Figura, C.C., et al., 2011. The Red MSX Source survey: ammonia and water maser analysis of massive star-forming regions. *MNRAS*, 418(3):1689.

Urquhart, J.S., Morgan, L.K., and Thompson, M.A., 2009b. Observational study of sites of triggered star formation. CO and mid-infrared observations. *A&A*, 497(3):789.

Urquhart, J.S., Thompson, M.A., Moore, T.J.T., et al., 2013. ATLASGAL - properties of compact H II regions and their natal clumps. *MNRAS*, 435:400.

Walsh, A.J., Breen, S.L., Britton, T., et al., 2011. The H_2O Southern Galactic Plane Survey (HOPS) - I. Techniques and H_2O maser data. *MNRAS*, 416(3):1764.

Walsh, A.J., Burton, M.G., Hyland, A.R., et al., 1998. Studies of ultracompact HII regions - II. High-resolution radio continuum and methanol maser survey. *MNRAS*, 301(3):640.

Wang, K.S., Bourke, T.L., Hogerheijde, M.R., et al., 2013. Dense molecular cocoons in the massive protocluster W3 IRS5: a test case for models of massive star formation. *A&A*, 558:16.

Wang, Y., Beuther, H., Zhang, Q., et al., 2012. Different Evolutionary Stages in the Massive Star-forming Region W3 Main Complex. *ApJ*, 754:22.

Ward-Thompson, D., Zylka, R., Mezger, P.G., et al., 2000. Dust emission from star-forming regions. VI. The submillimetre YSO cluster in NGC 2264. *A&A*, 355:1122.

Watanabe, Y., Sakai, N., López-Sepulcre, A., et al., 2017. Discovery of Striking Difference of Molecular-emission-line Richness in the Potential Proto-binary System NGC 2264 CMM3. *ApJ*, 847, 2.

Welch, W.J., Dreher, J.W., Jackson, J.M., et al., 1987. Star Formation in W49A: Gravitational Collapse of the Molecular Cloud Core toward a Ring of Massive Stars. *SCIENCE*, 238:1550.

White, R.L., Becker, R.H., and Helfand, D.J., 2005. New Catalogs of Compact Radio Sources in the Galactic Plane. *AJ*, 130(2):586.

Wienen, M., Wyrowski, F., Schuller, F., et al., 2012. Ammonia from cold high-mass clumps discovered in the inner Galactic disk by the ATLASGAL survey. *A&A*, 544:A146.

Wolf-Chase, G.A., Walker, C.K., and Lada, C.J., 1995. The Relationship of Dense Gas to Star Formation in the Monoceros OB1 Dark Cloud. *ApJ*, 442:197.

Wood, D., Churchwell, E., and Bieging, J., 1987. The Rotating and Collapsing Molecular Envelope of G34.25+0.14, the 'cometary' HII Region. In *Bulletin of the American Astronomical Society*, volume 19, page 726.

Wood, D.O.S. and Churchwell, E., 1989a. Massive Stars Embedded in Molecular Clouds: Their Population and Distribution in the Galaxy. *ApJ*, 340:265.

Wood, D.O.S. and Churchwell, E., 1989b. The Morphologies and Physical Properties of Ultracompact H II Regions. *ApJ*, 69:831.

Wouterloot, J.G.A., Brand, J., Burton, W.B., et al., 1990. IRAS sources beyond the solar circle. II. Distribution in the galactic warp. *A&A*, 230:21.

Wright, E.L., Eisenhardt, P.R.M., Mainzer, A.K., et al., 2010. The Wide-field Infrared Survey Explorer (WISE): Mission Description and Initial On-orbit Performance. *AJ*, 140(6):1868.

Xu, Y., Reid, M.J., Zheng, X.W., et al., 2006. The Distance to the Perseus Spiral Arm in the Milky Way. *Science*, 311:54.

Yang, A.Y., Thompson, M.A., Tian, W.W., et al., 2019. A search for hypercompact H II regions in the Galactic Plane. *MNRAS*, 482(2):2681.

Yang, A.Y., Urquhart, J.S., Thompson, M.A., et al., 2021. A population of hypercompact H II regions identified from young H II regions. *A&A*, 645:A110.

Young, E.T., Teixeira, P.S., Lada, C.J., et al., 2006. On the Formation of Massive Stars. *ApJ*, 642:972.

Zoonematkermani, S., Helfand, D.J., Becker, R.H., et al., 1990. A Catalog of Small-Diameter Radio Sources in the Galactic Plane. *ApJ*, 74:181.